Micro- and nanomechanical behavior of mullite-based environmental barrier coatings

Memory presented by

Carlos Alberto Botero Vega

Ph.D. Dissertation to opt for the degree of

Doctor in Materials Science by the Technical University of Catalonia

Advisors:

Luis Miguel Llanes Pitarch

Emilio Jimenez Piqué

Thesis developed at the Universitat Politècnica de Catalunya

Departament de Ciència dels Materials i Enginyeria Metal·lúrgica

2012

Acknowledgements

La culminación de los estudios doctorales es el mayor logro profesional que hasta ahora he alcanzado en mi carrera. Conseguirlo implicó emprender un viaje fuera de mi país, alejándome de mi gente y mis afectos. Una experiencia con episodios difíciles, pero también y sobre todo, otros inmensamente gratificantes en mi vida. Conseguirlo no hubiera sido posible sin la ayuda y el apoyo directo e indirecto de quienes me han rodeado durante todos estos años de investigación. A todos ellos quiero agradecer sincera, e infinitamente, y de antemano disculparme de inevitables e involuntarias omisiones..

En primer lugar, quiero hacer una mención especialmente a mis padres, Luz María y Libardo. Gracias por el apoyo constante, por enseñarme que el conocimiento es el bien más preciado que puede adquirirse; y a la vez, que en la vida todo lo que se quiere se puede conseguir con honestidad, nobleza, dedicación y empeño. Gracias por enseñarme a leer desde que era apenas un bebé, y por estimularme a hacerlo siempre. Por su honestidad y ejemplo. Por el cariño, acompañamiento y aprecio de siempre.

A mi hermano y mejor amigo Juan Felipe le estaré eternamente agradecido por el "aguante", complicidad e incondicionalidad, especialmente durante este último lustro. Por escucharme, entenderme y apoyarme en tantos buenos momentos, y en otros no tan buenos. Por enseñarme con el ejemplo y por sus consejos de hermano mayor. A mi hermana, gracias por todo. Por ser un ejemplo de independencia, coraje, personalidad e inteligencia. A toda mi gran y numerosa familia; tíos y tías, primos y primas, y a mi abuela. Viajar a mi Medellín a verlos y llenarme de su alegría y locura, fueron motivaciones de cada día y alicientes de cada año.

A mis tutores los profesores Dr. Luis Llanes y Dr. Emilio Jiménez por compartir su inteligencia y por transmitirme de manera tan clara su inmenso conocimiento y pasión por la mecánica de los materiales. Por el respaldo de siempre, observaciones, consejos, y sobre todo, la confianza constante e indeclinable en mi trabajo. Gracias Luis por la confianza y paciencia, por haberme permitido formarme como investigador, profesional y persona. Por las grandes ideas en cada reunión y conversación. Por señalar el mejor camino y solución de cada caso. A Emilio por las discusiones y el positivismo ante cada

situación. Por confirmar en mí la pasión por la investigación y la ciencia. Y por la cerveza. A ambos gracias por su amistad, y por ratificarme que la ciencia no tiene sentido sin un poco de humanidad.

Agradezco sinceramente a todos los miembros docentes, técnicos y estudiantes del CIEFMA, por el acompañamiento a lo largo de estos años. A su director el profesor Marc Anglada, y demás profesores del centro: Antonio Mateo, Nuria Salán y Gemma Fargas, por sus observaciones y consejos. A Francesc, Álvaro, Jordi y Fernando, por la disposición de ayudar siempre, y tantos consejos prácticos y científicos. Finalmente a todos mis compañeros y amigos, quienes me motivaron e inspiraron a seguir siempre adelante. Especialmente a Giselle (gracias por ser mi mejor amiga en estos años), Ravi (por tu amistad y por enseñarme a disfrutar del buen picante!), David (asere, gracias por los cafés de todos los días y las discusiones, los Barca Madrid, etc. Gracias Gemma, Astrid, Alexey, Zamir, Ana, y todos los demás. Finalmente agradezco a todos los PFCs con quienes tuve la fortuna de trabajar, gracias por toda la ayuda (Manel, Lucile, Toni, Guillermo, Rodrigo).

I wish to let constancy of my sincere acknowledgement to all the colleagues of the laboratory of manufacturing engineering, in the mechanical engineering department at Boston University. Thanks a million for all the help and support during my stages at BU. My respect to Professor Vinod Sarin. Thanks for allowing me to work in such an interesting field of CVD mullite coatings, and for receiving me in Boston. For the advices, encouragement and interest in my work. Tushar, Stephen and JiaPeng, thanks for the help, and for teaching me the CVD mysteries.

A los estudiantes del instituto de cerámica y vidrio del CSIC Olga Burgos, y Emilio Lopez Lopez por su ayuda. A la profesora Dra. Carmen Baudín por sus consejos, opiniones y ayuda.

A mis amigos del mundo que conocí en Barcelona les debo que mi experiencia estos años de doctorado haya sido maravillosa. Imposible mencionarlos a todos. Gracias totales.

A Anna, mi mejor amiga, mi esposa, la hermosa mamá de mi bebé. Tack sa mycket for min lilla prinsessa. Detta ar alla din.

List of acronyms and symbols

MEMS	Micro electromechanical systems
NEMS	Nano electromechanical systems
TBCs	Thermal Barrier Coatings
EBCs	Environmental Barrier Coatings
CVD	Chemical Vapor Deposition
AFM	Atomic force microscopy
FIB	Focused ion beam microscopy technique
CSM	Continuous stiffness measurement
XRD	X-Ray diffraction
OM	Optical Microscopy
SEM	Scanning Electron Microscopy
EDX	Energy dispersive X-ray spectroscopy
LSCM	Laser Scanning Confocal Microscopy
FESEM	Field Emission Scanning Electron Microscopy
$3Al_2O_3{\cdot}2SiO_2$	Chemical formula of mullite
h	Penetration depth

$\boldsymbol{P}$	Indenter normal force
$\boldsymbol{P_{max}}$	maximum indenter load
$\boldsymbol{P_m}$	Contact pressure or indentation stress
$\boldsymbol{P_c}$	Critical load for damage onset
$\boldsymbol{S}$	Contact stiffness
$\boldsymbol{H}$	Hardness
$\boldsymbol{H_f}$	Intrinsic film hardness
$\boldsymbol{H_s}$	Intrinsic substrate hardness
$\boldsymbol{H_a}$	Apparent
$\boldsymbol{E}$	Elastic modulus
$\boldsymbol{E_s}$	Intrinsic substrate elastic modulus
$\boldsymbol{E_f}$	Intrinsic film elastic modulus
$\boldsymbol{E_{red}}$	Reduced elastic modulus
$\boldsymbol{E_a}$	Apparent elastic modulus
$\boldsymbol{G_{int}}$	Energy of adhesion
$\boldsymbol{K_c}$	Indentation fracture toughness of the material of interest
$\boldsymbol{K_{int}}$	Interface fracture toughness
$\boldsymbol{K_f}$	Intrinsic film fracture toughness
$\boldsymbol{K_c^0}$	Fracture toughness corrected by the effect of the residual stresses
$\boldsymbol{K_{\sigma_r}}$	Stress intensity factor due to σ_r
$\boldsymbol{K_c^1}$	Fracture toughness corrected by the residual stresses plus the substrate influence
$\boldsymbol{\sigma_y}$	Yield strength

r_{sph}	Radius of the indenter
a	Contact radius.
τ	Shear stress of around
c	Total crack length
h_c	Contact depth
h_f	Final displacement after unloading
ε	Constant depending on the indenter geometry
v	Poisson ratio
α	Indenter constant in toughness calculation
a	Crack length
t	Coating thickness
σ_r	Residual stresses
ψ	Crack geometric factor
e	Ellipticity of cracks
F_c	Geometric factor, function of the ellipticity of the radial crack e
$f_{\sigma r}$	Factor due to residual stresses, function of the geometric factor $\psi(e,a/d)$ and e.
ν_f	Film Poisson ratio
σ-ε	Stress strain
l	Scratch length
l_{max}	Scratch length
α	Coefficient of Thermal Expansion

ξ_v^R	Calibration coefficient depending on the type of indenter and crack geometry.
r_{del}	Equivalent delamination radius
V_I	Indentation volume
d_c	Critical scratch track width at interface delamination
μ	Friction coefficient

Abstract

Advanced turbine gas systems demand materials resistant to high temperatures and aggressive conditions. Traditionally, turbine components were based on superalloys coated with ceramic materials catalogued as thermal barrier coatings (TBCs). Nevertheless, these systems reached their maximum temperature limit. Si-based ceramics arose as excellent candidates to replace TBCs coated superalloys because their higher temperature resistance, excellent mechanical properties at high temperatures and lower density, improving efficiency and environment friendly operation. However, Si-based materials were found to be susceptible to hot corrosion and recession in aggressive combustion environments.

Mullite coatings deposited by chemical vapor deposition (CVD) have been introduced and proven as excellent candidates to protect Si-based substrates; especially silicon carbide (SiC), from severe pitting corrosion and recession, becoming part of the new generation of environmental barrier coatings (EBCs). In these coatings mullite columns nucleate from a thin vitreous silicon layer in contact with the substrate. Once nucleated, mullite can grow over a wide range of increasing Al/Si ratios in constant or graded compositions. This feature allows for obtaining Al-rich mullite coatings at the outer surface in contact with corrosive atmospheres (conferring superior corrosion protection to the substrate) while keeping the stoichiometric composition at the interface (representing great adhesion because of the good match of mullite with SiC). Although the excellent performance of these coatings in corrosive environments has been proved through extensive characterization, information gathered from open literature about the mechanical behavior of these systems is quite limited.

The mechanical properties and structural integrity of CVD mullite coatings on SiC substrates are key issues facing the implementation of these systems in real applications. The study of such aspects constitutes the basis of this investigation. Considering the compositional variations, microstructure and thickness of CVD mullite coatings, from a structural standpoint it is essential to evaluate their mechanical properties, and the structural integrity of the coated system, from a local perspective. In this regard, nanoindentation and nanoscratch appear as the most suitable techniques for this purpose.

Within the framework of the above ideas, this investigation is based on implementing nanoindentation and nanoscratch tests, together with advanced material characterization techniques, to evaluate the main local (micro/nano) mechanical properties of mullite-based EBCs and to investigate the structural integrity of the coated systems. In doing so, columnar mullite coatings composed of stoichiometric (≈ 3) and increasing (≈ 5 , 6 , 7 , 8, 1 1)Al/Si ratios, as well as compositionally graded coatings, were accounted for. From a mechanical standpoint, special attention is paid to the different features ascribed to the studied coated systems: coatings architecture (i.e. columnar configuration), residual stresses and compositional changes. Therefore, three approaches here referred to as “Top”, “Wedge” and “Cross-sectional”, directly linked to the testing methodology (nanoindentation and nanoscratch tests), are implemented.

Regarding the stoichiometric mullite coatings, main mechanical properties; i.e. hardness (H_f), elastic modulus (E_f), yield strength (σ_y) and fracture toughness (K_f), are asessed in relatively thick and thin film specimens by means of nanoindentation. As a consequence of the columnar nature of coatings as well as the vitreous silicon layer from which they grow, properties were found to be slightly lower than the ones reported for bulk stoichiometric mullite. Also, properties ascribed to the coated system intended as a structural unit such as energy of adhesion per unit area (G_{int}) and interface fracture toughness (K_{int}), are assessed. Nanoscratch tests demonstrate great resistance of coatings to the sliding contact, as considerable plastic deformation ocurrs without significant damage.

The effect of coating composition on its mechanical behavior is studied through evaluation of specimens with increasing Al/Si ratios. Nanoindentation's results indicate that the effect of the enrichment in Al is to increase hardness and stiffness of mullite coatings. Also, a consequent enbrittelment is evidenced. Nevertheless, nanoscratch tests show that, despite of the increase in cracking evidenced in coatings with higher Al/Si ratios, structural integrity of the systems is satisfactory since no complete loss of the coating material is registered under the load spectrum analysed.

An enhancement in H_f and E_f with increasing Al-content is evidenced through the thickness of coatings with graded compositions. By performing nanoscratch tests in the cross section, compositionally graded mullite coatings studied in this work present an optimum combination of stiffness/hardness and cohesive/adhesive scratch strength, as compared to coatings with stoichiometric or extreme Al-enriched compositions.

Finally, considering the potential application of CVD mullite coatings as environmental barriers, the influence of temperature and corrosion influences on the mechanical behavior of the coated systems are investigated. In stoichiometric mullite, the effect of high temperature is an increase in H_f and E_f, accompanied by a decrease in K_c, whereas none of these properties are altered for Al-rich mullite. Also, H_f and E_f remain unaltered for the compositionally graded coating under the same conditions. In addition, effect of temperature and hot-corrosion on the structural integrity of tested coatings, as asessed by nanoscratch tests, may also be considered as negligible. This is an interesting finding as CVD mullite coatings are expected to be used in gas turbines, under similar conditions.

Resumen

En algunas aplicaciones como en turbinas de gas para la generación de electricidad, se requieren materiales con resistencia a altas temperaturas. Es por ello que tradicionalmente algunos componentes de dichas turbinas se fabrican a partir de superaleaciones recubiertas con materiales cerámicos conocidos como barreras térmicas (TBCs). Sin embargo, estos sistemas alcanzaron su temperatura máxima de operación. Como consecuencia de ello, se propuso utilizar materiales cerámicos basados en silicio para reemplazar las superaleaciones recubiertas con TBCs, dado que éstos conservan sus propiedades mecánicas a altas temperaturas y presentan baja densidad, lo que deviene en procesos de generación de electricidad más eficientes y amigables con el medio ambiente.

Los recubrimientos de mullita depositados utilizando la técnica de deposición química de vapor (CVD) han sido propuestos como excelentes candidatos para proteger sustratos de carburo de silicio (SiC) de la corrosión y recesión, configurando la nueva generación de recubrimientos catalogados como barreras ambientales (EBCs). En estos recubrimientos, columnas de mullita nuclean a partir de una fina capa vítrea rica en silicio en contacto con el sustrato. Una vez nucleados, los recubrimientos pueden crecer en un amplio rango de composiciones, siendo posible incrementar la proporción Al/Si de manera constante y gradiente. De este modo se obtienen recubrimientos de mullita ricos en aluminio en la superficie exterior en contacto con las atmósferas corrosivas (confiriendo al sustrato una alta protección frente a la corrosion) y a su vez se mantiene la composición estequiométrica en la intercara (lo que supone gran adhesion dado el buen ajuste de la mullita con el SiC). A pesar de que se ha demostrado el excelente desempeño frente a la corrosion de estos recubrimientos, la información existente en la literatura acerca de su comportamiento mecánico es limitada.

Sin duda las propiedades mecánicas e integridad estructural de los recubrimientos de mullita depositados sobre SiC son factores cruciales a la hora de implementar dichos sistemas en aplicaciones reales. El estudio de dichos aspectos constituye la base de esta investigación. Desde el punto de vista estructural, y teniendo en cuenta las variaciones composicionales, microstructura y espesor de estos recubrimientos, resulta esencial evaluar sus propiedades mecánicas, así como la integridad estructural del sistema recubierto, desde una perspectiva local. En este sentido, la nanoindentación y el nanorayado son las técnicas más apropiadas para tal propósito.

En el marco de las ideas planteadas anteriormente, esta investigación se basa en la implementación de ensayos de nanoindentación y nanorayado, en complemento con técnicas avanzadas de caracterización de materiales, para evaluar a escala local las principales propiedades mecánicas de recubrimientos de barrera ambiental basados en mullita, así como para evaluar la integridad estructural de los sistemas recubiertos. Para ello, se dispuso de recubrimientos de mullita con composiciones de Al/Si estequiométricas (≈ 3), e incrementales (≈ 5, 6, 7, 8, 11), así como de recubrimientos de composición gradiente. Desde una óptica mecánica, se hace especial énfasis en las diferentes características de los recubrimientos estudiados: arquitectura columnar, tensiones residuales y cambios composicionales. Para su caracterización, se implementan tres enfoques directamente ligados a la metodología de ensayo, catalogados como “Superficial”, en “Cuña” y de “Sección transversal”.

En cuanto a los recubrimientos de composición estequiométrica, sus principales propiedades mecánicas, es decir: dureza (H_f), modulo elastico (E_f), límite elastico (σ_y) y tenacidad de fractura (K_f), se estiman mediante nanoindentación. Como consecuencia del carácter columnar de los recubrimientos, así como de la capa vítrea de silicio a partir de la cual ellos crecen, las propiedades mecánicas encontradas son ligeramente menores que las reportadas para mullita estequiométrica policristalina. Se estiman también las propiedades mecánicas relativas al sistema recubierto entendido como una unidad estructural, tales como la energía de adhesión (G_{int}) y la tenacidad de fractura de la

intercara (K_{int}). Los ensayos de nanorayado demuestran una alta resistencia de los recubrimientos al contacto deslizante, dado que soportan deformaciones plásticas considerables sin una generación importante de daño.

El efecto de la composición de los recubrimientos en su comportamiento mecánico es estudiado mediante la evaluación de muestras con composiciones Al/Si incrementales. Los resultados de nanoindentacion indican que el efecto del enriquecimiento en aluminio es el endurecimiento y el aumento en la rigidez de los recubrimientos de mullita. De igual manera se evidencia una fragilización de los mismos. No obstante, los ensayos de nanorayado demuestran que, pese al agrietamiento incremental que se evidencia en los recubrimientos al aumentar la proporción Al/Si, la integridad estructural del sistema puede catalogarse como satisfactoria, dado que no se observan pérdidas significativas de material de recubrimiento en el espectro de cargas analizado.

En recubrimientos de composición gradiente es posible observar un incremento en la dureza y el módulo elástico con el incremento en el contenido de aluminio a través del espesor. Mediante la implementación de ensayos de nanorayado sobre las secciones transversales de diferentes sistemas, es posible determinar que los recubrimientos de composición gradiente estudiados en esta investigación presentan una combinación óptma de rigidez/dureza y resistencia adhesiva/cohesiva al nanorayado, en comparación con sus contrapartes de composición estequiométrica o rica en aluminio.

Finalmente, y considerando la aplicación potencial de los recubrimientos de mullita depositados por CVD como barreras ambientales, se investigan la influencia de la temperatura y la corrosión sobre el comportamiento mecánico de dichos recubrimientos. Las altas temperaturas ocasionan un incremento de H_f y E_f, acompañado por una caida en K_c, en recubrimientos estequiométricos, mientras que dichas propiedades permanecen prácticamente constantes para recubrimientos ricos en aluminio. H_f y E_f permanecen también prácticamente inalterados para el caso de los recubrimientos de composición gradiente. Adicionalmente, el efecto combinado de la alta temperatura y la corrosión sobre la integridad estructural de los recubrimientos ensayados puede ser

considerado como menor tras los ensayos de nanorayado realizados. Éste es un resultado interesante dado que estos recubrimientos se espera que sean utilizados en aplicaciones bajo las condiciones similares a las aquí estudiadas.

Table of contents

1 Chapter Introduction *1*

1.1 Thesis Overview and Layout **1**

1.2 Micro- and nanomechanics of coatings **7**

1.2.1 Introduction to nanoindentation 7

1.2.2 Contact Mechanics 14

1.2.3 Micro- and nano- mechanical properties 20

1.2.4 Nanoindentation of coatings and thin films 28

1.3 Environmental barrier coatings (EBCs): The case of mullite **50**

1.3.1 Introduction to the CVD mullite/SiC system 50

1.3.2 Silicon Carbide 59

1.3.3 Mullite 60

1.4 References **68**

2 Chapter Objectives *79*

3 Chapter Experimental procedure *81*

3.1 Chemical vapor deposition of coatings **81**

3.1.1 CVD reactor 82

3.1.2 Coatings deposition 83

3.2 Microstructural characterization of coatings **87**

3.2.1 Composition and samples designation 87

3.2.2 Microstructure 89

3.3 Preparation of specimens **91**

3.3.1 Surface approach 92

3.3.2 Cross-sectional and wedge approaches 94

3.4 Mechanical characterization **96**

3.4.1 Testing methodologhy 96

3.4.2 Nanoindentation 97

3.4.3 Nanoscratch 99

3.5 Characterization of imprints and induced damage **100**

3.5.1 Laser Scanning Confocal Microscopy (LSCM) 100

3.5.2 Atomic Force Microscopy (AFM) 102

3.5.3 Focused Ion Beam microscopy (FIB) 103

3.5.4 3D focused ion beam tomography (3D FIB tomography) 104

3.6 Thermal treatments and corrosion **105**

3.6.1 Long term stability 105

3.6.2 Thermal shock 105

3.6.3 Corrosion 106

3.7 References 106

4 Chapter Micro- and nanomechanical properties of stoichiometric $3Al_2O_3{\cdot}2SiO_2$ coatings and performance of the system $3Al_2O_3{\cdot}2SiO_2$/SiC 109

4.1091 Introduction 109

4.2 111Experimental procedure 111

4.2.1 Nanoindentation tests 111

4.2.2 Nanoscratch tests 113

4.2.3 FIB cross-sectioning and 3D tomography 115

4.3 Mechanical behavior of $3Al_2O_3{\cdot}2SiO_2$ thin films and thick coatings 116

4.3.1 Hardness and elastic modulus of the SiC substrate 116

4.3.2 Apparent elastic modulus and hardness of the $3Al_2O_3{\cdot}2SiO_2$ thin films 117

4.3.3 Spherical nanoindentation stress-strain curves 122

4.3.4 Intrinsic hardness, elastic modulus and yield strength of the $3Al_2O_3{\cdot}2SiO_2$ film 123

4.3.5 Hardness and elastic modulus of $3Al_2O_3{\cdot}2SiO_2$ thick coatings 127

4.4 Structural integrity and mechanical performance of the system $3Al_2O_3{\cdot}2SiO_2$/SiC 131

4.4.1 Nanoindentation tests 131

4.4.2 Nanoscratch tests 142

4.5 Summary 157

4.6 References 160

5 Chapter Influence of the Al/Si ratio on the mechanical properties of the$3Al_2O_3{\cdot}SiO_2$ coatings:Al-rich compositions 165

5.1 Introduction 165

5.2 Experimental procedure 166

5.3 Results 167

5.3.1 Hardness and elastic modulus 167

5.3.2 Fracture toughness 170

5.3.3 Sliding contact resistance 175

5.4 Discussion 183

5.4.1 Influence of composition on H_f and E_f 188

5.4.2 Influence of composition on K_c 185

5.4.3 Influence of composition on sliding contact resistance 186

5.5 Summary 190

5.6 References 191

6 Chapter Influence of the composition on mechanical properties of functionally graded $3Al_2O_3{\cdot}SiO_2$ coatings 193

6.1 Introduction 194

6.2 Experimental 195

6.2.1 Composition of graded samples 195

6.2.2 Cross-sectional and wedge nanoindentation 195

6.2.3 Coating separation 197

6.2.4 Cross- sectional nanoscratch 198

6.3 Results and Discussion 199

6.3.1 Compositional profile of graded samples 199

6.3.2 Hardness and Stiffness 200

6.3.3 Cohesive and Adhesive Strength 207

6.4 Summary 219

6.5 References 219

7 Chapter Influence of temperature and corrosion on mechanical properties and structural integrity of mullite EBCs 215

7.1 Introduction 215

7.1.1 Thermal stability of CVD mullite coatings 215

7.1.2 Thermal shock of CVD mullite coatings 217

7.1.3 Corrosion of CVD mullite coatings 217

7.1.4 Temperature and corrosion effects on mechanical behavior of CVD mullite coatings 218

7.2 Experimental procedure 218

7.3 Influence of temperature on mechanical properties 219

7.3.1 Thermal stability test 219

7.3.2 Thermal shock 228

7.4 Influence of corrosion on mechanical properties 230

7.4.1 Hardness and elastic modulus 230

7.4.2 Structural integrity 231

7.5 Conclusions 233

7.6 References 234

8 Chapter Conclusions 237

9 Chapter Future Work 241

List of Figures

Chapter 1

Figure 1. *Transition from macro- to micro/nano- length scale in systems and components: (a) electron beam physical vapor deposited EB-PVD thermal barrier coating and temperature reduction in a turbine blade[3], (b) mullite environmental barrier coating deposited on SiC by chemical vapor deposition; and (c) MEMs device[1].* 2

Figure 2. *(a) Profiles of the main parameters involved in the nanoindentation tests, P and h, as a function of time[16], and (b) the typical P vs h curve representing the complete nanoindentation cycle, i.e. loading and unloading stages. P_{max} is the maximum indentation load, P_0 is the small residual load (~3-5% of P_{max}), τ_{up} is the duration of the active loading, τ_{cr} is the duration of exposure under constant load, τ_{down} is the time span increment corresponding to the unloading stage, h_{max} is the maximum indentation depth, Δhcr is the increment of the indentation depth due to the creep, Δh_e is the magnitude of the elastic recovery, $\Delta h_{v\text{-}e}$ is the magnitude of the viscoelastic recovery, and Δh is the total recovery.* 8

Figure 3. *Relative contributions of the plastic deformation to the formation of an indentation as the load P is increased, and a change of the corresponding stage of the penetration during the indentation process.[16]* 9

Figure 4. *General scheme of a nanoindenter, (1) load cell, (2) displacement sensor, (3) indenter, (4) springs of the rod suspension, (5) measuring head body, (6) controller assembly, (7) computer, (8) sample, and (9) objective stage.[16]* 11

Figure 5. *(a) Scheme of Blunt and Sharp indenters. Schemes of the tip geometry and some geometrical parameters, as well as SEM pictures of real examples of (b) Spherical, (c) Berkovich and (d) Cube corner indenters.* 12

Figure 6. *Scheme of spherical contact.* 15

Figure 7. *(a) Generic example of an indentation stress-strain curve. (b) Lines of maximum shear stress τ in the plane of the axial section and its dependence with the penetration depth[16].* 17

Figure 8. *Different cracks paths for Vickers indentation: (1) "Palmqvist" radial crack, (2) median crack, (3) lateral crack, and (4) half-disk crack. (a) Top view and (b) cross-section through the center of the indentation. Berkovich indentation: (c) cross-sectional view of a Palmqvist type cracking, (d) top view of cracking for a Berkovich indentation.* 19

Figure 9. *Main quantities involved in the Oliver and Pharr method[50] for (a) a complete nanoindentation cycle, and (b) physical phenomenon taking place during the nanoindentation process.* 21

Figure 10. *Stress-strain curves obtained from spherical nanoindentation of (a) single crystals of YBCO textured by the Bridgman technique[58] and (b) porous nanocrystalline zirconia[24]. (c,d) Respective P-h curves showing "Pop-In" events and a Hertzian fit.* 25

Figure 11. *Elastic and plastic deformation fields for indentations of relatively "thick" coatings (a, small h/t ratios) and thin films (b, high h/t ratios).* 30

Figure 12. *(a) Scheme of the variation of H with the parameter h/t (normalized thickness) for two generic coated systems: hard thin film/soft substrate and soft thin film/ hard substrate. (b) Variation of E_{red} with h/t for the coated systems stiff thin film/compliant substrate and compliant thin film/ stiff substrate.* 32

Figure 13. *Configuration of different models for E_{film} calculation. "Song and Pharr" (a), "Hay and Crawford" (b), "Saha and Nix" (c) and "Bec et al." (d) models.* 35

Figure 14. *(a) General scheme denoting the ellipticity (e) of a radial crack induced by the sharp indentation of a stressed film. Examples of e in cracks produced by Vickers indentation at different loads (b) P= 0.98 N and (c) P= 4.9 N on a glass coating on a metal substrate*[83]. 37
Figure 15. *(a) Geometric factor F_c as a function of the ellipticity of the radial crack e and (b) factor due to residual stresses $f_{\sigma r}$ as a function of the geometric factor ψ(e,a/d) and e.* 38
Figure 16. *Differences in nanoindentation hardness, as a function of the indentation depth, due to the effect of coating microstructure for a zirconia doped with 8% yttria TBC on a nickel superalloy.*[66] 39
Figure 17. *Configuration of some of the principal methods for assessment of thin film adhesion evaluation. (a) Superlayer test*[11]*, (b) Bulge test*[11]*, (c) Four-point bending tests*[22]*, (d) Double cantilever beam test*[22]*, (e) Microcantilever deflection test*[22] *and (f) Cross-section indentation test*[22,96]. 44
Figure 18. *(a) Schemes of events occurring during nanoindentation of soft films, i. No buckling during indentation, ii. double-buckling during indentation and iii. single-buckling after indenter removal*[11]*. (b) Corresponding FIB cross-sections of the indents in the Cu/SiO_2 system*[11]*. (c) Schemes of events occurring during nanoindentation of brittle coated systems*[22]. 45
Figure 19. *(a) Schemes and real micrographs of the nanoscratch functioning. (b) Nanoscratch at i. relatively low loads and ii. relatively high loads in amorphous carbon films*[99]*. (c) Scratch buckling cracking, (d) buckling spallation, and (c) chipping of DLC films on steel substrates. Extracted from ASTM C1624-05.* 49
Figure 20.*Section of a gas turbine engine*[100]. 51
Figure 21. *Evolution and improvements in the last 60 years of the turbine firing temperatures and its materials, processing techniques, and protective methods.*[101] 51
Figure 22. *A compact gas micro-turbine and its elements.*[101] 52
Figure 23. *(a) Ceramic combustor* [108]*. (b) Different gas turbine parts of Si_3N_4. (c) Uncoated SiC hot corrosion*[7]. 54
Figure 24. *(a) Plots of weight gain vs. exposure time for uncoated (Δ) and coated (x) SiC fibres and (b) the appearance of the cross-section of both specimens after exposure to combustion environments containing $NaSO_4$ at 1200°C for 100 h.*[121] *(c) Optical cross-section micrograph of an uncoated and (d) mullite coated SiC exposed to an acidic Fe based coal slag after 300 h at 1260ºC.*[6] 56
Figure 25. *Binary Al_2O_3-SiO_2 phase diagram, where the narrow compositional gap is highlighted*[127]. 60
Figure 26. *(a) [001] Projection of the unit cell of sillimanite and (b) derivated structure of mullite.*[136] *3D structure of sillimanite in projections down the (c) c axis and (d) b axis.*[134,135] 61
Figure 27. *Schematic of the variation growth rate and microstructure of CVD mullite coatings with increasing deposition temperature, total pressure and metal chloride pressure*[6,121]. 63
Figure 28. *(a) Cross-section of a compositionally graded mullite coating etched to reveal its microstructure and (b) corresponding composition profile in terms of Al/Si ratio. (c) Bush like microstructure formed at high Al/Si compositions.* 65

Chapter 3

Figure 1. *(a) CVD unit. Hot wall reactor, (b) vacuum pump, (c) mobile furnace, (d) mass flow controllers (e) aluminium chips and container tube, (f) system for production of $AlCl_3$, (g) control panel and (h) neutralizing tank.* 82
Figure 2. *(a) Typical XRD spectrum found for very thin and (b,c) thicker stoichiometric mullite coatings.* 85
Figure 3. *(a-d) Different powder formations found on the top surface of deposited coatings in the deposition stage, and (e-h) coatings without considerable powder deposition.* 86
Figure 4. *(a) Micrographs and element maps obtained by means of EDX analysis of cross-sections of different samples showing absence of silicon and (b,c) presence of silicon in the coatings.* 87
Figure 5. *Microstructure of the coatings after etching. Samples M3-III (a), M5 (b), M6 (c), M7 (d), M8 (e) and Graded-I (f).* 89

Figure 6. *(a)Typical columnar microstructure of coatings. (a) Confocal micrograph of a partially etched cross-section in sample M11. (b) Optical and (c)confocal micrographs of the fully etched cross-section of sample Graded-I . (d) Detail of a corner for sample Graded-I.* 90
Figure 7. *(a,b) 3D Confocal micrographs and profiles of the top surfaces of the sample Changing, and (c) M11 in the "As-deposited" state.* 92
Figure 8. *(a) Images and profile of top surface for M3 specimen before and (b,c) after two steps of polishing. The decrease of roughness is clear. These images were obtained by interferometry.* 93
Figure 9. *(a) Configuration of the cast cross-section, and (b) the wedge of samples. Corresponding micrographs of the resulting polished surfaces are also shown.* 94
Figure 10. *(a) 3D confocal micrographs showing the lack of planarity in a cross-section due to the differences in hardness of the components, and (b) a flat cross-section optimum for the nanoindentation tests. (c) Roughness in the coating after the polishing process, as measured through confocal microscopy.* 95
Figure 11. *(a) Scheme of the "Top", (b) "Cross-sectional" and (c) "Wedge" approaches for the nanoindentation and nanoscratch tests together with corresponding micrographs.* 96
Figure 12. *Nanoindentation equipment used for the mechanical characterization.* 97
Figure 13. *(a) Scheme of the principle of a laser scanning confocal microscope[32]. (b) LSCM used in this thesis: Olympus LEXT OLS 3100.* 101
Figure 14. *(a) Scheme of the principle of functioning of an atomic force microscope[33]. (b) AFM used in this thesis, Veeco Dimension 3100.* 103
Figure 15. *(a) Schematic illustration of a dual beam FIB instrument and its principle[34]. (b) FIB used, Zeiss Neon 40.* 103

Chapter 4

Figure 1. *Scheme illustrating the conditions used for nanoindentation and nanoscratch tests performed on thin films and thick coatings.* 114
Figure 2. *Schematic of the FIB sequential sectioning for 3D tomography. Gallium ions are bombarded perpendicular to the sample surface and 2D xy images are taken with the coupled SEM at 54° respect to the surface. A volume of material comprising the nanoindentation imprint and cracking is analyzed.* 115
Figure 3. *Partial FIB 3D tomography superimposed to a x-y 2D cross-section. The microstructural features involved in the tomography construction such as the "Indentation imprint", the film/substrate "Interface" and the subsurface "Crack" are identified.* 116
Figure 4. *LSCM images of indentations performed on uncoated SiC at (a) h_{max} = 1000 nm, (b) h_{max} = 300 nm and 100 nm.* 117
Figure 5. *Average (a) H_s vs h and (b) E_s vs h curves of the uncoated SiC for indentations at h_{max} = 1000 nm (●), 300 nm (▲) and 100 nm (■).* 118
Figure 6. *(a) FIB cross-section of a Berkovich nanoindentation performed on sample M3thin at h_{max} = 1000 nm. Higher magnification micrographs of the (b) left and (c) right sides of the imprint cross-section.* 119
Figure 7. *(a) FIB cross-section of three Berkovich nanoindentations performed on on sample M3thin at h_{max} = 500 nm. (b-d) Micrographs corresponding to cross-section of individual imprints.* 120
Figure 8. *Apparent hardness H_a (left vertical axis) and E_a (right vertical axis) as a function of penetration depth for (a) h_{max} = 100 nm, (b) h_{max} = 500 nm and (c) h_{max} = 1000 nm.* 121
Figure 9. *Spherical nanoindentation stress-strain curves, and fitting line for the first 150 nm of penetration. The inset image corresponds to a 3D AFM micrograph of a residual spherical nanoindentation imprint performed in the film at a load of 300 mN.* 123
Figure 10. *Average curves of the reduced apparent elastic modulus E_a and its standard deviation, together with the reduced E_f predicted by the implemented models, as a function of penetration depth for (a) h_{max} = 100 nm, (b) h_{max} = 500 nm and (c) h_{max} = 1000 nm.* 125

Figure 11. *P-h curves of indentations performed at (a) h_{max} = 100 nm, (b) h_{max} = 300 nm, and (c) h_{max} = 2000 nm on the polished top surface of sample M3-I.* 127
Figure 12. *Optical micrographs of a matrix of Berkovich nanoindentations at (a) h_{max} = 2000 nm on the polished top surface of sample M3-I. (b) Optical and (c) LSCM micrographs at higher magnification of the same matrix of indents.* 128
Figure 13. *Curves of H vs h corresponding to 100 nm (a), 300 nm (b), and 2000 mm (c) penetration depths. Nanoindents were performed on the polished top surface of sample M3-I.* 129
Figure 14. *Curves of E vs h corresponding to (a) 100 nm, (b) 300 nm, and (c) 2000 mm penetration depth nanoindents. Tests were performed on the polished top surface of sample M3-III.* 130
Figure 15. *Sequence of 3D-AFM micrographs depicting the evolution of surface damage induced by cube corner nanoindentations at loads of (a) P_{max} = 30 mN, (b) 35 mN, (c) 40 mN, (d) 50 mN and (d) 70 mN. Pile up profiles measured at a distance of 2/3 c for indents corresponding to applied loads of 30 mN, 35 mN, 40 mN° and 50 mN.* 132
Figure 16. *SEM images corresponding to different stages of the FIB sputtering process. Indentations at (a-c) P_{max} = 30 mN and (d-f) 50 mN.* 133
Figure 17. *(a,d) Oblique, (b,e) top and (c,f) frontal views of the 3D FIB tomographies constructed for indentations at (a-c) P_{max} = 30 mN and (d-f) 50 mN.* 134
Figure 18. *Detail of the 3D FIB tomography corresponding to the cube corner nanoindentation at P_{max} = 30 mN, showing the elipticity in one of the radial cracks.* 137
Figure 19. *Matrix of cube corner indentations performed on the polished top surface of sample M3-I.* 138
Figure 20. *Penetration depth as a function of scratch distance and load for three scratches performed on sample M3thin at the low load condition.* 142
Figure 21. *Optical micrograph corresponding to the scratch imprints performed at the conditions P_{max} = 50 mN – l_{max} = 50 µm.* 143
Figure 22. *FIB cross-section performed at the midpoint of the scratch length for the scratch at (a) P_{max} = 50 mN – l_{max} =50 µm. (b) Magnification of the cross-section at the center of the track.* 144
Figure 23. *Optical micrograph showing a detail of two imprints of the scratch performed at P_{max} = 50 mN – l_{max} = 50 µm. The damage characteristics are indicated by arrows.* 145
Figure 24. *Images of the FIB cross-sections performed at two points along a scratch performed at the high load condition. Surface (a) before the FIB sectioning process and (b) after the FIB sectioning process.* 146
Figure 25. *Cross-section of the zone 1 of Figure 22. (a) General, (b,c) lateral, and (d) central details of the cross-section.* 147
Figure 26. *Cross-section of the zone 2 of Figure 22.* 148
Figure 27. *Curves of the scratches at the high load condition on sample M3thin. (a) Indenter penetration vs scratch distance in the pre-loading, loading and post-loading stages. (b) Friction coefficient and (c) friction force vs scratch distance.* 149
Figure 28. *AFM micrograph of the first section of one of the scratches performed at the high load condition together with profiles right (1) before and (2) after film delamination and chipping.* 151
Figure 29. *(a) LSCM micrograph of three imprints corresponding to the scratches performed on sample M3-I at the low load condition. (b) Optical image of the same scratch imprints.* 153
Figure 30. *LSCM 3D image of the scratches performed on sample M3-III at the low load condition, together with the surface profile at maximum load.* 154
Figure 31. *Curves of scratches performed at the low load condition on sample M3-I. (a) Indenter penetration vs scratch distance in pre-loading, loading and post-loading stages. (b) Friction coefficient and (c) friction force as a function of scratch distance.* 155
Figure 32. *LSCM micrograph of three imprints corresponding to the scratches performed at a load of (a) 500 mN and a scratch length of 200 µm. (b) Optical image of the same scratch imprints.* 156
Figure 33. *Curves of scratches at the high load condition on sample M3-I. (a) Indenter penetration vs scratch distance in pre-loading, loading and post-loading stages. (b) Friction coefficient and (c) friction force vs scratch distance.* 157

Chapter 5

Figure 1. *(a) Confocal micrograph of three indentations at h_{max} = 2000 nm in sample M7. SEM image of a nanoindentation at (b) h_{max} = 100 nm and (c) its FIB cross-section in sample M8.* 168
Figure 2. *Average curves of (a) H_a and (b) E_a vs h corresponding to indentations at P_{max} = 300 nm penetration depth nanoindents on the polished top surface of samples M5, M6, M7 and M8. Curves of H_f and E_f for sample M3, as calculated in Chapter 4, are also included.* 169
Figure 3. *Average curves of (a) H_a and (b) E_a vs h corresponding to nanoindentations at P_{max} = 2000 nm penetration depth on the polished top surface of samples M5, M6, M7 and M8. Curves of sample M3 attained in Chapter 4 are also included.* 169
Figure 4. *AFM micrographs of a matrix of cube corner indentations performed on the polished top surface of sample M8 at different loads. (a) Height image and (b) amplitude image.* 171
Figure 5. *AFM micrographs of the cracks arising from a cube corner indentation at P_{max} = 20 mN in sample M7. (a) Height image and (b) amplitude image.* 172
Figure 6. *AFM micrographs of the cracks arising from a cube corner indentation at P_{max} = 30 mN in sample M7. (a) Height image and (b) amplitude image.* 172
Figure 7. *Matrix of cube corner indentations performed on the polished top surface of sample M8 at (a) P_{max} = 30 mN. (b) Detail of an individual indentation.* 174
Figure 8. *Optical image of high and low load scratches performed on sample M5. Scratches are displayed horizontally in the micrograph, with the applied load increasing from left to right.* 175
Figure 9. *Three low load scratches performed on sample M5. Scratches are positioned vertically in the micrograph, with the applied load increasing upwards.* 176
Figure 10. *Confocal image of two of the high load scratches performed on sample M5. Scratches are displayed horizontally in the micrograph, with the applied load increasing from left to right.* 177
Figure 11. *Optical image of high and low load scratches performed on sample M7. Scratches are displayed horizontally in the micrograph, with the applied load increasing from left to right.* 178
Figure 12. *Low load scratch performed on sample M7. Scratches are displayed horizontally in the micrograph, with the applied load increasing rightwards.* 179
Figure 13. *Two of the high load scratches performed on sample M7. Scratches are displayed horizontally in the micrograph, with the applied load increasing from left to right.* 179
Figure 14. *(a) Confocal micrograph of three low load scratches performed on sample M8. These scratches are displayed vertically in the micrograph, with the applied load increasing upwards. (b) Detail of an individual scratch depicting slight cracking. This scratch is displayed horizontally in the micrograph, with the applied load increasing from left to right.* 180
Figure 15. *Optical image of a high load scratch performed on sample M8. (a) Focus on the substrate and (b) on the coating top surface. This scratch is displayed horizontally in the micrograph, with the applied load increasing from left to right.* 181
Figure 16. *SEM image of a high load scratch in sample M8 denoting the positions 1 and 2 for the FIB cross-sectioning. This scratch is displayed horizontally in the micrograph, with the applied load increasing from left to right.* 182
Figure 17. *(a) FIB cross-sections of the high load scratch of sample M8 at position 1, and (b) position 2 of Figure 16.* 183
Figure 18. *Increase in (a) H_f and (b) E_f values with the Al/Si ratio for the coatings studied.* 184
Figure 19. *Fracture toughness vs Al/Si ratio for samples M3, M7 and M8. Estimated K_f is included for sample M7 (□).* 186
Figure 20. *(a) Curves of the indenter penetration vs scratch distance in the pre-loading, loading and post-loading stages for scratches performed at the low load condition on samples M3, M5, M7 and M8. (b) Curves of the indenter penetration vs scratch distance in the loading and post-loading stages for scratches performed at the low load condition on samples M3 and M8.* 187

Chapter 6

Figure 1. *Mechanical tests in the cross-sectional approach : (a) Nanoindentation; and (b) Nanoscratch, UP ("Bottom to top") and DOWN ("Top to bottom") directions. (c)Nanoindentation in the wedge approach.* 196
Figure 2. *LCSM image of prepared cross-section, sample M11.* 197
Figure 3. *Illustration of the process followed to detach the coating in sample Graded II. (a) "Supported" coating, (b) coating separation by mechanical means and (c) "freestanding" coating.* 197
Figure 4. *FIB cross-section of Graded-II sample. Superposed, Al/Si ratio vs distance from the interface.* 198
Figure 5. *Matrix of nanoindentations, sample M11.* 200
Figure 6. *Cross-sectional intrinsic (a) hardness and (b) stiffness of mullite coatings with constant Al/Si ratios as a function of the Al/Si ratio.* 201
Figure 7. *Average hardness of studied samples as a function of the input Al/Si ratio (bottom horizontal axis); and of the distance from the interface for sample Graded (top horizontal axis).* 202
Figure 8. *Average elastic modulus of the studied samples as a function of the input Al/Si ratio (bottom horizontal axis); and of the distance from the interface for sample Graded (top horizontal axis).* 203
Figure 9. *Separation process of the mullite coating from the SiC substrate in sample Graded-II. (a) Supported coating, (b) intermediate step in separation process and (c) freestanding coating.* 204
Figure 10. *Comparison between the (a) hardness and (b) elastic modulus of supported (▲) and freestanding (■) coatings for sample Graded-II.* 204
Figure 11. *(a) AFM image of a matrix of 10x6 indentations in a freestanding portion of the coating of sample Graded-II. (b) Hardness and (c) elastic modulus maps for a coating area of 30x15 µm.* 205
Figure 12. *(a) Top optical micrograph indicating indentation sites in the polished wedge of sample Graded -II. (b) Top confocal micrograph showing imprints across coating thickness.* 206
Figure 13. *(a) Hardness and (b) elastic modulus profiles using the wedge approach in sample Graded-II (▲). Data obtained in the cross-section of sample Graded-II (■) is also included for comparison reasons.* 207
Figure 14. *Tracks of nanoscratches performed at different loads in DOWN direction on sample M11.* 208
Figure 15. *Different damage morphologies evidenced: (a) adhesive at the interface; (b) cohesive in the coating; (c) combined adhesive and cohesive; and (d) catastrophic failure.* 209
Figure 16. *Damage at 150 mN in DOWN-direction nanoscratch track for samples: (a) M3-I; (b) M11; and (c) Graded.* 210

Chapter 7

Figure 1. *(a,c) Hardness and (b,d) elastic modulus vs penetration depth obtained for samples (a,b) M3-III and (c,d) M7. Filled symbols correspond to indentations in the "As-deposited" condition and void symbols correspond to indentations after thermal stability test.* 220
Figure 2. *AFM micrographs of cube corner indents at P = 20 mN in (a,b) sample M3-III, and (c,d) sample M7. (a,c) Height images and (b,d) phase images.* 221
Figure 3. *Penetration as a function of applied load, and corresponding micrographs of the scratch paths, for (a) samples M3-III and (b) M7. Load increase downwards in the image of sample M3-III and from left to right in the case of sample M7. Filled and void symbols correspond to scratches in the "As-deposited" condition and after thermal stability test respectively.* 223
Figure 4. *Surface aspect of sample Graded-III in the (a) As-deposited condition and (b) after the thermal stability test perfomed. Detail of the bright spots observed after thermal exposure (c).* 224
Figure 5. *Polished wedge and nanoindentation sketch superposed for sample Graded-II.* 225

Figure 6. *(a) Hardness and (b) elastic modulus for sample Graded-II in the As-deposited condition (■) and after thermal stability treatment (▲).* 226
Figure 7. *(a) Optical and (b) LSCM micrographs of nanoscratches performed on the "non-polished" surface of sample Graded-II, after the thermal stability test. (c) Detail of the scratch tracks. (d) 3D-perspective of surface. In the images nanoscratches are placed in an oblique situation, from up right towards bottom left.* 227
Figure 8. *(a) LSCM and (b) optical images of nanoscratches performed on the surface of sample Graded-II in the "semi-polished" condition, after the thermal stability test.* 228
Figure 9. *Surface appearances of samples (a)* M3-I *and (b)* M8-I *after the thermal shock test. (c)* H *and* E *as a function of penetration depth for samples* M3-I *and* M8-I *evaluated after the thermal shock. (d) Nanoscratches performed after the thermal shock of sample* M8-I. 229
Figure 10. *Nanoindentations matrix crossing the coating cross-section of sample M8, subjected to the corrosion test.* 230
Figure 11. *Cross-sectional (a) hardness and (b) elastic modulus of sample M8-II after the corrosion test. The meshed zone superposed to the plots indicates the average values found for sample M8-I in the "As-deposited" condition.* 231
Figure 12. *(a) General optical and (b) LSCM micrographs of three nanoscratches performed on the surface of coating M8 in the "non-polished" condition. (c) Detailed 2D and (d) 3D views of the scratch track.* 232
Figure 13. *(a) LSCM and (b) optical micrographs of a nanoscratch performed on the polished surface of sample M8-II after being subjected to corrosion test.* 233

A mis padres y hermanos

A Anna y nuestro primer bebé

“Why cannot we write the entire 24 volumes of the

Encyclopaedia Brittanica on the head of a pin? ”

…There is plenty of room at the bottom

Richard P. Feynman

December 29th 1959
at the annual meeting of the American Physical Society
at the California Institute of Technology (Caltech)

1 *Chapter*

Introduction

1.1 Thesis overview and layout

As it is the case in many fields of science and engineering, materials technology is witnessing an ever continuing miniaturization, predominantly marked by the rapid growth of the microelectronics industry in the last decades. As a consequence, a large number of micro/nano structured systems and devices for a variety of applications have been introduced. Among others, protective coatings and thin film systems as well as micro- and nano electromechanical systems (MEMS and NEMS)[1,2], where the transition from macro- to micro/nanoscale in systems and components can be appreciated (Figure 1), may be cited. Moreover, characteristic dimensions of these systems, represented by their individual components and associated interfaces, together with underlying microstructural features and architectures, lie in the micro/nanometer range. Within this context, the understanding of the properties of materials at such small scale, and the validity of extrapolating established knowledge from the macro- into the micro/nano-ranges, are challenging topics under continuous investigation.

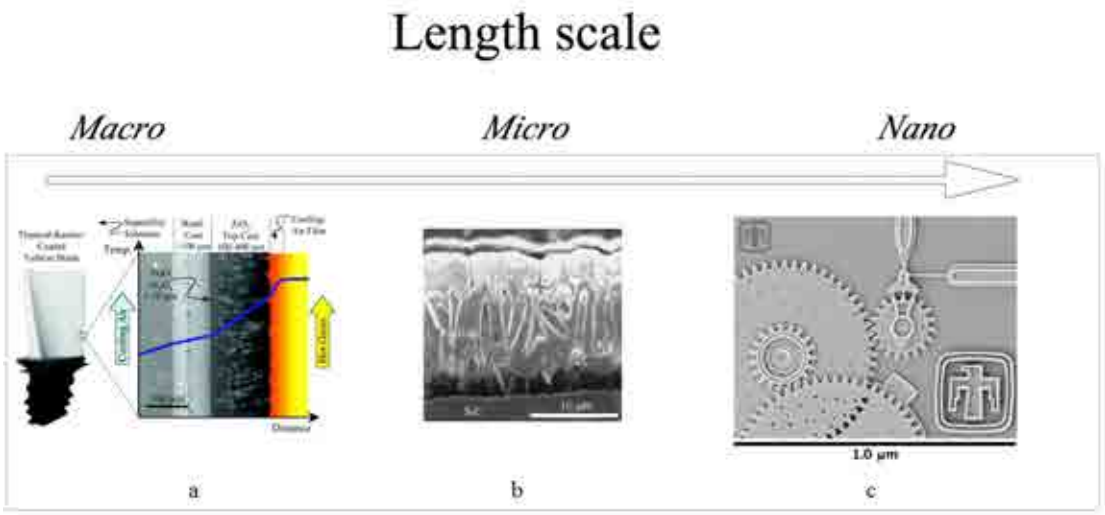

Figure 1. Transition from macro- to micro/nano- length scale in systems and components: (a) electron beam physical vapor deposited EB-PVD thermal barrier coating and temperature reduction in a turbine blade[3], (b) mullite environmental barrier coating deposited on SiC by chemical vapor deposition; and (c) MEMs device[1].

The emergence of such structures has brought the topic of mechanical behavior of materials at the micro/nanometer scale into the domain of engineering. From this perspective, it must be pointed out that many current and potential applications of such systems have not been consolidated, or even attempted, in practice because the mechanical properties of these structures have not been established, and are, to a large extent, still unknown.[4] Accordingly, the study of the intrinsic micro/nano mechanical properties, aimed to guarantee the structural integrity and reliability of such systems, is crucial for their practical application and subsequent commercialization. These statements partly justify the aim of the present dissertation, which focuses on the study of the micro/nano mechanical integrity of mullite-based Environmental Barrier Coatings (EBCs) deposited on silicon carbide.

Mullite coatings have been introduced and proven to be excellent candidates to protect Si-based ceramics from severe pitting corrosion and recession in high temperature applications such as gas turbines[5–7], becoming part of the new generation of the so-called protective EBCs. These coatings have been deposited by means of Chemical Vapor Deposition (CVD), resulting in a columnar configuration of mullite grains that nucleate from a very thin layer of a vitreous silica matrix, as presented in figure 1 b. In

order to enhance the corrosion protection of the coatings, mullite columns may be grown over a wide range of increasing Al/Si ratios in constant or graded fashions[6]. Mullite EBCs are fully dense and adherent to the substrate, and have demonstrated good thermal stability and corrosion protection to SiC under aggressive environments[7,8]. However, although the microstructure and corrosion protection of these coatings are well characterized through extensive studies carried out in the last decade, similar information on their mechanical performance is quite scarce. Since the mechanical integrity within the coating/substrate system is critical, it is evident that the assessment and documentation of the mechanical properties of EBCs are essential for optimizing their microstructural design and performance.

Following the above ideas, the implementation of adequate tools for investigating and characterizing the mechanical behavior at small scales emerges as a key issue. In this regard, it is interesting to mention that the referred advances in microelectronics (initiated about 30 years ago), also allowed for measuring displacement and load in the order of magnitude of nm and μN respectively. It enabled then development of several types of instrumented micro/nanoindentation test systems and their application to study characteristic material parameters at micro/nano- length scales[9]. Nowadays, the instrumented indentation technique known as "nanoindentation" is the best suited and most used experimental tool to extract intrinsic mechanical properties of small volumes of materials such as thin coatings and film systems[1,2,10–17]. The principle of this technique lies in the evaluation of the material response when a load is locally applied by means of a small sized indenter. When nanoindented using different indenter tips, materials can undergo elastic and elastoplastic deformation, as well as fracture. Attempting to rationalize the responses attained, different equations and methods have been developed to construct stress-strain curves[18,19] and to calculate critical parameters such as hardness and elastic modulus,[13,20–22], yield strength[18,19,23,24], and fracture toughness[25,26], among others.

Nanoindentation has been also potentiated as a tool to evaluate the integrity of micro- and nanostructures and coated systems by inducing controlled delamination. Thus, some

parameters as the energy of adhesion and interface fracture toughness can be estimated[27–29]. Furthermore, most of the nanoindentation apparatus available permit lateral movement of the sample whilst a normal force is applied by the indenter. This derivation of the nanoindentation technique, commonly referred to as "nanoscratch", may also be used to induce delamination at relatively low loads in coated systems, and thereby to determine the critical load at which cohesive and decohesive damage occurs. Additionally, characterization of different modes of failure in materials as well as their ability to withstand abrasion without fracturing during sliding contact, can also be investigated through this technique.[12]

Progress in the implementation of the nanoindentation technique has been assisted with parallel developments in advanced characterization techniques. Two examples that deserve special mention are atomic force microscopy (AFM)[30] and focused ion beam microscopy technique (FIB)[31–33]. FIB has also given rise to new possibilities for reconstruction of three-dimensional (3D) microstructural features of materials, providing clear insights into the understanding of their properties[34]. Despite of its novelty, FIB tomography applied to the cracking phenomena caused by indentation appears as a promising tool for the precise evaluation and analysis of failure phenomena at small scale[30,35–37].

In this thesis, nanoindentation and nanoscratch tests together with advanced materials characterization techniques are implemented to investigate the main micro/nano mechanical properties of mullite-based EBCs on SiC as well as the structural integrity of the coated systems. In doing so, columnar mullite coatings composed of stoichiometric (≈ 3) and increasing (≈ 5, 6, 7, 8, 11) Al/Si ratios, as well as compositionally graded coatings, were deposited by means of CVD. From a mechanical standpoint, special attention is paid to the different features ascribed to the studied coated systems: coatings' architecture (i.e. columnar configuration), residual stresses and compositional changes, as well as substrate influence. Therefore, two approaches here referred to as "Top" and "Cross-sectional", directly linked to the testing methodology (nanoindentation and nanoscratch tests), are invoked. In addition, the

effect of coating composition on its mechanical behavior is studied. Finally, taking into consideration the potential application of these coatings as environmental barriers, the temperature and corrosive effects on the mechanical behavior of the coated systems are also investigated.

The dissertation is structured in eight chapters. The first introductory chapter (*Chapter 1*) describes evolution in micro- and nano technologies during the past few decades, pointing out the importance of nanoindentation and the relevance of the micro/nano mechanical behavior of mullite-based EBCs deposited on SiC. Additionally, a brief review on the mechanical properties at small scale is presented with particular emphasis given to capabilities of nanoindentation and nanoscratch tests to study different mechanical properties and structural integrity of coated systems. Finally, several aspects concerning mullite-based EBCs are indicated.

The general and specific objectives of this thesis are included in *Chapter 2*.

The description of the procedure used for the deposition of coatings and the routes followed for the preparation of specimens, facing the subsequent micro/nanomechanical characterization, are presented in *Chapter 3*. Also, experimental details of the implementation of nanoindentation and nanoscratch tests, and the techniques used for the characterization of the imprints and the damage produced, are briefly summarized in this chapter.

Chapter 4 is devoted to the study of the mechanical behavior of stoichiometric $3Al_2O_3{\cdot}2SiO_2$ (Al/Si≈ 3) mullite coatings on SiC, considered in this research as the "standard" system. Systematic nanoindentation and nanoscratch tests are conducted on the top surface of this reference system to assess the intrinsic mechanical properties of the coatings: stress-strain curves, yield strength, hardness, elastic modulus, fracture toughness and cohesive resistance. The structural integrity of the coated

$3Al_2O_3 \cdot 2SiO_2$/SiC system is also investigated through estimation of the energy of adhesion and the interface fracture toughness, as well as of the decohesive resistance.

The same set of tests performed on the "standard" system is conducted on alumina enriched coatings in *Chapter 5*, where the influence of the coating composition on the studied mechanical properties and integrity is analyzed and critically compared.

In *Chapter 6* the cross-sectional and wedge approaches are implemented to evaluate through both nanoindentation and nanoscratch the mechanical properties and structural integrity of the compositionally graded coated systems.

Considering the final application of mullite-based EBCs, in *Chapter 7* the temperature and corrosive effects are investigated. The influence of temperature on the mechanical behavior is studied through long term stability tests, whereas corrosion effect on the mechanical behavior of the coatings subjected to aggressive corrosive environments is characterized.

In *Chapter 8*, the main conclusions raised in this thesis are drawn.

Finally, some ideas regarding future work required on the mechanical behavior of mullite-based EBCs are presented in *Chapter 9*.

1.2 Micro- and nanomechanics of coatings

1.2.1 Introduction to nanoindentation

1.2.1.1 Principles and capabilities

Indentation is a method used to measure the mechanical properties of a material. From a very general viewpoint, it consists in contacting the material of interest, whose mechanical properties such as hardness and elastic modulus are unknown; with another material whose properties are known[12]. Traditionally, the indentation of a material is performed with indenters of different geometries (Brinell, Knoop, Vickers, Rockwell, etc.), to calculate different mechanical properties, particularly hardness. The nanoindentation technique (also known as kinetic or continuous indentation, depth sensing test, ultralow-load indentation, instrumented indentation, etc.) has been catalogued as an extension of the conventional indentation test in which the length scale of the indentation is measured in nanometers (10^{-9} m) rather than in microns (10^{-6} m) or millimeters (10^{-3} m), as it is the case of conventional hardness tests. Similarly, to induce such small penetrations in materials, very small loads in the range of micronewtons (10^{-6} N) and milinewtons (10^{-3} N) are applied through the indenter.

A conventional nanoindentation test could be simplified as the indentation process of a geometrically calibrated tip penetrating a material under the action of a normal force P (t), and the simultaneous measurement of the depth h (t) of its penetration into the tested material, as it is shown in Figure 2 a[16]. This process is characterized by a loading phase in which the indenter is pushed into the material of interest until maximum load P_{max} is reached, a holding phase along which P_{max} is maintained, and a final unloading phase during which the indenter is withdrawn from the material as the load is removed. The most used representation of the nanoindentation data is that given by the curves of load as a function of penetration depth, also known as P vs h curves, as illustrated in Figure 2 b[38].

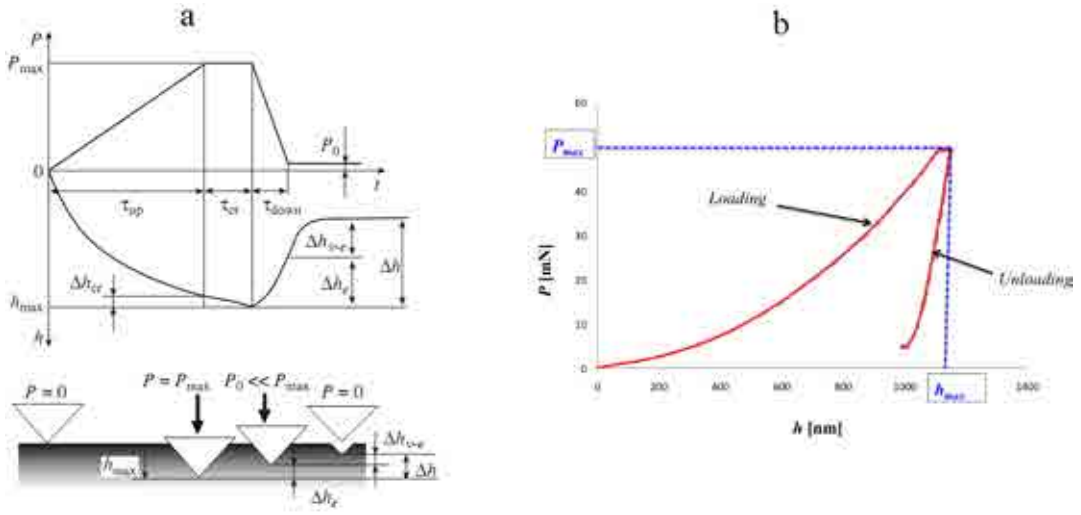

Figure 2. (a) Profiles of the main parameters involved in the nanoindentation tests, P and h, as a function of time[16], and (b) the typical P vs h curve representing the complete nanoindentation cycle, i.e. loading and unloading stages. P_{max} is the maximum indentation load, P_0 is the small residual load (~3-5% of P_{max}), τ_{up} is the duration of the active loading, τ_{cr} is the duration of exposure under constant load, τ_{down} is the time span increment corresponding to the unloading stage, h_{max} is the maximum indentation depth, Δhcr is the increment of the indentation depth due to the creep, Δh_e is the magnitude of the elastic recovery, $\Delta h_{v\text{-}e}$ is the magnitude of the viscoelastic recovery, and Δh is the total recovery.

The response of a given material under nanoindentation depends on several factors. Among others, the main ones are the indenter geometry and material, the applied load, and more importantly, the nature of the tested material. In general terms, during indentation materials can undergo elastic and elasto-plastic deformation, and fracture (in the case of brittle materials). As the applied load is increased, the characteristic size of the locally deformed zone beneath the indenter together with the relative contributions of the elastic and plastic deformation, and the atomic mechanisms of deformation, controls the material behavior. Accordingly, a more physical classification of the indentation regime is presented in Figure 3[16]. During the initial stage of the loading process a purely elastic contact takes place. At higher loads the elastic deformation is followed by a combination of elastic and inelastic deformation within the specimen. At even higher loads, the inelastic deformation, also known as plastic flow or yield in metallic materials, dominates the deformation process, and the elastic contribution to deformation can be neglected in practical terms.

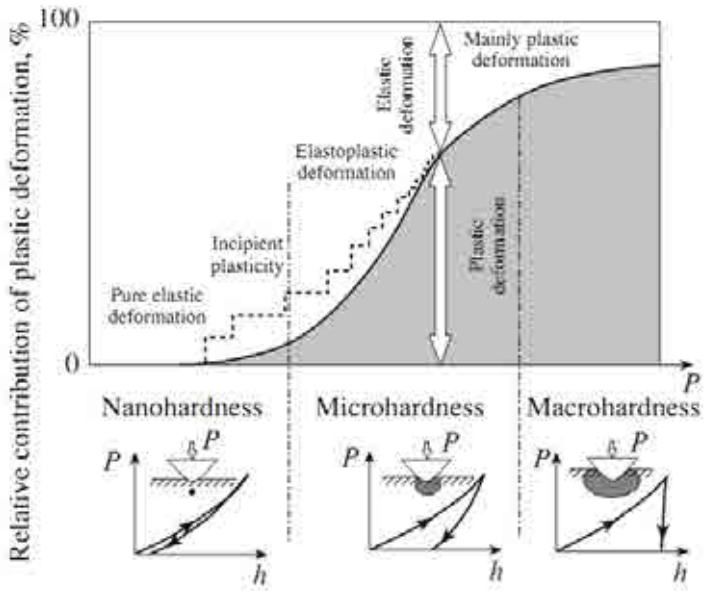

Figure 3. Relative contributions of the plastic deformation to the formation of an indentation as load *P* is increased, and a change of the corresponding stage of penetration during the indentation process.[16]

Upon unloading, if yield has occurred, the load-displacement data follow a different path and a residual impression is left under the surface of the tested material[12]. It is important to comment that, as the penetration depth is recorded and the geometry of the indenter is known, the contact area at full load can be indirectly estimated during the nanoindentation test, and it is therefore not necessary to image and measure the residual imprint after the test. Accounting for the contact area, the maximum penetration for a given load, and the slope of the unloading curve measured at the tangent to the data point at a maximum load (also known as the contact stiffness *S*), both hardness *H* and elastic modulus *E* of a material can be estimated.

In addition, by means of the implementation of a technique known as continuous stiffness measurement (CSM), a small varying perturbation of the load can be superimposed at any point of the loading curve, allowing for continuous measurement of *S*. In consequence, *H* and *E* may be monitored from the early stages of the indentation process, pointing out this technique as ideal for the characterization of coating and thin film properties[2].

In the case of brittle materials such as ceramics, and as a consequence of the implementation of sharp indenters, fracture process in the form of cracking can also be induced by nanoindentation. The length of the cracks, often emerging at the corner of an indentation impression, may then be used to calculate the fracture toughness K_c of the material of interest[2,12,38].

Nowadays, the determination of the "conventional" mechanical properties mentioned above (H, E and K_c) is typically done through well-accepted definitions and the aid of established algorithms and programs[16,38]. However, an additional set of properties and phenomena, whose definitions and methods for their experimental characterization are not yet universally adopted, may also be evaluated using nanoindentation involving the use of indenters with particular geometries. Among the properties included in this group, two of them may be underlined within the scope of this study. The first one refers to the stress-strain curves reconstructed from the P vs h curves, and consequently the yield strength σ_y of a material or coating. The second one is related to the coated system as structural unit, and is given by the energy of adhesion G_{int} and the associated interface fracture toughness K_{int}.

1.2.1.2 Instrumentation

Nanoindentation tests are carried out using instruments commonly referred to as nanoindenters, nanoindentometers or nanotesters. The design of most of the nanoindenters is very similar and can be generalized by the scheme of Figure 4. In these instruments the load can be applied by the expansion of a piezoelectric element, the movement of a coil in a magnetic field or electrostatically, whilst the depth of penetration is typically measured using either an inductance or a capacitance displacement sensor. The displacement resolution of conventional nanoindenters is less than a tenth of a nanometer and the force resolution lies in the order of several nanonewtons, whereas the maximum loads are usually limited to the milinewton range[12].

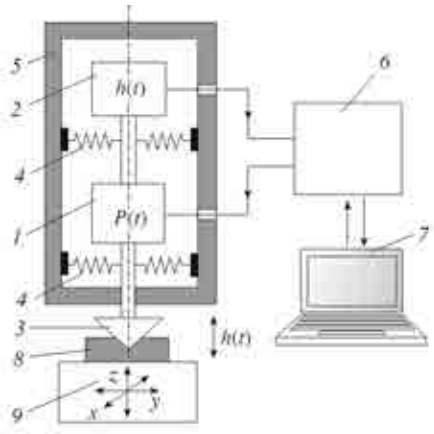

Figure 4. General scheme of a nanoindenter, (1) load cell, (2) displacement sensor, (3) indenter, (4) springs of the rod suspension, (5) measuring head body, (6) controller assembly, (7) computer, (8) sample, and (9) objective stage.[16]

During a nanoindentation test, the indentation location is selected through an optical microscope usually coupled to the nanoindenter. The positioning and displacement of the sample are accomplished using a two-coordinate or three-coordinate stage, as shown in Figure 4 (9). The elements of the system illustrated in Figure 4 (1 to 4) are structurally combined into a single measuring head regulated by a controller assembly (6). The latter in turn, transduces the information to a computer (7) with a software package designed to control all the operating cycles of the instrument, and the collection, processing, and storage of the nanoindentation data.

1.2.1.3 Indenters

As mentioned previously, the response of a material upon indentation strongly depends on the indenter geometry as well as the indenter material. The stress-strain fields and the deformation and fracture mechanisms experienced by materials under indentation are conditioned to a large extent by these variables. Therefore, among the elements constituting the nanoindenters described in the previous section, one of the most important is the indenter and particularly its tip. Indenter tips are usually made of several different materials, amongst which diamond is one of the most used due to its extremely high stiffness and hardness.

Because their geometries and capacity to produce permanent deformation in the tested material, the indenter tips can be classified in blunt and sharp indenters (see Figure 5 a). The selection of an appropriate indenter tip depends primarily on the specific properties of interest or the phenomena to analyze. The most used blunt indenters in nanoindentation are the spherical ones, whilst the Berkovich and the cube corner indenters are the most used indenters of sharp geometry. Among these, the tip geometries of interest for this dissertation such as spherical, Berkovich, and cube corner (see Figure 5 b-d) are further detailed below. In doing so, special attention is paid to the tip geometry effects on the measured material response and the corresponding capability of property extraction.

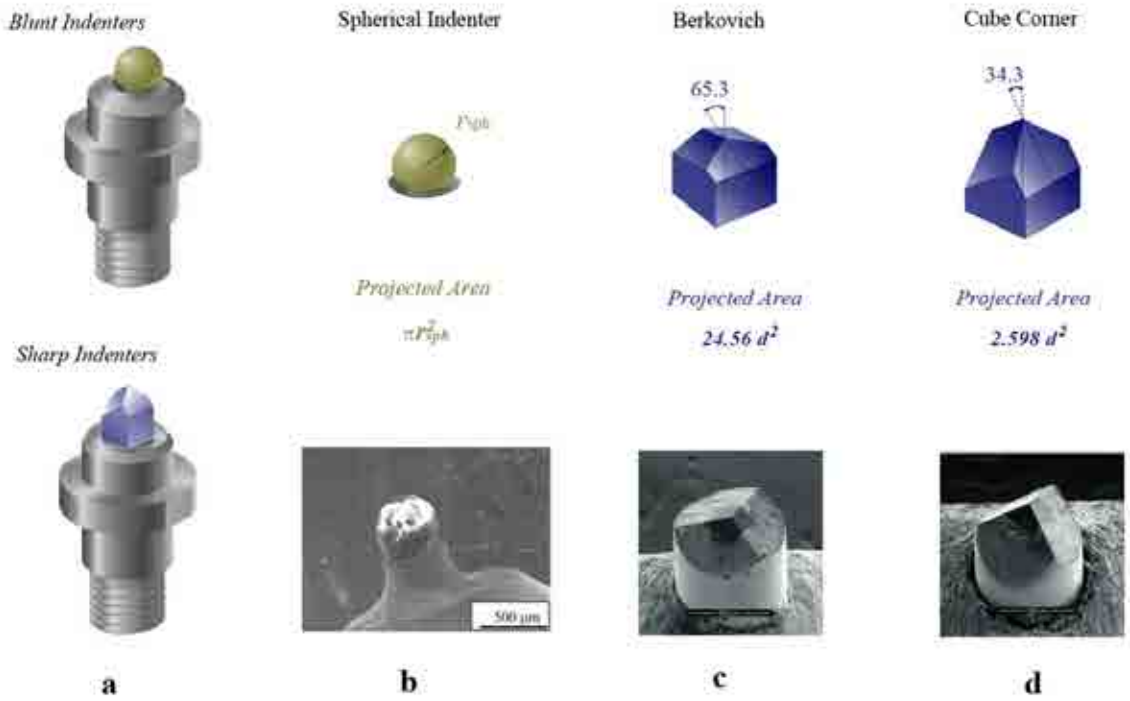

Figure 5. (a) Scheme of Blunt and Sharp indenters. Schemes of the tip geometry and some geometrical parameters, as well as SEM pictures of real examples of (b) Spherical, (c) Berkovich and (d) cube corner indenters.

- ***Spherical Indenter***

Spherical indenters (see Figure 5 b) are increasingly being used in nanoindentation because they produce a fully elastic contact at the beginning of the indentation regime, during which the contact stresses are small and produce elastic deformation exclusively. As a consequence, only the very tip of the indenter is used to penetrate the surface of the material of interest. Diamond indenters with a radius of less than 1 micrometer can be fabricated.[12] By using the CSM modulus, spherical indenters can be used to estimate the stress-strain curves of a material as well as its E and σ_y.[18,19,23,24]

- ***Berkovich Indenter***

The Berkovich indenter (see Figure 5 c) is the most used sharp indenter for nanoindentation. This pyramidal indenter has the same projected area to depth ratio as the conventional Vickers indenter used in microhardness testing[39]. Besides, from a fabrication perspective Berkovich tips have the advantage that the edges of the pyramid are more easily constructed to meet a single point. The face angle of this indenter is $\Psi = 65.3º$ and the tip radius is in the order of 50-100 nm.[12] This indenter is customarily used to extract H and E, and in the case of very brittle materials, it can also be used to calculate K_c.

- ***Cube corner indenter***

The cube corner indenter (see Figure 5 d) is a three sided pyramidal indenter in which the faces are arranged in a perpendicular geometry, forming a corner of a cube. In this case the face angle of the tip is $\Psi = 34.3º$. This sharp tip generates a higher concentration of strains and stresses in the tested material underneath the indenter, allowing for the generation of cracks around the imprints in many brittle materials. This indenter can be used to overcome the problems imposed by the cracking threshold below which most materials do not form cracks under low loads. Therefore, cube corner nanoindentation tests can be tailored to measure the K_C of small volumes such as hard second phases in tool steels and cemented carbides,[40] and thin films[25,26].

1.2.2 Contact Mechanics

Once reviewed the main concepts related to the nanoindentation technique, it is suitable to describe briefly some of the principles involved in the interaction between the indenter and the tested material as well as the effects of this interaction. In this regard, the study of the contact mechanics associated with the indentation process of materials is a key issue not only for understanding the nature of the induced deformation and fracture, but also for formulating expressions and methods that allow for the estimation of many related mechanical properties. It should be commented that, in many cases, the contact mechanics approach and concepts introduced at a macroscopic scale have been extrapolated and adapted to the micro- and nanoscale. Accordingly, the most important basic remarks concerning the mechanics of elastic and elastic-plastic deformations caused by indentation, together with the cracking processes induced in some brittle materials, are presented in this section.

1.2.2.1 Elastic contact

Due to the bluntness inherent to spherical tips, spherical indentation tests have traditionally been invoked for the study of elastic contact mechanics as well as of the elasto-plastic transition of different materials. In the case of ceramics, the mathematical framework and the equations ruling the elastic contact were first formulated by Hertz in the late 1880s through the analysis of spherical indentation on flat surfaces [41].

Hertz theory is derived from the analysis of the well-known scenario of the contact between a rigid sphere and a flat material surface, as illustrated by the scheme in Figure 6. The main parameters involved in such a contact are included in the same figure.

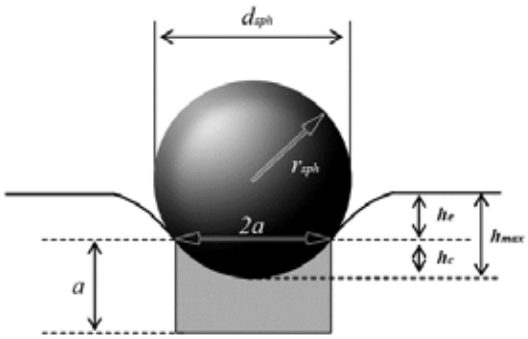

Figure 6**.** Scheme of spherical contact.

Based on the parameters indicated in Figure 6, the Hertz theory describing the elastic regime of spherical indentation may be written as[13,18,19,42]:

$$P = \frac{3}{4} E_{red} \sqrt{r_{sph}} h_{max} \qquad \textbf{Equation 1.1}$$

and

$$\frac{1}{E_{red}} = \frac{1-\nu^2}{E} + \frac{1-\nu_i{}^2}{E_i} \qquad \textbf{Equation 1.2}$$

where P is the applied load, r_{sph} is the radius of the indenter, h_{max} is the maximum displacement into the surface, E_{red} is the reduced elastic modulus (also referred to in different literature as the effective modulus E_{eff} or E'), and ν is the Poisson's ratio of the material. The subindex i denotes the values of the indenter material. This expression is valid for small deformations of the solid.

In the very first stages of the nanoindentation process, almost any indenter geometry used produces an elastic contact. This is due to the fact that roundness of the tip is often unavoidable because of the difficulties ascribed to the hard and stiff indenter materials and the tip fabrication processes.[43] Furthermore, in the case of spherical nanoindentation of stiff materials such as ceramics, the Hertz theory (equations 1.1 and 1.2) have been used to describe the material behavior at loads below the yielding point, where inelastic deformation processes take place.

1.2.2.2 Elasto-Plastic contact

Once the yield point is reached during nanoindentation, materials may undergo inelastic or permanent deformation upon higher loads. This can be easily achieved in relatively ductile materials with almost any indenter geometry, whereas in brittle materials, sharp indenters are more suited to induce inelastic deformation. Hardness *H*, indicates the resistance of a material to permanent deformation. It may thus be inferred that elasto-plastic contact mechanics is directly linked with hardness assessment.

Taking into consideration the scheme of Figure 6 for spherical contact, Sneddon[44] provided a relationship in which the elastic displacement of a plane surface above and below a contact circle can be equated as:

$$h_{max} = \frac{a^2}{r_{sph}} \qquad \textbf{Equation 1.3}$$

where *a* denotes the contact radius. By using equations 1.2 and 1.3, the contact pressure or indentation stress P_m (P divided by the projected contact area), also known as the Meyer's hardness, may be equated to the indentation strain or a/r_{sph},[42] as shown in equation 1.4:

$$\frac{P}{\pi a^2} = P_m = \frac{4}{3\pi} E_{red} \left(\frac{a}{r_{sph}}\right) \qquad \textbf{Equation 1.4}$$

Based on the above equation, the indentation stress-strain curves can be constructed. A generic example of such curves is illustrated in Figure 7, where the characteristic stages (zones 1, 2 and 3) of the elasto-plastic deformation of a material indented with a sphere are depicted.

Within Figure 7, zone 1 corresponds to the elastic contact regime described in the previous section for a spherical indentation. It is defined by a linear proportional behavior between indentation stress and strain. The $4E_{red}/3\pi$ term in equation 1.4 corresponds to the constant slope of the curve in this region. Here, it is important to

recall that among the stresses developed during contact, the shear stress is the one responsible for yielding of the material. Below the indenter, yield occurs when $P_y = 0.48P_m$, and $h = 0.5a$ [45], condition which can be observed in Figure 7 b. Hence, in order to analyze yielding in the material, the Tresca and Von Misses shear stress criteria need to be accounted for. Accordingly, a shear stress τ of around $0.5\sigma_y$ is required to produce plastic flow beneath the indenter, which implies that the yield onset takes place when $P_m \sim 1.1\ \sigma_y$.[46] This transition from purely elastic to elasto-plastic deformation regimes may be inferred in zone 2 of Figure 7 a). In this transition region, a plastic zone beneath the indenter starts to develop.

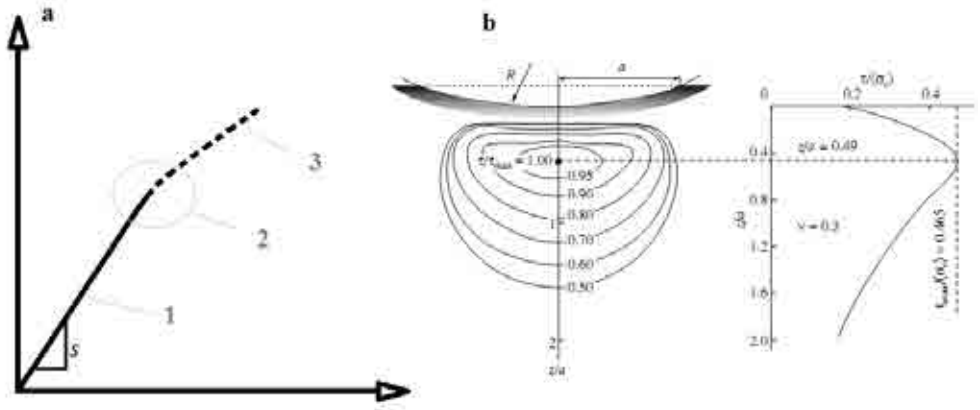

Figure 7. (a) Generic example of an indentation stress-strain curve. (b) Lines of maximum shear stress τ in the plane of the axial section and its dependence with the penetration depth[16].

At loads above the yield point, stress-strain behavior of the material departs from linearity. A fully plastic zone develops and any further increase in load causes a proportional increase in the contact radius. Therefore, the contact pressure P_m tends to remain constant with increasing load. At this point, P_m can be directly related with the material hardness H. There exists a relationship between hardness H and yield strength σ_y as follows:

$$H \approx C\sigma_y \qquad \textbf{Equation 1.5}$$

Throughout an indentation test, the volume of material beneath the indenter subjected to stress is constrained by a surrounding matrix. As a consequence, there is a considerable hydrostatic component and the P_m required to induce inelastic deformation or plastic flow is higher than that needed in uniaxial compressive stresses. The C in equation 1.5

is referred to as the constraint factor and depends on some parameters such as the type of specimen, the indenter, etc.[12] Depending on the E/ σ_y ratio, C values vary from aproximately 3 (metals) to 1.5 (glasses).

It is important to recall that, even in indentation tests performed with sharp tips such as Berkovich, the early stages of contact are elastic due to the rounding of the tip. Consequently, the measured contact pressure increases with the load until the penetration depth becomes larger than the tip radius. At higher loads, the pyramidal shape of the indenter comes into play and becomes dominant. A fully plastic contact takes place, and as a result the P vs h unloading curve does not match with that of loading (see Figure 2 b), resulting in a residual permanent indentation imprint.

1.2.2.3 Fracture

The interaction between an indenter and a brittle material may result in the fracture of the latter, most frequently manifested in the form of cracking. In the case of nanoindentation of ceramics using sharp indenters, cracks emanating from the imprint corners can be generated. These cracks have been used to measure one of the key properties of materials, the fracture toughness K_c, regarded as a measure of the resistance to the propagation of cracks.

Upon sharp indentation, brittle materials may develop two types of cracks, frequently named “radial” cracks, visible from the surface: the Palmqvist-radial cracks which extend from the corners of the indentation imprint but remain close to the surface, and the median-radial cracks which take the form of a “Half-Penny” centered on the imprint.[47] An example of the different cracking systems developed in brittle materials after a Vickers indentation is given in Figure 8 a-b, where l is the length of the radial crack and c is the crack length measured from the center of the indentation.[16] The same type of cracking can be developed under Berkovich indentation, as shown in Figure 8 c-d [48].

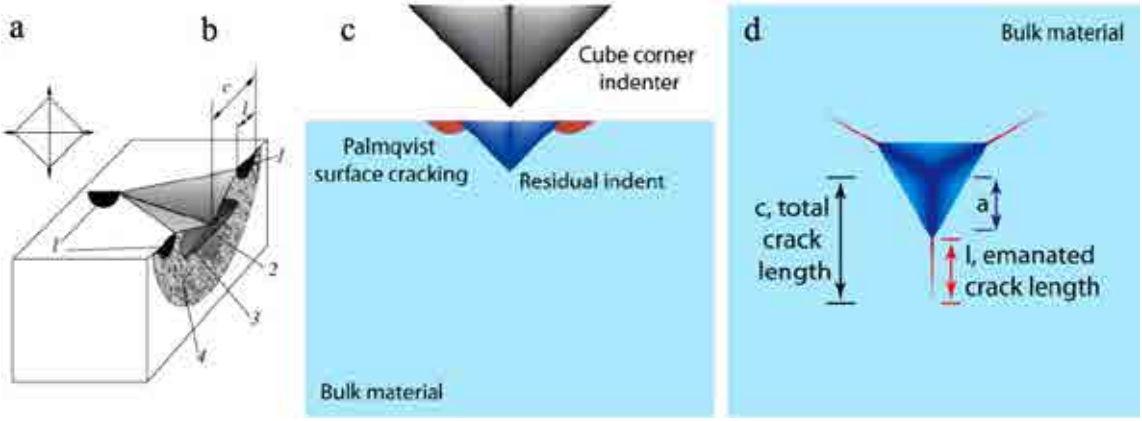

Figure 8. Different cracks paths for Vickers indentation: (1) "Palmqvist" radial crack, (2) median crack, (3) lateral crack, and (4) half-disk crack. (a) Top view and (b) cross-section through the center of the indentation. Berkovich indentation: (c) cross-sectional view of a Palmqvist type cracking, (d) top view of cracking for a Berkovich indentation.

The methodologies developed for calcualting K_c were initially developed for micro-hardness testing systems using the Vickers indenter, where loads in the range of 1 Kg or greater are applied, generating cracks of 100 µm length or longer. However, as the crack length limits the resolution of the technique for the assessment of K_c, the necessity of generating controlled cracks of small size, fine enough to be included in thin films for instance, motivated the use of acute indenters.

The existence of cracking thresholds (i.e. well-defined loads necessary to generate cracks) limit the use of indenters such as Berkovich and Vickers due to their relatively high values (cracking tresholds about 250 mN or more for most ceramic materials). The use of cube corner indenters was therefore proposed due to the fact that cracking thresholds are significantly reduced[49]. The lower face angle of this indenter (see Figure 5 d) implies that, at a given indentation load, the material displaced by the cube corner indenter is more than three times the one displaced by a Berkovich tip. This produces greater stresses and strains in the surrounding material, promoting nucleation and propagation of cracks.[38]

1.2.3 Micro- and nano- mechanical properties

The contact mechanics concepts introduced in the previous section are the general basis for the development of methodologies and formulations used to extract the mechanical properties of materials through nanoindentation. Those methodologies and equations, especially the ones of relevance for this thesis, are briefly presented in this section.

1.2.3.1 Hardness and Elastic Modulus

Hardness H and elastic modulus E are the main material properties conventionally extracted through the nanoindentation technique. Hence, in general terms it is convenient to define hardness as the resistance to permanent, inelastic, or plastic deformation, and elastic modulus as the measurement of stiffness. Among the existing methodologies for the calculation of H and E through nanoindentation, the one proposed by Oliver and Pharr[50], which is an extension of the earlier works by Loubet *et al* [51] and Doener and Nix [52], is by far the most used by researchers.

To describe the Oliver and Pharr method, a nanoindentation test performed with a Berkovich indenter must be considered, as well as the continuous measurement of the load P and the displacement h during the loading and unloading cycles (see Figure 2 b). The key quantities involved in the method and the physical phenomena taking place are presented in the schemes of Figure 9 a-b. The maximum values of load and displacement (P_{max} and h_{max}), and the contact stiffness S denoted as the slope of the unloading curve at the maximum point ($S = \mathrm{d}P/\mathrm{d}h$), are illustrated in the same figure. As it was mentioned in previous sections, during indentation of a material elastic and plastic deformation occurs, leading to the formation of an imprint with the shape of the indenter to a contact depth h_c. In the process of the indenter withdrawal, the elastic portion of the displacement is recovered, and therefore, the aforementioned elastic formulations can be used for the analysis.

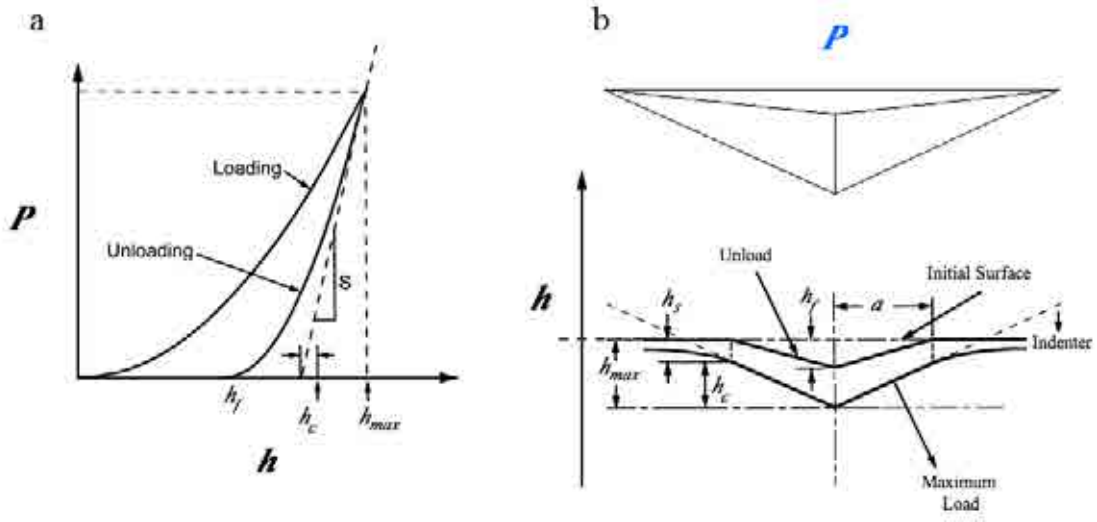

Figure 9. Main quantities involved in the Oliver and Pharr method[50] for (a) a complete nanoindentation cycle, and (b) physical phenomenon taking place during the nanoindentation process.

The first step in the method consists in the fitting of the unloading curve to a power-law relation of type:

$$P = B(h - h_f)^m \qquad \textbf{Equation 1.6}$$

where B and m are parameters determined empirically, and h_f is the final displacement after the unloading process. As the S value is determined from the slope at the maximum load and displacement peak, where $h = h_{max}$, the equation 1.6 may be differentiated as:

$$\frac{dP}{dh}_{(h=h_{max})} = mB(h_{max} - h_f)^{m-1}\,. \qquad \textbf{Equation 1.7}$$

With the known value of S, the contact depth h_c can also be calculated from the P vs h curves according to:

$$h_c = h_{max} - \varepsilon\frac{P_{max}}{S} \qquad \textbf{Equation 1.8}$$

where ε is a constant depending on the indenter geometry, approximately equal to 0.75 in the case of the Berkovich indenter.[38]

One of the main advantages of the nanoindentation technique is that the contact area can be estimated without a direct measurement of the indentation imprint after the test, which experimentally would be a difficult task due to the small indentation sizes. The contact area may be estimated by an empirically determined indenter shape function at the contact depth h_c, $A = f(h_c)$. This function $f(d)$ relates the cross-sectional area a of the indenter with the distance d from its tip. In the case of a geometrically perfect Berkovich indenter, the area function for this tip geometry is:

$$f(d) = 24.56d^2 \qquad \textbf{Equation 1.9}$$

However, real Berkovich indenters are not perfect, and their tips are round at the end, usually with tip radii in the range of 10-100 nm.[50] Furthermore, the roundness of the indenter tip increases with the continued use. To overcome this, a simple experimental procedure of calibration was developed[50], consisting in performing indentations of different penetration depth in a material with well-known isotropic elastic properties, assuming that those properties do not change with depth (typically fused silica E = 72 GPa[13]). Through indentation tests of this standard material, the deviation of the non-ideal indenter geometry is accounted. The equation for the correct contact area of a Berkovich indenter is hence given by:

$$A(h) = \sum_{n=0}^{8} C_n(h_c)^{2-n} = C_0h^2 + C_1h + C_2h^{1/2} + C_3h^{1/4} \ldots\ldots + C_8h^{1/128} \qquad \textbf{Equation 1.10}$$

where the constants C_0 to C_8 are determined by curve-fitting procedure. The first term of the equation 1.10 represents a perfect pyramid cone whilst the second describes a paraboloid of revolution which approximates to a sphere at small penetration depths.[13] The relative importance of the terms decreases in the same order.

As the area is calculated, and taking into consideration the parameters described previously, hardness and the reduced elastic modulus can be calculated using equations 1.10 and 1.11 respectively, as follows:

$$H = \frac{P_{max}}{A}$$ **Equation 1.10**

and

$$E_{red} = \frac{1}{\beta}\frac{\sqrt{\pi}}{2}\frac{S}{\sqrt{A}}.$$ **Equation 1.11**

In equation 1.11, β is a parameter which depends on the geometry of the indenter (β = 1.034 for Berkovich geometry). Again, the reduced modulus E_{red} accounts for the fact that the elastic deformation takes place both in the indenter and the material, and the elastic modulus of the material E can be calculated using the equation 1.2. In the case of diamond indenters, E = 1141 GPa and ν = 0.07.[53]

As it was commented before in section 1.2.1.1, the *CSM* modulus permits the continuous measurement of the contact stiffness during the loading portion of the test. In doing so, a small sinusoidal varying signal is imposed on the output, which drives the motion of the indenter whilst the resulting response is analyzed by means of a frequency amplifier [38,50]. As a consequence, a continuous measurement of H and E can be done as a function of depth in one simple experiment. Generally, during nanoindentation of monolithic isotropic materials it is expected that both H and E remain constant and independent of the penetration of the indenter.

- ***Method considerations***

The Oliver and Pharr method[50] has successfully been applied for the calculation of H and E in different materials of diverse nature[13]. However, some of the aspects regarding the indentation process, especially those related with the indenter itself and its interaction with the materials as well as their response, need to be taken with care. Among these aspects there may be recalled the indenter shape and the errors induced due to the sinking in and the piling up processes taking place during nanoindentation.

1.2.3.2 Stress-strain curves

As it was described in section 1.2.2.2, the stress-strain (σ-ε) behavior of a material can be described by the relation presented by Hertz for spherical indentation (see equation 1.4), where the indentation stress P_m is equated to the indentation strain or a/r_{sph}. Furthermore, if a spherical nanoindentation test is carried out, and the CSM modulus is used, the load and displacement (P-h) information as well as the stiffness (S) can be recorded during the test. Using the formulations given by Oliver and Pharr[13] as well as by Field and Swain[18], the contact depth (h_c) and the contact radius (a) can be calculated from S in the elasto-plastic regime, according to:

$$h_c = h_t - \frac{3P}{4S}. \qquad \textbf{Equation 1.12}$$

and, once h_c is calculated, the contact radius yields:

$$a = \sqrt{2Rh_c - {h_c}^2} \qquad \textbf{Equation 1.13}$$

Then, by using the outputs of equations 1.12 and 1.13 as inputs in equation 1.4, it is possible to construct the stress-strain curves. An important issue to account for in the correct assessment of σ-ε curves, is the determination of the initial contact point where both load and displacement are zero. This is not an easy task due to the reduced length scale in which this contact takes place, especially for tips with a large radius of curvature, where interactions between the surface and the tip such as capillary forces or electrostatic interactions can mask the physical contact response. Different methods to determine the point zero of contact may be found in the literature[54–57]. Using the linear dependency of contact stiffness S and the contact radius a expressed in equation 1.14, the curve may be fit through the origin, and therefore the correct the contact point can be obtained.

$$S = 2E_{red}a \qquad \textbf{Equation 1.14}$$

Different examples of σ-ε curves can be found in the literature for a variety of materials. Two examples are presented in Figure 10, where the stress-strain curves for superconductor YBCO crystals[39,58] (a) and porous zirconia[24] (b) are presented.

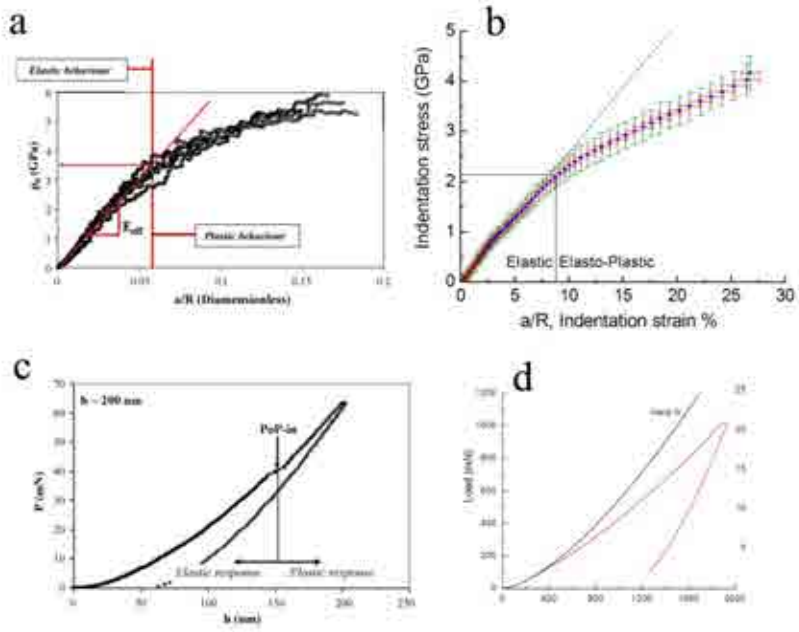

Figure 10**.** Stress-strain curves obtained from spherical nanoindentation of (a) single crystals of YBCO textured by the Bridgman technique[58] and (b) porous nanocrystalline zirconia[24]. (c,d) Respective *P-h* curves showing "Pop-In" events and a Hertzian fit.

1.2.3.3 Elastic modulus from spherical nanoindentation

Once the contact point is correctly determined, the constructed σ-ε indentation curves show the elastic and elasto-plastic deformation zones of the tested materials. The first linear range of the penetration regime, associated with the elastic deformation zone, is related to the elastic modulus E of the sample. In this range, the nanoindentation σ-ε behavior can be described, as in the case of the typical traction test in the elastic region, by a linear equation of type:

$$\sigma = E\varepsilon \qquad \textbf{Equation 1.14}$$

In this equation, the linear slope corresponds to the elastic modulus E of the tested material. Consequently, after the correct construction of the nanoindentation σ-ε curves for a given material, the elastic modulus may be calculated by a simple linear regression of the elastic region [24,58].

1.2.3.4 Yield Strength

The yield strength or yield point σ_y can also be extracted from the spherical nanoindentation test. Depending on the specific mechanisms taking place in the material during indentation, the onset of yielding can be distinguished from the *P-h* curves as a discontinuity during the loading process, especially at very small loads. Such discontinuities are often called "pop-in" events, and have been related to different phenomena occurring in materials promoted by the indentation process, such as dislocation movement responsible for yielding in metals or cracking in some ceramics. These events have also been directly related to σ_y and the transition between elastic and plastic behavior[58] (see Figure 10 c).

However, the Pop-in events indicating the onset of yielding are not always distinguishable from the *P-h* curve. A Hertzian fit of the experimental *P-h* curve may be performed by using the *E* value, also calculated by spherical indentation as described in the last section by means of equation 1.1 (see also Figure 10 d). The deviation from the experimental curve from the Hertzian fit is directly related to the yield strength.

Regarded as the point in which the elastic behavior departs of linearity, σ_y can also be identified in the nanoindentation σ-ε curves. If a linear fit is performed on the elastic linear region, it is possible to determine the yield strength as the stress at which the slope of the experimental curves change, as clearly shown in Figure 10 a-b.

1.2.3.5 Fracture toughness

As it was mentioned in section 2.2.3, fracture toughness K_c of brittle materials may be measured at a very small scale through nanoindentation. The techniques used for the calculation of K_c are similar to those developed for microindentation testing[38], which are based on the measurement of the radial cracks induced through nanoindentation (see Figure 8), often with sharp tips such as of those of Berkovich and cube corner

indenters.[59,60] Evans *etal* proposed a relationship between fracture toughness K_c and the length of the radial cracks c (see Figure 8) for Vickers indentation:

$$K_c = \alpha\left(\frac{E}{H}\right)\left(\frac{P_{\max}}{c^{3/2}}\right) \qquad \textbf{Equation 1.16}$$

In equation 1.16 the P_{max} corresponds to the maximum applied load and α is an empirical constant, which depends on the indenter geometry and on the crack geometry. It has been demonstrated that the relationship between K_c and crack length c applies satisfactory for Berkovich and cube corner nanoindentation using different α values. Anstis *et al* proposed an α value of 0.016 ± 0.004 for Vickers and Berkovich tip geometries, whereas Oliver and Pharr have used a value of α = 0.04 for cube corner indenters. On the other hand, other researchers have proposed different values for these indenters α = 0.033 and 0.036[49,61].

As E and H values can be obtained with relative simplicity following the Oliver and Pharr method described in section 1.2.3.1, and the cracks can be measured by the use of different available advanced characterization techniques, the assessment of fracture toughness of materials in small volumes becomes a straightforward process using equation 1.16. Nevertheless, it should be recalled here that the applicability of this equation for fracture toughness assessment is limited by the condition $c > 2a$.

Furthermore, some authors suggest that, owing to the low variation in the $(E/H)^{1/2}$ factor in most ceramic materials ($E/H^{1/2} \approx 2$), the equation 1.16 can be rewritten in a simpler form:

$$K_c = \beta\frac{P_{\max}}{c^{3/2}} \qquad \textbf{Equation 1.17}$$

where β denotes a new factor also depending on the indenter and crack geometries. This factor has been found to be 0.0874 for Vickers and Berkovich, and 0.1476 for cube corner tips.[47]

The referred methodologies for K_c calculation based on equations 1.16 and 1.17 are well suited approaches especially for crack geometries with the form of "median" or "half-penny type" in which cracks meet below the surface of the material. In the case of crack morphologies of the "Palmqvist" type, where cracks remain spatially separated beneath the indented material's surface, other expressions have been proposed by Laugier[62] (equation 1.18) and Shetty *et al*.[63] (equation 1.19):

$$K_c = \chi_v \left(\frac{a}{l}\right)^{1/2} \left(\frac{E}{H}\right)^{2/3} \frac{P_{\max}}{c^{3/2}} \qquad \textbf{Equation 1.18}$$

and

$$K_c = \frac{1}{3\left(1-\nu^2\right)\left(\pi\sqrt{2}\tan\psi\right)^{1/3}} \left(\frac{HP_{\max}}{4l}\right)^{1/2} \qquad \textbf{Equation 1.19}$$

where χ_v is a constant evaluated as 0.015, ν is the poisson ratio of the material and Ψ is the face angle of the indenter (see different Ψ indenter values in Figure 5).

The correct determination of K_c is thus given by the selection of the adequate expression together with the correct use of the equation parameters. Both requirements depend, in turn, on the correct estimation of the intrinsic mechanical properties for the material (E, H and ν) and the crack and indenter geometries (α, β, χ_v and Ψ), as well as the precise crack length measurement (c, a and l).

1.2.4 Nanoindentation of coatings and thin films

The mechanical properties extracted through nanoindentation are expected to be practically independent of the penetration depth in the case of homogeneous monolithic materials. However, when nanoindentation is performed on heterogeneous materials such as gradient materials, particles embedded in a matrix, thin coatings or films, multilayers, etc., these properties may drastically vary with the indentation depth, especially because of the influence of an underlying interface and/or the presence of an elastically and plastically different material[14,39,64–66].

Taking into consideration the coated nature of the system under study in the present thesis -a columnar mullite coating deposited on silicon carbide substrate-, the main aspects related with the evaluation of the mechanical behavior of ceramic coatings and films through nanoindentation are presented in this section. It includes the influence of coating thickness and microstructure, as well as substrate nature on the measurement of the intrinsic coating or film properties, the effect of the internal stresses present in coatings and films, and the fracture of coatings during indentation and its interaction with the interface and substrate, among others.[39,66] Furthermore, the methodologies for the calculation of some additional key properties associated with the adhesion between coating and substrate, i.e. energy of adhesion G_{int} and interface fracture toughness K_{int}, are also included in the survey presented below.

1.2.4.1 Coating thickness influence

As the indenter penetrates a coating deposited on a bulk substrate, the response obtained in the first stages of the process is mostly given by the sole coating properties, up to a point in which the underlying substrate influences significantly such response. At that stage, any further increase in load will induce a composite response, which combines the influences of both coating and substrate. The obtained response in turn, corresponds to the affiliated elastic and plastic deformation fields developed in the indented material (see Figure 11), as well as to the additional fracture mechanisms eventually promoted during the process (often cracking in brittle materials). The interaction of such deformation fields and fracture processes with the coating itself and with the interface and substrate, are essential for the interpretation of the extracted properties. As the load is increased, the indenter penetrates and the ratio between its penetration and the coating thickness, h/t (also known as the normalized penetration depth), becomes a key parameter to determine the extent of substrate effects, together with the intrinsic film and substrate properties (H_f, E_f, H_s and E_s).

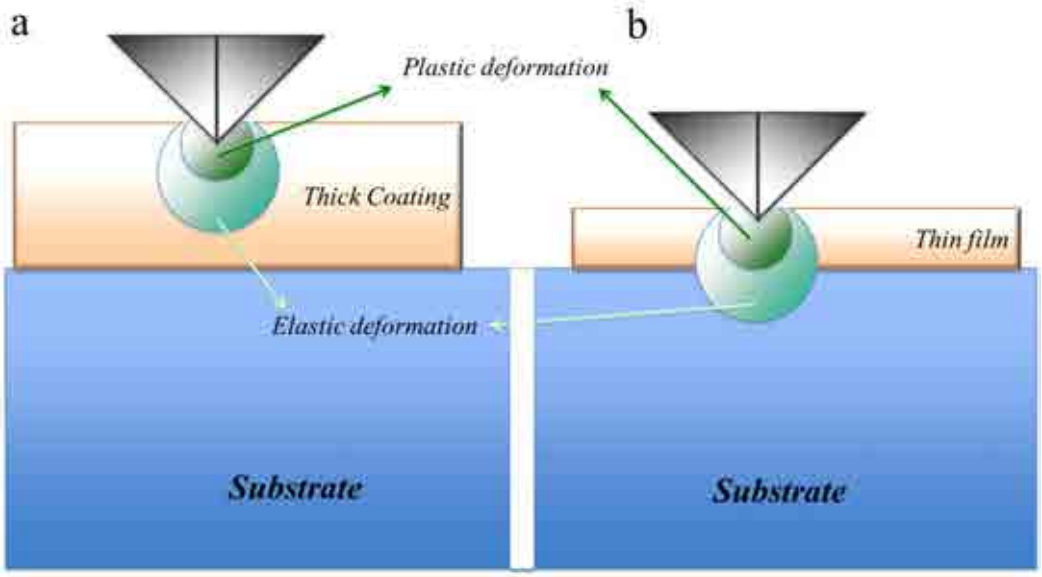

Figure 11. Elastic and plastic deformation fields for indentations of relatively "thick" coatings (a)- small *h*/*t* ratios, and thin films (b)- high *h*/*t* ratios.

The penetration depth of the indenter may be controlled as an input parameter in most nanoindenters, and depending on the specific testing system, very small penetrations can be applied. Therefore, in the case of relatively "thick" coatings (see Figure 11 a), small *h*/*t* ratios are easily achieved and the intrinsic mechanical properties of the coating such as *H* and *E*, without any substrate influence, may be directly extracted by means of the Oliver and Pharr methodologhy[50,67]. Similarly, sharp nanoindentation can be used to produce controlled cracks fully confined in the coating, valid for assessing the coating fracture toughness. Nonetheless, the coating thickness is often limited by the specific application or the deposition technique used. Thus, simple extraction of the intrinsic mechanical properties directly from the obtained response becomes a difficult task. This is the case of many of the thin coatings and the so-called "thin films", in which thicknesses are lower than 1 μm (see Figure 11 b).

The coating thickness is also a limiting factor in terms of the cracking scenario needed for calculating fracture toughness. The difficulties in producing controlled cracks, small enough to be fully comprised within the film, and consideration of the influence of the internal film stresses on the formation and propagation of such cracks, are some of the

issues to dealt with in order to set effective estimations for fracture toughness of thin coatings and films, K_f.

Accounting for the concepts previously described, the h/t parameter as well as the intrinsic film and substrate properties must be analyzed within the framework of the plastic and elastic deformation fields referred above. Similarly, in the case of film and interfacial fracture toughness, special considerations must be taken for the interface and substrate effects in addition to the internal or residual stresses present in the films and their microstructure.

- ***Hardness***

In the case of hardness assessment, particular attention must be paid to the plastic deformation zone generated by the nanoindentation process. In the case of relatively "thick" coatings (see Figure 11 a), the measured hardness is practically unaffected by the substrate as the plastic zone do not interact with the substrate. Conversely, in "thin" coatings and films even if small loads are applied, the induced plastic deformation zone is affected by the substrate during loading (see Figure 11 b).

If the film hardness H_f evaluated during the loading process is plotted versus the h/t parameter, three different stages may be discerned as the indenter penetrates.[39] They are evident in Figure 12 a, where plots of H_f vs h/t corresponding to hard film/soft substrate and soft film/ hard substrate pairs, are presented.

For shallow penetration depths (zone 1), the response is only product of the film properties; and therefore, H present a constant value directly affiliated with the intrinsic film hardness H_f. Further increases in load induces a variation in H towards higher or lower values depending on the substrate properties, as a result of its influence of the measured data. The combination of film and substrate influences on the obtained H

determines zone 2. At higher loads the response is mostly dominated by the substrate, and H may be associated with the substrate hardness H_s.

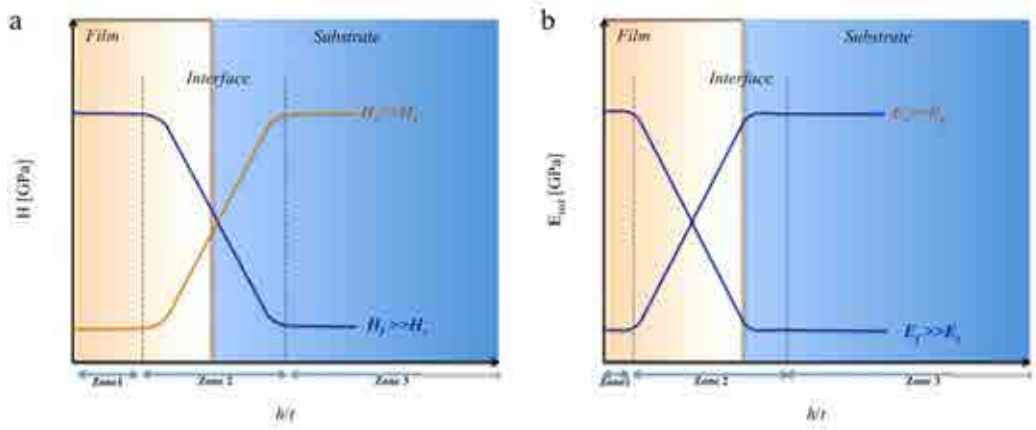

Figure 12**.** (a) Scheme of the variation of H with the parameter h/t (normalized thickness) for two generic coated systems: hard thin film/soft substrate and soft thin film/ hard substrate. (b) Variation of E_{red} with h/t for other two generic coated systems: stiff thin film/compliant substrate and compliant thin film/ stiff substrate.

There is a standard rule for assessing the indentation hardness of coatings that is customary used in the field of coatings, also known as the "rule of 10%" or "rule of thumb".[68] It is based on the experimental fact that the penetration depth h should not be larger than 10% of the coating thickness t (h_{max}<0.1t) if the intrinsic hardness of a coating (or film) wants to be measured correctly, i.e. without any substrate influence.[12,39] However, there are some matters to be analyzed regarding the application of this rule. On one hand, although for most coating/substrate combinations at reasonable penetration depths the rule of the 10% is applicable, it has been found that depending on the specific coating/substrate pair, and particularly on the corresponding elastic mismatch, this rule could be too strict or too loose.[68] On the other hand, in the case of thin films a penetration of less than a tenth of the film thickness is often very difficult to achieve, and experimental limitations in the technique such as the roundness of the tips at small penetrations may imply difficulties for interpreting the attained results.

To account for the limitations mentioned above, some models have been developed to extract the film hardness H_f when the hardness of the substrate H_s and the combined or composite hardness H_c (also known as the apparent hardness H_a) at different depths are known, through data extrapolation to "zero depth" point[39,66]. The correct choice of a model depends on the relative properties between film and substrate (H_f/H_s and E_f/E_s). An example of one of the most used models for a generic coated system corresponding to hard coating / hard substrate is the one proposed by Tuck *et al.*[69], and governed by the following relationship:

$$H_a = H_s + \frac{H_{film} - H_s}{1 + \kappa\left(\frac{h}{t}\right)^{\alpha}} \qquad \textbf{Equation 1.20}$$

In this model the apparent hardness H_a may be expressed as a function of the film and substrate hardness H_f and H_s respectively, the penetration depth h, the coating thickness t, and the numerical parameters κ and α. Others authors[39,70–72] have also proposed the use of the law of mixtures by using the total contact area between the tip and the film as well as their relative contact areas.

Finally, it can be said that although some specific cases of coated pairs require the utilization of these methodologies for a more accurate analysis, no general expression has been proposed for the assessment of H_f of very thin films, and the rule of 10% is nowadays successfully employed.

- ***Elastic Modulus***

In the case of extracting the elastic modulus of thin films through nanoindentation, similar issues as those indicated for the measurement of hardness arise. However, it must be highlighted that in this case the substrate presents an influence in the response at much lower penetration depths (see Figure 12 b) due to the fact that the elastic deformation field involved in the measurement of E has a larger volume than the one

(plastic) associated with the evaluation of H[39,66,72]. Consequently, the penetration depth necessary to obtain the sole film elastic modulus E_{film} is even lower than that proposed by the rule of the 10% ($h < 0.1t$) to estimate the H_{film}.[73]

If the reduced elastic modulus E_{red} (combining the moduli of both tested and indenter materials, see equation 1.2) is plotted as a function of the h/t parameter, for generic cases corresponding to stiff film / compliant substrate and stiff substrate / compliant film pairs (Figure 12 b), it may be observed that the influence of the substrate occurs at smaller penetration depths than in the case of H (see Figure 12 a). Consequently, stationary (constant) value for the elastic modulus of the film, even at very low penetration depths, is hardly achievable. The zone 1 associated with the film response is therefore smaller than zone 2. Hence, for characterizing the intrinsic response of the coating, smaller penetration depths are required. If these penetration depths are in the order of some tenths of nanometers, a careful calibration of the indentation tip has to be made[39,50,72].

Similar to the case of hardness, different models have been proposed to extract the film modulus (E_{film}) from the measured substrate-affected modulus (E_c or E_a). In general, most of them assume that film thickness (t) and substrate modulus (E_s) are known.

Gao and coworkers proposed a simple model including two functions I_0 and I_1 to govern the transition in elastic properties from film to substrate[74]. Later, some modifications were introduced by Song, Pharr and colleagues leading to the so called "Song and Pharr" model[75–77] whose configuration is presented in Figure 13 a, and the expression that describes this behavior is given by in equation 1.21. Recently, Hay and Crawford introduced a new modification to the Song and Pharr model to account for the significant lateral support in highly stiff films under compliant substrates[67]. Such modification proposes that the film may also act as a layer in parallel with the substrate, as shown in the configuration of Figure 13 b, and includes an additional moderation factor F. The formulation of this model is presented in equation 1.24. Bec *et al.* and Saha and Nix also proposed simple closed form models[78,79], and they are

mathematically described by equations 1.22 and 1.23. The configuration of these models is presented in the scheme of Figure 13 a (Bec *et al.*) and Figure 13 c (Saha and Nix). These models are nowadays well established and widely used methods to effectively extract the intrinsic film elastic properties through nanoindentation of thin films systems[66,67,72,80,81].

"Song and Pharr model" $\mu_a = (1 - I_0)\frac{1}{\mu_s} + I_0\frac{1}{\mu_s}$, **Equation 1.21**

"Bec *et al.* model" $\frac{1}{E_{red}} = \frac{1-\nu_i^2}{E_i} + \frac{1-\nu_f^2}{E_f}(1 - e^{-\frac{\alpha(t-h)}{a}}) + \frac{1-\nu_s^2}{E_s}(e^{-\frac{\alpha(t-h)}{a}})$ **Equation 1.22**

"Saha and Nix" $\frac{1}{2E_{red}a} = \frac{1}{1+2t/\pi a}\left(\frac{t}{\pi a^2 E_f} + \frac{1}{2aE_s}\right)$ **Equation 1.23**

"Hay and Crawford"

$$\frac{2\left(1-\nu_a{}^2\right)}{E_{red}} = \frac{\left(1-\nu_s\right)\left(1-\nu_f\right)}{\left[1-\left(1-I_1\right)\nu_f - I_1\nu_s\right]}\left[\left(1-I_0\right)\frac{2(1+\nu_s)}{E_s} + I_0\frac{2(1+\nu_f)}{E_f}\right] \quad \textbf{Equation 1.24}$$

where μ_a, μ_f and μ_s are the apparent, the film, and the substrate shear modulus.

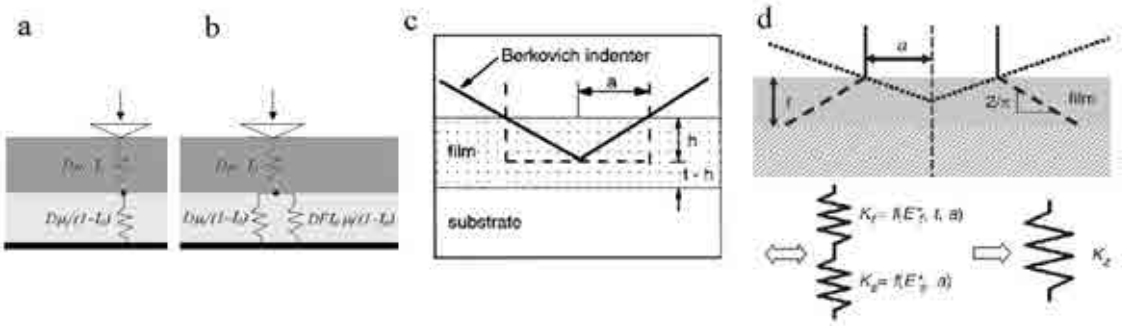

Figure 13. Configuration of different models for E_{film} calculation. "Song and Pharr" (a), "Hay and Crawford" (b), "Saha and Nix" (c) and "Bec *et al.*" (d) models.

Alternatively, and according to the justification given in previous sections, the use of spherical indenters as opposed to sharp indenters allows for characterizing the elastic

modulus at much lower penetration depths. Therefore, the use of this geometry of indenters is a powerful tool, especially if the sample is probed with different spheres of different radii, in order to correctly calibrate the influence of the substrate.

- ***Fracture toughness***

Following the ideas introduced in section 1.2.2.3, fracture toughness K_c of a bulk monolithic material may be calculated through nanoindentation by measuring the growth resistance of radial cracks induced through sharp indenters. However, in the case of the indentation of coatings and films, some critical matters must be considered if film fracture toughness K_f wants to be assessed.

When indenting a film attempting to determine its intrinsic fracture toughness, the induced cracks should be fully contained within the layer. This requirement implies by itself an intrinsic experimental limitation, particularly in very thin films. Furthermore, the cracks should remain away from the interface, as otherwise they could either be strongly affected by the elastic mismatch with the substrate material or become directly involved in other fracture events, such as delamination or radial cracking at the interface, invalidating then simple K_f estimation based on indentation fracture mechanics. The internal or residual stresses (σ_r) present in coatings and thin films due to the elastic mismatch with the substrate, usually induced during the deposition process, can drastically influence not only the cracks formation but also their propagation in the film. Finally, for the sake of a precise fracture toughness assessment, some of the proposed methods demand a relatively significant crack length, as mentioned in section 1.2.3.5., a requirement difficult to fulfill without overriding the ones just referred.

Moreover, as a consequence of the internal stresses, and depending on the magnitude of the elastic mismatch between the substrate and the film, the geometry of a crack induced in a coating or film by nanoindentation, can be distorted in comparison with the

shape of the same crack in a bulk monolithic material. All these effects need to be taken into account for the estimation of the intrinsic film fracture toughness K_f.

To account for the residual stresses influence on K_f, Marshall and Lawn[82] proposed a modification of the equation 1.17, according to:

$$K_c^0 = K_c + K_{\sigma_r} = \xi_v^R \left(\frac{E}{H}\right)^{1/2} \frac{P}{c^{3/2}} + \psi_0 \sigma_r c^{1/2} \qquad \textbf{Equation 1.25}$$

In this equation, the fracture toughness corrected by the effect of the residual stresses (K_c^0) is equated as the sum of the stress intensity factor due to the applied indentation load (K_c) and the stress intensity factor due to σ_r ($K_{\sigma r}$). The geometric factor ψ = 1.29 corresponds to a semi-circular crack configuration.

The substrate influence on K_f estimation, especially its effect in the change of crack geometry in stressed films should also be taken into account. In the case of a film deposited on a stiffer substrate, the geometry of cracks induced in the film by sharp indenters has usually proved to be altered from the ideal semi-circular half penny shape to a deformed semi-elliptical one, as detailed in Figure 14.[83] Hence, in such a case an increase in the ellipticity of cracks e, where $e = c/a$ and a denotes the median crack extent, is evident as the crack approaches the interface.

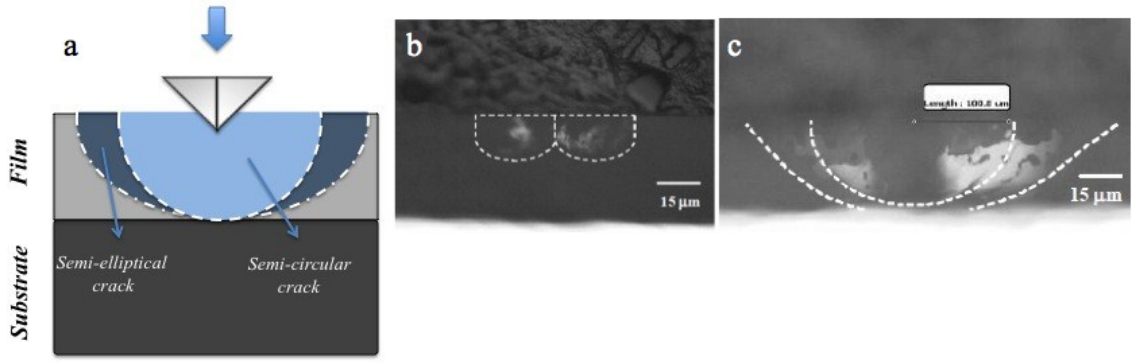

Figure 14. (a) General scheme denoting the ellipticity (e) of a radial crack induced by the sharp indentation of a stressed film. Examples of e in cracks produced by Vickers indentation at different loads (b) P= 0.98 N and (c) P= 4.9 N in a glass coating on a metal substrate[83].

The increase in *e* reflects the effect resulting from the presence of a stiffer substrate both on crack generation (due to the mismatch in the elastic-to-inelastic deformation) as well as on crack propagation (due to the constraining effect on the crack once formed)[84]. To account for such substrate effects, the stress intensity factors K_c and $K_{\sigma r}$ of equation 1.25 should be modified by the F_c and $f_{\sigma r}$ correction factors respectively, yielding:

$$K_c^1 = F_c K_c + f_{\sigma_r} K_{\sigma_r} = F_c \xi_v^R \left(\frac{E}{H}\right)^{1/2} \frac{P}{c^{3/2}} + f_{\sigma_r} \psi_0 \sigma_r c^{1/2} \qquad \textbf{Equation 1.26}$$

where F_c can be calculated as a function of *e* by using the plot of Figure 15 a, and $f_{\sigma r}$ can also be extracted as a function of *e* and the ratio *a*/*t* from Figure 15 b.[84]

The fracture toughness corrected by the residual stresses plus the substrate influence (K_c^1) can now be calculated from equation 1.26 by using the already estimated H_f and E_f values together with c, σ_r, *P*, F_c and $f_{\sigma r}$.

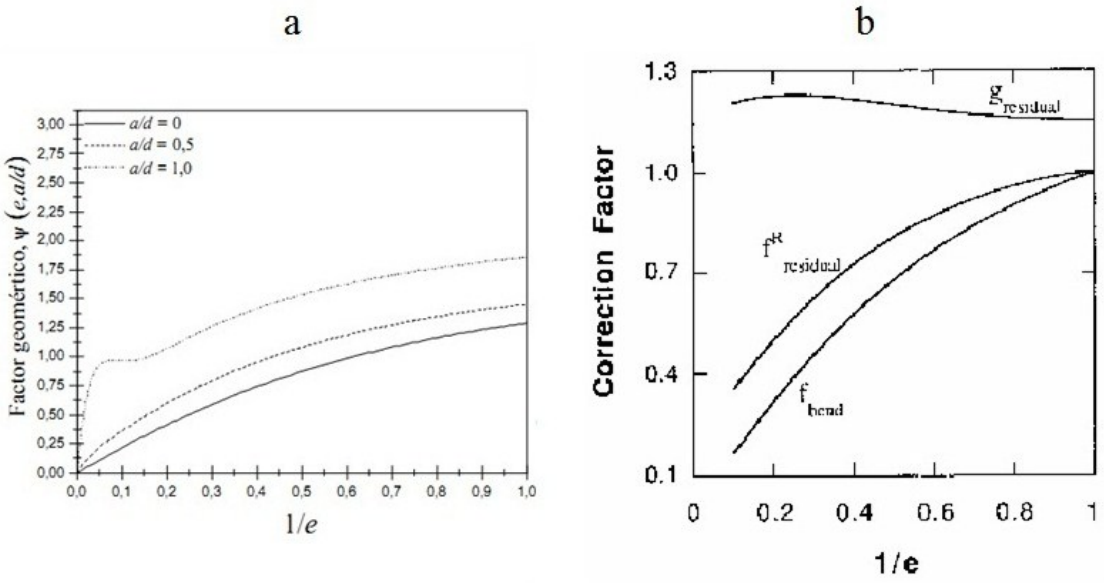

Figure 15. (a) Geometric factor F_c as a function of the ellipticity of the radial crack *e* and (b) factor due to residual stresses $f_{\sigma r}$ as a function of the geometric factor $\psi(e,a/d)$ and *e*[84].

1.2.4.2 Coating microstructure effects

As applied load and the induced deformation are reduced to a very low range in nanoindentation, the influence of microstructure becomes a determinant factor on the extracted properties for the coating. Most of the methodologies of analysis in nanoindentation assume that the materials are homogeneous and continuous. However, it is well-known that this is not the case for real materials, in which continuum is broken at a given length scale. This fact is particularly pragmatic in the case of coatings, where heterogeneous microstructures such as columns, layers, splats, etc, are often present due to the deposition process. Accordingly, the microstructural aspects of coatings must be taken into account in the analysis of the extracted data. Within this context, the deformation mechanisms activated during indentation and the type of fracture and its interaction with the microstructure, are key parameters.[20,66,85]

An example of the influence of microstructure on nanoindentation hardness is presented in Figure 16. The data corresponds to two thermal barrier coatings (TBCs) of the same composition (zirconia doped with 8% yttria), deposited on a nickel superalloy by Atmospheric Plasma Spray (APS) and Electron-Beam Physical Vapour Deposition (EB-PVD).

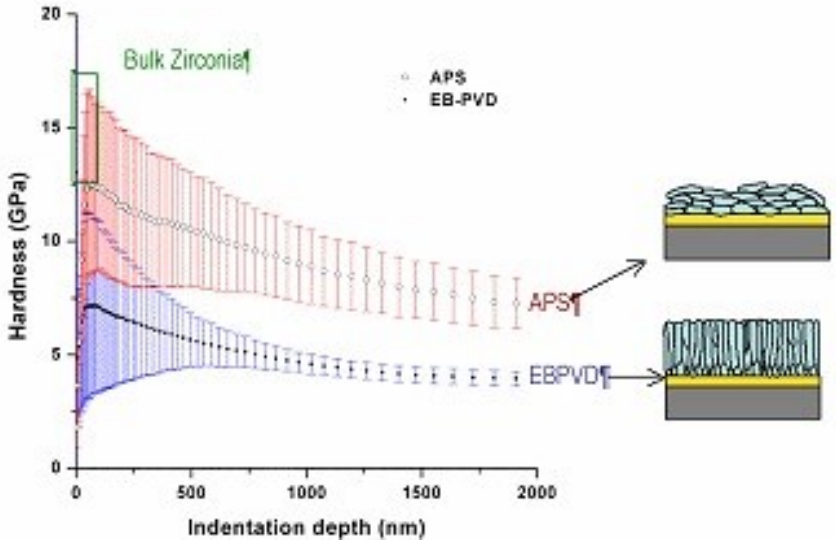

Figure 16. Differences in nanoindentation hardness, as a function of the indentation depth, due to the effect of coating microstructure for a zirconia doped with 8% yttria TBC on a nickel superalloy.[66]

The APS process produces a splat layered microstructure whereas the EB-PVD produces a columnar one. Although the composition of both coatings is essentially the same, their responses are quite distinct, and different in turn to that of bulk zirconia. It may be seen that hardness decreases with the penetration depth already from the beginning, implying that coatings deform by several deformation mechanisms: column sink-in in the case of EB-PVD or splat fracture in the case of APS, besides the conventional plasticity expected for zirconia.

1.2.4.3 Mechanical integrity

Coatings and thin films are used in numerous applications where properties such as resistance to abrasion, corrosion, permeation, and oxidation, as well as magnetic and dielectric properties are needed to meet specialized functional requirements.[86] Although in many of such cases the final functional requirements are not mechanical and structural in nature, the qualitative and quantitative knowledge of the mechanical and structural integrity of coated systems are essential for their practical implementation.

In the case of ceramic coated systems, which correspond to those studied in this investigation, fracture is an almost inevitable consequence of highly loaded contacts[87]. For a relatively thick coating, fracture is often similar to that observed in bulk samples of the coating material. However, as the coating thickness is reduced, the substrate plays an increasing role in influencing or even controlling fracture behavior. Moreover, for thin coatings and film applications, the performance, reliability and durability are tied directly to the interface structure and composition, and depend on the as-deposited properties such as hardness, elastic modulus, toughness and especially adhesion[11,86]. As a consequence, the study of the mechanical integrity of thin coated systems is not only related to the coating integrity and its intrinsic properties such as E, H and K_c, but it is also directly linked to the interface and particularly to the effective adhesion between coating and substrate. The following section is devoted to the description of adhesion and the methodologies developed for its measurement in thin coated systems.

In the previous section, it was described how nanoindentation can be implemented to evaluate fracture toughness by inducing controlled cracking in coatings and films. This section points out how this technique can also be used to induce controlled coating delamination and therefore to calculate adhesion strength. Nevertheless, despite the fact that these methodologies are being increasingly used, there are still not well-established methods for the assessment of toughness and adhesion as in the case of intrinsic *H* and *E* of films. The reason for this is that the mechanism of fracture failure around an indentation is complex, and depends on the relative properties of coating, substrate and interface, and therefore a universal analysis method is unlikely to be developed.[29,87] However, it is possible to identify different typical failure modes that are amenable to analysis, resulting in reasonable toughness data. Upon nanoindentation, a number of different indentation fracture events might occur in a coated system. Some of the more typical may be defined in terms of the relative nature of the substrate/coating pair, as follows[87]:

- ✓ *Ductile substrate on a brittle coating*: Through-thickness fracture, brittle-fracture in coating parallel to interface, ductile interfacial fracture, and microfracture in coating.

- ✓ *Brittle substrate on a brittle coating*: Bulk chipping, through-thickness fracture, microfracture in coating, and microfracture in substrate.

The occurrence of each fracture event depends on the relative toughness of coating/substrate and any interfaces present. These failure modes will be altered by plastic deformation in the substrate, which may lead to the superposition of bending stresses to those generated by the indentation.

- ***Adhesion***

Attempting to evaluate the integrity of coated systems, one of the key factors to account for is the presence of interfaces. These are created by the deposition of dissimilar materials, which in turn suppose the introduction of significant demands concerning thermomechanical integrity and reliability, especially when at least one of the constituents is brittle[88]. These challenges arise from changes in residual stresses, structure and composition. Mismatch in thermal coefficient and high-energy deposition can result in films with high residual stress levels capable of driving fracture along well-bonded film interfaces[86]. All these statements suggest that interfaces are critical sites for the failure occurrence not only during the deposition process but also as a consequence of "in-service" conditions, and hence its role in the reliability of coated systems deserves to be analyzed.

The fundamental property which often dictates the performance of a coating, and which is consequently critical for almost all coating applications, is its adhesion to the substrate.[29] Adhesion of thin coatings and films is becoming very important for optimizing the performance of small volume systems and components, such as the ones inherent to microelectromechanical systems (MEMS), nanoelectromechanical systems (NEMS), and semiconductor devices, among others.[11,14, ,27-29, 31,33,65,89–94]

ASTM standard D907-70 defines adhesion as the state in which two surfaces are held together by interfacial forces which may consist of valence or interlocking forces, or both. Delamination, another important concept in the mechanics of coated systems, is also defined as the phenomenon in which a layer (fiber or coating) separates from the matrix or the substrate (composites materials or coated systems respectively). The adhesion failure or delamination is often considered as a cracking event that can be described by an interfacial toughness parameter, which together with the mechanical properties of the coating and substrate, may be used to predict the onset and propagation rate of failure.

Essentially, adhesion can be quantitatively understood in terms of two energy parameters: the thermodynamic or true work of adhesion (W_A) between the materials of an interface, and the practical work of adhesion ($W_{A,P}$), which comprises the inelastic contributions occurring at and near the interface during the separation process. Most of the different methods for measuring adhesion consist in delaminating the films from the substrate. However, during this process the film and/or the substrate usually experiences plastic deformation, making it difficult to extract the true adhesive energy. Consequently, the parameter measured is the practical work of adhesion:

$$W_{A,P} = W_A + U_f + U_s + U_{fric} \qquad \textbf{Equation 1.27}$$

where U_f and U_s are the energies spent in plastic deformation of the film and the substrate respectively, and U_{fric} corresponds to the energy losses due to friction. From the standpoint of fracture mechanics, the amount of energy necessary for the process of delamination is calculated per unit area of removed film. This energy parameter is known as the strain energy release rate or the energy of adhesion per unit area G, and is a measure of the practical work of adhesion.

There are more than two hundred different methods for measuring thin film adhesion that employ different sample geometries[28,29,86]. Some of the methods use continuous films, some require certain patterning, but all tests use some driving force or stored energy to achieve thin film delamination. The energy may come from an external mechanical force imposed on the film or it can be stored in the film itself (through the internal film stress). The indentation and scratch tests have the widest range of applicability, and are the most used methods. These are described in more detail below. The configurations of some other important methods for thin film adhesion assessment are presented in Figure 17.

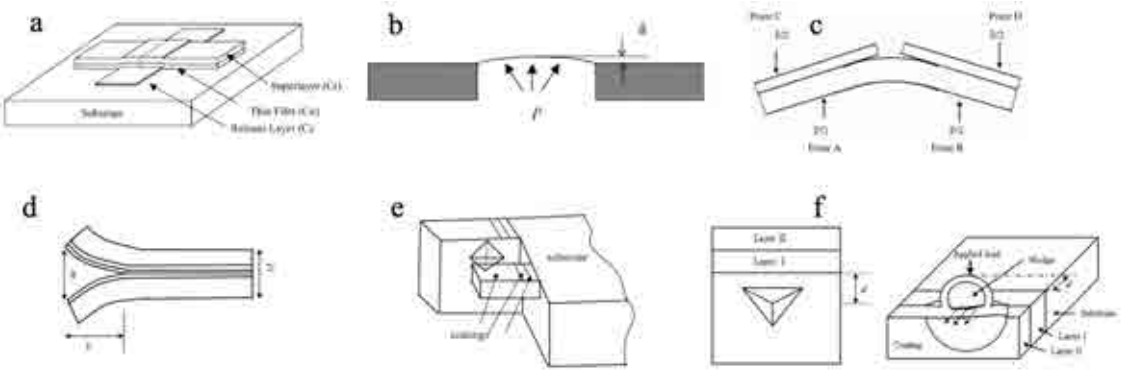

Figure 17. Configuration of some of the principal methods for assessment of thin film adhesion evaluation. (a) Superlayer test[11], (b) Bulge test[11], (c) Four-point bending tests[29], (d) Double cantilever beam test[29], (e) Microcantilever deflection test[29] and (f) Cross-section indentation test[29,96].

Through tests as those attained in Figure 17, the adhesion per unit area G can be calculated. Different G values may be found in the literature for various coated systems of different nature[11,29,31,33,86,91,97]. Nonetheless, as it was pointed out before, the adhesion is a very complex property, strongly dependent on the specific nature of the particular coated pair. Furthermore, taking into consideration the broad spectrum of existing methods for adhesion measurement, the generalization of "typical" or "standard" G values is also complex and comparisons are to be made with care. As it may be observed in table 2, there exists a wide range of G values as evaluated for different coated systems.

System	σ_y (MPa)	E (GPa)	*Thickness* (nm)	G (Jm^{-2})
Ta*/Al/C/Al_2O_3	298	70	500	1.05
W*/Al/Cu/C/SiO_2/Si	298-203	70	500-3200	0.2-0.65
W*/Al/Cu/Cu/SiO_2/Si	700-203	70	40-3200	0.3-27
W*/Al-Cu/SiO_2/Si	329-252	70	340-1000	7.7-8.2
Au/Al_2O_3	338	80.8	15000	80-230

** Used as superlayer on top of the film of interest.*

Table 2. Adhesion energy G values for different coated systems.[28]

(i) Nanoindentation tests

By means of nanoindentation, a controlled delamination can be induced in thin coated systems, especially in the case of brittle and relatively weakly bonded films. As the film is delaminated from the substrate, the thin film interfacial strength may be assessed. Marshall and Evans[27] formulated an expression for G based on the delamination induced by conical indentation:

$$\frac{GE_f}{(1-\nu_f)} = \frac{1}{2}h\sigma_I^2(1+\nu_f)+(1-\alpha)(h\sigma_r^2)-(1-\alpha)h(\sigma_I-\sigma_B)^2 \quad \textbf{Equation 1.28}$$

where E_f and ν_f are the thin film elastic modulus and Poisson ratio respectively, h is the film thickness and σ_r are the residual stresses in the film.

In Figure 18 a the different three phenomena associated with the sharp indentation of relatively soft coatings (*i*. non-buckling, *ii*. double-buckling, and *iii*. single-buckling), are presented together with corresponding real examples for the Cu/SiO_2 system (Figure 18).[11]

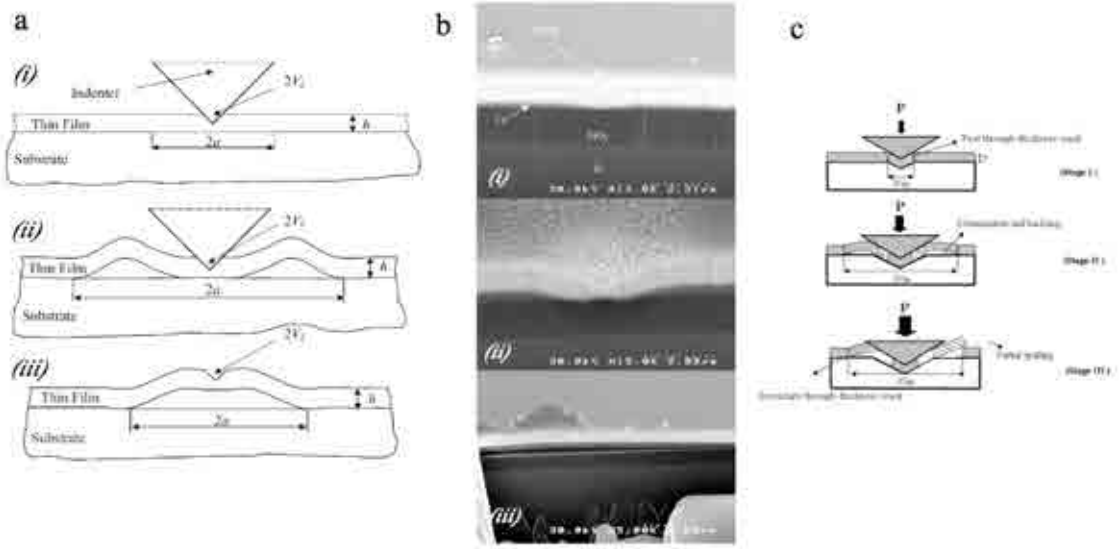

Figure 18. (a) Schemes of events occurring during nanoindentation of soft films, *i*. No buckling during indentation, *ii*. double-buckling during indentation and *iii*. single-buckling after indenter removal[11]. (b) Corresponding FIB cross-sections of the indents in the Cu/SiO_2 system[11]. (c) Schemes of events occurring during nanoindentation of brittle coated systems[29].

As it may be seen in the scheme of Figure 18 a, the sharp indentation plastically deforms a volume equal to $2V_I$. As a consequence, an interfacial crack is nucleated and propagated (*i*). If the indenter is driven deep enough, so that the crack reaches the critical buckling length, the film double buckles during indentation (*ii*). In the case that the crack length does not reach the critical buckling length during indentation, a single buckling can be formed upon tip removal *(iii*). After the tip removal, even if double-buckling occurs during indentation, a single buckle may form because the film is no longer under constraint.[11]

Using the equation 1.29, the indentation stress σ_I can be calculated as a function of the indentation volume V_I, which in turn may be assessed using the penetration depth and the crack length a:

$$\sigma_I = \frac{V_I E_f}{2\pi h a^2 (1-\nu_f)} \qquad \textbf{Equation 1.29}$$

If the crack is driven far enough by the indenter for film buckling, the Euler stress comes into play:

$$\sigma_B = \frac{\mu^2 h^2 E_f}{12 a^2 (1-\nu_f)} \qquad \textbf{Equation 1.30}$$

where μ is a constant that depends on the boundary condition. If the film does not buckle, the parameter α is equal to 1 and delamination is only driven by the indentation stress.[11] The residual stresses do not come into play and the last two terms in equation 2.28 turn zero.

On the other hand, when the coating or film is brittle, the mechanisms involved in the nanoindentation of the system may be more complex. In Figure 18 c the different stages in the nanoindentation fracture of a brittle coating on a hard substrate are presented.[29] In stage I a ring, picture frame, or radial crack may occur depending on the coating/substrate system and indenter geometry. These radial cracks can be used for

measuring K_f following the methodologies described in section 1.4.4.1. As the load is increased, the crack opening also increases and the coating delaminates and buckles, as depicted in the scheme of stage II. Further increases in load may cause secondary through-thickness cracks, followed by either partial or full coating spallation processes that may occur depending on the flaw distribution at the interface. Again, it should be commented that accounting for the small size of the indentation, the film and the cracks produced, adequate use of complementary characterization techniques is needed not only for precise measurement of the delamination crack length *a*, but also for evaluation of buckling occurrence[29].

(ii) Nanoscratch tests

The scratch test is a common technique used to assess adhesion of thin films and protective coatings. In this test, a stylus or diamond indenter is drawn across the coated surface under an increasing load (either stepwise or continuous) up to a specific level. During this scratch, deformation and failure events may occur. If the failure event represents coating detachment, then the critical load can be used as a qualitative measurement of coating-substrate adhesion. This critical load can be determined by inspection, and in some cases, it may be detected by a sudden change in the friction coefficient, acoustic emission, or penetration depth.[12]

Although the conical indenter is the most implemented one, the use of different indenter geometries together with other variables such as scratching speed, loading rate, tip radius, film thickness, substrate hardness, film and substrate roughness, friction coefficient, and friction force, make the use of a critical load as a measure of adhesion complicated. In spite of this, the scratch method enables reliable comparisons of the mechanical performance of coated systems to be performed.[12]

The conventional scratch test is traditionally carried out in specifically designed scratch test equipment. However, if very low and localized loads are desired, many

nanoindenters can be configured to operate in the scratch testing mode. Under this conditions, the normal force is applied to the indenter, while at the same time, the coated specimen is moved sideways, as shown in Figure 19 a. This extension of the nanoindentation technique is often termed nanoscratch. In some instruments, an optional force transducer can be used to measure the friction by measuring the lateral force.[12]

In the case of relatively thick coatings or relatively small applied loads, in which the substrate have little or practically negligible influence (for example Figure 19 b (*i*)) the nanoscratch test can also be used to characterize the intrinsic coating performance. Furthermore, it is well recognized that during scratching a wide range of possible failure modes can occur, although only some of them are indeed dependent on adhesion[29].

In the case of thin coatings or relatively high applied loads, in which the substrate has a marked effect as in the example of Figure 19 b (*ii.*), the main adhesion-related failure modes induced by the scratch test are spallation and buckling (see Figure 19 c-d). Both types of failure are common in the case of hard coatings on soft substrates, and from them it is possible to quantify the adhesion through several mathematical formulations.[98]

In hard coatings deposited on hard substrates, a chipping of material similar to the lateral cracking generated in the scratch testing of bulk ceramics is observed. This failure occasionally coincides with the coating/substrate interface (see Figure 19 e). However, this is not always the case, making the interpretation of results rather difficult. Consequently, the assessment of the adhesion is often limited to the cases of hard coating deposited on softer substrates.

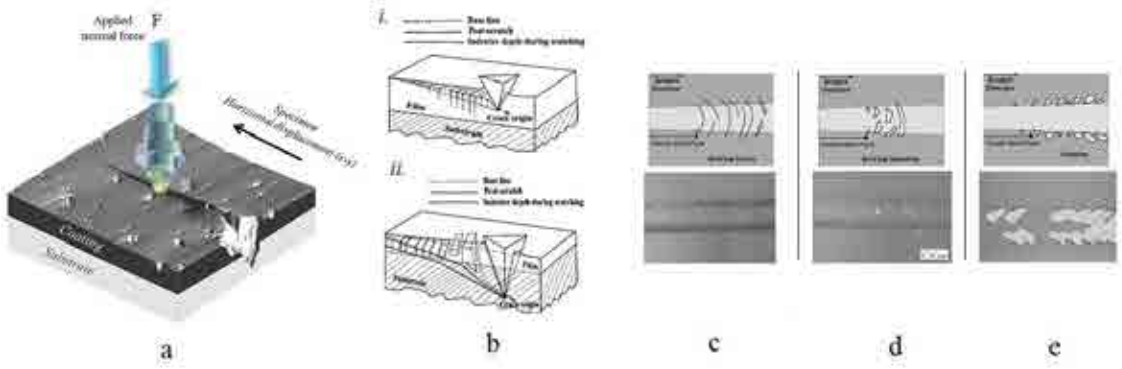

Figure 19. (a) Schemes and real micrographs of the nanoscratch functioning. (b) Nanoscratch at *i*. relatively low loads and *ii*. relatively high loads in amorphous carbon films[99]. (c) Scratch buckling cracking, (d) buckling spallation, and (c) chipping of DLC films on steel substrates. Extracted from ASTM C1624-05.[100]

There are different formulations for the calculation of thin films adhesion based on the nanoscratch testing. Among them, it is interesting to cite one of the first energy based models developed to determine the energy release rate of an induced interfacial crack. It is associated with the in-plane stresses stored in the coating ahead of the sliding stylus[11,29]:

$$G = \frac{\sigma_c^2 t}{2E_f}. \qquad \textbf{Equation 1.31}$$

In equation 1.31, t denotes the thickness and E_f is the elastic modulus of the coating or film, and σ_c is the critical stress given by

$$\sigma_c = \sigma_x + \sigma_r \qquad \textbf{Equation 1.31}$$

where σ_x and σ_r denote the applied stress component in the sliding direction (x) and the residual stresses. In this approach, the applied stress can be defined by:

$$\sigma_x = \frac{P_c}{2\pi a^2}\left[(1-2\nu_s) - \mu\frac{3\pi(4+\nu_s)}{8}\right] \qquad \textbf{Equation 1.33}$$

where P_c is the critical load, ν_s is the Poisson ratio of the substrate, a is the contact radius, and μ is the friction coefficient between the coating and the indenter. In this model, no plastic deformation is accounted for and it is assumed that the contact radius is higher than the coating thickness.[29]

1.3 Environmental barrier coatings (EBCs): The case of mullite

1.3.1 Introduction to the CVD mullite/SiC system

The motivation behind the introduction of mullite coated silicon-based ceramics principally arise from the limitations around the materials used in some applications where high temperature and corrosion resistance are needed, principally in gas turbines systems. Consequently, it is suitable to present a brief overview of these systems and their components, as well as the associated implementation of materials and manufacturing techniques along the last decades, in order to understand the need for introducing novel ceramic materials in gas turbines. In this section, these aspects are presented together with a brief outline of the more recent developments in the fabrication and performance of mullite coatings deposited by chemical vapor deposition (CVD) on silicon carbide (SiC) substrates, the object of this thesis work.

1.3.1.1 Gas turbines applications

A gas turbine is a category of the internal combustion engines used to extract energy in the form of shaft power, compressed air or thrust, or any combination of these. Such energy is used to power aircrafts, trains, ships, generators, etc. As shown in Figure 20, gas turbines have an upstream rotating compressor (I) coupled to a downstream turbine (III), and a combustion chamber in-between (II), that allow them to produce great amount of energy by expanding an axial gas flow at high pressure and temperature. The expansion promotes the rotation of the turbine, enabling it to activate the compressor (in jet engines) or the electric generator (in power plant gas turbines). In the first stage, turbine blades must withstand the most severe combination in the whole system: high temperature, important stresses and corrosive environment; hence, it is generally the limiting component in the machine.

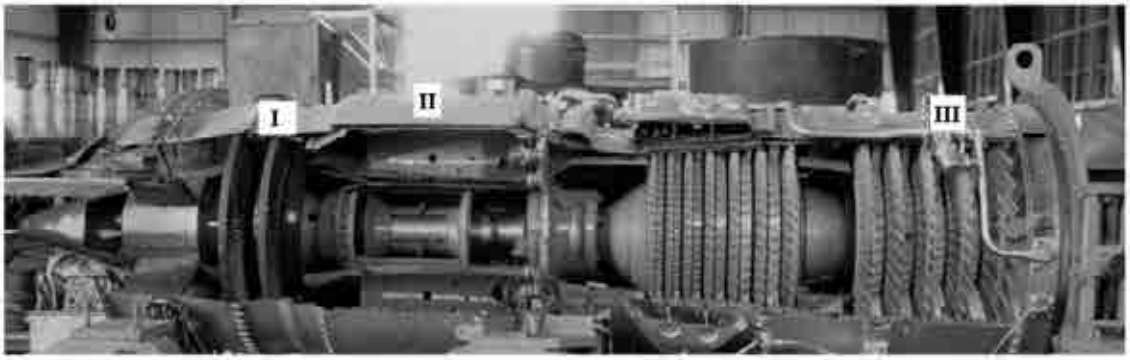

Figure 20.Section of a gas turbine engine[101]

The development of new materials and cooling systems has brought the rapid rise of the turbine firing temperature leading to higher turbine efficiencies[102]. As an example, Figure 21 shows the trend in the capability of the material for turbine blades to withstand high temperatures. Since the 1950s, this capability has raised approximately 500°C (≈ 8-10°C per year). The importance of this achievement may be appreciated by noting that an increase of 56°C in the turbine firing temperature grants a corresponding improvement of 8-13% in output and 2-4% in cycle efficiency. Consequently, advanced materials and processing techniques provide increased power density and improved efficiency.[102]

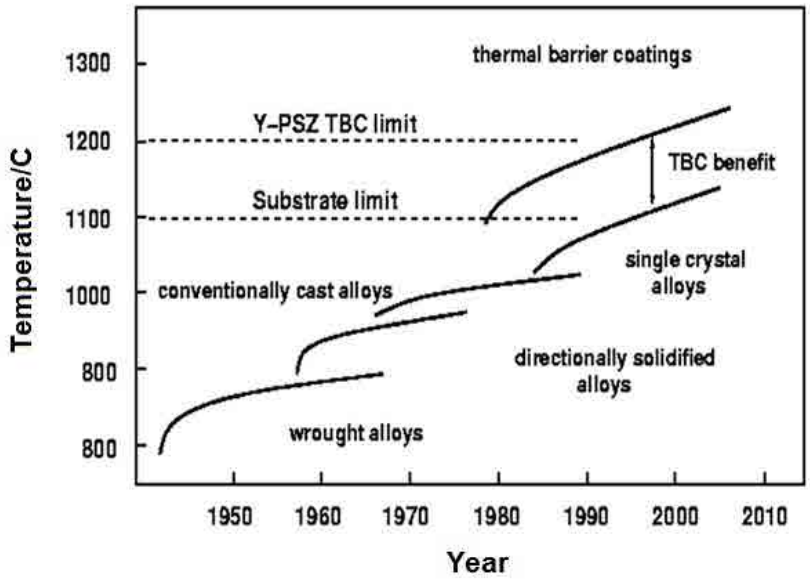

Figure 21. Evolution and improvements in the last 60 years of the turbine firing temperatures and its materials, processing techniques, and protective methods.[102]

Furthermore, for a cleaner power generation with higher efficiencies, small turbines known as micro-turbines have been introduced in last decades, experiencing a dramatic growth up to date. Micro-turbines have compact sizes, low manufacturing costs, high efficiencies, quiet operation, quick startups and minimal emissions. An example of a micro-turbine is presented in Figure 22.

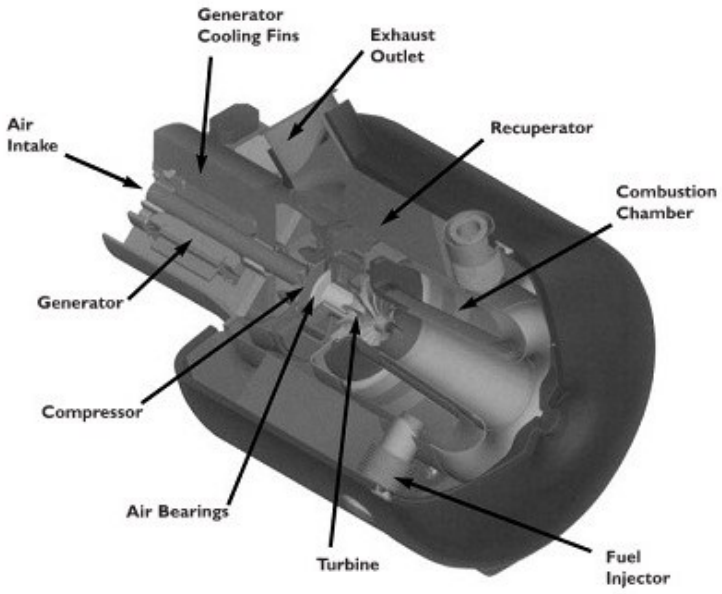

Figure 22. A compact gas micro-turbine and its elements.[102]

1.3.1.2 Thermal barrier coatings (TBCs) for nickel superalloys

Nickel-based superalloys have been used in the hot sections of gas turbines due to their ability to withstand loading at high operating temperatures (close to their melting point), resistance to creep and tolerance to severe working environments. The need for increasing the firing temperature of the engine of gas turbines, to achieve higher efficiencies, has been pushing the capability of superalloys to sustain extreme temperatures to its limit for decades.

In parallel to the progress of modern processing techniques for superalloys, protective coatings have been under development since the 1960s to increase the resistance of nickel alloys to high temperature corrosion and, more recently, to rise their maximum temperature of service in combination with cooling air. Nowadays, turbine blades are covered with thermal barrier coatings (TBCs)[101,103,104]. TBCs consist of a first layer of MCrAl-type materials (M corresponds to Ni or Co) that protects against corrosion due to the formation of protective Cr and Al layers, and a second top layer constituted by a thermal insulator material, generally yttria-stabilized zirconia (YSZ). This top layer in combination with an inner cooling air flow, allows for a temperature reduction up to 200°C in the substrate[105]. An example of this configuration can be observed in Figure 1 a.

Although the existing coating-substrate combinations currently withstand temperatures around 1500°C or even higher, the only way to significantly increase this temperature resistance, and thus, develop more efficient gas-turbine engines; is to increase the cooling air flow. However, this is counterproductive and technically hard to achieve. Hence, efforts are been made in order to introduce novel materials that preserve their properties at even higher temperatures, allowing for higher efficiencies. Ceramic materials stand as excellent candidates for such purposes due to their superior high-temperature, chemical and corrosion resistance.

1.3.1.3 The introduction of silicon-based ceramics

An increase in gas turbines efficiency with a simultaneous decrease in emissions (CO, NO_x) requires high-temperature materials that can operate at temperatures considerably higher than those attainable with the superalloys currently in use. In principle, two requirements must be fulfilled for the development of these materials[106]:

- They must present an optimum combination of mechanical (reliable strength level, toughness, fatigue and creep), chemical (oxidation and corrosion

resistance) and thermo-physical properties (thermal shock resistance) required during service at elevated temperatures.

- Since most of the applications at elevated temperatures are long-term applications, the materials must exhibit superior long-term stability, i.e. the high level of properties required must be maintained as much as possible throughout the entire duration of operation.

Si-based ceramics are attractive materials for use in the hot sections of gas turbine owing to their excellent mechanical properties at high temperature and lower density compared with their metal counterparts. Many researchers in the field focused in silicon-based ceramics such as silicon nitride (Si_3N_4) or silicon carbide (SiC) for their use as structural components in the referred high temperature applications[106]. Potential ceramic gas turbine components include combustion liners and turbine shrouds, vanes and blades, as shown in Figure 23 a-b. It has been demonstrated that the use of ceramic materials in the hot sections of gas turbines can considerably increase the system efficiency to over 40%.[107]

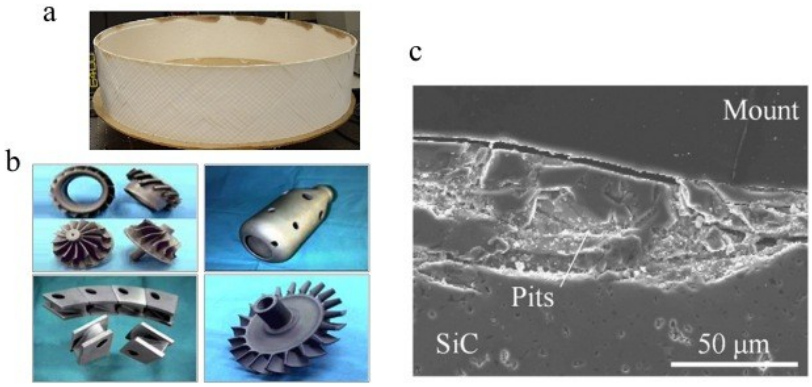

Figure 23. (a) Ceramic combustor [108]. (b) Different gas turbine parts of Si_3N_4. (c) Uncoated SiC hot corrosion[7].

However, silicon-based ceramics are silica former under oxidizing conditions and it has been shown that they undergo accelerated oxidation due to the steam present in high temperature combustion environments, such as those found in the gas turbine hot section (see Figure 20). Thus, prior to the successful introduction of these materials for

long life applications in gas turbines, the problem of accelerated oxidation must be resolved.

1.3.1.4 High temperature corrosion of Si-based ceramics

At high temperatures in dry air or oxygen, SiC reacts with oxygen to form a thin protective silica (SiO_2) layer preventing further oxidation. Nevertheless, in combustion environments, water vapor reacts with the SiO_2 layer to form volatile silicon hydroxide ($Si(OH)_4$), leading to severe surface recession depending on the temperature of exposure and the velocity of combustion gases[109,110]. Furthermore, when these engines operate under certain service conditions such as in marine application, sodium salt present in the environment reacts with sulphur impurities in the fuel during combustion to form sodium sulphate (Na_2SO_4) that gets deposited in the engine components.

Previous studies on hot corrosion of monolithic ceramics revealed that the Na_2SO_4 dissolves the protective SiO_2 layer, accelerates the oxidation and leads to formation of a thick glassy liquid on the surface of the substrate, as well as extensive cavities.[109–111] Therefore, to improve the resistance to water vapor oxidation and hot corrosion in combustion environments, protective coatings against water vapor and salt attacks are crucial to improve the environmental durability of silicon-based ceramic engine components[112,113]. This new generation of coatings to protect Si-based ceramics has been termed environmental barrier coatings (EBCs)[104,114–116].

1.3.1.5 Environmental barrier coatings

The need to reduce or prevent high temperature corrosion in Si-based materials has led to the development of protective thin refractory oxide coatings. Due to their superior corrosion resistance, alumina coatings have been proposed and studied to protect Si-based ceramics, but issues associated with their thermal shock resistance makes them unsuitable in these high temperature applications.

Mullite ($3Al_2O_3 \cdot 2SiO_2$) has also been considered as a potential coating material because of the similarities between its coefficient of thermal expansion and the one of SiC, as well as its stability at elevated temperatures, excellent corrosion resistance and low thermal conductivity[117], together with its excellent creep and thermal shock resistance, and the ability to retain the strength at elevated temperatures.[118]. Mullite coated silicon carbide has been already introduced in gas turbines as a material for combustor chambers in the Ceramic Stationary Gas Turbine Program[119]. There combustor liners fabricated of a SiC/SiC composite were coated by thermal spraying with a three-layer EBC consisting of silicon, mullite and barium strontium aluminium silicate (BSAS). An increase from 5000 to 14000 hours in the component durability was achieved[120]. Other promising mullite coatings include a slurry based mullite/gadolinium silicate (Gd_2SiO_5) EBCs[113].

The CVD mullite coatings materials under investigation in this thesis have been proven to be excellent protective coatings for silicon carbide. Tests have included a wide range of high-temperature and corrosive conditions: pure oxygen at 1300°C, combustion environments containing $NaSO_4$ at 1200°C for 100 h (see Figure 24 a-b), and acidic Fe-based coal slags at 1260°C for 300h (see Figure 24 c-d)[121]. Although the performance of the different protective coatings based in mullite is still under investigation, it is clear that mullite is the key material to achieve the optimal corrosion protection needed to increase and extend the durability of silicon-based ceramics in combustion environments.

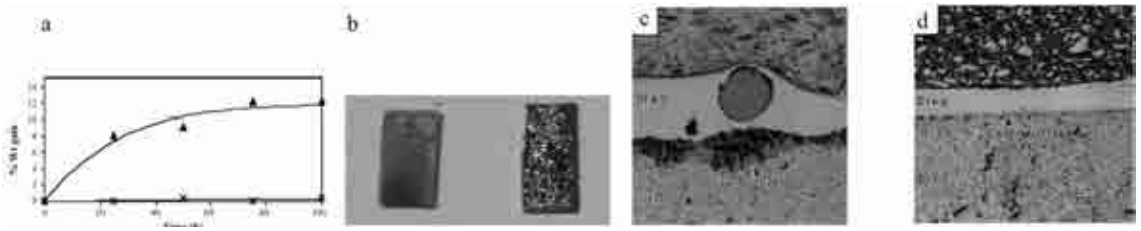

Figure 24. (a) Plots of weight gain vs. exposure time for uncoated (Δ) and coated (x) SiC fibres and (b) the appearance of the cross-section of both specimens after exposure to combustion environments containing $NaSO_4$ at 1200°C for 100 h.[121] (c) Optical cross-section micrograph of an uncoated and (d) mullite coated SiC exposed to an acidic Fe based coal slag after 300 h at 1260ºC.[6]

1.3.1.6 CVD mullite on SiC

Early works on protective mullite coatings were focused on the protection of Si-based ceramics from molten salts. The development of plasma sprayed mullite coatings for protecting SiC initiated with heat exchangers in solar turbines.[114] By mid 1990s, the research group led by Professor V.K. Sarin in Boston University first presented its idea of chemically vapor deposited mullite. In 1996 they published the first report about the equilibrium of the reactants in the system to deposit mullite by CVD. The initial process parameters were determined and crystalline mullite with different morphologies was successfully grown on silicon-based substrates [122]. Later, the versatility of the CVD technique to deposit mullite coatings with varied physical and chemical properties, by modifying the deposition parameters, was reported. The preliminary results showed CVD mullite as an effective barrier to combustion environments at high temperatures, even in atmospheres containing sodium salts[123]. Encouraged by the initial results, a continued investigation in this topic has been carried out ever since in order to completely understand the deposition process and the resulting coating characteristics. Further information about the different coating structures obtained for near stoichiometric mullite (Al/Si input ratio close to 3), as well as the transformations of such coatings under annealing was revealed in a later report in 1998. This report also established how mullite, once nucleated, can continue growing towards Al-rich composition by tailoring the Al/Si input gases[5].

As it is the case for silicon-based ceramics exposed to combustion environments at elevated temperatures, Sarin's group has also found that the silica content within the mullite coating might be susceptible to hot-corrosion and recession during extended exposure to combustion atmospheres containing NaCl and water vapor[6]. Previous reports also show that thermally sprayed mullite can suffer the preferential loss of silica when exposed to combustion environments, leaving behind an alumina skeleton[112,114]. Since it was evidenced that the activity of the silica present in the mullite may result in corrosion and loss of material in the coating, especially in long term applications, different strategies were proposed to overcome such problem. Within this context, it is interesting to underline the ideas indicated by Lee to deal with the difficulties to adequately protect Si-based ceramics with thermally sprayed stoichiometric mullite: the

need of a silica bonding layer to grant coating adherence together with an additional layer of BSAS (BaO-SrO-Al_2O_3-SiO_2) to avoid silica loss from the mullite coating[114].

The idea of a mullite enriched in alumina at the outer surface of the coatings arose as the key improvement factor to successfully protect the Si-based substrate. This is achieved by means of a compositional gradation of the coatings that allows obtaining silica-rich amorphous aluminosilicates in the interface, granting a high adhesion; and alumina-rich mullite in the outer coating surface, allowing a better protective performance in combustion environments. This gradation in the composition of mullite coatings is also achieved by tailoring the Al/Si ratio in the input gases during the deposition. Following this approach, two key articles were published in early 2000s. The first one presented an exhaustive analysis of CVD mullite structures and their evolution and stability when annealed at different temperatures. It also emphasized the importance of completely transforming the interfacial layer into a crystalline mullite, to avoid the devitrification of the amorphous silica to form cristobalite that promotes coating cracking and spallation[8]. The second contribution corresponded to a detailed review of the kinetics of CVD mullite deposition and the influence of the different deposition parameters (reactor total pressure, temperature, metal chlorides concentration and Al/Si input ratio) in coating structure and growth[117], enabling the upcoming optimization of the deposition parameters for mullite coatings with different compositions.

Further research in compositionally graded mullite coating was presented later, implementing laser-based ultrasonics to measure the composition and to evaluate indirectly some of the elastic properties of these coatings[124]. Recently, the finding of an almost silica-free mullite on the top of the coatings has been reported. The importance of obtaining graded coatings with ultrahigh-alumina mullite (Al/Si ratios above 15) in the outer surface was presented, together with their superior properties and better protective performance in corrosive environments while maintaining their thermal shock resistance[6,121]. In addition, the formation of a different outer layer of bush-like fibrous alumina with infiltrated silica for Al/Si ratios above 25 was presented and described in detail[125].

The most recent work published on CVD mullite coatings by Sarin's group compares the hot corrosion resistance of different samples in combustion environments with sodium salts. In the study there were included uncoated SiC, bulk alumina, bulk mullite and four CVD mullite coatings with different Al/Si ratios deposited on SiC. The report shows no corrosion in bulk alumina and a similar behavior of the mullite coating with the richest composition in alumina[7].

1.3.2 Silicon Carbide

Silicon carbide (SiC) is a ceramic material formed by carbon and silicon tetrahedrons. Carbon atoms are bonded to four silicon atoms forming a tetrahedron, in the same way that every silicon atom is bonded to four carbon ones in the same structure[126]. Although SiC can exist in many polymorphs, the two main crystallographic structures are: (i) hexagonal α-SiC with a wurtzite-type lattice, and (ii) cubic β-SiC, with a zinc blend type lattice[127].

Owing to its high proportion of covalent bonding, silicon carbide has very high hardness and stiffness, and hence it has been traditionally used in applications such as grinding or cutting media, bearings and seals, or wear and corrosion resistant machine parts[127].

Other applications have recently emerged, which exploit the numerous functional properties of silicon carbides such as the high-temperature mechanical stability (it can almost maintain its mechanical properties until 1600°C), low coefficient of thermal expansion, high thermal conductivity, excellent thermal shock resistant, great chemical stability with no oxidation until 800°C, and the generation of an oxidized layer that protects it until 1600°C from further oxidation[127]. Among these innovative applications, gas and jet engine turbines are continuously gaining importance. Some of the properties of SiC of special interest for this thesis are presented in Table 1.

	ρ[g/cm^3]	v	α[10^{-6}/K]	H [GPa]	E [GPa]	K_c [MPam$^{1/2}$]	Ref.
SiC	2.5-3.2				430-445	3	[128]
	3.15				485	2-3.2	[129]
	3.21	0.16	3.5-4.8		480	4	[130]
				35-39	500-520		[131]
		0.19			340		[132]
	3.16	0.16		32	415	3.1	[133]

Table 1. Average density (ρ), poisson ratio (v), coefficient of thermal expansion (α), hardness (H), Young´s modulus (E) and fracture toughness (K_c) of bulk silicon carbide.

1.3.3 Mullite

Mullite is a characteristic ceramic compound of the family of aluminosilicates. It has achieved considerable importance, especially as a refractory material, due to its capacity to retain good mechanical properties at high temperatures, being catalogued as an advanced ceramic. Within the Al_2O_3-SiO_2 system, mullite exists in a narrow range of compositions, forming a solid solution with a nominal stoichiometric composition of $3Al_2O_3 \cdot 2SiO_2$, as it can be observed in the phase diagram of Figure 25. However, mullite can exist in different series with the limiting compositions: $3Al_2O_3 \cdot 2SiO_2$ (3:2 mullite) with 72 mass% alumina, and $2Al_2O_3 \cdot SiO_2$ (2:1 mullite) with 78 mass% alumina[127].

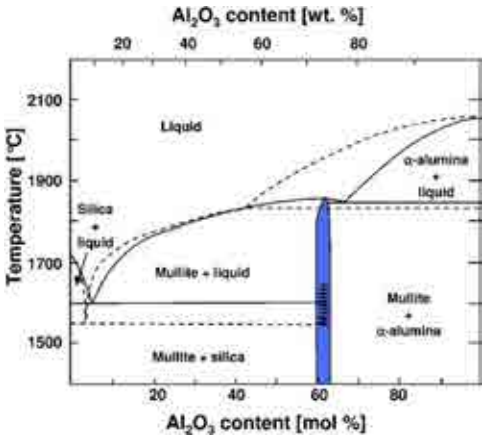

Figure 25. Binary Al_2O_3-SiO_2 phase diagram, where the narrow compositional gap is highlighted[127].

Mullite is a structure derivated of sillimanite ($Al_2O_3 \cdot SiO_2$), as shown in the Figure 26 (a,b). The chains of AlO_6 octahedrons are aligned perpendicular to the plane of the same figure. These chains are linked by double chains of AlO_4 and SiO_4 tetrahedrons that are arranged in an ordered sequence along the same direction[8,134,135]. Mullite is derived from sillimanite by substituting Al^{3+} ions for Si^{4+} ones in the tetrahedral positions, and removing oxygen atoms to balance the electric charge. The formation of an oxygen vacancy causes the two cations (Al, Si) in the tetrahedral positions (T) to shift to the neighbouring one (T*). Correspondingly, an oxygen atom adjusts its position from O_c to O_{c*}. Therefore, the resulting average crystal structure of stoichiometric mullite is orthorhombic in which edge-sharing AlO_6 octahedral chains are cross-linked by SiO_4 and AlO_4 tetrahedrons arranged in a random fashion. It is important to highlight the corresponding capability of mullite to accommodate different Al/Si ratios, very distant for the stoichiometric one (3:1)[8].

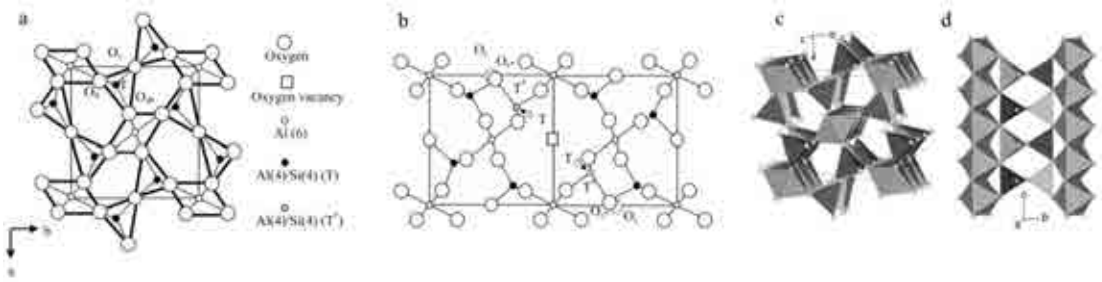

Figure 26. (a) [001] Projection of the unit cell of sillimanite and (b) derivated structure of mullite.[8] 3D structure of sillimanite in projections down the (c) c axis and (d) b axis.[134,135]

The properties of mullite that make it interesting for high technology applications are mainly related to its ability to retain good mechanical and durability properties at high temperature. Thus, properties like high-temperature mechanical stability, good resistance to creep, and corrosion and oxidation resistance at high temperatures, enables mullite to have a very high maximum useful temperature (1700°C) very close to its melting temperature (≈ 1830°C).[137] Therefore, mullite is widely used as a refractory material in applications like crucibles and furnaces. As it was commented before, due to the fact that the coefficient of thermal expansion of mullite (≈ 5.05 x10^{-6}/K) is very similar to that of silicon carbide (≈ 4.7 x 10^{-6}/K), coatings fabricated of mullite are expected to give to silicon-based materials a long term protection in oxidative environments at high temperatures[138].

1.3.3.1 Chemical vapor deposition of mullite

Through CVD, uniform, adherent, pore-free, crystalline and phase-pure coatings can be deposited on substrates with complex shapes. This technique also allows adjusting the composition along the coating thickness to obtain different properties of the coating in the interface and in the outer surface. CVD involves flowing a precursor gas or gases into a chamber or reactor where the substrate to be coated is contained. This substrate is usually heated in order to facilitate that chemical reactions of gases take place on its surface, resulting in the formation of a thin solid film of the desired material. Some gases produced from the reaction must be exhausted out of the chamber with unreacted precursor gases[139,140].

Mullite is typically formed by a high temperature reaction occurring on an alumina-silica interface. The first attempt to fabricate mullite coatings on SiC consisted on the deposition of alternating layers of alumina and silica by CVD, followed by a high temperature anneal to transform these layers into a single layer of crystalline mullite coating. However, it was found that mullite formation was very slow and the unreacted silica crystallized and fractured, leading to coating spallation[5]. Therefore, efforts were focused to directly deposit mullite coatings in a single step using CVD.

- ***Coating deposition***

Columnar crystalline mullite is deposited in a hot-wall CVD reactor from the thermally activated reaction between aluminium and silicon chloride with carbon dioxide and hydrogen, following the overall reaction of mullite formation[6]:

$$6AlCl_{3\,(g)} + 2SiCl_{4\,(g)} + 13CO_{2\,(g)} + 13H_{2\,(g)}$$

$$\rightarrow 3Al_2O_3 \cdot 2SiO_{2\,(s)} + 13CO_{(g)} + 26HCl_{(g)} \qquad \textbf{Equation 1.34}$$

$AlCl_3$ vapor is generated by passing Cl_2 gas through overheated Al chips, while $SiCl_4$ vapor is produced by heating liquid $SiCl_4$ using Ar as a carrier gas. The metal chlorides

are pre-mixed before being introduced into the hot-wall reactor (the whole chamber is heated). An excess of hydrogen is supplied into the chamber in order to guarantee the complete reduction of the metal chlorides[123]. This process is carried out in a CO_2-rich regime to avoid the incorporation of C and the formation of carbides in the coating[6].

The gaseous products are then passed through a neutralizing tank and a chill shower before release in the atmosphere. The typical deposition temperature, total reactor pressure and deposition time are 950°C, 75 Torr and 3h respectively.

- ***Control parameters and microstructure***

It is important to summarize the influence of the different parameters of control in the CVD process of mullite, to understand the effects that they have on the microstructure of coatings and the resulting properties. The main control parameters in the deposition process are temperature, total reactor pressures and total metal chlorides partial pressures. The effect of such parameters on the deposition rate and the microstructure of coatings are summarized in Figure 27.

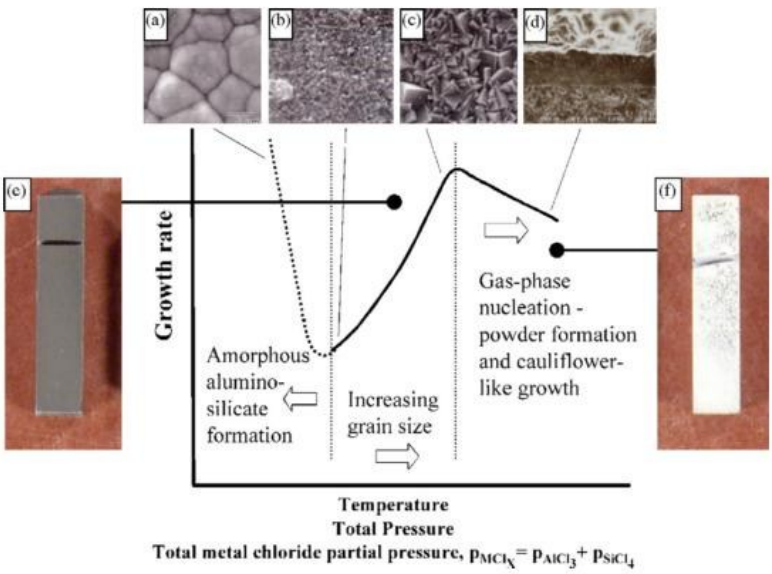

Figure 27. Schematic of the variation growth rate and microstructure of CVD mullite coatings with increasing deposition temperature, total pressure and metal chloride pressure[6,121].

Three critical zones separated by dotted lines can be recognized in the scheme of Figure 27. In the first zone (left hand one), amorphous aluminosilicate is formed instead of crystalline mullite at low temperature, low total pressures and low total metal chloride partial pressures (a). If these parameters are increased, crystalline mullite starts to grow with a fine grain size in the second zone (b). The coating growth rate and grain size increase with similar rises in the mentioned parameters (c). Further increases in the control parameters provoke a decrease in the coating growth rate. This is a consequence of the formation of powders in the gas phase that limits the amount of reactants that reaches the surface of the substrate. This powder formation also promotes a cauliflower growth on the surface (d).

- ***Al-rich and graded compositions***

As indicated in previous sections, there is a strong motivation to reduce or even to eliminate the silica component from the coating surface, which is in direct contact with environment corrosive compounds. By tailoring the Al/Si input ratio during the CVD process, mullite coatings can be grown in a wide spectrum of Al-rich compositions. Furthermore, it is now well-established that gradation of the composition of mullite coatings during the deposition process may be successfully accomplished. It allows obtaining alumina-rich mullites on the outer surface while maintaining the stoichiometric compositions in the interface for good matching with the SiC substrate, and avoiding then the introduction of relevant residual stresses. Graded mullite coatings with high alumina-rich compositions in the outer surface have shown greater protection than stoichiometric mullite, by reducing silica reactions and with negligible Na salts penetration[7]. Previous reports present mullite coating with Al/Si ratios up to 16, but also suggest the break of mullite structure and the formation of bush-like outgrowths of fibrous alumina for Al/Si ratios near 30[6].

Figure 28 a and Figure 1 b show a cross-section of a typical compositionally graded mullite coating deposited on a SiC substrate. In such figures, microstructure has been

revealed by chemical etching. The coating is dense, uniform and adherent. It can be clearly divided in 3 zones according to the deposited structure.

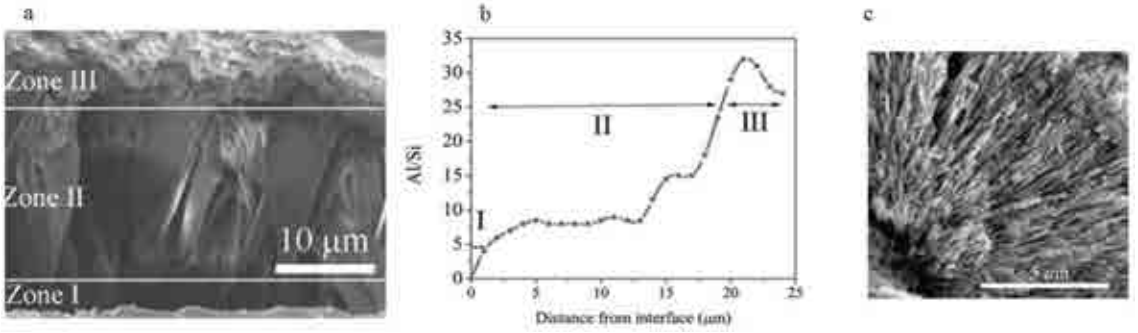

Figure 28. (a) Cross-section of a compositionally graded mullite coating etched to reveal its microstructure and (b) corresponding composition profile in terms of Al/Si ratio. (c) Bush like microstructure formed at high Al/Si compositions.

Just on top of the substrate (low part of the Figure 28 a), an amorphous aluminosilicate (zone I) is formed, also termed the "nanocrystalline layer". It consists of alumina nanocrystals in a vitreous matrix rich in silica. This layer appears in the same figure as the darkest film between the substrate and the crystalline mullite columns (zone II). Its deposition is promoted by the thin oxide layer formed on the SiC substrate during the sintering process at elevated temperature, resulting in a great adherence between coating and substrate.

Along the nanocrystalline layer, the Al/Si ratio rapidly increases to the stoichiometric Al/Si ratio, and crystalline mullite begins to nucleate. Thus, the lower the input Al/Si ratio, the thicker this layer becomes as more time is required to deposit the extra alumina needed to get stoichiometric ratios. The nanocrystalline layer have shown a linear dependence with the Al/Si input ratio, being about 1 μm thick for Al/Si = 1, and near 0.3 μm for a ratio of 4. Once crystalline mullite has nucleated, mullite grains tend to grow in a columnar fashion, typically with a strong texture in the [001] direction[5]. The columnar grains may be observed in the zone II of Figure 28 a. If the Al/Si input ratio is near stoichiometric mullite, the coating will be constituted by the nanocrystalline

layer at the coating/substrate interface and columnar mullite grains on the top of it. However if the Al/Si ratio is increased towards high values, the mullite columnar structure can break down into a bush-like morphologies on the top of the columns, as shown in zone III of Figure 28 a, and in the micrograph of Figure 28 b.

After the deposition process, it has been suggested that prior to the coating implementation in real applications, the nanocrystalline layer must be transformed into crystalline mullite by conducting an annealing treatment between 1150 and 1300°C. This is due to the fact that, by directly heating the coatings to temperatures above 1400°C, devitrification of the amorphous silica tends to occur, promoting coating cracking and spallation. Devitrification is produced by the transformation of the amorphous silica matrix in the nanocrystalline layer into crystobalite, which has a larger thermal expansion coefficient than mullite (10.3×10^{-6}/K) as compared to that of of SiC (4.7×10^{-6}/K).[8] The mentioned annealing process also leads to a tetragonal-to-orthorhombic transformation in crystalline mullite, due to the relatively high growth rates (≈ 5 μm/h) and low temperatures (≈ 950 °C). This forces the AlO_4 and SiO_4 tetrahedra to take the metastable tetragonal structure as a result of the lack of enough time and mobility. Therefore, when annealed at elevated temperatures, the tetrahedra undergoes local readjustment to thermodynamically favorable positions, forming the stable orthorhombic structure.[8]

1.3.3.2 Mechanical properties of bulk mullite materials

Although mullite has never been considered suitable for high strength applications at low temperatures, it has been recongnized as a high temperature material for its resistance to creep and thermal shock. A summary of the main physical and mechanical properties of interest for this thesis is presented in Table 2.

ρ [g/cm^3]	v	α[10^{-6}/K]	H [GPa]	E [GPa]	K_c [MPam$^{1/2}$]	σ_y [MPa]	Ref.
	0.25				2	550	[141]
		4			2.2		[118]
3.16-3.22		3.1-4.1	13-15	140-250	1.5-3.0		[142]
		5.13	11	220	1-2		[143]
					2.0-2.7		[144]
	0.27	4.1		220-226			[145]
3.16	0.20	4-6		144			[130]
		4.1	12-16				[134]
3.08	0.28			214	2.4		[146]
3.05	0.22			190			[124]
3.16	0.28			227			[147]
			11	220			[143]

Table 2. Average density (ρ), poisson ratio (v), coefficient of thermal expansion (α), hardness (H), Young´s modulus (E), fracture toughness (K_c), and yield strength (σ_y) of bullk mullite materials of different nature.

Although the mechanical behavior of bulk mullite materials is well known, and there exist general guidelines of the range in which their mechanical properties varies (as observed from the values included in Table 2), similar knowledge on the mechanical properties of mullite coatings is scarce. Furthermore, in contrast with the wide information existing in the literature about the CVD process of mullite and its parameters, the resulting microstructure of the coating and their corrosion protection, etc., the lack of knowledge of the mechanical behavior of such coatings and the structural integrity of the coated mullite/SiC systems are limiting factors facing their potential application. Investigation, documentation and analysis of these topics are indeed main actions within the scope of the present Ph.D. thesis.

1.4 References

1. Lawn, B.R. Fracture and deformation in brittle solids: A perspective on the issue of scale. *J. Mater. Res.* **19**, 22-29 (2004).

2. Li, X., Bhushan, B. A review of nanoindentation continuous stiffness measurement technique and its applications. *Mater. Charact.* **48**, 11-36 (2002).

3. Padture, N.P., Gell, M., Jordan, E.H. Thermal barrier coatings for gas-turbine engine applications. *Science* **296**, 280-284 (2002).

4. Li, X., Bhushan, B., Takashima, K., Baek, C.-W., Kim, Y.-K. Mechanical characterization of micro/nanoscale structures for MEMS/NEMS applications using nanoindentation techniques. *Ultramicroscopy* **97**, 481-94 (2003).

5. Basu, S., Hou, P., Sarin, V.K. Formation of mullite coatings on silicon-based ceramics by chemical vapor deposition. *Int. J. Refract. Met. Hard Mater.* **16**, 343-352 (1998).

6. Basu, S., Kulkarni, T., Wang, H., Sarin, V.K. Functionally graded chemical vapor deposited mullite environmental barrier coatings for Si-based ceramics. *J. Eur. Ceram. Soc.* **28**, 437-445 (2008).

7. Kulkarni, T., Wang, H.Z., Basu, S.N., Sarin, V.K. Protective Al-rich mullite coatings on Si- based ceramics against hot corrosion at 1200°C. *Surf. Coat. Technol.* **205**, 3313-3318 (2011).

8. Hou, P., Basu, S.N., Sarin, V.K. Structure and high-temperature stability of compositionally graded CVD mullite coatings. *Int. J. Refract. Met. Hard Mater.* **19**, 467-477 (2001).

9. Yang, F., Li, J. *Micro and nano mechanical testing of materials and devices*. p. 387 (Springer Science+Business Media: New York, USA, 2008).

10. Vanlandingham, M.R. Review of instrumented indentation. *J. Res. Natl. Inst. Stan.* **108**, 249-265 (2003).

11. Volinsky, A.A. Nanoindentaion techniques for assessing mechanical reliability at the nanoscale. *Microelectron. Eng.* **69**, 519-527 (2003).

12. Fischer-Cripps, A.C. *Nanoindentation*. p. 260 (Springer Verlag: New York, USA, 2004).

13. Oliver, W.C., Pharr, G.M. Measurement of hardness and elastic modulus by instrumented indentation: advances in understanding and refinements to methodology. *J. Mater. Res.* **19**, 3-20 (2004).

14. Bull, S.J. Nanoindentation of coatings. *J. Phys. D: Appl. Phys.* **38**, R393-R413 (2005).

15. Mukhopadhyay, N.K., Paufler, P. Micro- and nanoindentation techniques for mechanical characterisation of materials. *Int. Mater. Rev.* **51**, 209-245 (2006).

16. Golovin, Y.I. Nanoindentation and mechanical properties of solids in submicrovolumes, thin near-surface layers, and films: A review. *Phys. Solid State* **50**, 2205-2236 (2008).

17. Hay, J. Introduction to instrumented indentation testing. *Exp. Techniques* **33**, 66-72 (2009).

18. Field, J.S., Swain, M.V. A simple predictive model for spherical indentation. *J. Mater. Res.* **8**, 297-306 (1993).

19. Herbert, E. On the measurement of stress–strain curves by spherical indentation. *Thin Solid Films* **398-399**, 331-335 (2001).

20. Gaillard, Y., Jiménez-Piqué, E., Anglada, M. Scale dependence of the Young's modulus measured by nanoindentation in columnar YSZ EB-PVD thermal barriers coatings. *Philos. Mag.* **86**, 5441-5451 (2006).

21. Gaillard, Y., Rico, V.J., Jiménez-Piqué, E., González-Elipe, A.R. Nanoindentation of TiO_2 thin films with different microstructures. *J. Phys. D: Appl. Phys.* **42**, 1-9 (2009).

22. Rayón, E., Bonache, V., Salvador, M.D., Roa, J.J., Sánchez, E. Hardness and Young's modulus distributions in atmospheric plasma sprayed WC–Co coatings using nanoindentation. *Surf. Coat. Technol*. **205**, 4192-4197 (2011).

23. He, L.H., Swain, M.V. Nanoindentation derived stress-strain properties of dental materials. *Dent. Mater.* **23**, 814-821 (2007).

24. Chintapalli, R.K., Jiménez-Piqué, E., Marro, F.G., Yan, H., Reece, M., Anglada, M. Spherical instrumented indentation of porous nanocrystalline zirconia. *J. Eur. Ceram. Soc.* **32**, 123-132 (2011).

25. Chen, J., Bull, S. Assessment of the toughness of thin coatings using nanoindentation under displacement control. *Thin Solid Films* **494**, 1-7 (2006).

26. King, S., Chu, R., Xu, G., Huening, J. Intrinsic stress effect on fracture toughness of plasma enhanced chemical vapor deposited SiN_x:H films. *Thin Solid Films* **518**, 4898-4907 (2010).

27. Marshall, D.B., Evans, A.G. Measurement of adherence of residually stressed thin films by indentation. I. Mechanics of interface delamination. *J. Appl. Phys.* **56**, 2632-2638 (1984).

28. Volinsky, A.A., Moody, N.R., Gerberich, W.W. Interfacial toughness measurements for thin films on substrates. *Acta Mater.* **50**, 441-466 (2002).

29. Chen, J., Bull, S.J. Approaches to investigate delamination and interfacial toughness in coated systems: an overview. *J. Phys. D: Appl. Phys.* **44**, 1-19 (2011).

30. Gaillard, Y., Jiménez-Piqué, E., Soldera, F., Mücklich, F., Anglada, M. Quantification of hydrothermal degradation in zirconia by nanoindentation. *Acta Mater.* **56**, 4206-4216 (2008).

31. Volinsky, A.A. Fracture toughness, adhesion and mechanical properties of low-K dielectric thin films measured by nanoindentation. *Thin Solid Films* **429**, 201-210 (2003).

32. Galvan, D., Pei, Y., De Hosson, J. Deformation and failure mechanism of nano-composite coatings under nano-indentation. *Surf. Coat. Technol.* **200**, 6718-6726 (2006).

33. Chang, S., Huang, Y. Analyses of interface adhesion between porous SiO_2 low-k film and SiC/SiN layers by nanoindentation and nanoscratch tests. *Microelectron. Eng.* **84**, 319-327 (2007).

34. Thornton, K., Poulsen, H.F. Three-dimensional materials science : An intersection of reconstructions and simulations. *MRS Bulletin* **33**, 587-595 (2008).

35. Elfallagh, F., Inkson, B.J. Evolution of residual stress and crack morphologies during 3D FIB tomographic analysis of alumina. *J. Microsc.* **230**, 240-51 (2008).

36. Elfallagh, F., Inkson, B.J. 3D analysis of crack morphologies in silicate glass using FIB tomography. *J. Eur. Ceram. Soc.* **29**, 47-52 (2009).

37. Singh, D.R.P., Chawla, N., Shen, Y.-L. Focused Ion Beam (FIB) tomography of nanoindentation damage in nanoscale metal/ceramic multilayers. *Mater. Charact.* **61**, 481-488 (2010).

38. Pharr, G. Measurement of mechanical properties by ultra-low load indentation. *Mater. Sci. Eng. A* **253**, 151-159 (1998).

39. Roa, J.J. Mechanical properties of HTSC at micro/nanometric scale.Ph.D. Thesis. Universidad de Barcelona. Barcelona, Spain. p. 201 (2010).

40. Casellas, D., Caro, J., Molas, S., Prado, J.M., Valls, I. Fracture toughness of carbides in tool steels evaluated by nanoindentation. *Acta Mater.* **55**, 4277-4286 (2007).

41. Hertz, H. On the contact of elastic solids. *J. Reine Angew. Math* **92**, 156-171 (1881).

42. Tabor, D. The hardness of solids. *Phys. Technol.* **1**, 145-179 (1970).

43. Bei, H., George, E.P., Hay, J.L., Pharr, G.M. Influence of indenter tip geometry on elastic deformation during nanoindentation. *Phys. Rev. Lett.* **95**, 045501-045502 (2005).

44. Sneddon, I.N. The relation between load and penetration in the axisymmetric boussinesq problem for a punch of arbitrary profile. *Int. J. Eng. Sci.* **3**, 47-57 (1965).

45. Huber, M.T. Contact of solid elastic bodies. *Ann. Phys-New York* **14**, 153-163 (1904).

46. Tabor, D. *The hardness of metals*. (Oxford, UK, 1951).

47. Harding, S. Cracking in brittle materials during low-load indentation and its relation to fracture toughness. Ph.D. Thesis. Rice University. Houston, USA. p. 207 (1995).

48. Kruzic, J.J., Kim, D.K., Koester, K.J., Ritchie, R.O. Indentation techniques for evaluating the fracture toughness of biomaterials and hard tissues. *J. Mech. Behav. Biomed.* **2**, 384-95 (2009).

49. Harding, S., Oliver, W.., Pharr, G.M. Cracking during nanoindentation and its use in the measurement of fracture toughness. *Mater. Res. Soc. Symp. Proc.* 663-668 (1995).

50. Oliver, W.C., Pharr, G.M. An improved technique for determining hardness and elastic modulus using load and displacement sensing indentation experiments. *J. Mater. Res.* **7**, 1564-1583 (1992).

51. Loubet, J.L., Georges, J.M., Marchesini, G., Meille, J. Vickers indentation curves of magnesium oxide (MgO). *Tribology* **106**, 43-48 (1984).

52. Doener, M.F., Nix, W.D. A method for interpreting the data from depth-sensing indentation instruments. *J. Mater. Res.* **1**, 601-609 (1986).

53. Simmons, G., Wang, H. *Single crystal elastic constants and calculated aggregate properties: A handbook*. (MIT Press: Cambridge M.A, USA, 1971).

54. Fischer-Cripps, A. Critical review of analysis and interpretation of nanoindentation test data. *Surf. Coat. Technol.* **200**, 4153-4165 (2006).

55. Kalidindi, S.R., Pathak, S. Determination of the effective zero-point and the extraction of spherical nanoindentation stress–strain curves. *Acta Mater.* **56**, 3523-3532 (2008).

56. Linss, V., Schwarzer, N., Chudoba, T., Karniychuk, M., Richter, F. Mechanical properties of a graded B-C-N sputtered coating with varying Young's modulus: deposition, theoretical modelling and nanoindentation. *Surf. Coat. Technol.* **195**, 287-297 (2005).

57. Liang, Y.-H., Arai, Y., Ozasa, K., Ohashi, M., Tsuchida, E. Simultaneous measurement of nanoprobe indentation force and photoluminescence of InGaAs/GaAs quantum dots and its simulation. *PhyE* **36**, 1-11 (2007).

58. Roa, J.J., Jiménez-Piqué, E., Capdevila, X.G., Segarra, M. Nanoindentation with spherical tips of single crystals of YBCO textured by the Bridgman technique: Determination of indentation stress–strain curves. *J. Eur. Ceram. Soc.* **30**, 1477-1482 (2010).

59. Anstis, G.R., Chantikul, P., Lawn, B.R., Marshall, D.B. A critical evaluation of indentation techniques for measuring fracture toughness: I, direct crack measurements. *J. Am. Ceram. Soc.* **64**, 533-538 (1981).

60. Lawn, B.R., Evans, A.G., Marshall, D.B. Elastic plastic indentation damage in ceramics: the median radial crack system. *J. Am. Ceram. Soc.* **63**, 574-581 (1980).

61. Cuadrado, N., Casellas, D., Anglada, M., Jiménez-Piqué, E. Evaluation of fracture toughness of small volumes by means of cube-corner nanoindentation. *Scr. Mater.* **66**, 670-673 (2012).

62. Laugier, M.. Palmqvist indentation toughness in WC-Co composites. *J. Mater. Sci. Lett.* **6**, 897-900 (1987).

63. Shetty, D.K., Wright, I.G., Mincer, P.N., Clauer, A.H. Indentation fracture of WC-Co cermets. *J. Mater. Sci.* **20**, 1873-1882 (1985).

64. Gouldstone, A., Koh, H.-J., Zeng, K.-Y., Giannakopoulos, A., Suresh, S. Discrete and continuous deformation during nanoindentation of thin films. *Acta Mater.* **48**, 2277-2295 (2000).

65. Bhushan, B., Li, X. Nanomechanical characterisation of solid surfaces and thin films. *Int. Mater. Rev.* **48**, 125-164 (2003).

66. Jiménez-Piqué, E., Gaillard, Y., Anglada, M. Instrumented indentation of layered ceramic materials. *Key Eng. Mater.* **333**, 107-116 (2007).

67. Hay, J., Crawford, B. Measuring substrate-independent modulus of thin films. *J. Mater. Res.* **26**, 727-738 (2011).

68. Chen, J., Bull, S. On the factors affecting the critical indenter penetration for measurement of coating hardness. *Vacuum* **83**, 911-920 (2009).

69. Tuck, J.R., Korsunsky, A.M., Bull, S.J., Davidson, R.I. On the application of the work-of-indentation approach to depth-sensing indentation experiments in coated systems. *Surf. Coat. Technol.* **137**, 217-224 (2001).

70. Jönsson, B., Hogmark, S. Hardness measurements of thin films. *Thin Solid Films* **114**, 257-269 (1984).

71. Burnett, P.J., Rickerby, D.S. The mechanical properties of wear-resistant coatings I: modeling of hardness behavior. *Thin Solid Films* **148**, 41-50 (1987).

72. Roa, J.J., Gilioli, E., Bissoli, F., Pattini, F., Rampino, S., Capdevila, X.G., Segarra, M. Study of the mechanical properties of CeO_2 layers with the nanoindentation technique. *Thin Solid Films* **518**, 227-232 (2009).

73. Sakai, M., Zhang, J., Matsuda, A. Elastic deformation of coating/substrate composites in axisymmetric indentation. *J. Mater. Res.* **20**, 2173-2183 (2005).

74. Gao, H., Chiu, C.-H., Lee, J. Elastic contact versus indentation modeling of multi-layered materials. *Int. J. Solids Struct.* **29**, 2471-2492 (1992).

75. Song, H. Selected mechanical problems in load- and depth-sensing indentation testing. Ph.D. Thesis. Rice University. Houston, USA. p. 85 (1999).

76. Rar, A., Song, H., Pharr, G.M. Assessment of new relation for the elastic compliance of a film-substrate system. *Mater. Res. Soc. Symp. Proc.* 431-436 (2002).

77. Xu, H., Pharr, G.M. An improved relation for the effective elastic compliance of a film/substrate system during indentation by a flat cylindrical punch. *Scr. Mater.* **55**, 315-318 (2006).

78. Bec, S., Tonck, A., Loubet, J. A simple guide to determine elastic properties of films on substrate from nanoindentation experiments. *Philos. Mag.* **86**, 5347-5358 (2006).

79. Saha, R., Nix, W.D. Effects of the substrate on the determination of thin film mechanical properties by nanoindentation. *Acta Mater.* **50**, 23-38 (2002).

80. Hay, J. Measuring substrate-independent modulus of dielectric films by instrumented indentation. *J. Mater. Res*. **24**, 667-677 (2009).

81. Botero, C.A. Jiménez-Piqué, E. Baudín, C. Salán, N. y Llanes, L. Nanoindentation of Al_2O_3/Al_2TiO_5 composites: Small-scale mechanical properties of Al_2TiO_5 as reinforcement phase. *J. Eur. Ceram. Soc.* **32**, 3723-3731 (2012).

82. Marshall, D.B., Lawn, B.R. An indentation technique for measuring stresses in tempered glass surfaces. *J. Am. Ceram. Soc.* **60**, 86-87 (1977).

83. Pavón, J. Fractura y fatiga por contacto de recubrimientos de vidrio sobre Ti6Al4V para aplicaciones biomédicas. Ph.D. Thesis. Universidad Politécnica de Cataluña. Barcelona, Spain. p. 404 (2007).

84. Smith, S.M., Scattergood, R.O. Crack-shape effects for indentation fracture toughness measurements. *J. Am. Ceram. Soc.* **75**, 305-315 (1992).

85. Gaillard, Y., Jiménez-Piqué, E., Bartsch, M., Anglada, M. Nucleation of shear bands on EB-PVD thermal barriers coatings under hertzian indentations. *Key Eng. Mater.* **333**, 277-280 (2007).

86. Volinsky, A., Bahr, D.F., Kriese, M.D., Moody, N.., Gerberich, W.W. Nanoindentation methods in interfacial fracture testing. *Comprehensive Structural Integrity* 453-493 (2003).

87. Bull, S. Modelling of the indentation response of coatings and surface treatments. *Wear* **256**, 857-866 (2004).

88. Evans, A.G., Hutchinson, J.W. The thermomechanical integrity of thin films and multilayers. *Acta Metall. Mater.* **43**, 2507-2530

89. Dauskardt, R. Adhesion and debonding of multi-layer thin film structures. *Eng. Fract. Mech.* **61**, 141-162 (1998).

90. Kriese, M. Nanomechanical fracture-testing of thin films. *Eng. Fract. Mech.* **61**, 1-20 (1998).

91. Zheng, X. Use of nanomechanical fracture-testing for determining the interfacial adhesion of PZT ferroelectric thin films. *Surf. Coat. Technol.* **176**, 67-74 (2003).

92. Zhang, T., Huan, Y. Nanoindentation and nanoscratch behaviors of DLC coatings on different steel substrates. *Compos Sci Techno* **65**, 1409-1413 (2005).

93. Bull, S., Berasetegui, E. An overview of the potential of quantitative coating adhesion measurement by scratch testing. *Tribol. Int.* **39**, 99-114 (2006).

94. Pavón, J., Jiménez-Piqué, E., Anglada, M., Saiz, E., Tomsia, a. P. Delamination under Hertzian cyclic loading of a glass coating on Ti6Al4V for implants. *J. Mater. Sci.* **41**, 5134-5145 (2006).

95. ASTM, Definition of terms relating to adhesión. D907-70, ASTM, Philadelphia, USA (1970).

96. Ocaña, I., Molina Aldareguia, J., Gonzalez, D., Elizalde, M., Sanchez, J., Martinez Esnaola, J., Gil Sevillano, J., Scherban, T., Pantuso, D., Sun, B. Fracture characterization in patterned thin films by cross-sectional nanoindentation. *Acta Mater.* **54**, 3453-3462 (2006).

97. Chang, S.-Y., Lin, S.-Y., Huang, Y.-C., Wu, C.-L. Mechanical properties, deformation behavior and interface adhesion of (AlCrTaTiZr)N_x multi-component coatings. *Surf. Coat. Technol.* **204**, 3307-3314 (2010).

98. Bull, S.J. Failure mode maps in the thin film scratch adhesion test. *Tribol. Int.* **30**, 491-498 (1997).

99. Huang, L. Nano-scratching process and fracture mechanism of amorphous carbon films. *Wear* **254**, 1032-1036 (2003).

100. ASTM, Standard Test Method for Adhesion Strength and Mechanical Failure Modes of Ceramic Coatings by Quantitative Single Point Scratch Testing. C1624-05, ASTM, West Conshohocken, USA (2010).

101. Eliaz, N. Hot corrosion in gas turbine components. *Eng. Fail. Anal.* **9**, 31-43 (2002).

102. Boyce, M.P. *Gas turbine engineering handbook*. Second Edi, p. 956 (El Sevier: Oxford, UK, 2006).

103. Cao, X. Ceramic materials for thermal barrier coatings. *J. Eur. Ceram. Soc.* **24**, 1-10 (2004).

104. Lee, K.N. Protective coatings for gas turbines. *The gas turbine handbook.* 419-437 (2006).

105. Reed, R.C. *The Superalloys: fundamentals and applications*. p. 372 (Cambridge University Press: New York, USA, 2006).

106. Klemm, H. Corrosion of silicon nitride materials in gas turbine environment. *J. Eur. Ceram. Soc.* **22**, 2735-2740 (2002).

107. Kaya, H. The application of ceramic-matrix composites to the automotive ceramic gas turbine. *Comp. Sci. Technol.* **59**, 861-872 (1999).

108. Wright, I., Gibbons, T. Recent developments in gas turbine materials and technology and their implications for syngas firing. *Int. J. Hydrogen Energy* **32**, 3610-3621 (2007).

109. Ueno, S., Jayaseelan, D., Kondo, N., Ohji, T., Kanzaki, S. Water vapor corrosion of mullite containing small amount of sodium. *Ceram. Int.* **31**, 177-180 (2005).

110. Ueno, S., Ohji, T., Lin, H. Corrosion and recession of mullite in water vapor environment. *J. Eur. Ceram. Soc.* **28**, 431-435 (2008).

111. Jacobson, N.S., Lee, K.N., Yoshio, T. Corrosion of mullite by molten salts. *J. Am. Ceram. Soc.* **79**, 2161-2167 (1996).

112. Lee, K.N. Key durability issues with mullite-based environmental barrier coatings for Si-based ceramics. *Trans. ASME* **122**, 632 (2000).

113. Ramasamy, S., Tewari, S.N., Lee, K.N., Bhatt, R.T., Fox, D.S. Environmental durability of slurry based mullite–gadolinium silicate EBCs on silicon carbide. *J. Eur. Ceram. Soc.* **31**, 1123-1130 (2011).

114. Lee, K. Current status of environmental barrier coatings for Si-Based ceramics. *Surf. Coat. Technol.* **133-134**, 1-7 (2000).

115. Eaton, H. Accelerated oxidation of SiC CMC's by water vapor and protection via environmental barrier coating approach. *J. Eur. Ceram. Soc.* **22**, 2741-2747 (2002).

116. Levi, C.G. Emerging materials and processes for thermal barrier systems. *Curr. Opin. Solid St. M.* **8**, 77-91 (2004).

117. Auger, M., Sarin, V.K. A kinetic investigation of CVD mullite coatings on Si-based ceramics. *Int. J. Refract. Met. Hard Mater.* **19**, 479-494 (2001).

118. Aksay, I.A., Dabbs, D.M., Sarikaya, M. Mullite for structural, electronic, and optical applications. *J. Am. Ceram. Soc.* **74**, 2343-2358 (1991).

119. Price, J.R., Jimenez, O., Faulder, L., Edwards, B., Parthasarathy, V. Ceramic Stationary Gas Turbine Development Program—Fifth Annual Summary. J. *Eng. Gas Turb. Power* **121**, 586 (1999).

120. Kimmel, J., Miriyala, N., Price, J., More, K., Tortorelli, P., Eaton, H., Linsey, G., Sun, E. Evaluation of CFCC liners with EBC after field testing in a gas turbine. *J. Eur. Ceram. Soc.* **22**, 2769-2775 (2002).

121. Basu, S.N., Kulkarni, T., Wang, H.Z., Steen, T., Murray, T.W., Sarin, V.K. Structure and properties of functionally graded environmental barrier coatings for ceramic components in gas turbines. *Proc. Int. Conf. Adv. Mat. Comp.* 1050-1060 (2007).

122. Mulpuri, R.P., Sarin, V.K. Synthesis of mullite coatings by chemical vapor deposition. *J. Mater. Res.* **11**, 1315-1324 (1996).

123. Auger, M., Sarin, V.K. The development of CVD mullite coatings for high temperature corrosive applications. *Surf. Coat. Technol.* **94-95**, 46-52 (1997).

124. Murray, T., Balogun, O., Steen, T., Basu, S., Sarin, V.K. Inspection of compositionally graded mullite coatings using laser based ultrasonics. *Int. J. Refract. Met. Hard Mater.* **23**, 322-329 (2005).

125. Kulkarni, T., Wang, H.Z., Basu, S.N., Sarin, V.K. Compositionally graded mullite-based chemical vapor deposited coatings. *J. Mater. Res.* **24**, 470-474 (2009).

126. Smith, W.F., Hashemi, J. *Foundations of materials science and engineering*. (McGraw-Hill Science/Engineering/Math: New York, USA, 2006).

127. Heimann, R. *Classic and advanced ceramics: From fundamentals to applications*. p. 553 (Wiley-VCH Verlag GmbH & Co. KGaA: Darmstadt, Germany, 2010).

128. Ashby, M.F., Jones, D.R.H. *Engineering Materials 2: An introduction to microstructures, processing and design*. p. 388 (El Sevier: Oxford, UK, 1998).

129. Mitchell, B.S. *Materials engineering and science: An introduction to materials engineering and science for chemical and materials engineers*. p. 954 (Wiley-Interscience: New Jersey, USA, 2004).

130. Munz, D., Fett, T. *Ceramics*. p. 298 (Springer: Berlin, Germany, 1999).

131. Tromas, C., Audurier, V., Leclerc, S., Beaufort, M., Declemy, A, Barbot, J. Evolution of mechanical properties of SiC under helium implantation. *J. Nucl. Mater.* **373**, 142-149 (2008).

132. Shackelford, J.F. *Introduction to materials science for engineers*. p. 848 (John Willey and Sons: New York, USA, 2007).

133. NIST Properties data summary, SiC. at <http://www.ceramics.nist.gov/srd/summary/scdscs.htm>

134. Schneider, H., Komarnerni, S. *Mullite*. p. 487 (Weinheim, FRG, 2005).

135. Schneider, H., Schreuer, J., Hildmann, B. Structure and properties of mullite-A review. *J. Eur. Ceram. Soc.* **28**, 329-344 (2008).

136. Hamidouche, M., Bouaouadja, N., Olagnon, C., Fantozzi, G. Thermal shock behaviour of mullite ceramic. *Ceram. Int.* **29**, 599-609 (2003).

137. Carter, C.B., Norton, M.G. *Ceramic materials : science and engineering*. p. 716 (Springer: New York, USA, 2007).

138. ASM *ASM handbook engineered materials: Ceramic and glasses*. p. 1217 (ASM International: Metals Park Ohio, USA, 1991).

139. Choy, K. Chemical vapour deposition of coatings. *Prog. Mater. Sci.* **48**, 57-170 (2003).

140. Park, J.-Hee *Chemical vapor deposition*. p. 481 (ASM International: Metals Park Ohio, USA, 2001).

141. Yan, J., Karlsson, A., Chen, X. On internal cone cracks induced by conical indentation in brittle materials. *Eng. Fract. Mech.* **74**, 2535-2546 (2007).

142. Anggono, J. Mullite Ceramics : Its Properties , Structure , and Synthesis. *J. Tek. Mes.* **7**, 1-10 (2005).

143. Bartolome, J.F., Diaz, M., Moya, J.S. Influence of the metal particle size on the crack growth resistance in mullite-molybdenum composites. *J. Am. Ceram. Soc.* **85**, 2778-2784 (2002).

144. Casellas, D., Baudin, C., Osendi, M., Llanes, L., Anglada, M. Fracture resistance of mullite under static and cyclic loads. *Scr. Mater.* **38**, 39-44 (1997).

145. Burgos-Montes, O., Moreno, R., Baudín, C. Effect of mullite additions on the fracture mode of alumina. *J. Eur. Ceram. Soc.* **30**, 857-863 (2010).

146. Hamidouche, M. Thermal shock behaviour of mullite ceramic. *Ceram. Int.* **29**, 599-609 (2003).

147. H, L., Kim, S., Balzar, D., Crudele, S., Kriven, W. Elastic properties of mullite. *J. Am. Ceram. Soc.* **81**, 1025-1028 (1998).

2 *Chapter*

Objectives

The principal objective of this thesis is to study the mechanical properties of mullite coatings deposited by chemical vapor deposition on silicon carbide substrates, as well as to evaluate the mechanical integrity of these coated systems. Attending to the thickness and the microstructural features of the coatings, the mechanical behavior is evaluated at a micro/nanoscale using nanoindentation and nanoscratch techniques.

Knowledge of the intrinsic mechanical properties of stoichiometric mullite coatings ($3Al_2O_3{\cdot}2SiO_2$) such as elastic modulus, hardness, fracture toughness, stress-strain curves, and yield strength, as well as rationalization of these as a function of microstructure of the coatings, internal stresses, and influence of the underlying substrate on the measurements, constitute one of the aims of this investigation.

The mechanical integrity of mullited coated SiC is a key issue towards its effective implementation in real gas turbine systems. Accordingly, another objective of this thesis lies in the determination of the mechanical integrity of the coating ($3Al_2O_3{\cdot}2SiO_2$), and that of the coated system intended as a structural unit ($3Al_2O_3{\cdot}2SiO_2$/SiC). The cohesive and decohesive properties of the mullite coatings, as well as their adhesion to the substrate and the toughness of the interface, are assessed.

Since the enrichment in alumina of mullite coatings is one of the most important factors proposed to improve their protection to SiC in combustion environments, the

determination of the influence of composition in the mechanical behavior of the coatings is another important purpose of this work. This is accomplished by means of mechanical evaluation of mullite coatings enriched in alumina through constant and graded compositions.

Finally, it is crucial to understand how the service conditions that mullite is expected to face in applications such as gas turbines, affects its main mechanical properties. Consequently, the effects of annealing, prolongued exposure to high temperatures, corrosion, and thermal shock, on the mechanical behavior of mullite EBCs, are also studied.

3 *Chapter*

Experimental procedure

The mullite coatings evaluated in this thesis were deposited on silicon carbide substrates using the Chemical Vapor Deposition (CVD) technique. Deposition of coatings was carried out in the facilities of the manufacturing laboratory of the Department of Mechanical Engineering, at Boston University. Subsequently, the coated specimens were microstructurally and mechanically characterized in the laboratories of both the Center for Structural Integrity and Reliability of Materials (CIEFMA) and the Center for the Research in nanoEngineering (CRnE), at the Technical University of Catalonia – Barcelona Tech (UPC).

The description of the procedure used for the deposition of coatings, and several aspects regarding the characterization of their microstructure, are presented in the following sections. In addition, the routes followed for the preparation of specimens for facing subsequent micro/nanomechanical characterization are described. Details concerning the approaches implemented for nanoindentation and nanoscratch tests are also given, together with general information of the parameters used for such tests. Finally, the techniques used for the characterization of the imprints as well as of the damage produced by these tests on the evaluated materials are briefly summarized.

3.1 Chemical vapor deposition of coatings

Some of the main concepts involved in the CVD process of mullite implemented in the present investigation are presented in this section. The CVD reactor and its components,

as well as the procedure followed for the deposition is detailed. In addition, details of the characterization conducted to the coatings in parallel to the deposition process are given.

3.1.1 CVD reactor

The deposition process of the mullite coatings investigated in this thesis was carried out in a CVD unit whose principal components are shown in Figure 1.

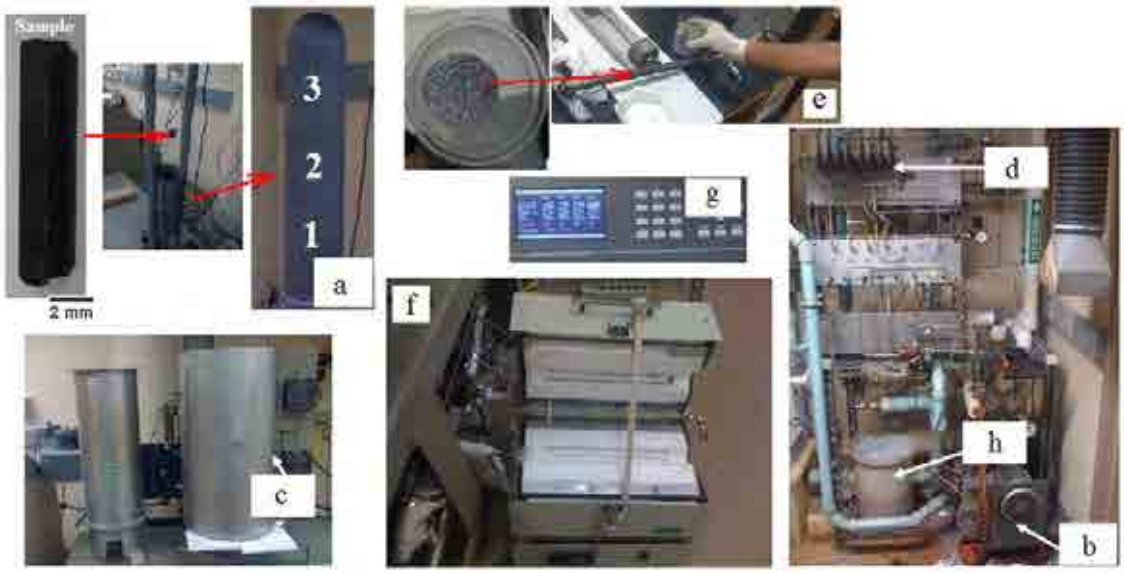

Figure 1. (a) CVD unit. Hot wall reactor, (b) vacuum pump, (c) mobile furnace, (d) mass flow controllers (e) aluminium chips and container tube, (f) system for production of $AlCl_3$, (g) control panel and (h) neutralizing tank.

The bars to be coated are hung vertically in the hot wall reactor where the reaction for the formation of mullite takes place, as presented in Figure 1 a. The reactor is divided in three regions according to its temperature distribution. Temperature in each region is monitored through sensors placed at different height levels.

The SiC substrate is placed at the hot zone of the reactor (zone 3). As it was commented in the *Chapter 1*, the reaction for the deposition of mullite occurs in a narrow range of pressure, temperature and gases compositions. Hence, the manipulation

and control of these parameters is crucial for obtaining CVD mullite coatings with optimum properties.

Pressure within the reactor is controlled and regulated by means of a vacuum pump (Figure 1 b) and flow of an inert gas with no interference in the reaction, in this case argon. Temperature is supplied to the reaction chamber by means of a mobile furnace of refractory walls (Figure 1 c). The gases used in the system $AlCl_3$-$SiCl_3$-CO_2-H_2, and Ar, are flowed into the reaction chamber and their partial pressures are regulated through elements or valves known as MFCs (Mass Flow Controllers, as shown in Figure 1 d). $AlCl_3$ gas is formed "in-situ" by means of the injection of Cl_2 in a tube containing pure aluminum chips (Figure 1 e). The tube containing Al-chips is heated up to temperatures high enough for Al volatilization. $AlCl_3$ gas is thus formed in an independent system attached to the CVD unit (Figure 1 f), whereas $SiCl_4$ is directly injected. Argon is also used as a carrier gas for $AlCl_3$ and $SiCl_4$ gases, which are premixed previous to their introduction into the hot zone of the reactor.

Individual and total control parameters, such as temperatures and pressures, are manipulated in a control panel (Figure 1 g). The output gases of the CVD system are passed through a neutralizing tank and a chill shower before being released into the atmosphere (Figure 1 h).

3.1.2 Coatings deposition

Reaction bonded SiC samples (Hexaloy®, St. Gobain) were cut in rectangular bars of ≈ 4x4x10 mm (Figure 1 a), then ground and rinsed, and finally dried with acetone. Samples were hung in the CVD unit, as shown in Figure 1 a. After the set-up of the CVD unit, and once SiC substrates were placed in the hot wall reactor, the system was prepared for the deposition of mullite coatings. $AlCl_3$ vapor was produced by passing Cl_2 gas over heated Al chips, while $SiCl_4$ vapor was produced by heating liquid $SiCl_4$ and using Ar as a carrier gas. The metal chlorides ($AlCl_3$ and $SiCl_4$) were pre-mixed before being introduced into the hot zone of the CVD reactor for mullite deposition on

SiC substrates. Composition of the deposited coatings was tailored by manipulating the individual partial pressures of the input $SiCl_4$ and $AlCl_3$ gases, while keeping the total metal chloride flow constant ($SiCl_4$+$AlCl_3$). The gaseous products were then passed through a neutralizing tank and a chill shower before release into the atmosphere. Deposition temperature and total reactor pressure were typically 975 ºC and 75 Torr.

Due to the narrow range of mullite occurrence, any instability or modification of parameters may result in deviation of conditions within the reaction chamber, with effects on deposition of optimum dense crystalline coatings. One issue commonly observed during deposition of mullite coatings by CVD is the formation of powders in the gas phase. This occurs when parameters within the reaction chamber are out of equilibrium. Deposition of powder may take place during the shutdown stage of the process, and it is difficult to avoid completely. Consequently, some deposition of powders was often observed on the top of crystalline coatings already formed.

Characterization of crystalline nature and crystallographic phases present in the deposited coatings was carried out by means of X-Ray diffraction (XRD), using monochromatic Cu K_α radiation with a dwell time of 0.05 s. The XRD analyses were performed in the manufacturing laboratory of the Department of Mechanical Engineering at Boston University. The phases present in the coatings were identified from the XRD spectra. Mullite peaks, and some SiC peaks in the case of thin coatings (ascribed to the substrate), were found in XRD scans. Figure 2 shows three examples of typical XRD spectrum found for thin (a) and thicker (b,c) stoichiometric mullite coatings. For thin coatings, SiC peaks of the substrate dominate the spectrum, and just few weak mullite peaks could be evidenced. On the other hand, in XRD spectra of thicker specimens mullite peaks are manifest. Spectra found are similar to the ones reported by previous works on CVD of mullite[1–5].

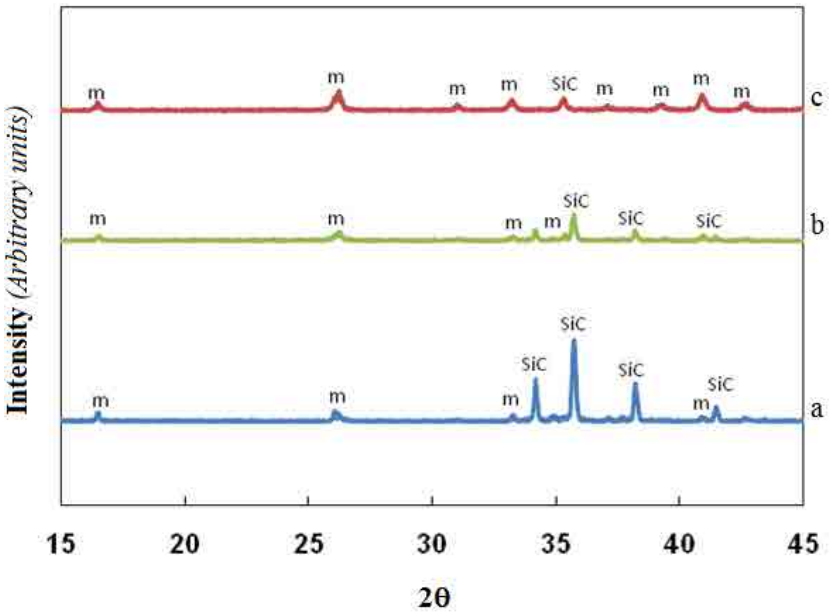

Figure 2. (a) Typical XRD spectrum found for very thin and (b,c) thicker stoichiometric mullite coatings.

Morphology and microstructure of the deposited coatings were studied through extensive micrographic analysis of their top surfaces and cross-sections. This analysis was performed in parallel to the deposition process, by means of Optical Microscopy (OM) and Scanning Electron Microscopy (SEM). The composition of the coatings was determined using chemical analysis through EDX (Energy Dispersive X Ray spectroscopy) coupled to the SEM used.

As it was commented before, during the deposition stage of the coatings it was common to find powder formation on the gas phase. This powder was eventually deposited on the top of the coatings, as it can be observed in Figure 3 at the top surface a-b and cross-section c-d of a stoichiometric mullite coated specimen.

Specimens with insignificant, or no powder formation, were achieved by adjusting and optimizing the different deposition parameters during the deposition stage of coatings, as shown in the top surface and cross-section micrographs included in Figure 3 e-h.

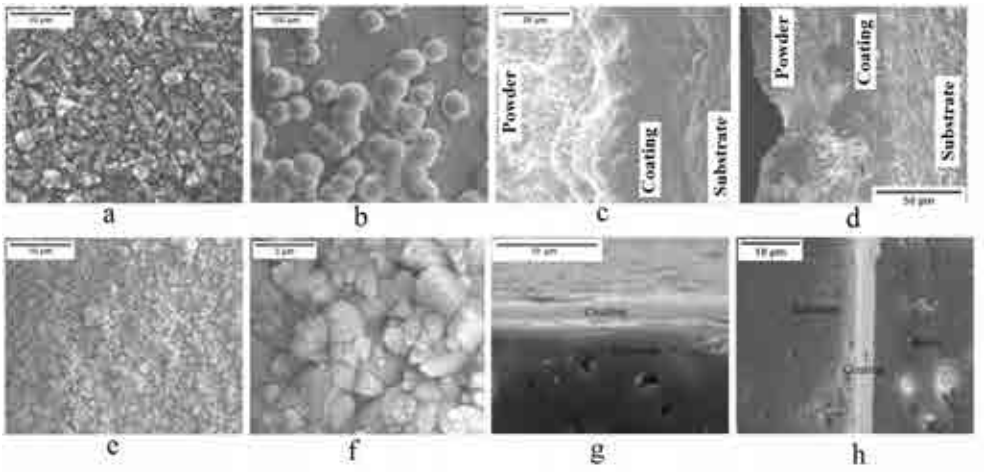

Figure 3. (a-d) Different powder formations found on the top surface of deposited coatings in the deposition stage, and (e-h) coatings without considerable powder deposition.

Chemical nature of the deposited coatings, as well as some of the powder deposits formed on top of both SiC and the deposited coatings, was investigated through EDX analysis performed on prepared cross-sections. As an example of the powder formation occurring during the optimization of the deposition process, the composition maps of Figure 4 a shows powder formation of alumina and oxygen on the top of SiC substrate. The absence of silicon in the powder suggests that such powders correspond to alumina or other aluminium oxides.

After adjusting the parameters for the deposition, the presence of silicon in addition to alumina and oxygen on the top of the silicon carbide substrates was confirmed, as shown in Figure 4 b-c. This evidence, together with the compact and cystalline nature of the coatings, indicated by the presence of mullite peaks in the XRD spectra, permitted the identification of crystalline mullite coatings in the deposited films.

The Al/Si ratio of the input gases was maintained during the course of the experiment to get stoichiometric mullite coatings (Al/Si) with nearly constant composition across the thickness. Similarly, the stoichiometry of the input gases was tailored to obtain coatings with higher Al/Si ratios. Coatings were also deposited with input gas ratios of Al/Si: 5, 7, 10 and 11, sustained constant during the process. In addition, compositionally graded

coatings were deposited by adjusting stoichiometry of input $SiCl_4$ and $AlCl_3$ gases from 3 to 11 during the experiment.

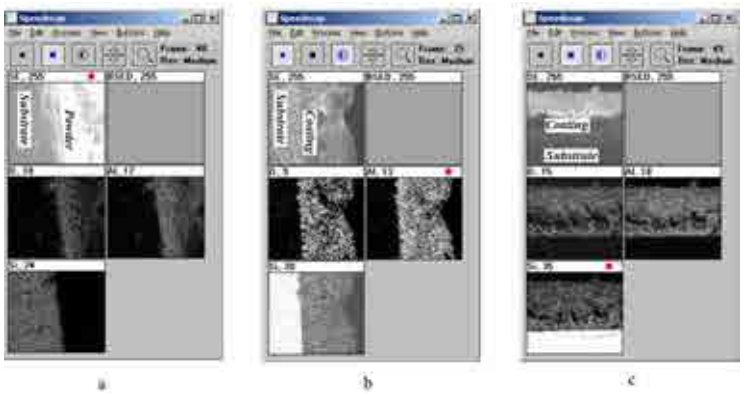

Figure 4. (a) Micrographs and element maps obtained by means of EDX analysis of cross-sections of different samples showing absence of silicon and (b,c) presence of silicon in the coatings.

3.2 Microstructural characterization of coatings

It is essential to perform an adequate characterization of the microstructure of the deposited mullite coatings not only in parallel to the deposition process, as a key parameter for its optimization (as described in section 3.1), but also previous to the mechanical testing, due to the importance of understanding microstructural aspects for rationalizing of the mechanical properties of the coatings investigated.

3.2.1 Composition and samples designation

Mullite coatings with different thicknesses ranging from 1 to 30 μm were obtained. Coating thickness was found to vary across the surface at the different faces of samples, especially at the edges. Average thicknesses measured on the cross-section of coatings, in zones far from the edges, are included in Table 1.

Composition of coatings was investigated by chemical analysis through EDX . EDX analyses were performed on several points along cross-sections of studied coatings. Average values for the molar Al/Si ratio of each coating are also presented in Table 1, together with the corresponding input gas ratio used for their deposition.

The nomenclature of the coated specimens studied in this thesis is done through codes combining the letter "*M*" (from mullite) and a number equivalent to the Al/Si ratio in the coatings (3, 5, 6, 7, and 8). Exceptions are the cases of compositionally graded samples which are referred to as "*Graded*". A final digit (I, II or III) is added to the end of the code (only for *M3* and graded conditions) to differentiate when there is more than one specimen per composition.

Samples designation	**Al/Si Input ratio**	**Al/Si Coating composition**	**Thickness (Average value, µm)**
M3Thin	3	3 ± 1	2 ± 1
M3-I			9 ± 3
M3-II			8 ± 2
M3-III			16 ± 8
M5	5	5 ± 1	6 ± 3
M6	7	6 ± 1*	21 ± 3
M7	10	7 ± 2	15 ± 4
M8	11	8 ± 1	20 ± 3
M11	11	x	20 ± 2
Graded I	Changing 3 to 11	Increasing 3 to 18	15 ± 4
Graded II			15 ± 5

** Al content in sample M6 was found to increase abruptly in the outer 5 µm of the coating. As it was later found, an Al-rich layer was deposited on top of the mullite coating for this condition. Values included in this table correspond to the inner mullite layer.*

Table 1. Sample designation, Al/Si ratios in the input gases, final composition of coatings and average thickness in the "as-deposited" state for all the coatings studied.

3.2.2 Microstructure

In order to reveal the microstructure of the coatings, it was necessary to perform a chemical etching in the cross-sections of the specimens with a diluted solution of fluorhidric acid (HF 5% Vol.). This etching solution attacks and dissolves the silica present in the coatings as well as the interfacial nanocrystalline layer.

Etching was carried out in sequential and short (2 minutes each) multiple steps, consisting of inmersion of the specimens in the HF solution. Between steps, coatings were cleaned and dried, and their condition was observed by means of optical microscopy, in order to decide whether further etching was necessary. When the microstructure of the coatings was fully revealed, images of the most representative sections were taken, as shown in Figure 5.

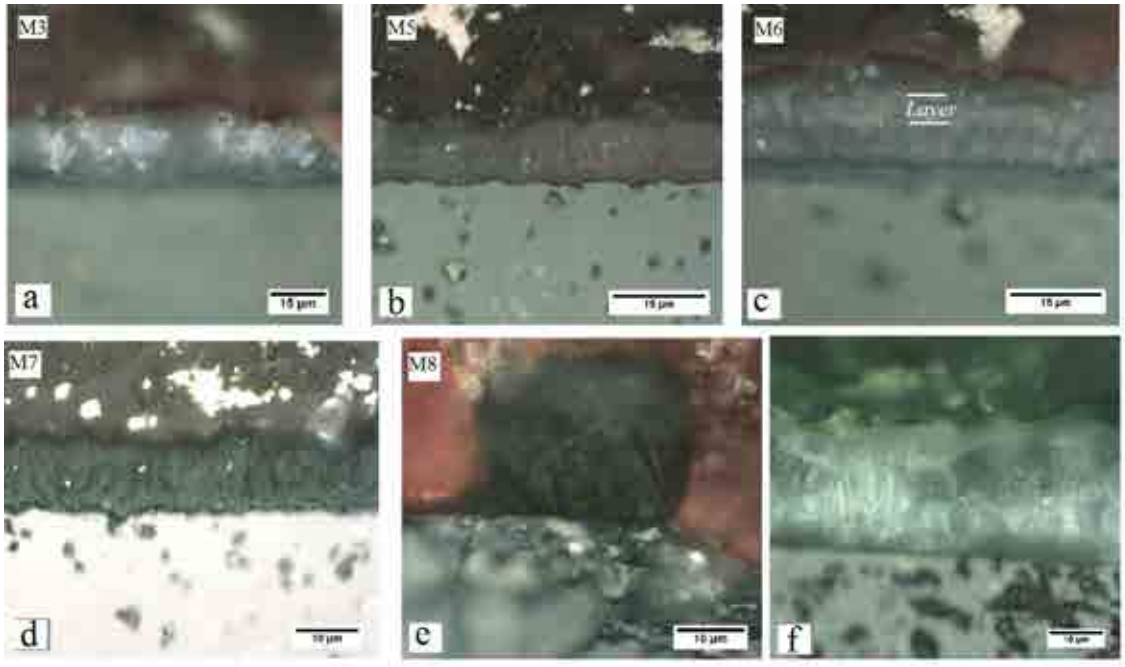

Figure 5. Microstructure of the coatings after etching. Samples *M3-III* (a), *M5* (b), *M6* (c), *M7* (d), *M8* (e) and *Graded-I* (f).

In general, a columnar microstructure is discerned for all the studied coatings. However, the columnar character observed in the etched cross-sections appears clearer as the Al/Si

ratio increases. For the particular case of sample *M6*, a layer of about 5 μm thickness was evidenced on top of the mullite coating, as shown in Figure 5 c. This layer persisted intact after the multiple step etching. Detailed confocal and optical micrographs of the microstructure for samples *M11* and *Graded-I* are presented in Figure 6.

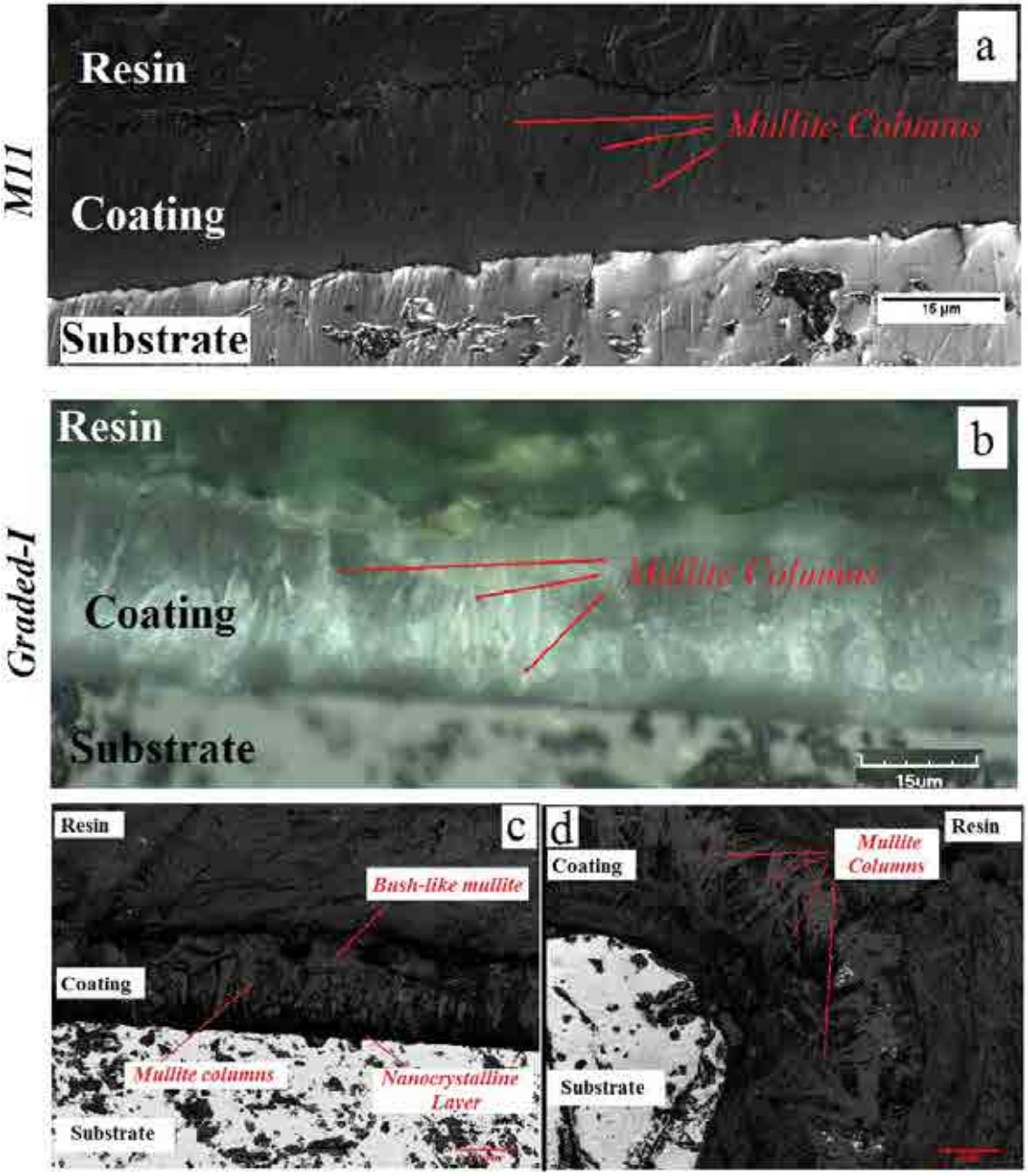

Figure 6. (a) Typical columnar microstructure of coatings. (a) Confocal micrograph of a partially etched cross-section in sample *M11*. (b) Optical and (c) confocal micrographs of the fully etched cross-section of sample *Graded-I* . (d) Detail of a corner for sample *Graded-I*.

As observed from Figure 6, mullite coatings studied in the present investigation have a columnar microstructure. Columns are arranged perpendicular to the substrate and grow from a nanocrystalline layer. The former is especially true at zones far from the corners of the specimens. In the corners of coated specimens columns grew randomly, as shown in Figure 6 d. As a consequence, for mechanical tests zones close to corner of specimens were avoided.

3.3 Preparation of specimens

Success in the analysis and interpretation of the results obtained from nanoindentation and nanoscratch tests, as well as the reliability of these results, is directly linked with the surface preparation of specimens. Moreover, considering for the micro- and nano-scale of the mechanical characterization proposed in this thesis, together with the length scale of the features ascribed to tested coatings (thickness, microstructure, and compositionally changes) to be studied, preparation of specimens becomes a crucial step.

Specimens to be subjected to mechanical tests consisted in prismatic bars of SiC coated with mullite ($3Al_2O_3 \cdot 2SiO_2$). In general, the surfaces of the coated specimens in the "As-deposited" state were not excessively rough (see Figure 7). However, surface condition for nanoindentation and nanoscratch tests are quite restrictive, because flat and smooth surface conditions are essential for the suppression of artifacts associated with irregularities at the surface during the tests. In addition, it is mandatory to keep the tested surface parallel to the horizontal plane so that the load is perpendicularly applied through the indenter.

Accounting for the microstructural features of CVD mullite coatings and aiming to probe the potential variation in mechanical properties, especially in the case of the compositionally graded ones, three approaches for the mechanical testing methodology are proposed: "surface", "cross-sectional" and "wedge". The preparation of the specimens following each of these approaches is described below.

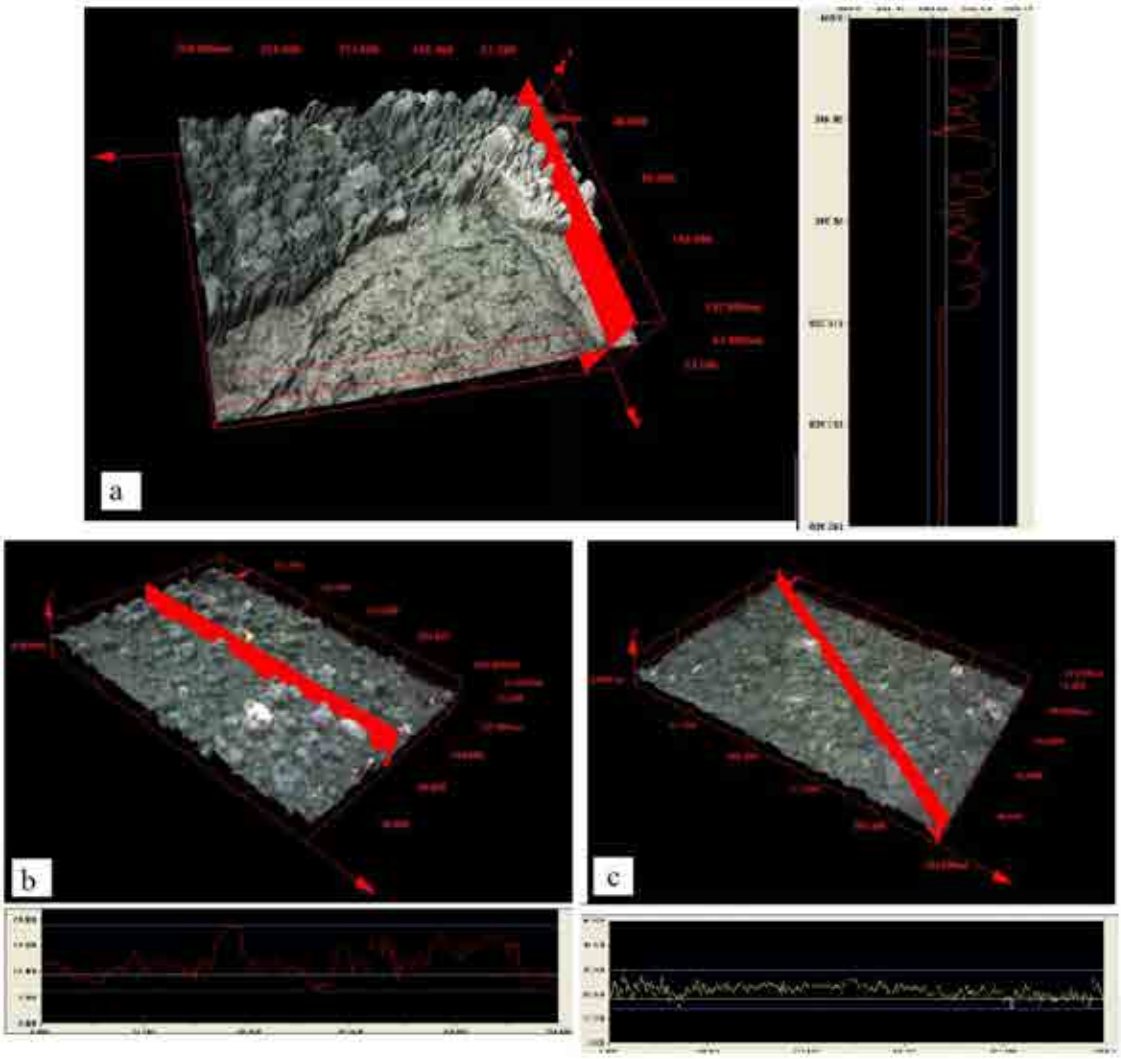

Figure 7. (a,b) 3D Confocal micrographs and profiles of the top surfaces of the sample *Changing*, and (c) *M11* in the "As-deposited" state.

3.3.1 Surface approach

Top surfaces for the different specimens were polished manually. It was carried out by handling the specimens directly on selected polishing cloths. In doing so, special care was taken for avoiding complete removal of the coating and simultaneously achieving surfaces perfectly polished, while preserving the coatings as thick as possible.

The polishing procedure consisted of different stages, starting with diamond suspensions of grain size 6 μm using a disk rotation rate of 300 rpm. The subsequent stage consisted of polishing with a 3 μm diamond paste until a mirror-like surface was attained. A colloidal silica suspension was used to finish all the samples using the same rotation rate conditions during a 10-minutes period. As a result, a surface condition was attained where it was possible to measure the mechanical properties of specimens as closest as possible to the "As deposited" state of coatings, i.e. avoiding roughness artifacts.

Due to the transparency inherent to mullite at small thicknesses, it was of great importance to combine short stages of polishing with interrupted microscopic inspection of the surface condition, in order to prevent any excessive coating removal. As an example, Figure 8 shows the improvement on surface condition for sample *M3* after two polishing steps .The decrease in roughness is evident from such a figure. In this case, roughness of the samples (R_a) was reduced from 0.78 to 0.07 μmafter two steps. Final roughness of the top surface for all the studied samples, as measured using AFM, was found to be lower than 6 nm. A similar polishing process was used for uncoated SiC samples.

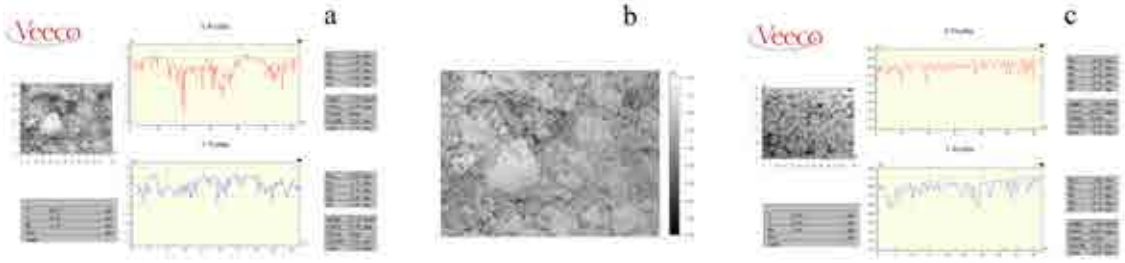

Figure 8. (a) Images and profile of top surface for *M3* specimen before and (b,c) after two steps of polishing. The decrease of roughness is clear. These images were obtained by interferometry.

3.3.2 Cross-sectional and wedge approaches

For the preparation of cross-sections, SiC coated bars were sliced in a cutting machine, using a diamond disk with low cutting load and speed. The resulting pieces were casted in resin, placing the cross-section of the coated specimen perpendicular to the base of the mount, as shown in Figure 9 a.

Once cast, the cross-sections were polished with a 30 μm diamond suspension at 200 rpm to remove the resin at the surface, until the cut cross-section was reached.

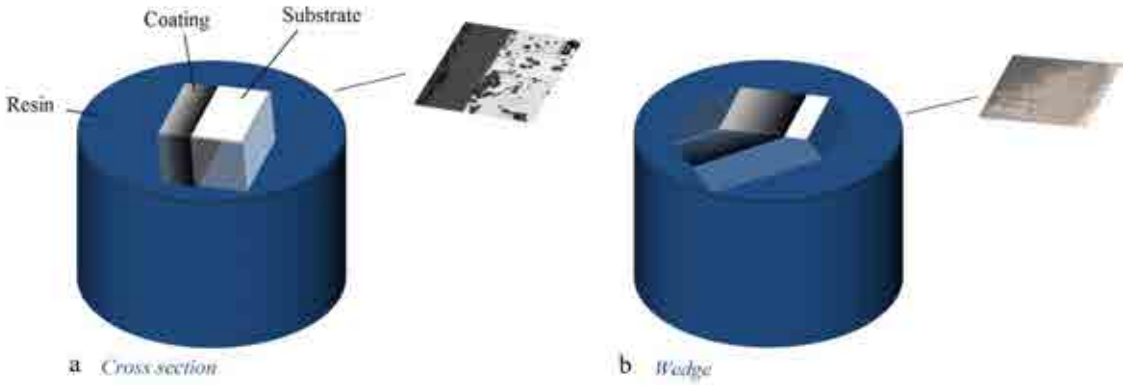

Figure 9. (a) Configuration of the cast cross-section, and (b) the wedge of samples. Corresponding micrographs of the resulting polished surfaces are also shown.

Due to the differences in hardness for the three components at the cross-sections (resin, coating and substrate), special care was taken in order to avoid the differential removal of material for each of them (see Figure 10 a) during the polishing process. Low polishing forces were applied in order to obtain flat surfaces (see Figure 10 b). Thus, it was possible to obtain flat and planar cross-sections of the coatings for the subsequent finishing stages of the preparation process.

Finally, cut cross-sections were finely polished with a 6 μm and 3 μm diamond suspensions, at 300 rpm for about 45 minutes, to remove the marks from the cutting

procedure and the previous polishing stage. A final polishing step with colloidal silica suspension during 10 minutes was carried out.

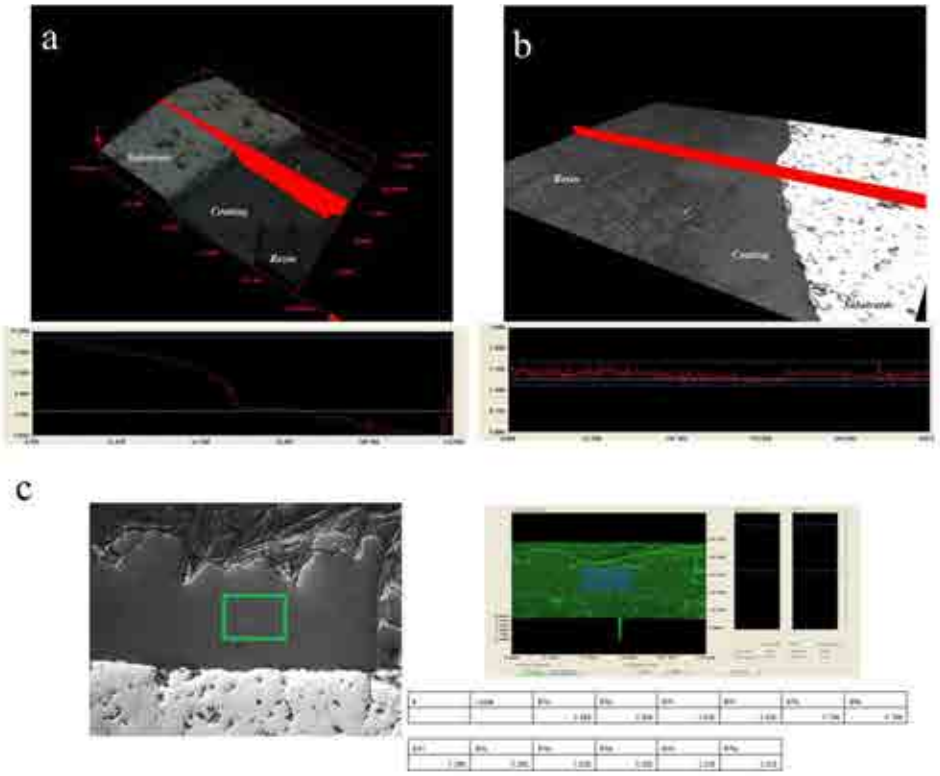

Figure 10. (a) 3D confocal micrographs showing the lack of planarity in a cross-section due to the differences in hardness of the components, and (b) a flat cross-section optimum for the nanoindentation tests. (c) Roughness in the coating after the polishing process, as measured through confocal microscopy.

Similar procedure as that described for preparing cross-sections was implemented for attaining "wedge" specimens. However, in this case the coated specimen was tilted at the casting stage, aiming to obtain a polished and flat surface of the tilted coating on top of the mount, as illustrated in Figure 9 b.

After polishing, flat and smooth cross-sections ideal for micro and nanomechanical testing were obtained. Roughness of polished section was found to be lower than 2 nm, as measured through LSCM (see Figure 10 c).

3.4 Mechanical characterization

In this section, a general overview of the methodology used for the micro/nano-mechanical characterization conducted in this thesis is presented. Moreover, it must be pointed out that a more detailed experimental description of the characterization performed in each sample, including testing parameters, are given in the specific experimental sections of *Chapters 5*, *6, 7* and *8*.

3.4.1 Testing methodologhy

Attempting to account for the different microstructural, compositional and geometrical features of the coatings, and especially regarding assessment of mechanical properties in specimens with compositional changes along the thickness (*Graded* samples), the mechanical testing was conducted following the "top", the "cross-sectional" and the "wedge" approaches, as illustrated in the scheme of Figure 11 (a,b and c respectively). Once the samples were metallographically prepared, as detailed in the previous section, nanoindentation and nanoscratch tests were performed both in the polished top surface of the coatings (Figure 11 a) as well as in polished cross-sections (Figure 11 b). In the case of the samples prepared following the wedge approach, testing was limited to nanoindentation (Figure 11 c).

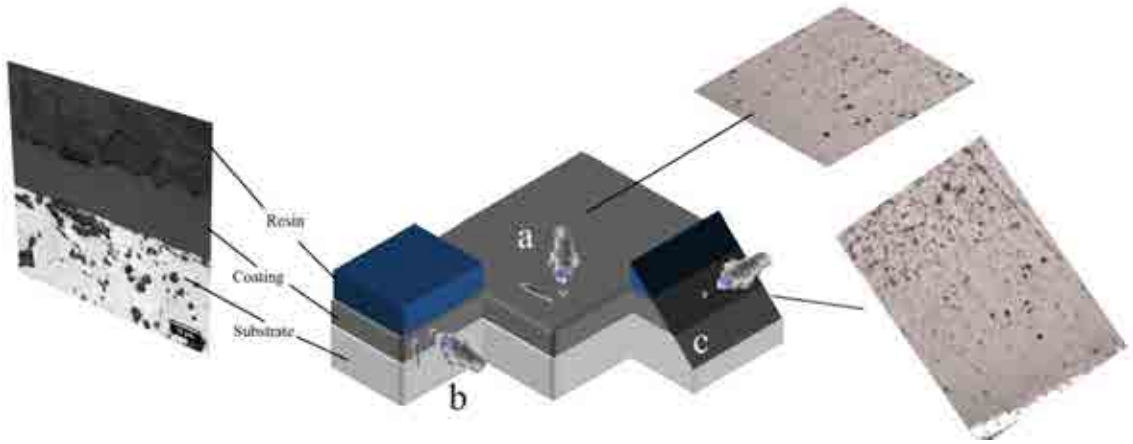

Figure 11. (a) Scheme of the "Top", (b) "Cross-sectional" and (c) "Wedge" approaches for the nanoindentation and nanoscratch tests together with corresponding micrographs.

Tests were performed using a MTS Nanoindenter® XP (Figure 12). This equipment operates in a configuration similar to the general schematic system illustrated in Figure 4 of *Chapter 1*.

Figure 12. Nanoindentation equipment used for the mechanical characterization.

The nanoindenter used is equipped with a Continuous Stiffness Measurement (CSM) modulus, allowing for the continuous record of stiffness (S) and applied load (P) as a function of penetration depth (h).

3.4.2 Nanoindentation

3.4.2.1 Elastic modulus (E) and hardness (H)

Nanoindentation tests were performed in all the studied systems using a Berkovich tip with its area function calibrated through a fused silica standard, and enabling the CSM unit. The CSM allows for the extraction of these properties along the penetration depth. Therefore, E and H values were calculated as a function of h according to the model proposed by Oliver and Pharr[6]. Tests were performed at a constant strain rate of 0.05 s^{-1}.

Regarding the indentations performed following the surface approach, nanoindentations matrices were performed at random locations. Maximum penetration depths were selected in each case according to the thickness of the coatings. In the case of thin coatings, a maximum penetration depth of $h_{max}/t = 0.1$ was used in order to calculate the intrinsic hardness of the coating without any substrate influence. Intrinsic E values for the coatings were deconvoluted from the apparent obtained response by using thin film models.[7–13]

On the other hand, concerning the cross-section and wedge approaches, matrices were placed across the coating aiming to observe the potential variation in E and H with thickness. Indentation rows were positioned parallel to the substrate/coating interface. A maximum penetration depth value of h_{max} = 100 nm was used. This penetration depth allowed performing several rows of indentations along the coating thickness; and thus assessing potential variations in mechanical properties.

For all the nanoindentation matrices placed, minimum separation between indentations was 25 times the maximum penetration depth (25 h_{max}). Hence, possible effects of the deformation field generated by each indentation on subsequent ones were completely suppressed.

Nanoindentation tests were also performed on uncoated silicon carbide substrates to calculate its E and H.

3.4.2.2 Stress-strain (σ-ε) curves

Aiming to investigate the elasto-plastic transition during nanoindentation, indentation matrices using a spherical indenter of radius r_{sph}= 25 μm were conducted on the top surface of stoichiometric coatings (Al/Si= 3). A maximum load of P_{max} = 300 mN was used.

Stress-strain curves for these coatings were constructed by using the Hertz formulations described in section 1.2.2 of *Chapter 1*.[14–23] Yield strength σ_y and elastic modulus E for these coatings were also calculated following the procedure described there[21,23].

3.4.2.3 Fracture toughness

Indentation tests using a cube corner tip were performed on top surfaces of coatings for measuring K_c. The load applied was controlled to identify suitable levels to induce cracks that allow for toughness estimation.

Different cube corner nanoindentations were carried out, and the cracks produced on the coatings were used both to study cracking behaviour, and to estimate K_c. Crack lengths at the surface were measured and fracture toughness was estimated following the formulations introduced in section *1.2.3.5* of *Chapter 1*.[24–28]

3.4.2.4 Adhesion strength and interface fracture toughness

Cube corner indents were performed on thin stoichiometric $3Al_2O_3{\cdot}2SiO_2$ films (sample *M3Thin*) at increasing maximum loads, P_{max} = 20 mN, 30 mN, 35 mN, 40 mN, 50mN and 70 mN, to induce controlled delamination. The energy of adhesion per unit area, or strain energy release rate (G_{int}) as well as the interface fracture toughness (K_{int}) were calculated as proposed in section 1.2.4.3 of *Chapter 1*.[29–31]

3.4.3 Nanoscratch

Nanoscratch tests were carried out using a Berkovich indenter, at a constant speed along the test of 1 μm/s, following the surface and cross-sectional approaches.

In the case of tests performed at top surfaces of specimens, a linearly increasing load along the scratch length was applied. Two different conditions were selected: (i) maximum load of P_{max} = 50 mN and a scratch length of 50 μm, and (ii) a maximum load of P_{max} = 500 mN and a scratch length of 200 μm. Such conditions permitted evaluation of damage evolution of coatings under sliding contact conditions.

On the other hand, nanoscratch tests were performed at constant loads across the polished cross-sections of the studied specimens. Tests were conducted following two opposite direction paths; (i) from the substrate, through the coating, into the resin (i.e. "bottom to top"); and (ii) from the resin, through the film, into the substrate (i.e. "top to bottom"). In both cases, tests were performed with one corner of the Berkovich indenter in the scratch direction.

Experiments were conducted as series of constant load tests with 50 mN step-increasing applied loads: 50 mN, 100 mN, 150 mN, 200 mN, 250 mN and 300 mN.

3.5 Characterization of imprints and induced damage

A brief description of the main techniques used in this investigation for the characterization of the imprints and damage induced by nanoindentation and nanoscratch tests implemented is now presented. Additionally, experimental details of the equipment used as well as testing conditions for the characterizations conducted are given in this section.

3.5.1 Laser Scanning Confocal Microscopy (LSCM)

Confocal microscopy is an optical imaging technique that achieves great optical resolution and contrast, by using point illumination and eliminating out-of-focus light.

Therefore, it enables the reconstruction of three-dimensional (3D) surface morphologies from the obtained images at different focal planes, as illustrated in Figure 13 a.

The Laser Scanning Confocal Microscope (LSCM) uses a focused laser that scans the surface to produce a two-dimensional (2D) reconstruction of the surface at every focal plane, with the signal received in the focus. Coupling several 2D reconstructions made at close focal planes, it is possible to obtain detailed 3D reconstructions of the surface morphology of a sample.[32]

The LCSM technique was implemented in this thesis locating, imaging, and examining nanoindentation imprints and nanoscratch tracks, and the associated damage at the surface level in both cases. The equipment used, an Olympus LEXT OLS 3100 microscope, is presented in Figure 13 b.

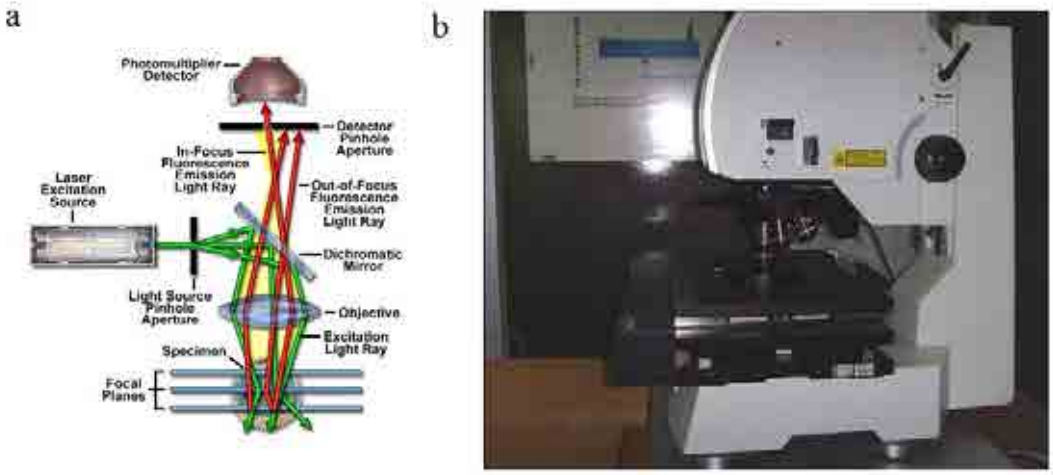

Figure 13. (a) Scheme of the principle of a laser scanning confocal microscope[32]. (b) LSCM used in this thesis: *Olympus LEXT OLS 3100*.

3.5.2 Atomic Force Microscopy (AFM)

The atomic force microscope is a powerful tool for imaging, measuring and manipulating at the nanoscale. It uses piezoelectric actuators and sensors that allow the small but precise movements of a sharp tip that follows the surface when performing a scan.

The tip is mounted at the end of a cantilever and brought into the proximity of the surface of the tested sample. Different surface forces acting on the tip can cause the deflection of the cantilever. This deflection is accurately measured by a laser beam that aims to the back side of the cantilever, right behind the tip. The beam is reflected to a photodiode that captures the variations in the laser incidence. This system, schematized in Figure 14 a, permits generating precise images of surface topography by performing a complete scan of the desired area with the mentioned tip, by moving the sample or the cantilever with piezoelectric actuators.

The residual imprints induced by the Berkovich, spherical and cube corner indenters, as well as the associated deformations and fracture phenomena, were imaged by using AFM in the tapping mode. The AFM used in this investigation is a Veeco Dimension 3100, as shown in the Figure 14 b. Length of the radial cracks induced by cube corner indentation, used for the calculation of K_c, was also measured by means of AFM.

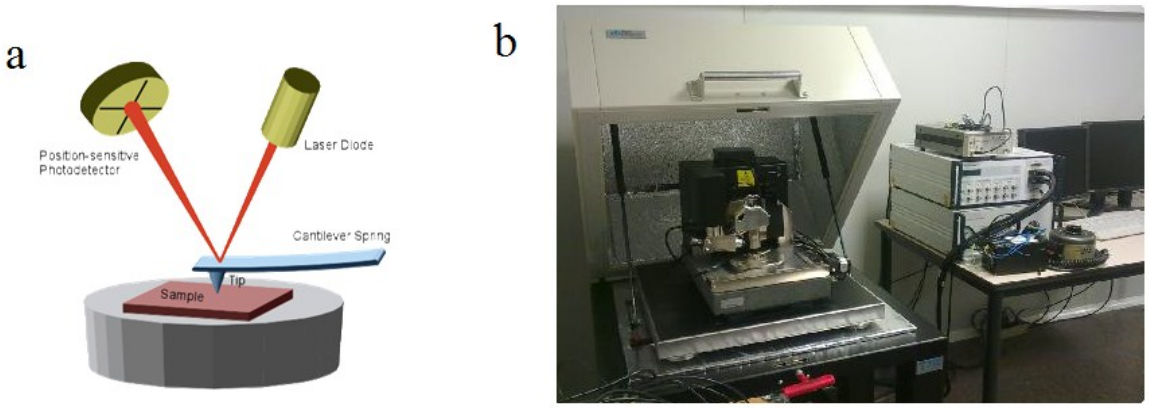

Figure 14. (a) Scheme of the principle of functioning of an atomic force microscope[33]. (b) AFM used in this thesis, *Veeco Dimension 3100*.

3.5.3 Focused Ion Beam microscopy (FIB)

Focused ion beam (FIB) is a technique increasingly used in the materials science field for site-specific analysis, deposition and ablation of materials. FIB uses a beam of finely focused ions (usually gallium) that are accelerated at low currents for imaging, or at high currents for site-specific sputtering or milling. A sketch illustrating the functioning of a typical FIB is shown in Figure 15 a.

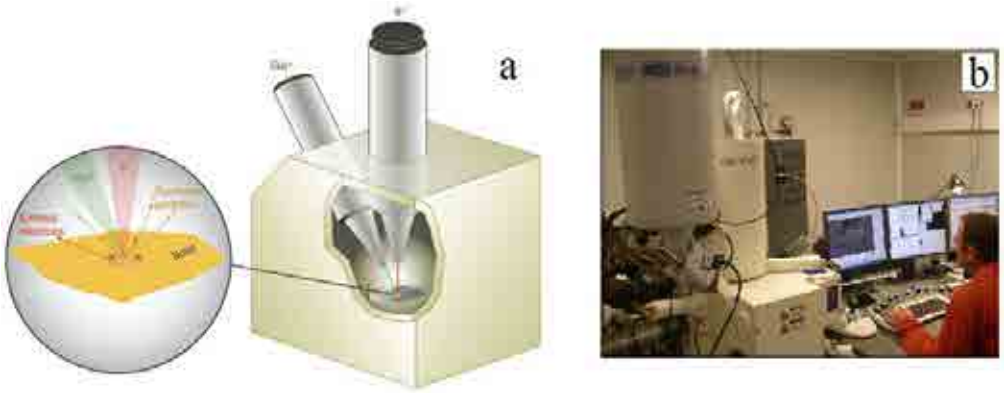

Figure 15. (a) Schematic illustration of a dual beam FIB instrument and its principle[34]. (b) FIB used, *Zeiss Neon 40*.

FIB was here used to investigate the different deformation and cracking features induced by nanoindentation and/or nanoscratch at the subsurface, and their interaction with the coating microstructure and the coating/substrate interface. Cross-sections were prepared using a FIB equipment (FIB Zeiss Neon 40) coupled with a scanning electron microscope (FE-SEM Neon 40 Carl Zeiss), as shown in Figure 15 b.

FIB cross-sections were performed in the mullite coatings below residual nanoindentation imprints and nanoscratch tracks. In doing so, indented and scratched FIB-SEM samples were pre-coated with a fine carbon coating to prevent charging and reduce ion beam damage. Platinum layers were subsequently deposited on top surface of imprints and tracks, to protect the surface while milling. In these areas, FIB trenches were bombarded using a Ga+ ion beam perpendicular to the surface with decreasing currents and a final polishing step with a beam of 50 pA at 30 kV to reveal the film microstructure. Finally, SEM images were acquired. Final dimensions of trenches permitted the observation of the entire film thickness and a significant substrate zone.

3.5.4 3D focused ion beam tomography (3D FIB tomography)

Aiming to examine subsurface cracking in a more comprehensive manner, 3D FIB tomographies were constructed for cube corner imprints. In this case, the gallium focused ion beam was used to cross-section the indentation sites locally, whilst SEM secondary electron images were taken for each sequential x-y 2D slice. This process was repeated until the material volume of interest, comprising indentation imprint and neighboring cracking zones, was covered. Separation between each cross-section was $z \approx 0.07$ μm. 2D SEM images were aligned and corrected for drift and main features involved in the analyzed volumes, such as indentation imprint, film/substrate interface and subsurface crack were segmented in each 2D section. The 3D volume reconstruction was done by means of the software AVIZO.

3.6 Thermal treatments and corrosion

In addition to the highly aggressive environments that materials for gas turbines must endure "in-service" conditions, they must present an optimum combination of mechanical properties that guarantee their structural integrity. High chemical (oxidation and corrosion resistance) and thermo-physical (thermal shock resistance) properties are required during service at elevated temperatures. Moreover, since most of the applications at elevated temperatures are long-term ones, the materials must exhibit superior long-term stability too.

The influence of "in service" conditions on the mechanical properties and performance of CVD mullite coatings was also evaluated in this investigation. In doing so, nanoindentation tests are conducted on selected samples after long term thermal stability, thermal shock, and corrosion tests. Experimental details regarding the conditions used for particular tests are briefly described in this section.

3.6.1 Long term stability

Specimens were subjected to a thermal stability test consisting of heating them until 1250°C and sustaining this temperature for 100 hours in a tubular furnace, with heating and cooling ramps of 5°C/minute.

3.6.2 Thermal shock

Samples were subjected to a thermal shock treatment consisting of heating of the specimens at 1250°C for 3 hours in a tubular furnace (heating rate of 5°C/minute), followed by rapid cooling given by quick removal of coated specimens from the furnace and cooling at normal room conditions (until 25º).

3.6.3 Corrosion

Corrosion tests were carried out in association with the research group of Professor V. K. Sarin in the manufacturing laboratory of the department of Mechanical Engineering at Boston University. Specimens were loaded with about 15 mg/cm^2 of Na_2SO_4, applied by spraying a solution of reagent grade Na_2SO_4 in distilled water on the SiC heated on a hot plate. The Na_2SO_4 loaded specimens were subsequently placed on an alumina holder and exposed to a flowing oxygen environment in an alumina tube heated by an electric furnace at 1200 °C (heating rate of 5 °C/min). The oxygen flow rate was 200 cm^3/min at standard temperature and pressure. It was controlled using a mass flow meter. Oxygen was flown in order to have high Na_2O activity, which is a critical quantity. The specimens were exposed for 100 continuous hours.

3.7 References

1. Auger, M., Sarin, V. K. A kinetic investigation of CVD mullite coatings on Si-based ceramics. *Int. J. Refract. Met. Hard Mater.* **19**, 479-494 (2001).

2. Basu, S., Kulkarni, T., Wang, H., Sarin, V.K. Functionally graded chemical vapor deposited mullite environmental barrier coatings for Si-based ceramics. *J. Eur. Ceram. Soc.* **28**, 437-445 (2008).

3. Kulkarni, T., Wang, H.Z., Basu, S.N., Sarin, V.K. Compositionally graded mullite-based chemical vapor deposited coatings. *J. Mater. Res.* **24**, 470-474 (2009).

4. Kulkarni, T., Wang, H.Z., Basu, S.N., Sarin, V.K. Phase transformations in mullite-based nanocomposites. *Int. J. Refract. Met. Hard Mater.* **27**, 465-471 (2009).

5. Kulkarni, T., Wang, H.Z., Basu, S.N., Sarin, V.K. Protective Al-rich mullite coatings on Si- based ceramics against hot corrosion at 1200°C. *Surf. Coat. Technol.* **205**, 3313-3318 (2011).

6. Oliver, W.C., Pharr, G.M. An improved technique for determining hardness and elastic modulus using load and displacement sensing indentation experiments. *J. Mater. Res.* **7**, 1564-1583 (1992).

7. Gao, H., Chiu, C.-H., Lee, J. Elastic contact versus indentation modeling of multi-layered materials. *Int. J. Solids Struct.* **29**, 2471-2492 (1992).

8. Song, H. Selected mechanical problems in load- and depth-sensing indentation testing. Ph.D. Thesis. Rice University. Houston, USA. p. 85 (1999).

9. Saha, R., Nix, W.D. Effects of the substrate on the determination of thin film mechanical properties by nanoindentation. *Acta Mater.* **50**, 23-38 (2002).

10. Rar, A., Song, H., Pharr, G.M. Assessment of new relation for the elastic compliance of a film-substrate system. *Mater. Res. Soc. Symp. Proc.* 431-436 (2002).

11. Xu, H., Pharr, G.M. An improved relation for the effective elastic compliance of a film/substrate system during indentation by a flat cylindrical punch. *Scr. Mater.* **55**, 315-318 (2006).

12. Bec, S., Tonck, A., Loubet, J. A simple guide to determine elastic properties of films on substrate from nanoindentation experiments. *Philos. Mag.* **86**, 5347-5358 (2006).

13. Hay, J., Crawford, B. Measuring substrate-independent modulus of thin films. *J. Mater. Res.* **26**, 727-738 (2011).

14. Tabor, D. The hardness of solids. *Rev. Phys. Techn.* **1**, 145-179 (1970).

15. Field, J.S., Swain, M.V. A simple predictive model for spherical indentation. *J. Mater. Res.* **8**, 297-306 (1993).

16. Oliver, W.C., Pharr, G.M. Measurement of hardness and elastic modulus by instrumented indentation: advances in understanding and refinements to methodology. *J. Mater. Res.* **19**, 3-20 (2004).

17. Linss, V., Schwarzer, N., Chudoba, T., Karniychuk, M., Richter, F. Mechanical properties of a graded B-C-N sputtered coating with varying Young's modulus: deposition, theoretical modelling and nanoindentation. *Surf. Coat. Technol.* **195**, 287-297 (2005).

18. Fischer-Cripps, A. Critical review of analysis and interpretation of nanoindentation test data. *Surf. Coat. Technol.* **200**, 4153-4165 (2006).

19. Liang, Y.-H., Arai, Y., Ozasa, K., Ohashi, M., Tsuchida, E. Simultaneous measurement of nanoprobe indentation force and photoluminescence of InGaAs/GaAs quantum dots and its simulation. *PhyE* **36**, 1-11 (2007).

20. Kalidindi, S.R., Pathak, S. Determination of the effective zero-point and the extraction of spherical nanoindentation stress–strain curves. *Acta Mater.* **56**, 3523-3532 (2008).

21. Roa, J.J., Jiménez-Piqué, E., Capdevila, X.G., Segarra, M. Nanoindentation with spherical tips of single crystals of YBCO textured by the Bridgman technique: Determination of indentation stress–strain curves. *J. Eur. Ceram. Soc.* **30**, 1477-1482 (2010).

22. Roa, J.J. Mechanical properties of HTSC at micro/nanometric scale.Ph.D. Thesis. Universidad de Barcelona. Barcelona, Spain. p. 201 (2010).

23. Chintapalli, R.K., Jiménez-Piqué, E., Marro, F.G., Yan, H., Reece, M., Anglada, M. Spherical instrumented indentation of porous nanocrystalline zirconia. *J. Eur. Ceram. Soc.* **32**, 123-132 (2011).

24. Lawn, B.R., Evans, A.G., Marshall, D.B. Elastic plastic indentation damage in ceramics: the median radial crack system. *J. Am. Ceram. Soc.* **63**, 574-581 (1980).

25. Anstis, G.R., Chantikul, P., Lawn, B.R., Marshall, D.B. A critical evaluation of indentation techniques for measuring fracture toughness: I, direct crack measurements. *J. Am. Ceram. Soc.* **64**, 533-538 (1981).

26. Harding, S., Oliver, W.., Pharr, G.M. Cracking during nanoindentation and its use in the measurement of fracture toughness. *Mater. Res. Soc. Symp. Proc.* 663-668 (1995).

27. Harding, S. Cracking in brittle materials during low-load indentation and its relation to fracture toughness. Ph.D. Thesis. Rice University, Houston, USA. p. 207 (1995).

28. Pharr, G. Measurement of mechanical properties by ultra-low load indentation. *Mater. Sci. Eng. A* **253**, 151-159 (1998).

29. Marshall, D.B., Evans, A.G. Measurement of adherence of residually stressed thin films by indentation. I. Mechanics of interface delamination. *J. Appl. Phys.* **56**, 2632-2638 (1984).

30. Volinsky, A.A., Moody, N.R., Gerberich, W.W. Interfacial toughness measurements for thin films on substrates. *Acta Mater.* **50**, 441-466 (2002).

31. Chen, J., Bull, S.J. Approaches to investigate delamination and interfacial toughness in coated systems: an overview. *J. Phys. D: Appl. Phys.* **44**, 1-19 (2011).

32. Claxton N S, Fellers T J, Davidson M W. Laser scanning confocal microscopy. At <http://www.olympusconfocal.com/theory/LSCMIntro.pdf>

33. Biophysics and Soft Matter (Univerity Greifswald) AFM (Atomic Force Microscopy), at <http://www3.physik.uni-greifswald.de/method/afm/eafm.htm>

34. Volkert, C.A., Minor, A.M. Focused ion beam micromachining. *MRS Bulletin* **32**, 389-399 (2007).

4 *Chapter*

Micro- and nanomechanical properties of stoichiometric $3Al_2O_3{\cdot}2SiO_2$ coatings and performance of the system $3Al_2O_3{\cdot}2SiO_2$/SiC

Along this chapter, the integrity of the coated $3Al_2O_3{\cdot}2SiO_2$/SiC system intended as a structural unit, as well as the main intrinsic mechanical properties of mullite $3Al_2O_3{\cdot}2SiO_2$ coatings with stoichiometric composition (Al/Si: 3), regarded here as the "standard system", are investigated. In the former case, relatively thin mullite films are evaluated, whereas in the latter case "thick" coatings are studied.

Intrinsic hardness (H_f), elastic modulus (E_f), and fracture toughness (K_f) of stoichiometric CVD mullite coatings were found to lie in the low part of the range of values reported in the open literature for bulk mullite. The cohesive and decohesive properties of the mullite film were evaluated. The energy of adhesion of the mullite films to the SiC substrate, and the fracture toughness of the interface, were also assessed.

4.1 Introduction

The coatings investigated in this thesis are configured by columnar mullite grains that nucleate from a very thin nanolayer of a vitreous silica matrix with embedded nano-sized Al_2O_3 particles. When the composition of the emergent coating is close to the

value of the stoichiometric mullite (Al/Si ≈ 3), nucleation of mullite occurs and columns can grow over a wide range of increasing Al/Si ratios in constant or graded compositions[1,2]. Attending to this configuration, the knowledge of the mechanical behavior of stoichiometric $3Al_2O_3{\cdot}2SiO_2$ coatings becomes of primary importance. Moreover, considering these compositional variations from a structural standpoint, it is essential to evaluate the localized mechanical properties of these coatings, especially around the interface, i.e. the stoichiometric $3Al_2O_3{\cdot}2SiO_2$ columnar coating growing from the nanolayer which is in intimate contact with the SiC substrate. In this regard, nanoindentation and nanoscratch stand as appropriate techniques for assessing the mechanical behavior of such systems.

This chapter proposes a systematic study of the local mechanical properties of CVD stoichiometric $3Al_2O_3{\cdot}2SiO_2$ coatings as well as the evaluation of the integrity of $3Al_2O_3{\cdot}2SiO_2$/SiC systems. In doing so, relatively "thin" films ($t \sim 1$ μm after polishing, sample *M3thin*) and "thick" films or coatings ($t > 5$ μm after polishing, samples *M3-I* and *M3-III*) deposited on SiC are evaluated by means of nanoindentation and nanoscratch tests using tips with different geometries.

Regarding the mechanical properties of the "thin" films, H_f values are directly extracted using a Berkovich indenter whereas the E_f ones are deconvoluted from the measured E_a, by using indentation thin film models from literature[3–9]. Moreover, a spherical indenter is used to obtain the indentation stress-strain curves of the $3Al_2O_3{\cdot}2SiO_2$ film following the methodology proposed in previous studies[10,11]. From these data, σ_y is calculated, and a new E_f value was also estimated[10–13]. The latter is compared and critically analyzed with respect to the one deconvoluted from Berkovich nanoindentation. Concerning the mechanical integrity of the $3Al_2O_3{\cdot}2SiO_2$/SiC system, a cube corner tip geometry was used for inducing controlled film cracking, followed by film delamination as the nanoindentation applied load is increased. Complementary characterization techniques such as laser scanning confocal microscopy (LSCM), atomic force microscopy (AFM), FIB coupled with field emission scanning electron microscopy (FIB-FESEM), and 3D-FIB tomography are used to investigate damage features at both surface and

subsurface levels. Finally, K_f is calculated from the indentations confined to the film following the protocol proposed in the literature[14,15], whilst G_{int} and K_{int} are evaluated from the delaminated areas, according to the procedure proposed by several authors[16–18]. Similarly, nanoscratch tests allow to induce delamination in the films and to calculate complementary values of G_{int} and K_{int} [16,19–22].

In the case of "thick" coatings, nanoindentation and nanoscratch tests are also carried out on the polished top surfaces of the coatings in order to study their intrinsic mechanical properties and performance while minimizing the influence of the supporting SiC substrate on the measurements. The intrinsic hardness of the $3Al_2O_3{\cdot}2SiO_2$ coatings (H_f) as well as their intrinsic elastic modulus (E_f), are directly extracted using a Berkovich indenter. Controlled cracking within the coatings is induced by using a cube corner indenter, and their fracture toughness (K_f) is calculated similarly to the case of thin coated films. Moreover, increasing load nanoscratch tests are performed on the polished top surface of the coatings to evaluate their sliding contact resistance as well as to study the morphology and extent of the damage induced. Similar complementary characterization techniques as those used for thin films are used to investigate damage features at the surface level.

4.2 Experimental procedure

4.2.1 Nanoindentation tests

4.2.1.1 "Thin" films

Berkovich nanoindentations were performed on both polished uncoated SiC and coated *M3thin* sample. Substrate hardness (H_s) and elastic modulus (E_s) were evaluated to account for the substrate effect on the apparent film properties, H_a and E_a. On the other hand, nanoindentation using spherical and cube corner indenters was also performed on the polished surface of *M3thin* sample to estimate the intrinsic nanomechanical

properties of the film as well as to evaluate the mechanical integrity of the $3Al_2O_3{\cdot}2SiO_2$/SiC system.

For the Berkovich tests, matrices of 3x3 nanoindentations were performed on the polished uncoated SiC substrates at different penetration depths h_{max} = 1000 nm, 300 nm and 100 nm. These depths were selected to analyze the influence of porosity, inherent to the substrate used, on the measured H_s and E_s. Residual imprints were imaged by means of LSCM using an Olympus LEXT OLS 3100 microscope. Similar matrices were performed on the surface of *M3thin* sample at h_{max} = 1000 nm, 500 nm and 100 nm, attempting to penetration depth-to-film thickness ratios $h_{max}/t \approx 1$, 0.5 and 0.1 respectively. In this case, such ratios were selected to analyze the extent of the SiC substrate effect on the measured E_a and H_a. The residual imprints on the surface of the $3Al_2O_3{\cdot}2SiO_2$ films were imaged using a FESEM microscope (Neon 40, Carl Zeiss, Oberkochen, Germany). The values of H_a, E_a, H_s and E_s were evaluated, as a function of the penetration depth, by implementing the model proposed by Oliver and Pharr[23].

In addition, a matrix of 3 x 3 nanoindentations was also performed on *M3thin* sample at P_{max} = 300 mN employing a spherical indenter of radius R_{sph} = 25 μm. The area function of this indenter was also checked with a fused silica standard[13]. The resulting nanoindentation imprints were imaged by using AFM.

Finally, cube corner indents were performed on the *M3thin* sample at different maximum loads, P_{max} = 20 mN, 30 mN, 35 mN, 40 mN, 50 mN and 70 mN, to first induce radial cracks, then promote their extension with increasing loads, and eventually controlled fracture. Similarly, residual imprints were imaged by using AFM and the crack length c was measured from the micrographs.

4.2.1.2 "Thick" coatings

Similar to the case of *M3thin* sample, for the calculation of H_f and E_f, different matrices of indentations using a Berkovich tip were performed on the polished top surface of *M3-I* and *M3-III* samples. Matrices of 3 x 3 indentations at h_{max} = 2000 nm and 300 nm permitted an easy localization, observation and imaging of the resulting imprints. Similar matrices of indentations were performed at lower penetration depths (h_{max} = 100 nm). Such depths allowed satisfactory evaluation of the properties and their variation along a significant depth with respect to the thickness of the coatings, but avoiding the substrate influence on the obtained response.

Regarding calculation of K_f, controlled cracking was induced in the coatings by cube corner nanoindentations at P_{max} = 30 mN, 40 mN and 50 mN. Indentation imprints were imaged using AFM on tapping mode, and the length of the cracks produced were measured from the micrographs.

4.2.2 Nanoscratch tests

A Berkovich indenter was used to conduct different sets of nanoscratch tests on the polished top surfaces of *M3thin*, *M3-I* and *M3-III* samples. Tests were implemented both to assess the intrinsic resistance of the coatings to sliding contact (cohesive damage), and to induce damage in the $3Al_2O_3{\cdot}2SiO_2$ thin films for subsequent estimation of its adhesion to the SiC substrate (adhesive damage). A constant scratch rate of 1 μm/s was selected whilst increasing loads were applied by the indenter as it moved along the scratch length in all the experiments.

Two different conditions were selected for the tests. A maximum applied load of P_{max} = 50 mN and scratch length of l_{max} = 50 μm (corresponding to a loading rate of 1 mN/s, hereafter referred to as the "low load" condition), and a maximum applied load of P_{max} = 500 mN and scratch length of l_{max} = 200 μm (corresponding to a loading rate

of 2.5 mN/s, hereafter referred to as the "high load" condition). These conditions permitted to induce a progressive damage in the $3Al_2O_3{\cdot}2SiO_2$ coatings, and to promote their removal from the substrate in the case of thin coated specimens. The penetration of the tip during the scratch and the remaining inelastic deformation observed along the scratch track were analyzed, together with the fracture events induced.

The scheme of Figure 1 summarizes the different nanomechanical tests performed.

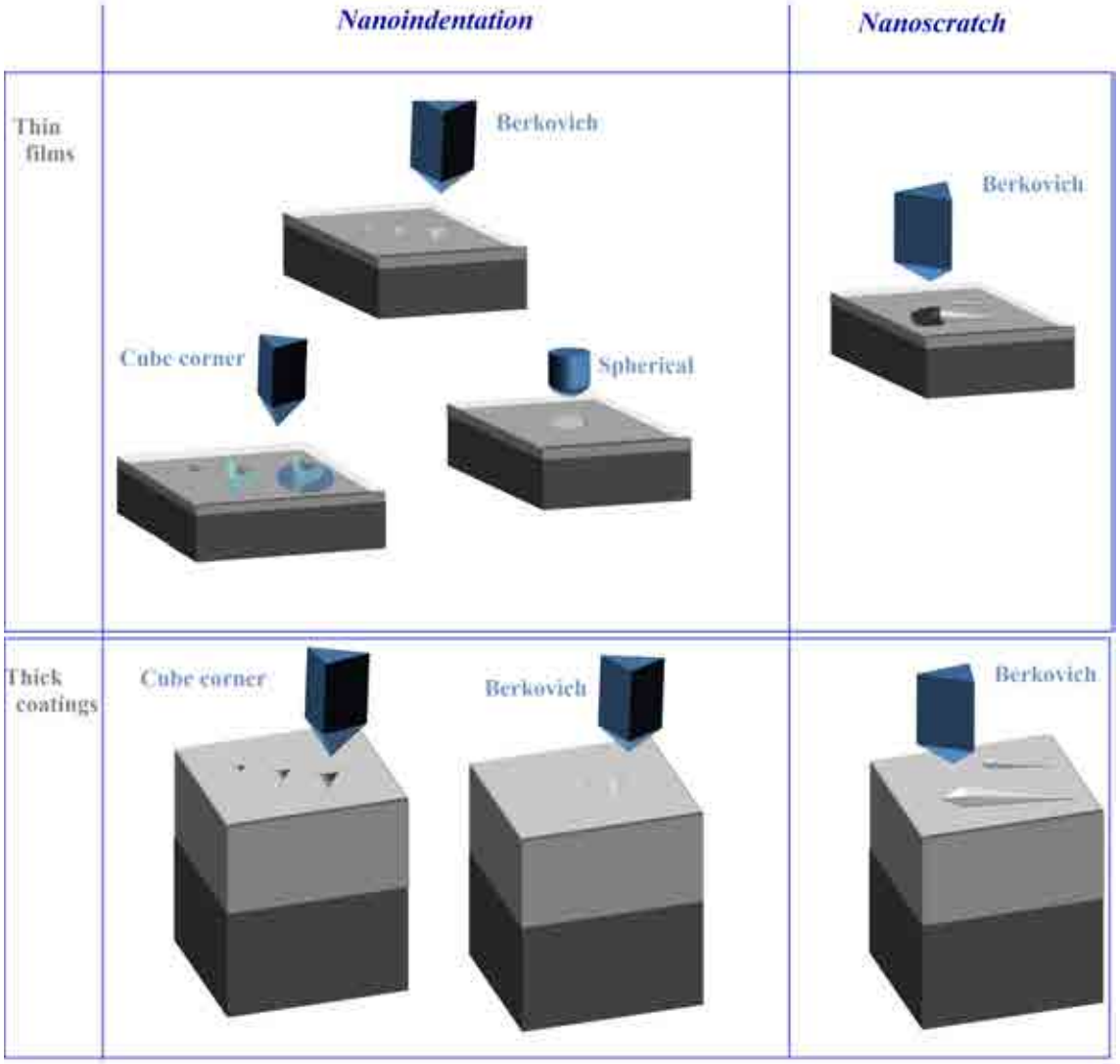

Figure 1. Scheme illustrating the conditions used for nanoindentation and nanoscratch tests performed on thin films and thick coatings.

4.2.3 FIB cross-sectioning and 3D tomography

The focused ion beam technique was used to characterize the subsurface damage induced by nanoindentation and nanoscratch tests performed on the coated $3Al_2O_3{\cdot}2SiO_2$/SiC system of *M3thin* sample.

FIB cross-sections were prepared as described in *Chapter 3* in imprints corresponding to indentations at h_{max} = 1000 nm and 500 nm, and tracks corresponding to scratches at the low and high load conditions. In addition, 3D-FIB tomographies were constructed for the imprints at P_{max} = 30 mN and 50 mN. In this case, the gallium FIB was used for local cross-sectioning the indentation sites whilst SEM secondary electron images were taken of each sequential x-y 2D slice. A schematic of the FIB sequential sectioning for 3D tomography is shown in Figure 2.

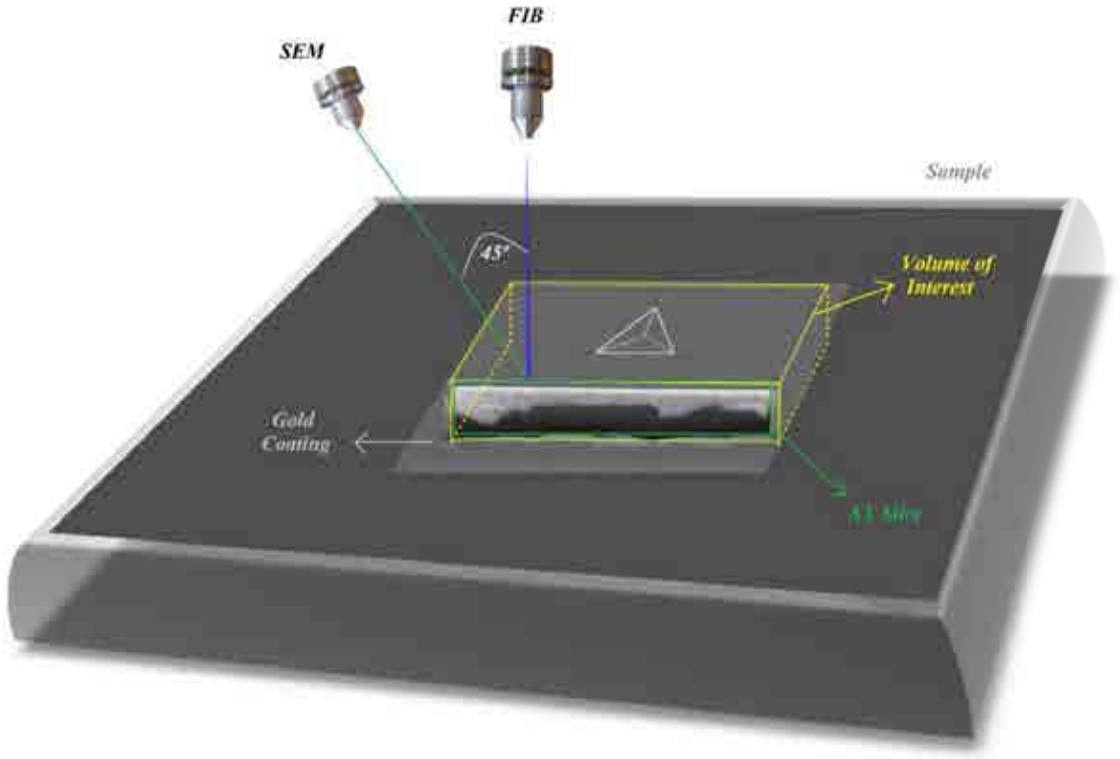

Figure 2. Schematic of the FIB sequential sectioning for 3D tomography. Gallium ions are bombarded perpendicular to the sample surface and 2D xy images are taken with the coupled SEM at 54° respect to the surface. A volume of material comprising the nanoindentation imprint and cracking is analyzed.

An example that illustrates an intermediate step in the tomography process is shown in Figure 3, where a partial FIB-3D tomography is superimposed to a micrograph of the corresponding x-y 2D cross-section. The features of interest are marked by arrows in the same figure.

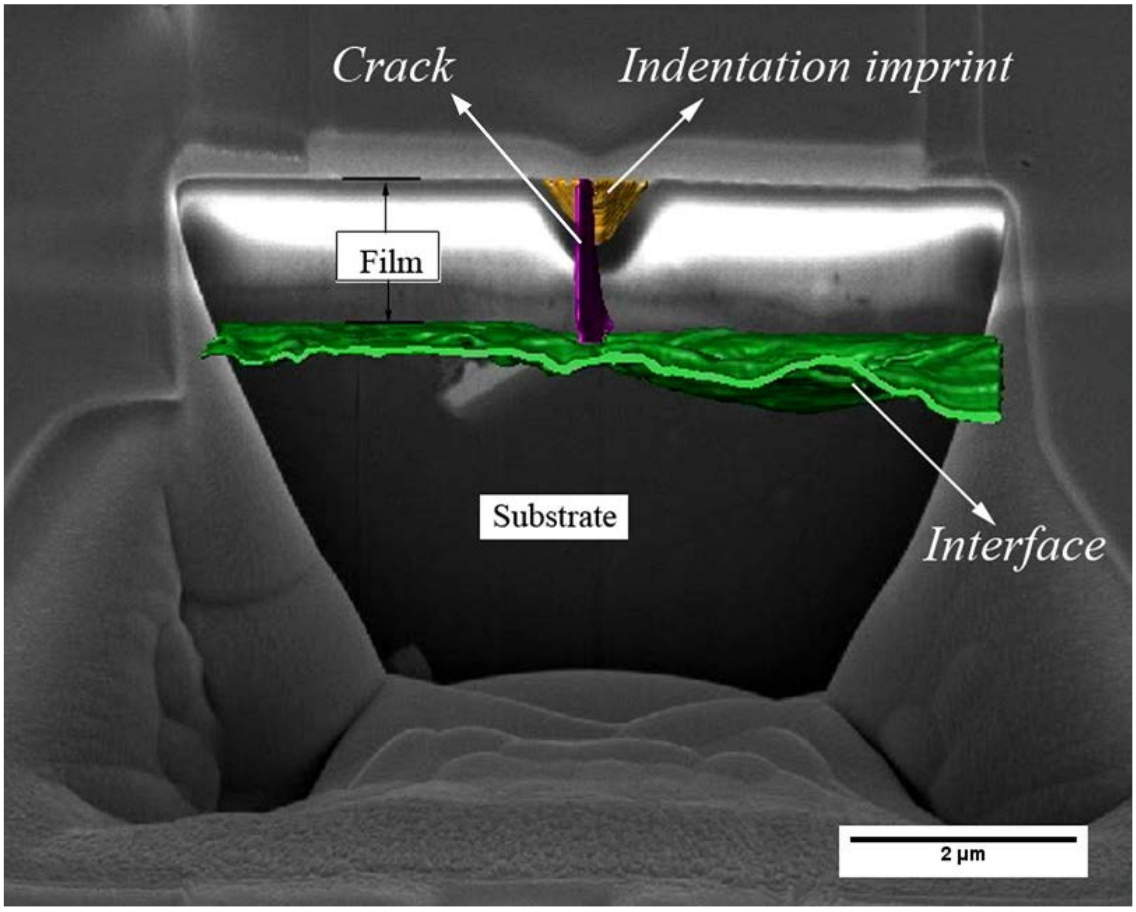

Figure 3**.** Partial FIB 3D tomography superimposed to a x-y 2D cross-section. The microstructural features involved in the tomography construction such as the "Indentation imprint", the film/substrate "Interface" and the subsurface "Crack" are identified.

4.3 Mechanical behavior of $3Al_2O_3{\cdot}2SiO_2$ thin films and thick coatings

4.3.1 Hardness and elastic modulus of the SiC substrate

Berkovich imprints of nanoindentations performed on the SiC substrate at h_{max} = 1000 nm, 300 nm and 100 nm are shown in Figure 4.

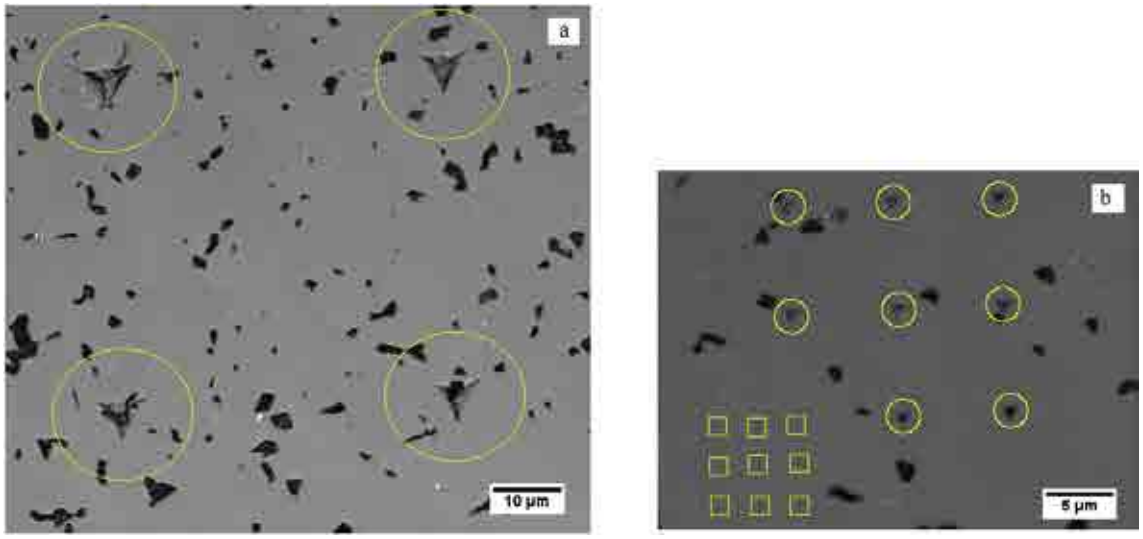

Figure 4. LSCM images of indentations performed on uncoated SiC at (a) h_{max} = 1000 nm, (b) h_{max} = 300 nm and 100 nm.

The corresponding curves of the average H_s and E_s are displayed, as a function of h, in Figure 5. For indentations at h_{max} = 300 nm and 100 nm, individual data are observed to overlap each other, although exhibiting a relatively high dispersion. In contrast, in the case of indentations at h_{max} = 1000 nm, E_s and H_s values as well as the corresponding dispersions tend to slightly decrease with h. It can be speculated that such behavior is related with the porosity of the SiC, clearly discerned in Figure 4.

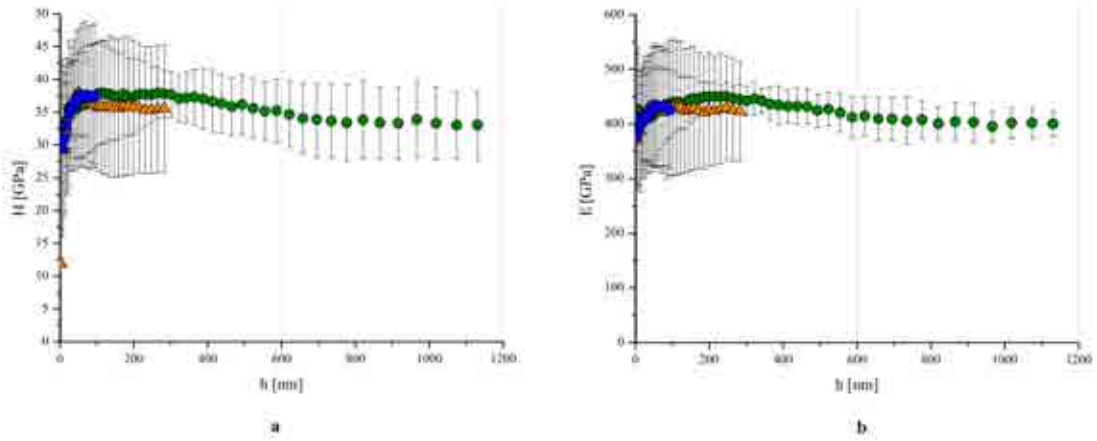

Figure 5. Average (a) H_s vs h and (b) E_s vs h curves of the uncoated SiC for indentations at h_{max} = 1000 nm (●), 300 nm (▲) and 100 nm (■).

As the indenter gets deeper, not only the measured properties but also the experimental scatter diminish as the length scale of the sample tested becomes representative of the whole substrate microstructure, including its porosity. This is especially true for penetrations higher than h = 600 nm. The average E_s and H_s values of the h_{max} = 1000 nm indentations in the range of h = 600-1000 nm, together with the average values for indentations at h_{max} = 300 nm and 100 nm are listed in Table 1.

	h_{max} = 100 nm	h_{max} = 300 nm	h_{max} = 1000 nm
H [GPa]	37 ± 11	36 ± 9	34 ± 5
E [GPa]	427 ± 109	427 ±108	410 ± 35

Table 1. Average H_s and E_s for the uncoated SiC at different h_{max}. The values at h_{max} = 1000 nm are averaged from those assessed in the range of h = 500-1000 nm in the curves shown in Figure 5.

4.3.2 Apparent elastic modulus and hardness of the $3Al_2O_3{\cdot}2SiO_2$ thin films

A FIB cross-section of a Berkovich indentation performed on the thin coated $3Al_2O_3{\cdot}2SiO_2$ film, at $h_{max}/t \approx 1$ (h_{max} = 1000 nm), is shown in Figure 6. Similarly, a FIB cross-section containing 3 indentations performed at $h_{max}/t \approx ½$ (h_{max} = 500 nm) is displayed in Figure 7.

In these micrographs, the $3Al_2O_3{\cdot}2SiO_2$ film appears as a white layer on top of the dark gray colored SiC substrate, as indicated in Figure 6 b. Within the film, some of the mullite columns can be distinguished growing from the nanolayer in immediate contact with the SiC, as indicated in Figure 6 c and Figure 7 b-d.

It should be noted that indentations performed at $h_{max}/t \approx 1$ induced some surface film chipping around the imprint and the onset of film spalling failure, as evidenced in Figure 6 a-b. The partial spalling is discernible from Figure 6 a-b as a surface crack deflecting at the interface is seen just in one of the sides of the imprint. Therefore, extreme care should be taken for extraction of properties at this penetration.

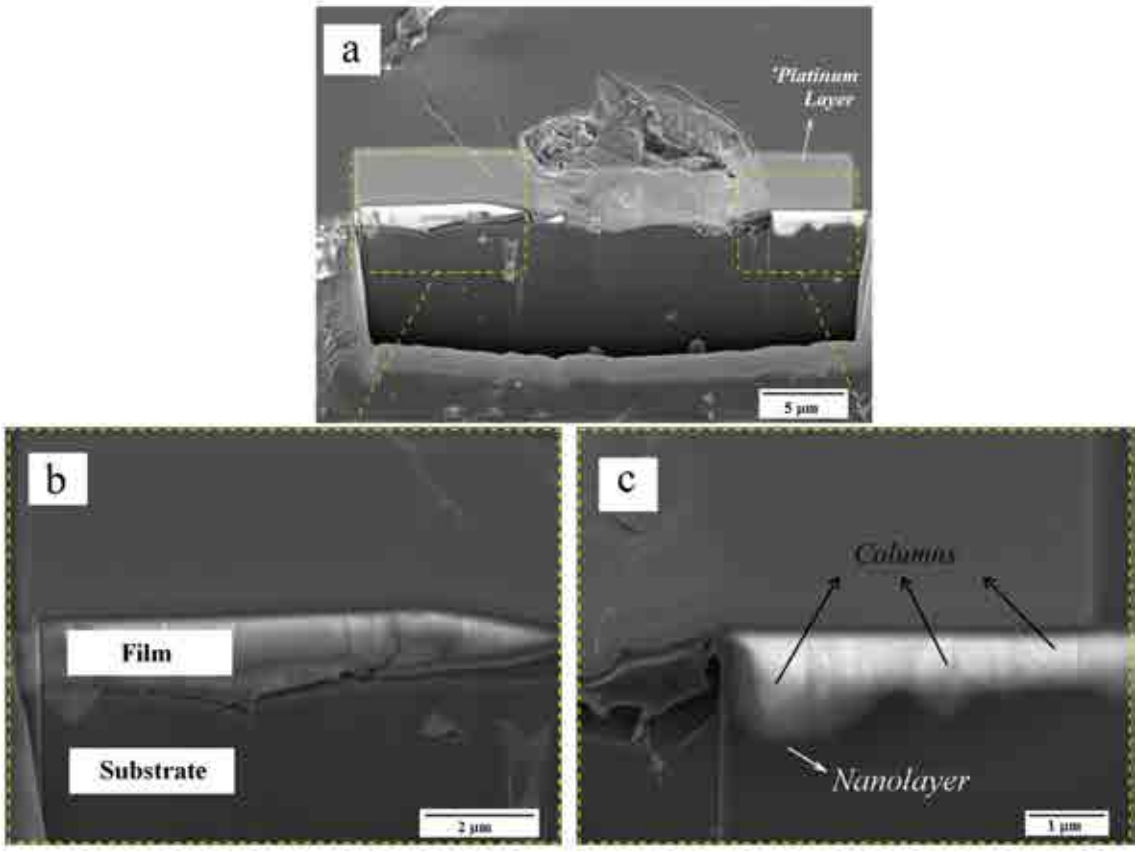

Figure 6. (a) FIB cross-section of a Berkovich nanoindentation performed on sample *M3thin* at h_{max} = 1000 nm. Higher magnification micrographs of the (b) left and (c) right sides of the imprint cross-section.

On the other hand, in the case of the indentation at $h_{max}/t \approx ½$ (Figure 6), the absence of any chipping or cracking at both surface and subsurface levels is clearly evident. At this relative depth, only inelastic deformation, in the form of residual indentation imprints in the film, can be observed. Therefore, the integrity of the system is kept throughout the tests.

This mechanical integrity is thus expected to be retained at the lower penetration depth indentation used in this investigation, i.e. $h_{max}/t \approx 1/10$ (h_{max} = 100 nm), validating the use of the properties measured from these nanoindentations for further evaluation of E_f and H_f.

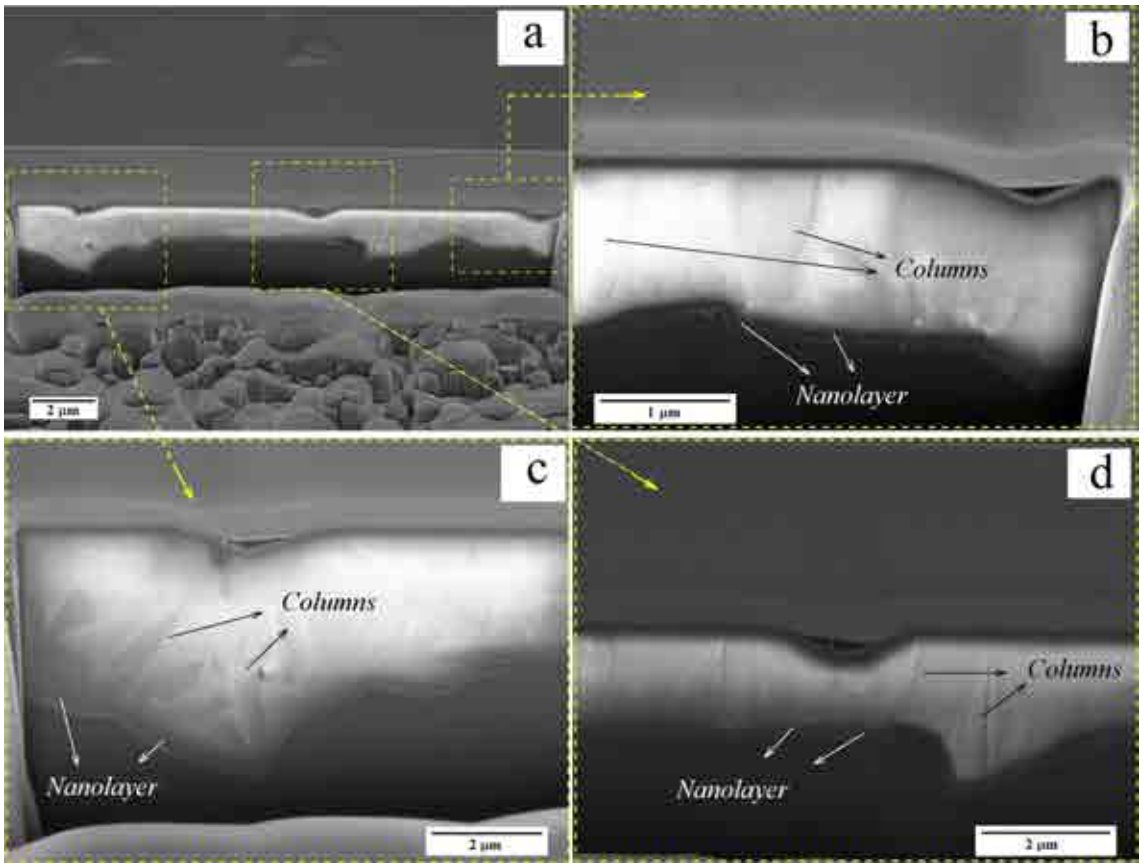

Figure 7. (a) FIB cross-section of three Berkovich nanoindentations performed on sample *M3thin* at h_{max} = 500 nm. (b-d) Micrographs corresponding to cross-section of individual imprints.

Average H_a and E_a curves measured for the $3Al_2O_3{\cdot}2SiO_2$ film from the Berkovich indentations at h_{max} = 1000 nm (a), h_{max} = 500 nm (b) and h_{max} = 100 nm (c), are shown in Figure 8.

At penetration depths lower than h = 200 nm, H_a values remain practically stable and independent of h for all the indentations. However, there is a significant increase in the H_a values for h > 200 nm, as a consequence of the influence from the stiffer SiC substrate underneath the $3Al_2O_3{\cdot}2SiO_2$ film (Figure 8 b-c).

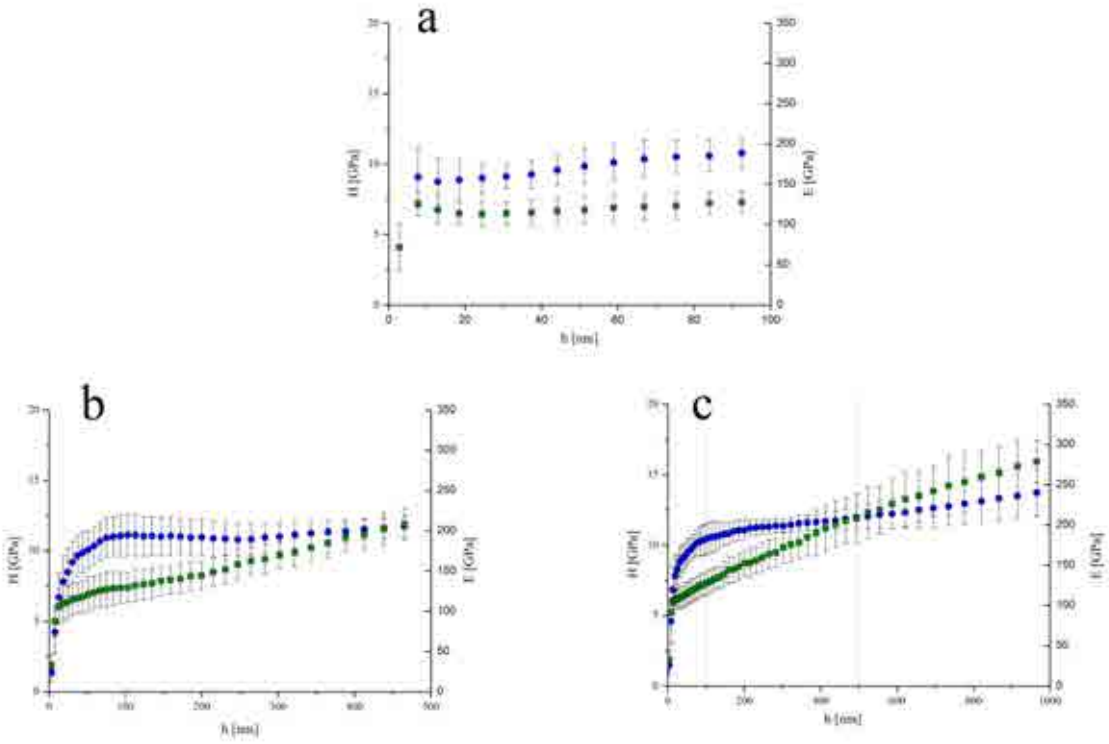

Figure 8. Apparent hardness H_a (left vertical axis) and E_a (right vertical axis) as a function of penetration depth for (a) h_{max} = 100 nm, (b) h_{max} = 500 nm and (c) h_{max} = 1000 nm.

Different from H_a values, E_a increases with h from the beginning of the indentation regime, due to the strong influence of the SiC substrate elastic field, as it is clearly observed in Figure 8 b-c. This behavior can be ascribed to the higher elastic

deformation field involved in stiffness calculation relative to the plastic one involved in hardness evaluation. Hence, measured E_a values should not be directly taken as the intrinsic film stiffness, E_f, and further analysis should be carried out on its deconvolution. The average H_a and E_a values and standard deviations attained for the different indentations are listed in Table 2.

	h_{max} = 100 nm	h_{max} = 300 nm	h_{max} = 1000 nm
H [GPa]	10 ± 1	11 ± 1	11 ± 1
E [GPa]	120 ± 16	149 ± 19	177 ± 22

Table 2. Average values of the apparent H_a and E_a for the indentations measured at different maximum penetration depths.

4.3.3 Spherical nanoindentation stress-strain curves

Nanoindentations using a spherical indenter were performed on the films at P_{max} = 300 mN. During the spherical indentation process, the initial contact is elastic, reaching elasto-plastic regime after a certain pressure. Following the procedure described in the literature for data analysis within the elastic regime[10–13], the Hertz and Sneddon formulations yield equation 4.1, in which the indentation stress, $P/\pi a_c^2$, is equated to the indentation strain, a_c/R_{sph}, according to:

$$\frac{P}{\pi {a_c}^2} = \frac{4}{3\pi} E_{red} \left(\frac{a_c}{R_{sph}}\right) \qquad \textbf{Equation 4.1}$$

The contact radius a_c can be calculated[24] in the elasto-plastic regime from the direct stiffness measurement obtained using the Continuous Stiffness Measurement (CSM) modulus, and the E_{red} corresponds to the reduced elastic modulus from the mentioned material-indenter couple.

By using equation 4.1, an indentation stress-strain curve can be constructed for each spherical nanoindentation test using the CSM modulus. The indentation stress-strain curves corresponding to different tests conducted on the film are plotted in Figure 9 for the first 150 nm of the penetration process. Curve fitting of the linear region of the curves is plotted in the same figure. In addition, a 3D-AFM micrograph of a residual spherical imprint is also included as an inset in Figure 9.

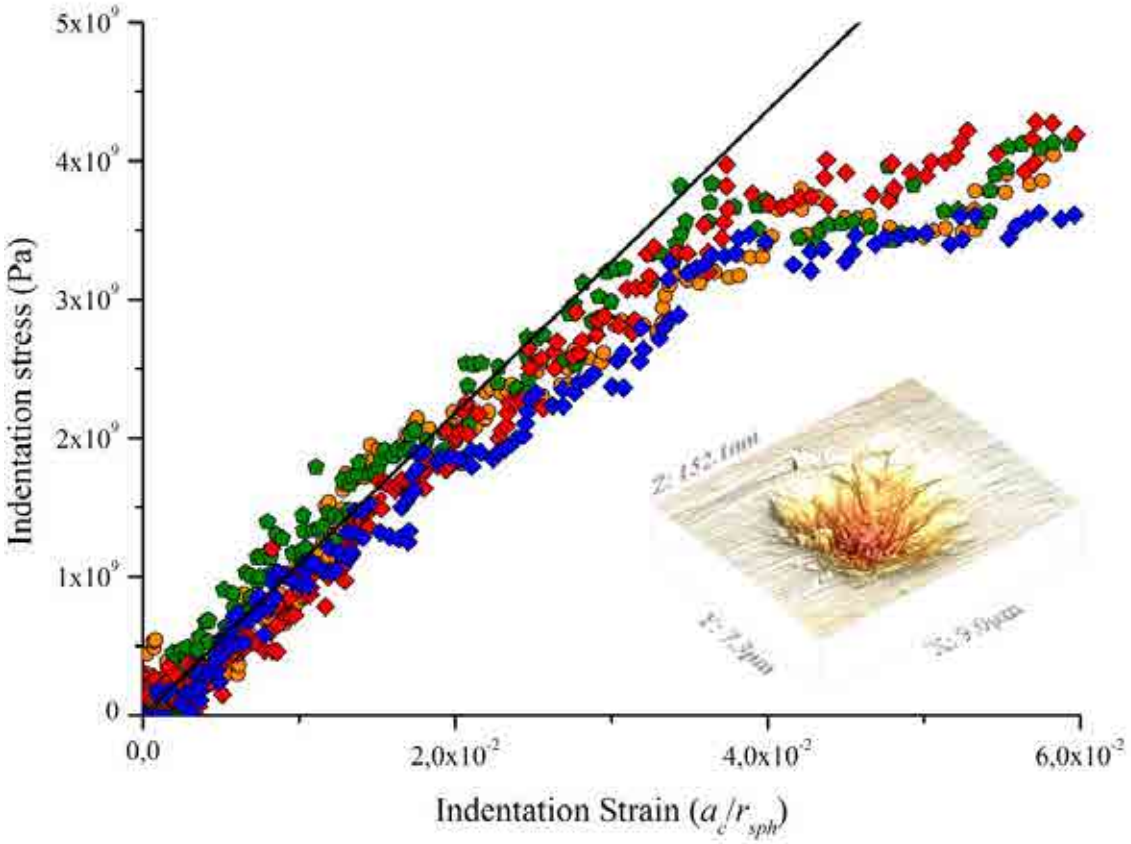

Figure 9. Spherical nanoindentation stress-strain curves, and fitting line for the first 150 nm of penetration. The inset image corresponds to a 3D AFM micrograph of a residual spherical nanoindentation imprint performed in the film at a load of 300 mN.

4.3.4 Intrinsic hardness, elastic modulus and yield strength of the $3Al_2O_3{\cdot}2SiO_2$ film

In order to evaluate the intrinsic mechanical properties of the $3Al_2O_3{\cdot}2SiO_2$ film, it is important to analyze the scenario in which the indentation process occurs in the $3Al_2O_3{\cdot}2SiO_2$/SiC system of sample *M3thin*. Considering the penetration depth-to-film

thickness ratios implemented for Berkovich nanoindentations ($h_{max}/t \approx 0.1$, 0.5 and 1) as well as the relatively rigid and hard nature of the SiC substrate (E_s = 410 ± 35 GPa, H_s = 34 ± 5 GPa), it must be pointed out that the apparent response measured when indenting the film is affected by the supporting substrate. Thus, any film property evaluation should take into account the SiC substrate influence. Besides, the residual stresses (σ_r) generated in the $3Al_2O_3{\cdot}2SiO_2$ film (due to CTE mismatch) during the cooling stage of the CVD process, are expected to have an additional effect on the apparent response measured by indentation. Two factors need to be taken in this regard: (*i*) the CTEs of mullite and SiC are quite similar ($\alpha_{mullite}$ = 4.80 x10^{-6} °C^{-1} and α_{SiC} = 5.05 x10^{-6} °C^{-1}), and consequently σ_r may be estimated to be just about 40 MPa, and (*ii*) it has been demonstrated that residual stresses have a negligible effect on the hardness and modulus measured by nanoindentation[25], if its value is not similar to or higher than the hardness of the material. Based on these considerations, the influence of residual stresses in the film was disregarded in evaluating H_f and E_f.

Considering the experimental fact that H_a remains practically independent of the penetration for the first 200 nanometers, and according to the 10% rule for the indentation of coatings, measured H_a values at h_{max} = 100 nm may be directly considered as the intrinsic hardness values of the film (H_f = 10 ± 1 GPa). This value is in good agreement with the H values reported in the literature for stoichiometric mullite[26–28].

However, as it was mentioned in the previous section, the intrinsic stiffness of the $3Al_2O_3{\cdot}2SiO_2$ film should not be taken directly from the E_a values obtained from the Berkovich nanoindentation tests. Consequently, it is necessary to deconvolute the E_f value by using proposed literature models for analyzing indentation data in the coated systems. In this investigation, the models considered for such a purpose correspond to those proposed by Song and Pharr[3,5,6], Bec *et al.*[7], Saha and Nix[4], and Hay and Crawford[9]. In general terms, all of them use the already known substrate stiffness (E_s) to deconvolute the intrinsic film (E_f) from the apparent measured response (E_a). Accordingly, in this investigation such models are implemented on the basis of the measured E_a values, as well as of the E_s ones already determined for the substrate.

Average curves of the reduced E_f, deconvoluted by using the referred thin film models, together with the reduced E_a are plotted in Figure 10 a-c for indentations at h_{max} = 1000 nm (a), h_{max} = 500 nm (b) and h_{max} = 100 nm (c).

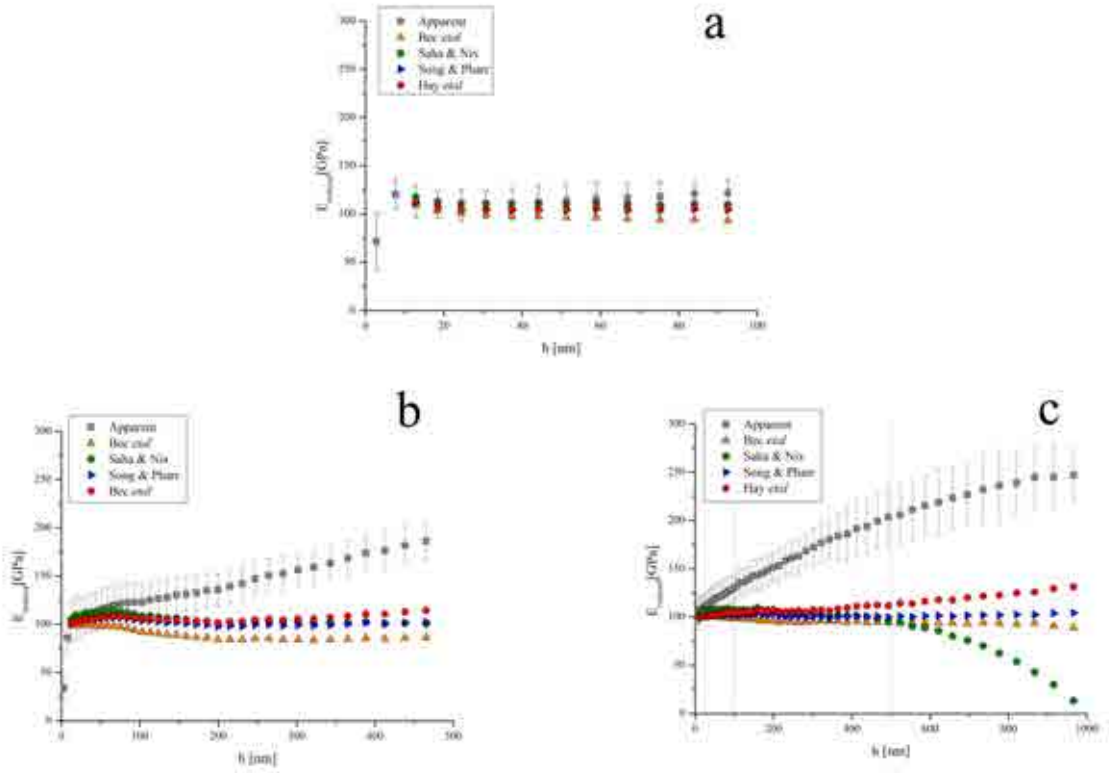

Figure 10. Average curves of the reduced apparent elastic modulus E_a and its standard deviation, together with the reduced E_f predicted by the implemented models, as a function of penetration depth for (a) h_{max} = 100 nm, (b) h_{max} = 500 nm and (c) h_{max} = 1000 nm.

It is clear that implementation of all the models yields an E_f value not only lower than the one calculated for E_a but also independent of the penetration depth. Apart from the depletion of the modulus values exhibited by the Saha and Nix model at penetrations close to the film thickness (h > 500 nm, Figure 10 c), it can be highlighted that all the models work reasonably well for the different indentations performed. Therefore, the deconvoluted E_f values in the penetration range below h = 500 nm can be considered as reliable and valid estimations of the intrinsic stiffness of the $3Al_2O_3{\cdot}2SiO_2$ film. The average E_f values obtained with the different models in the first 500 nm of penetration,

together with the standard deviation of the measurements, are presented in Table 3. From this data it may be stated that intrinsic elastic modulus of the $3Al_2O_3{\cdot}2SiO_2$ film (E_f) is in the range between 100 and 145 GPa.

	$E_{AVERAGE}$ [GPa]
Apparent	144 ± 19
Bec *et al.* [7]	114 ± 15
Saha & Nix [4]	130 ± 17
Song & Pharr [3,5,6]	125 ± 16
Hay *et al.* [9]	129 ± 17

Table 3. Apparent E_a values measured experimentally with its standard deviation, together with the average intrinsic film E_f values as deconvoluted from different models used.

Assessment of E_f may also be approached on the basis of the linear stress-strain data, corresponding to the first nanometers of penetration (Figure 9), attained in the spherical indentation tests. This behavior can be directly affiliated to the elastic indentation regime. It should be pointed out that the indenter penetration in such regime is quite low relative to the film thickness ($h < 0.08t$). Accordingly, it can be speculated that the influence of the elastic field of the SiC substrate underneath is consequently low, and the obtained elastic response arises for the most part from the $3Al_2O_3{\cdot}2SiO_2$ film. A linear regression analysis was performed on the elastic part of the curves, and the resulting fitting line is included in Figure 9. The slope of this line may thus be related with the intrinsic elastic modulus of the $3Al_2O_3{\cdot}2SiO_2$ film, yielding an effective value of 110 GPa. This E_f estimation from spherical indentation data is indeed within the range of values previously determined through Berkovich indentation, and it is particularly coincident with the one deconvoluted through the model of Bec *et al.* ($E_f \approx 114$ GPa).

In general, it can be concluded that elastic modulus values evaluated in this work fall in the lower part of the range of E values reported in the literature for stoichiometric mullite obtained by different techniques ($E \approx 140$ - 230 GPa)[29].

Finally, from the curves of Figure 9 the point at which the stress-strain curves deviate from linearity may also be distinguished. It denotes the transition from elastic into elasto-plastic indentation behavior; and therefore, the stress at such point can be directly linked to the indentation yield strength (σ_y) of the $3Al_2O_3{\cdot}2SiO_2$ film. Taking into account the data corresponding to the different curves, it may be discerned that $\sigma_y \approx 3.5$ GPa. To the best knowledge of the author of this thesis, there is not any report in open literature for σ_y values of stoichiometric $3Al_2O_3{\cdot}2SiO_2$ films. However, the calculated σ_y is in accordance with the Tabor's equivalence between yield strength and hardness for ceramic materials $H \approx (2\text{-}4){\cdot}\sigma_y$. Similar relationships are reported from spherical nanoindentation conducted on other ceramic materials[30].

4.3.5 Hardness and elastic modulus of $3Al_2O_3{\cdot}2SiO_2$ thick coatings

Hardness and elastic modulus of stoichiometric mullite coatings were also calculated in thick coated specimens. The *P-h* curves corresponding to the Berkovich indentations performed at h_{max} = 100 nm, 300 nm and 2000 nm in sample *M3-I* are presented in Figure 11 (a,b and c respectively).

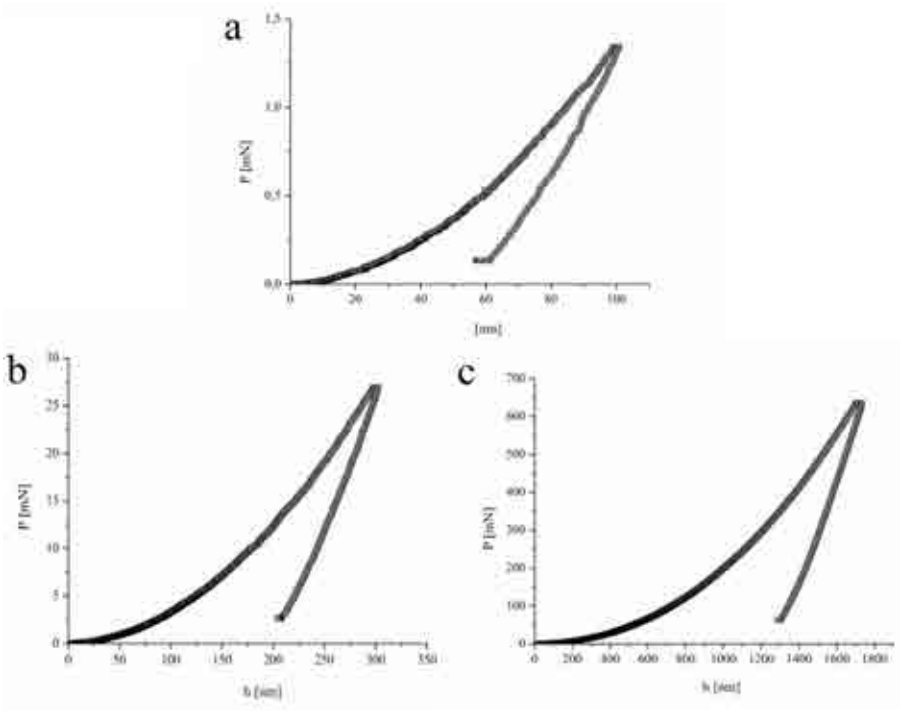

Figure 11. P-h curves of indentations performed at (a) h_{max} = 100 nm, (b) h_{max} = 300 nm, and (c) h_{max} = 2000 nm on the polished top surface of sample *M3-I*.

As it is evident from these curves, there are no significant discontinuities along the loading or unloading stages of the tests for any of the penetration ranges evaluated. This observation could suggest the absence of fracture events in the $3Al_2O_3{\cdot}2SiO_2$ coatings throughout the tests. The imprints of some of the indentations performed at 2000 nm for the H_f and E_f measurement are displayed in the micrographs of Figure 12. The transparence of the polished mullite coating is evident in the optical micrographs of Figure 12 a-b, as some of the features of the substrate underneath the coating may be discerned at the background of the figures. It is also clear from these micrographs the absence of any important damage on the coating at the surface or subsurface level.

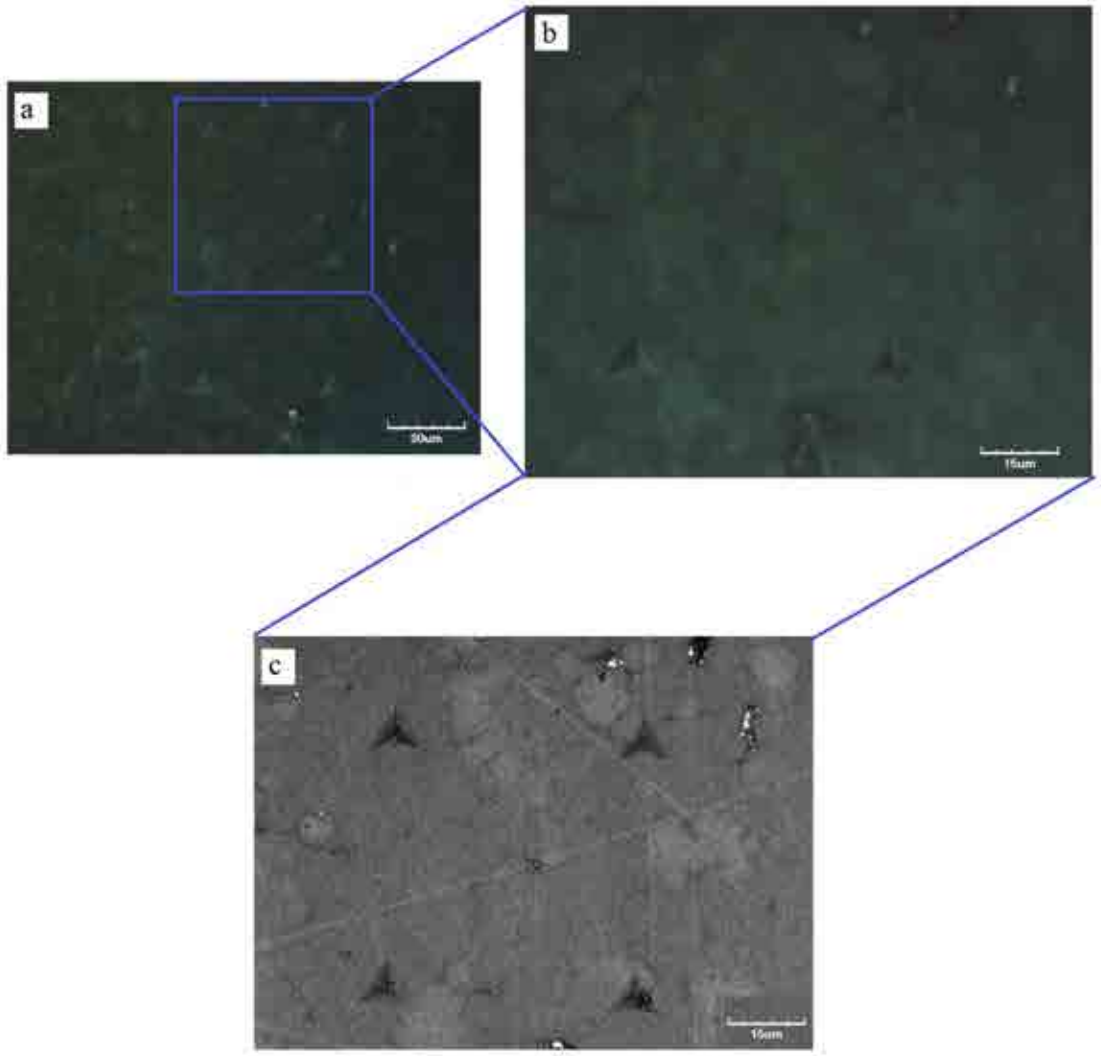

Figure 12. Optical micrographs of a matrix of Berkovich nanoindentations at (a) h_{max} = 2000 nm on the polished top surface of sample *M3-I*. (b) Optical and (c) LSCM micrographs at higher magnification of the same matrix of indents.

Moreover, to avoid the interference of the underlying substrate on the visualization of the indentation imprints at the surface level, LSCM images of the imprints were acquired, as it is presented in Figure 12 c. It can also be observed from this image the absence of coating failure at the surface. Since no apparent damage within the coating is evidenced from the referred micrographs after indentations at h_{max} = 2000 nm, it may be inferred that the integrity of the coatings is kept during the indentation tests at the lower penetration levels implemented (h_{max} = 300 nm and 100 nm). This observation together with the uniformity of the previously referred *P-h* curves, validate the reliability of the extracted data for the calculations of H_f and E_f.

Figure 13 and 14 include the curves of *H* and *E* (respectively) corresponding to four nanoindentations in sample *M3-I*.

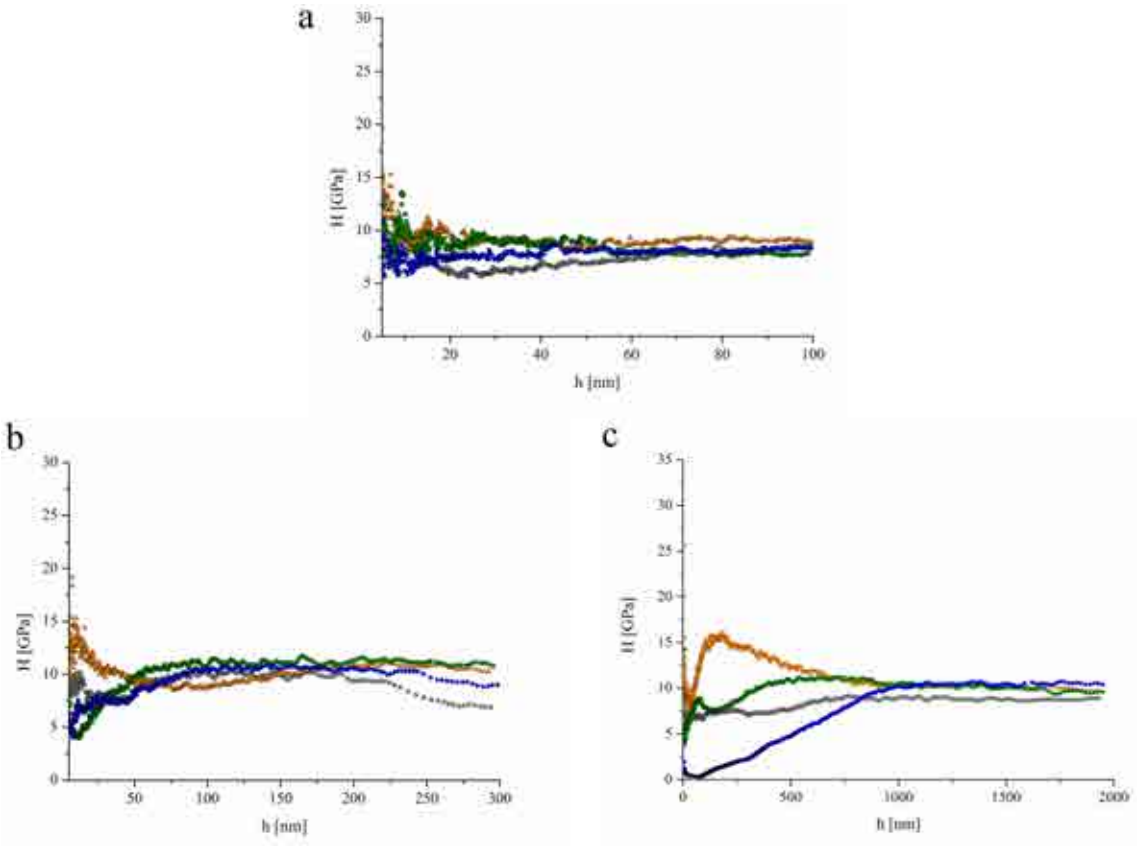

Figure 13. Curves of *H* vs *h* corresponding to 100 nm (a), 300 nm (b), and 2000 mm (c) penetration depths. Nanoindents were performed on the polished top surface of sample *M3-I*.

Such properties are plotted as a function of the penetration depth *h* for tests conducted at different values of h_{max}. Similarly, the average values of *H* and *E* obtained from the unloading part of the nanoindentation tests are included in Table 4. Concerning the hardness calculation, curves given in Figure 13 present great stability as the indenter penetrates, with little dispersion among tests. As it can be observed from these curves, and from Table 4, the intrinsic hardness of the stoichiometric $3Al_2O_3{\cdot}2SiO_2$ may be estimated as $H_f \approx$ 10 GPa. This value is coincident with the ones found for the hardness of $3Al_2O_3{\cdot}2SiO_2$ thin films presented in section 4.3.4, as extracted using the rule of the 10% for the indentation of coatings.

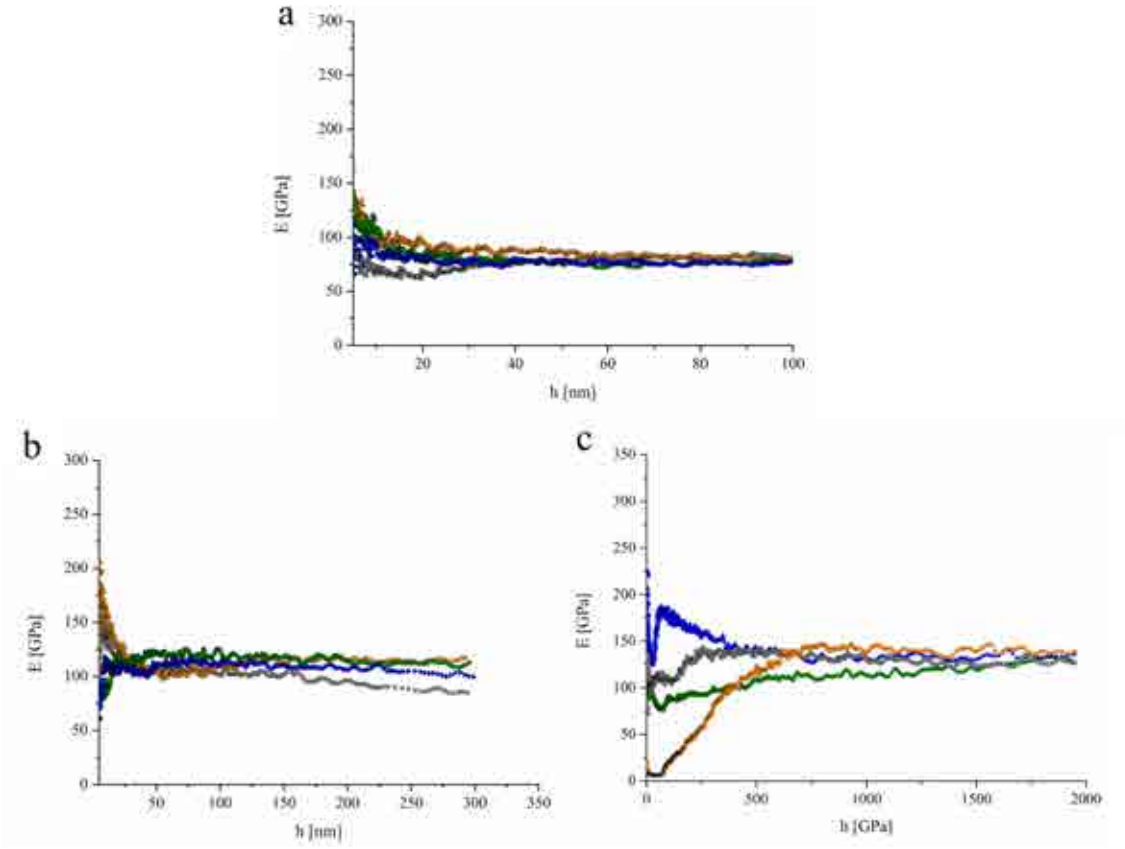

Figure 14. Curves of *E* vs *h* corresponding to (a) 100 nm, (b) 300 nm, and (c) 2000 mm penetration depth nanoindents. Tests were performed on the polished top surface of sample *M3-III*.

Regarding the estimation of the intrinsic elastic modulus of $3Al_2O_3{\cdot}2SiO_2$ thick coatings, curves in Figure 14 exhibit, similarly to the case of hardness, a very slight

variation among the different tests for every condition of h_{max} evaluated. They also present great stability along the whole penetration range studied, indicating the homogeneity of the coating within the tested volume. The absence of a significant increase in E values as the indenter penetrates, even for the h_{max} = 2000 nm condition, could be attributed to a minor effect of the underlying substrate on the indentation response. This can be asserted as the SiC substrate properties referred in section 4.3.1, also measured through nanoindentation, correspond to higher stiffness and hardness values in comparison to the ones of the $3Al_2O_3{\cdot}2SiO_2$ coating, (H_s = 34 ± 5 GPa, and E_s = 410 ± 35 GPa).

Accounting for the different penetrations implemented (see Figure 14), the average intrinsic elastic modulus of the stoichiometric $3Al_2O_3{\cdot}2SiO_2$ films may be estimated as $E_f \approx$ 130 GPa. This value is also coincident with the ones previously found for $3Al_2O_3{\cdot}2SiO_2$ thin films, as deconvoluted using different indentation thin film models.

	h_{max} = 100 nm	h_{max} = 300 nm	h_{max} = 2000 nm
***H* [GPa]**	11 ± 3	10 ± 2	9 ± 1
***E* [GPa]**	119 ± 37	127 ± 14	134 ± 5

Table 4. Average H and E of samples *M3-I and M3-III*, evaluated during the unloading part of the nanoindentation tests at different h_{max}.

4.4 Structural integrity and mechanical performance of the system $3Al_2O_3{\cdot}2SiO_2$/SiC

4.4.1 Nanoindentation tests

4.4.1.1 Surface characterization of fracture evolution

Radial cracks emanating from the corners of imprints were evident at the surface of $3Al_2O_3{\cdot}2SiO_2$ thin films for the entire load spectrum analyzed (P_{max} = 20 mN, 30 mN,

35 mN, 40 mN, 50 mN, and 70 mN). The progression of surface damage around these imprints, attained by using cube corner tips, was tracked by means of 3D-AFM micrographs, and an example sequence is given in Figure 15 a-e. Length *c* of such cracks was found to increase with load *P*, and material pile up around the imprints was evidenced from both the micrographs and the pile up profiles of Figure 15. It is important to mention that an incipient secondary cracking was observed for some of the indentations performed at P_{max} = 50 mN (Figure 15 d), and the onset of film spalling was evidenced for the indentation at P_{max} = 70 mN (Figure 15 e).

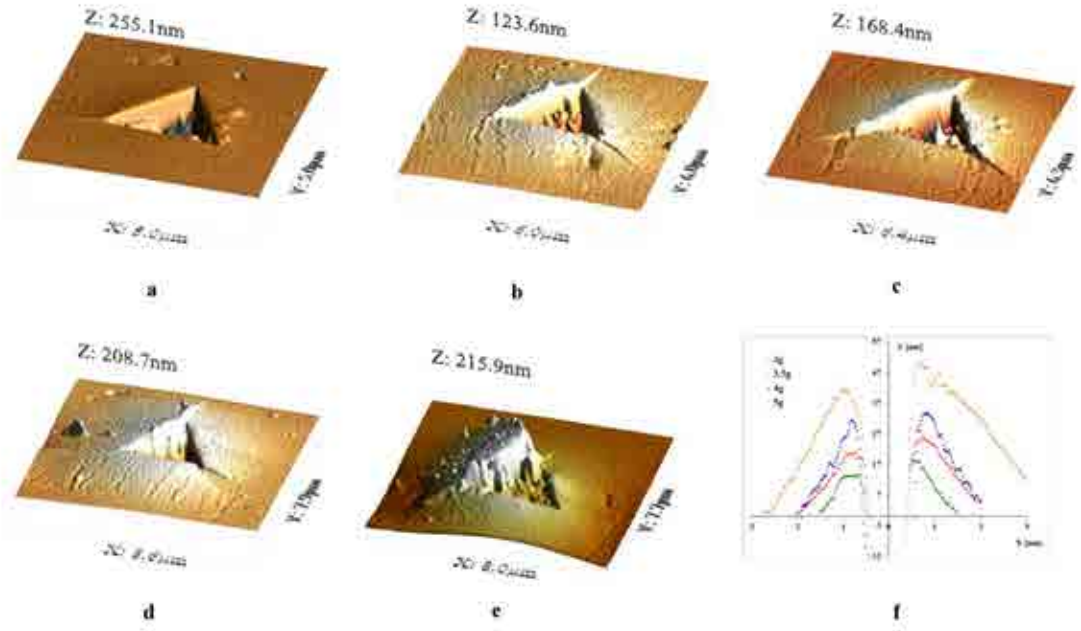

Figure 15. Sequence of 3D-AFM micrographs depicting the evolution of surface damage induced by cube corner nanoindentations at loads of (a) P_{max} = 30 mN, (b) 35 mN, (c) 40 mN, (d) 50 mN and (d) 70 mN. Pile up profiles measured at a distance of 2/3 *c* for indents corresponding to applied loads of 30 mN, 35 mN, 40 mN and 50 mN.

4.4.1.2 Characterization of subsurface damage in thin films

Examination of the damage at the subsurface level is essential to evaluate the character and magnitude of the cracks produced by the cube corner indenter, and to observe their interactions with the film/substrate interface and/or with the substrate.

Sequential FIB cross-sectioning through a volume comprising the imprints and surrounding cracks was performed for different levels of applied load. SEM images were taken during the process, as presented in Figure 16 a-f for indentations at P_{max} = 30 mN (a-c) and at P_{max} = 50 mN (d-f). In the former case, cracks arising from the imprint corners observed at the surface level are contained within the $3Al_2O_3{\cdot}2SiO_2$ film and do not progress either into the SiC substrate and/or through the interface. In the case of P_{max} = 50 mN, cracks are deflected and propagate through the interface as it can be observed in Figure 16 d-e.

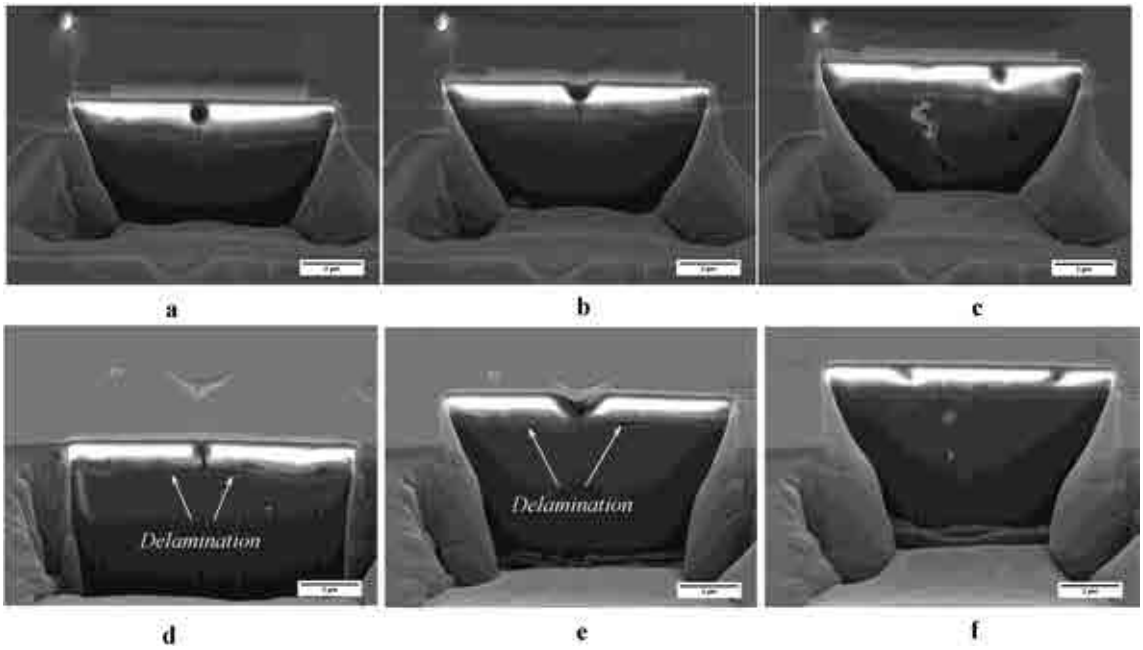

Figure 16. SEM images corresponding to different stages of the FIB sputtering process. Indentations at (a-c) P_{max} = 30 mN and (d-f) 50 mN.

In Figure 17 a-f**,** the oblique (a,d), top (b,e), and frontal (c,f) views of the 3D-FIB tomographies constructed for indentations at P_{max} = 30 mN (a-c) and 50 mN (d-f) are shown. In all these images, indentation imprint, cracks and substrate-coating interface may be clearly identified.

As it was previously mentioned, the 3D-FIB tomographies shown in Figure 17 a-c support the statement that cracks remain confined in the film and do not propagate any further in the case of P_{max} = 30 mN. These radial cracks emanating from the imprint corners are parallel to the load axis, and correspond to a semi-elliptical crack configuration.

Residual stresses due to the plastic deformation results in crack arrest underneath the imprint. Similar visual analysis allows the observation that for P_{max} = 50 mN cracks propagate through the interface generating a quasi-circular delamination area. Such description becomes completely clear from the top view of Figure 17 e. Finally, the onset of an incipient secondary crack in the tomography of the indentation at P_{max} = 50 mN is also discerned.

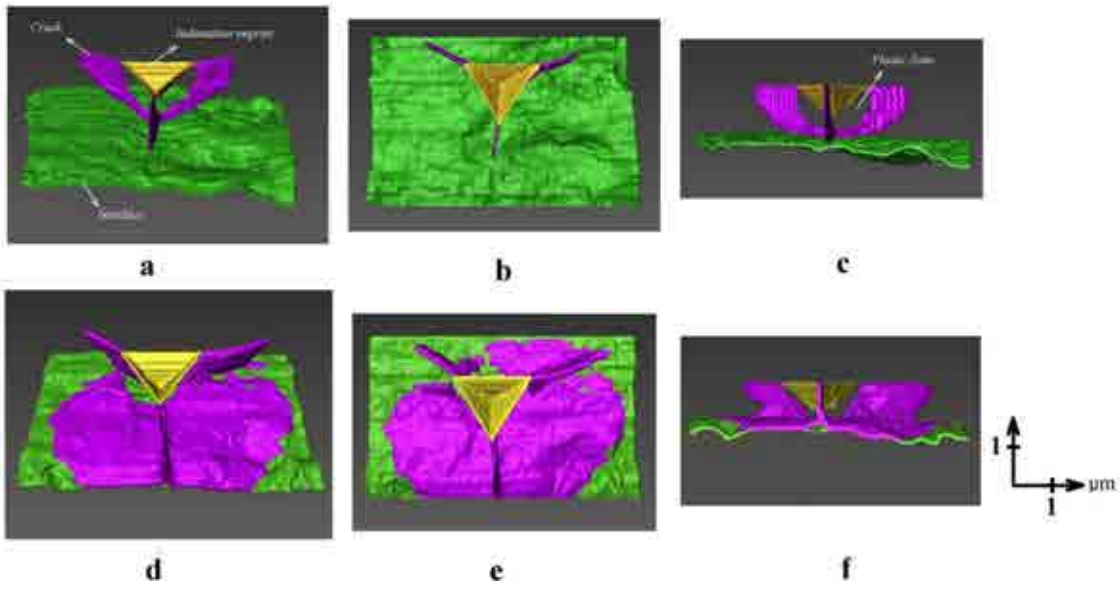

Figure 17. (a,d) Oblique, (b,e) top and (c,f) frontal views of the 3D FIB tomographies constructed for indentations at (a-c) P_{max} = 30 mN and (d-f) 50 mN.

4.4.1.3 Fracture toughness of the $3Al_2O_3{\cdot}2SiO_2$ thin film

Nanoindentations performed using Berkovich and spherical tips induced elastic and inelastic deformations whose extents may be rationalized on the basis of the determined E_f, H_f and σ_y parameters. On the other hand, nanoindentations using cube corner indenters promoted cracks in the $3Al_2O_3{\cdot}2SiO_2$ films, and the onset and propagation behavior of these damage features may be affected by the existing residual stresses (σ_r)[15]. Hence, in order to estimate the intrinsic film fracture toughness, K_f, the influence of σ_r should be considered, in addition to SiC substrate effects.

One of the most widely used methodology to calculate the fracture toughness of monolithic brittle solids (K_c) is the one proposed by Anstis *et al.*[31], given by equation 4.2:

$$K_c = \lambda \frac{P}{c^{3/2}} = \xi_v^R \left(\frac{E}{H}\right)^{1/2} \frac{P}{c^{3}/_{2}} \qquad \textbf{Equation 4.2}$$

where c is the crack length and ξ_v^R is a calibration coefficient depending on the type of indenter and crack geometry. For cube corner indenters, Pharr[32] has used the equation 4.2 with a ξ_v^R= 0.040 value. Moreover, to account for the residual stress influence on the fracture toughness, Marshall and Lawn[33] proposed a modification of Anstis *et al.* equation, as follows:

$$K_c^0 = K_c + K_{\sigma_r} = \xi_v^R \left(\frac{E}{H}\right)^{1/2} \frac{P}{c^{3/2}} + \psi_0 \sigma_r c^{1/2} \qquad \textbf{Equation 4.3}$$

In this equation, the fracture toughness corrected by the residual stresses effect (K_c^0) is equated as the sum of the stress intensity factor due to the indentation (K_c) plus the stress intensity factor due to σ_r (K_{σ_r}). The geometric factor ψ_0 = 1.29 corresponds to a semi-circular crack configuration.

Regarding the influence of the SiC substrate on K_f estimation, cracking extent as well as crack geometry deserves further analysis. In the particular case of the indentation at P_{max} = 30 mN, it must first be recalled that cracks generated were fully confined within the mullite film, as was plainly visible from the 3D-FIB tomographies of Figure 17 a-c. However, these cracks seem to be arrested at the interface, and their geometry appears altered from the ideal semi-circular half penny shape into a deformed semi-elliptical one, as detailed in Figure 18.

Thus, an increase in the ellipticity of the crack (e), where $e = c/a$ and a denotes the median crack extent, is evidenced. The increase in e reflects the relevant influence of the stiffer SiC substrate on both crack generation (due to the mismatch in the elastic-to-inelastic deformation) as well as on crack propagation (because the constraining effect on the crack once formed)[34]. To account for such substrate effects, the stress intensity factors K_c and K_{σ_r} of equation 4.3 must be modified by the F_c and f_{σ_r} correction factors respectively, yielding:

$$K_c^1 = F_c K_c + f_{\sigma_r} K_{\sigma_r} = F_c \xi_v^R \left(\frac{E}{H}\right)^{1/2} \frac{P}{c^{3/2}} + f_{\sigma_r} \psi_0 \sigma_r c^{1/2} \qquad \textbf{Equation 4.4}$$

where F_c can be calculated as a function of e, and f_{σ_r} can also be extracted as a function of e and the ratio a/t. From Figure 18, e and a/t values can be estimated yielding e =1.8 and a/t =1. The implementation of these parameters on the methodology proposed by Smith and Scatergood[34] permits the estimation of F_c = 1.037 and f_{σ_r}= 1.24. The fracture toughness corrected by both residual stresses and substrate influences (K_c^1) may now be calculated from equation 4.4 by using H_f and E_f (range) values determined before, together with P_{max} = 30 mN, c = 2.24 µm, F_c = 1.037 and f_{σ_r}= 1.24, and ξ_v^R = 0.040. The calculated K_c^1 values are found to oscillate between 1.21 and 1.73 MPa·m$^{1/2}$.

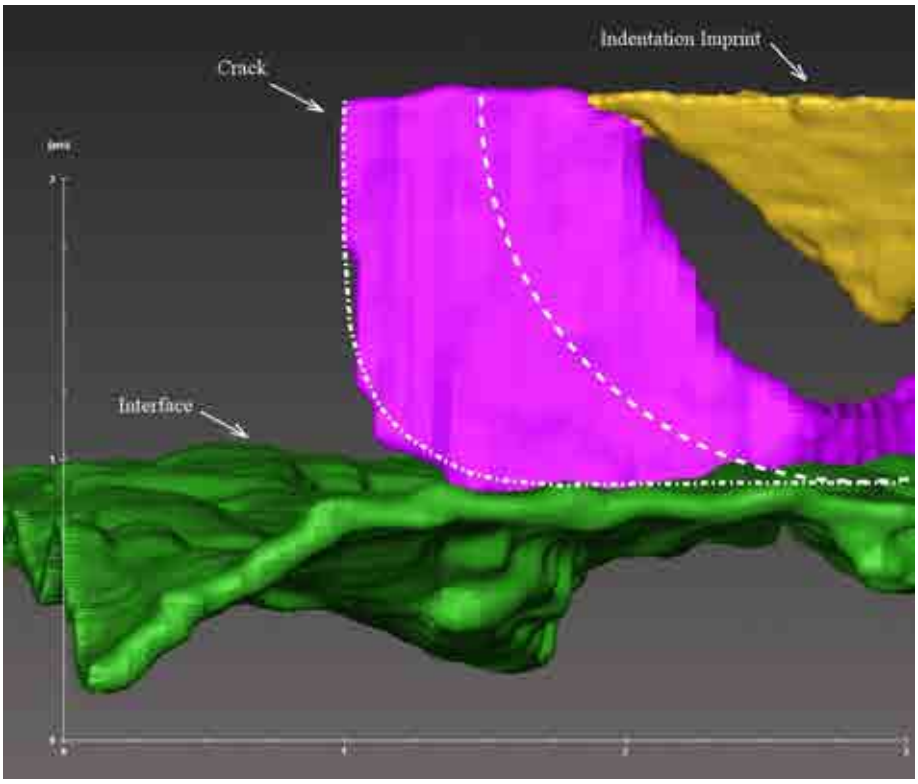

Figure 18. Detail of the 3D FIB tomography corresponding to the cube corner nanoindentation at P_{max} = 30 mN, showing the elipticity in one of the radial cracks.

As the influence of SiC substrate and residual stresses is considered in the analysis, the obtained K_c^1 values may be directly described as the intrinsic fracture toughness of the $3Al_2O_3{\cdot}2SiO_2$ thin film, K_f. As it was the case for the intrinsic stiffness determined above, these fracture toughness values are slightly lower than the ones previously reported by other research groups[29,35] for polycrystalline $3Al_2O_3{\cdot}2SiO_2$, $K_c \approx$ 2.0-2.5 MPa·m$^{1/2}$. Such slight discrepancies can be attributed to both the distinct microstructural features ascribed to the columnar nature of the $3Al_2O_3{\cdot}2SiO_2$ film, and the influence of the amorphous silicon matrix in which mullite columns are embedded.

4.4.1.4 Fracture toughness of thick $3Al_2O_3{\cdot}2SiO_2$ coatings

A general image of a matrix of cube corner indentations performed at increasing loads (20 mN, 30 mN, 40 mN and 50 mN), together with individual images of the imprints corresponding to each load level, are displayed in the AFM micrographs of Figure 19.

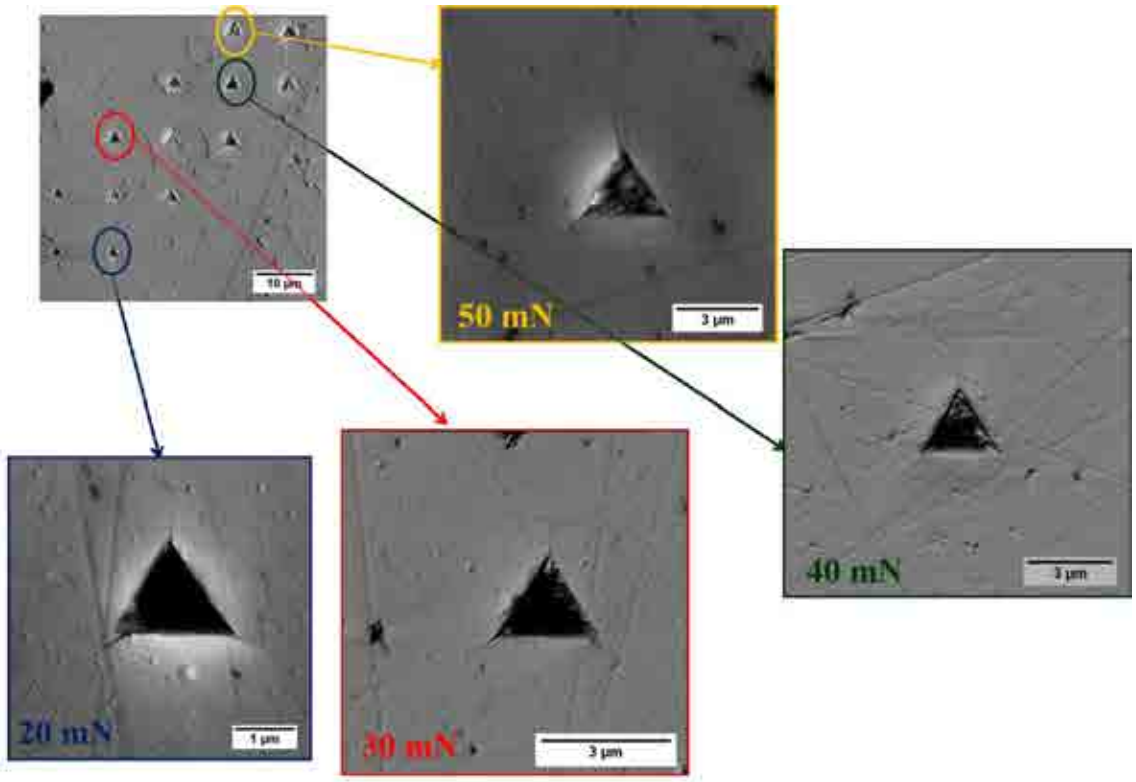

Figure 19. Matrix of cube corner indentations performed on the polished top surface of sample *M3-I*.

It should be highlighted that all the indentations induced radial cracks emanating from the corner of the imprints. From these images, crack lengths (c) of the different imprints were measured, and mean c values together with the standard deviation of their measurement are included in Table 5. In order to assess the fracture toughness of the coatings (K_f), the equation 4.3 was used. Accordingly, the condition of ideal straight superficial cracks that span at least twice the length of the imprint edges ($c \geq 2a$) was taken into account. It was found that only indentations in the range of loads between 30 mN and 50 mN produced cracks meeting such condition. Consequently, the indentations in this range were the ones used for K_f measurement.

By using crack length data presented in Table 5, together with the calculated H_f and E_f values, the load P_{max} applied in each case, and an indenter factor ξ_v^R of 0.040 for cube corner indenters, the intrinsic fracture toughness of the stoichiometric $3Al_2O_3{\cdot}2SiO_2$ coatings was calculated, yielding $K_f \approx 1.2$ MPa·m$^{1/2}$.

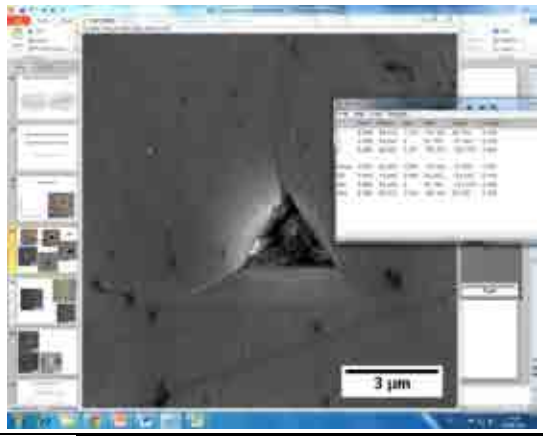

Load	**P = 3 gf**	**P = 4 gf**	**P = 5 gf**
c (µm)	2.3 ± 0.2	3,2 ± 0.6	3.7 ± 0.3
K^0_C (MPa·$m^{1/2}$)	1.3 ± 0.3	1.1 ± 0.3	1.1 ± 0.1

Table 5. Average cracks lengths measured from the cube corner indentations at different loads. Table summarizes measures in samples *M3-I and M3-III*.

4.4.1.5 Interface adhesion energy and fracture toughness

The mechanical properties of the interface were calculated in sample *M3thin*. From the 3D-tomography of the cube corner indentation at P_{max} = 50 mN (see Figure 17 d-f), it can be observed that the radial cracks induced by the indentation deflect at the interface and propagate afterwards, yielding as a result a delamination area with an approximately circular shape. Similar delaminated configurations, as induced by nanoindentation, have also been reported in the literature for comparable coated systems[18,36]. Thus, an equivalent delamination radius r_{del} may be calculated from Figure 17 e, r_{del} = 3.52 µm. In order to calculate the adhesion energy of the coated $3Al_2O_3{\cdot}2SiO_2$/SiC system, the expression proposed by Marshall and Evans[16] may be recalled for the calculation of G_{int} based on the analysis of thin film delamination induced by conical indenters:

$$\frac{G_{int}E_f}{(1-\upsilon_f)} = \frac{1}{2}t\sigma_1(1+\upsilon_f) + (1-\alpha)(h\sigma_r^2) - (1-\alpha)t(\sigma_1-\sigma_B)^2 \qquad \textbf{Equation 4.5}$$

where υ_f is the thin film poisson ratio (in this case $\nu_f = \nu_{mullite} = 0.25$), α is a factor accounting for film buckling ($\alpha = 1$ for the non-buckling fracture), σ_B is the Euler buckling stress, and σ_1 is defined by equation 4.6:

$$\sigma_1 = \frac{V_I E_f}{2\pi r^2 (1-\upsilon_f)} \qquad \textbf{Equation 4.6}$$

where V_I is the indentation volume. Through complementary use of surface AFM micrographs of the referred imprint and the constructed 3D-FIB tomography, the indentation volume was calculated as $V_I = 1.4\ \mu m^3$.

Based on the relatively low residual stresses value estimated for the film ($\sigma_r \approx 40$ MPa) as well as the insignificant buckling of the $3Al_2O_3{\cdot}2SiO_2$ film evidenced during the indentation process (see Figure 16 d-f), the α factor may be taken as 1; and therefore, the second and third terms of the right hand side of equation 4.5 can be neglected. By using this simplification, and including the obtained range of E_f values in equations 4.5 and 4.6, the energy release rate of the coated $3Al_2O_3{\cdot}2SiO_2$/SiC system yields a range of values for G_{int} between 21.3 and 30.9 $J{\cdot}m^{-2}$.

Extrapolating the relationship between G and K_c given by Evans and Hutchinson[37]:

$$K_{int} = \sqrt{\frac{G_{int} E_f}{(1-\upsilon_f{}^2)}}, \qquad \textbf{Equation 4.7}$$

the interfacial fracture toughness of the coated $3Al_2O_3{\cdot}2SiO_2$/SiC system K_{int} may be estimated as 1.5-2.2 $MPa{\cdot}m^{1/2}$.

Although there is a large dispersion of G_{int} and K_{int} values reported in the literature for coated systems of different nature[17,18], it should be underlined that the range of G_{int} and

K_{int} values found in this investigation are in the same order of magnitude of those reported for comparable ceramic coated pairs[18,38,39].

4.4.1.6 Fracture evolution on the $3Al_2O_3{\cdot}2SiO_2$/SiC system

The initiation and evolution of the fracture induced by the cube corner indentations on the $3Al_2O_3{\cdot}2SiO_2$/SiC system of sample *M3thin* can now be described on the basis of the properties evaluated in this investigation.

From very low applied loads (P_{max} = 20 mN) cracking is induced in the $3Al_2O_3{\cdot}2SiO_2$ films, accompanied by increasing piling up of material around the imprints over the complete spectrum of applied loads, as observed in the AFM micrographs of Figure 15. As the indentation load is increased, cracks propagate through the $3Al_2O_3{\cdot}2SiO_2$ film with the constraining effects exerted by the SiC substrate elastic field, until the cracks reach the $3Al_2O_3{\cdot}2SiO_2$/SiC interface at P_{max} = 30 mN (a/t = 1, see Figure 18). As the cracks are fully contained into the $3Al_2O_3{\cdot}2SiO_2$ film in this case case (P_{max} = 30 mN), it can be therefore expected that at a lower load (P_{max} = 20 mN) cracks are also confined into the film, and consequently, K_c^0 values should not diverge substantially.

When the propagating crack reaches the interface, further crack path is conditioned by the toughness competition between the interface and the substrate (K_{int} and K_{SiC}). Since the fracture toughness value of the rection bonded SiC, $K_{SiC} \approx 3.9$ MPa·m$^{1/2}$ is less energetically favorable path ($K_{int} < K_{SiC}$), the crack propagates at the interface. As expected, at higher loads the crack propagates through the interface, as observed in the case of P_{max} = 50 mN (Figure 17 d-f).

It must be mentioned that the onset of a minor secondary cracking was observed at P_{max} = 50 mN, as it can also be seen in Figure 17 e. It may be speculated that this secondary crack originates as a product of the brittle nature of the $3Al_2O_3{\cdot}2SiO_2$ film, and furthermore, due to its close toughness relative to the interface one, i.e. $K_f \sim < K_{int}$.

Further increases in indentation load exhibited more developed secondary cracking and the onset of film spalling, as it may be discerned in Figure 15 d-e. The failure mechanisms described in this work are very similar to the ones documented in the literature for brittle coatings on hard substrates[18,40].

4.4.2 Nanoscratch tests

4.4.2.1 Low load scratches in thin $3Al_2O_3{\cdot}2SiO_2$ film

The curves of penetration depth as a function of scratch distance are plotted in Figure 20 for three scratch tests performed at the low load condition.

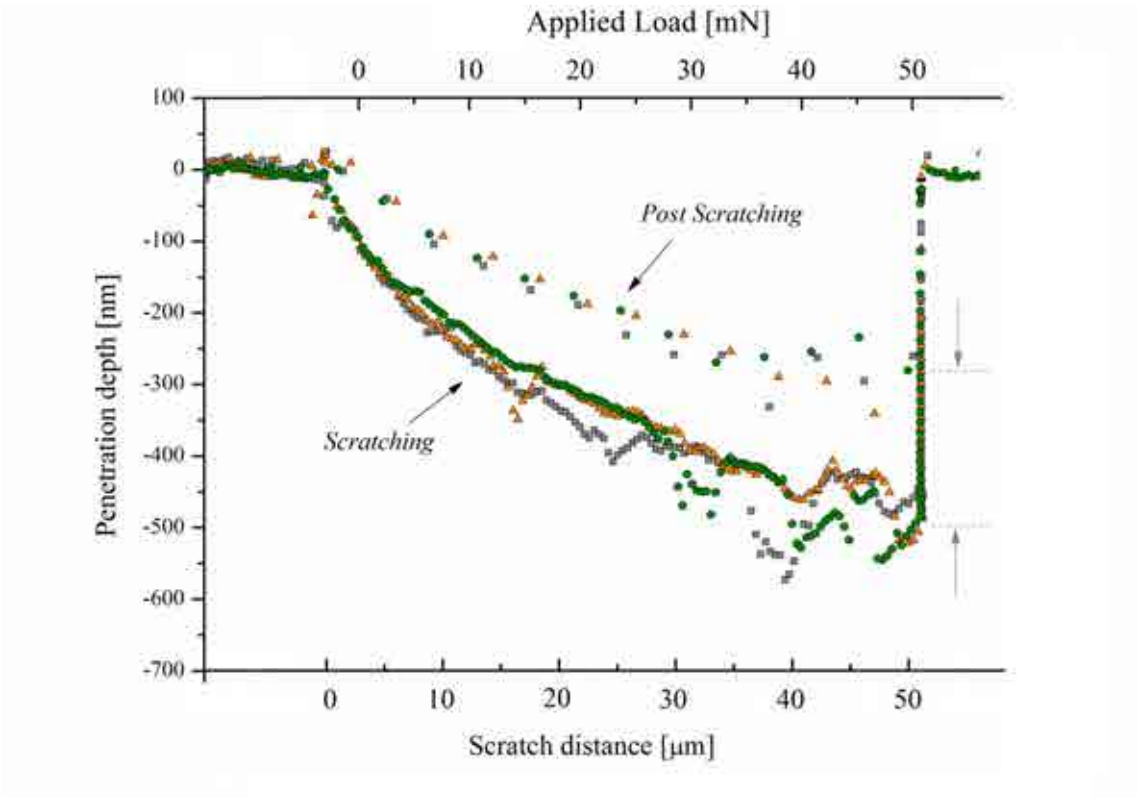

Figure 20. Penetration depth as a function of scratch distance and load for three scratches performed on sample *M3thin* at the low load condition.

These plots show a linear increase in the penetration as the indenter progress along the scratch track during the scratching and post scratching stages. As it may be observed in this figure, the curves are continuous and the lack of abrupt changes in penetration may indicate that films retain their integrity throughout the tests at the referred loading conditions. It can also be highlighted the considerable elastic recovery experienced by the film after the scratch test (40% at maximum load), denoted by the differences in the scratching and post scratching curves (indicated by the arrows at maximum load).

Imprints corresponding to the scratches performed at the low load condition are presented in Figure 21.

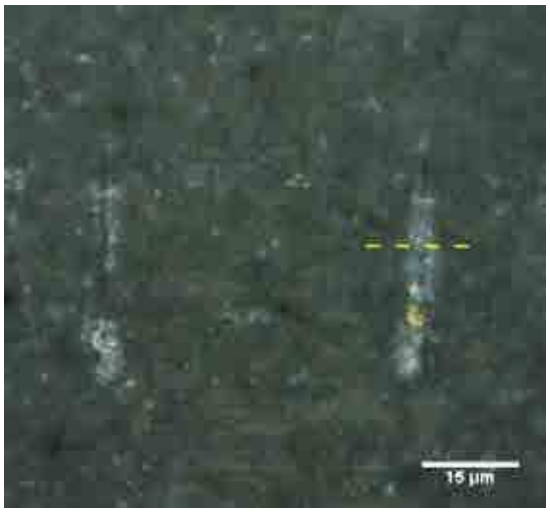

Figure 21. Optical micrograph corresponding to the scratch imprints performed at the conditions P_{max} = 50 mN – l_{max} = 50 µm.

The transparence of the polished mullite coating is evident from the image, as some of the features of the substrate underneath the coating may be discerned at the background of the micrograph. It is also evident from this image the absence of any failure in the film such as spallation, chipping or cracking at the surface level, denoting a good tolerance of the $3Al_2O_3{\cdot}2SiO_2$films to the normal and lateral forces imposed by the indenter during the scratching process.

However, from the same image it is difficult to discern if the scratches induced any damage below the surface of the film. Consequently, a cross-section was performed approximately in the center of one of the scratch tracks ($l \approx 25$ µm, and $P \approx 25$ mN), as indicated by the dotted line of Figure 21. This cross-section is presented in the micrograph of the Figure 22 a together with the magnification of a zone corresponding to the center of the scratch track, see Figure 22 b.

The micrograph of Figure 22 a confirms the lack of cracking or coating removal around the scratch track at the surface level. On the other hand, aiming to analyze the coated system at the subsurface level, the cross-section image of Figure 22 b show the entire coating thickness as well as some portion of the SiC substrate. Two cracks are evident in this micrograph. One is a small radial crack located within the coating, right beneath the center of the scratch track, and similar to the ones produced by the cube corner indenter referred in the previous section. This crack is contained within the film and do not progress either into the substrate or along the interface. The second one is a lateral crack located within the SiC substrate following an intergranular path, which coincides with the interface in one of the sides of the scratch track.

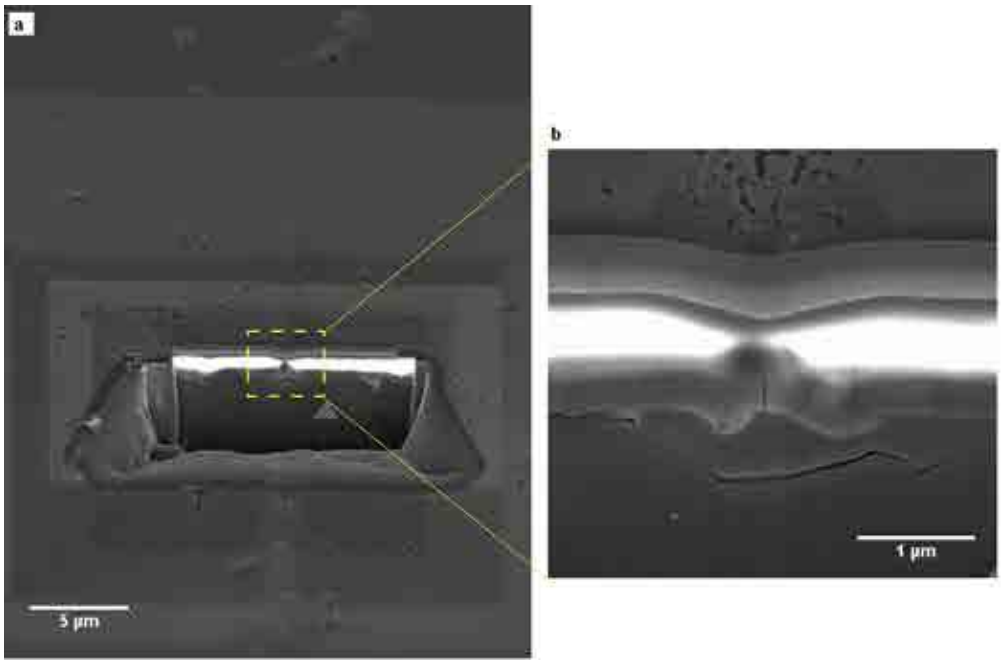

Figure 22. FIB cross-section performed at the midpoint of the scratch length for the scratch at (a) P_{max} = 50 mN – l_{max} =50 µm. (b) Magnification of the cross-section at the center of the track.

4.4.2.2 High load scratches in thin $3Al_2O_3{\cdot}2SiO_2$ film

The imprints of two of the scratches conducted on sample *M3thin* at the high load condition are presented in Figure 23. In this case, two damage features are evident in the scratch imprints. At lower loads, a well-marked "bright" zone can be distinguished around the tracks (indicated by a white arrow in Figure 23), suggesting a potential fracture event below the surface. This bright zone, here regarded as the zone 1, is followed by the chipping of portions of the $3Al_2O_3{\cdot}2SiO_2$ film around the scratch track at higher loads (zone 2, as indicated by a black arrow in Figure 23).

Chipping of the $3Al_2O_3{\cdot}2SiO_2$ film is well appreciated at the surface level in the SEM image of Figure 24 a. This damage configuration is similar to the one reported for the nanoscratch of hard and stiff nitride-based films deposited on silicon[41].

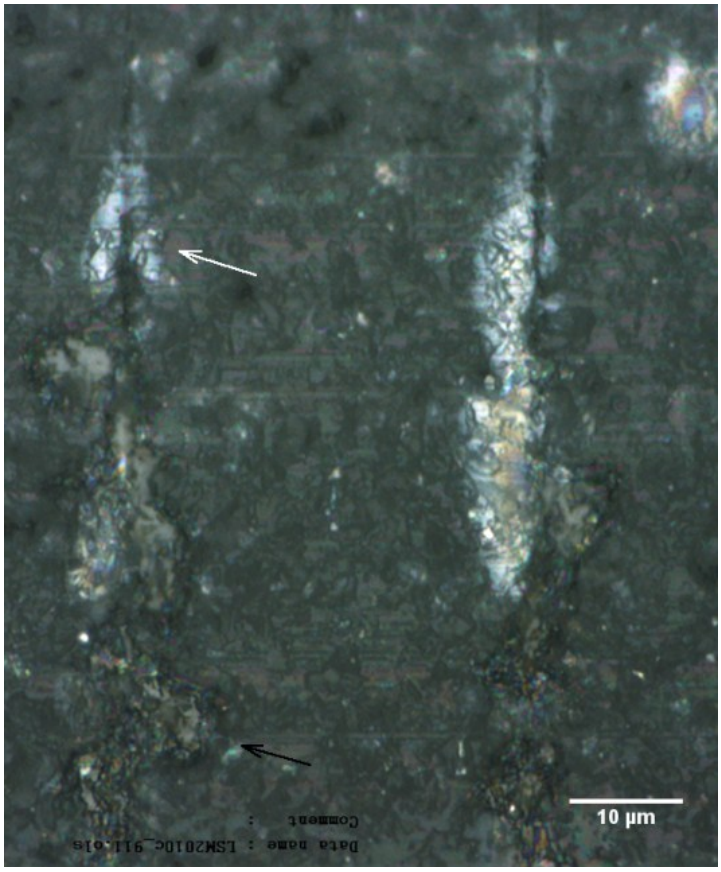

Figure 23. Optical micrograph showing a detail of two imprints of the scratch performed at P_{max} = 50 mN – l_{max} = 50 µm. The damage characteristics are indicated by arrows.

In order to investigate the damage below the surface, FIB cross-sections were prepared at two different locations along the scratch track. These locations were selected attending to the damage features observed at the top of the films in the optical micrographs: the bright zone (1) and the chipped zone (2), as it is indicated in Figure 24 a-b. The features of these cross-sections are detailed in the SEM micrographs given in Figure 25 and 26.

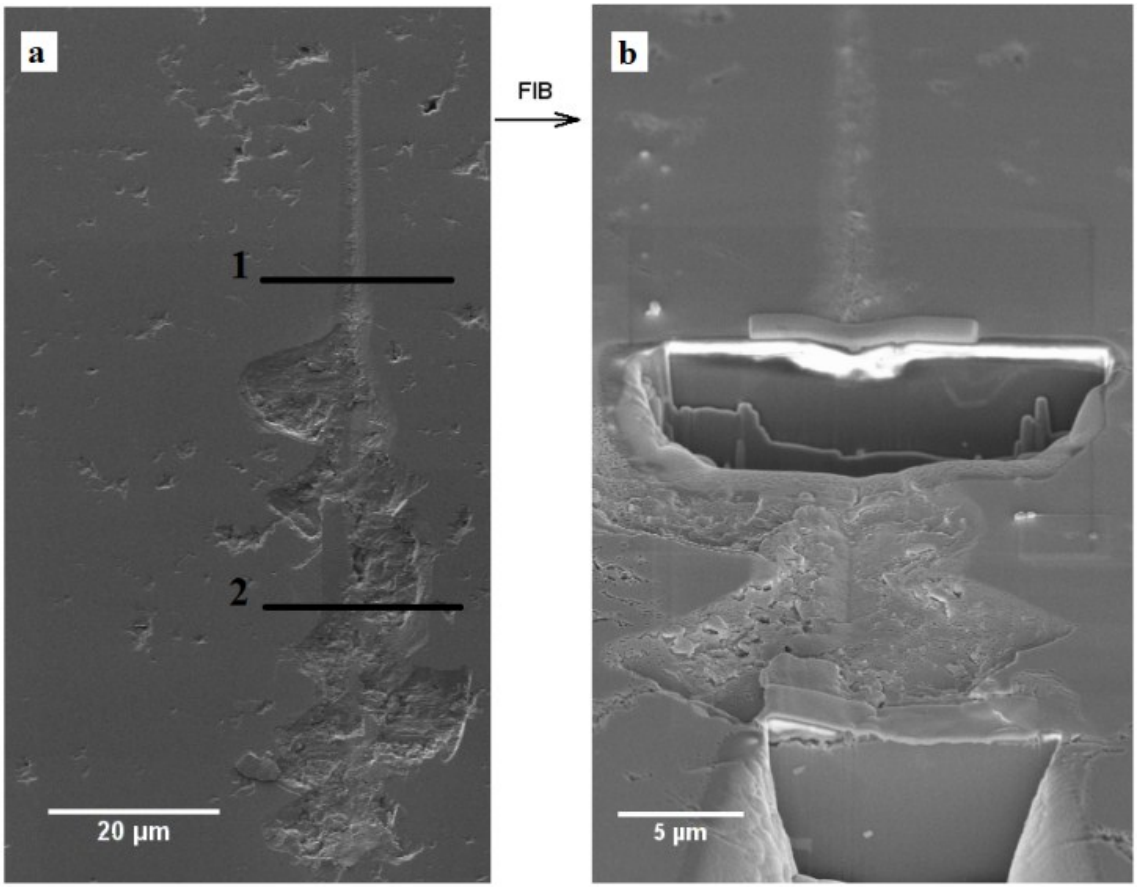

Figure 24. Images of FIB cross-sections performed at two points along a scratch performed at the high load condition. Surface (a) before the FIB sectioning process and (b) after the FIB sectioning process.

Three types of cracks may be observed in the cross-section shown in Figure 25 (corresponding to the zone 1 of Figure 24). (*i*) An intergranular crack within the SiC substrate is observed in one side of the scratch track as depicted in Figure 25 c. (*ii*) A radial crack within the $3Al_2O_3{\cdot}2SiO_2$ film, parallel to the normal load axis, located right beneath the center of the scratch track. This crack is also similar to the one found in the

scratches at the low load condition (see Figure 22) as well as in the cube corner indentations (see Figure 16 a-c). (*iii*) Lateral cracks within the $3Al_2O_3{\cdot}2SiO_2$ film arranged parallel to the surface. As it is observed from Figure 25 b-c, these lateral cracks propagate sideways from the center of the scratch, and transversally cut the $3Al_2O_3{\cdot}2SiO_2$ columns along their extension paths.

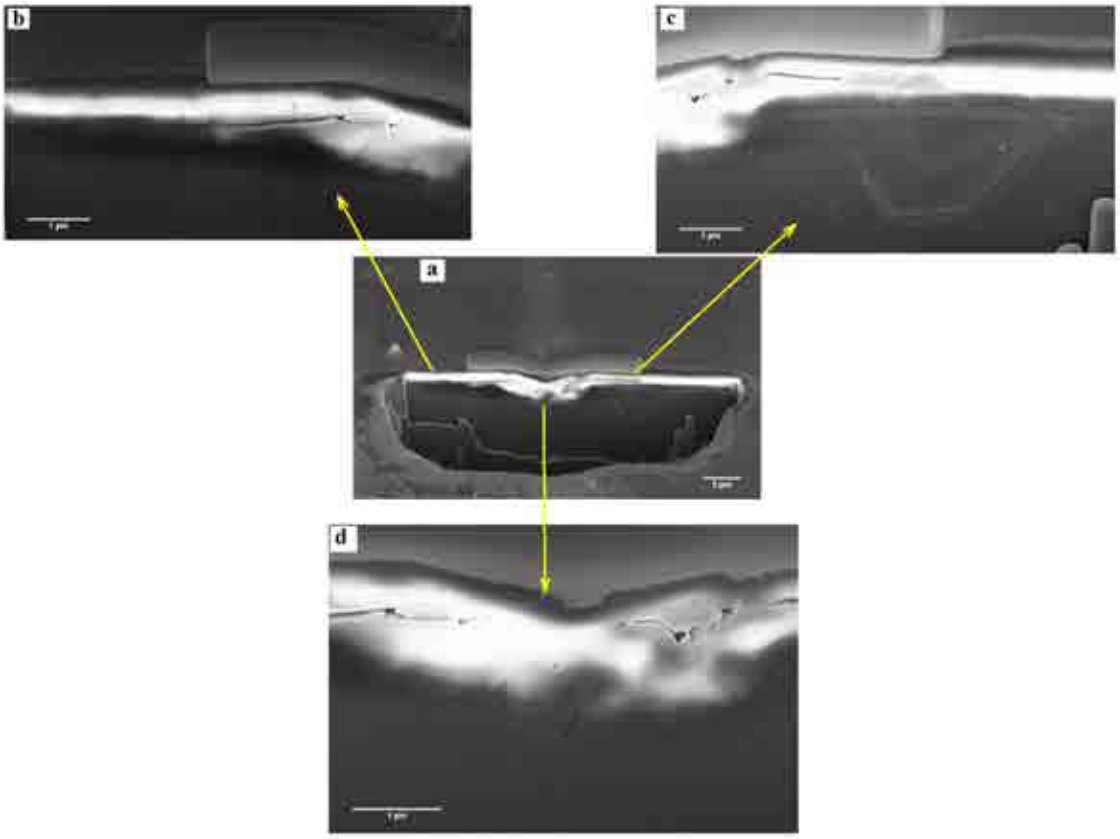

Figure 25. Cross-section of the zone 1 of Figure 23. (a) General, (b,c) lateral, and (d) central details of the cross-section.

The cross-section micrograph in Figure 26 illustrates the nature of the film chipping occurring at higher scratch loads. At the surface, the brittle character of the fracture taking place at the film is evidenced. At the subsurface, the remaining portions of a delaminated film can be observed at both sides of the track. At the left hand side, an interfacial crack suggests that the film is chipped out from the substrate after its delamination.

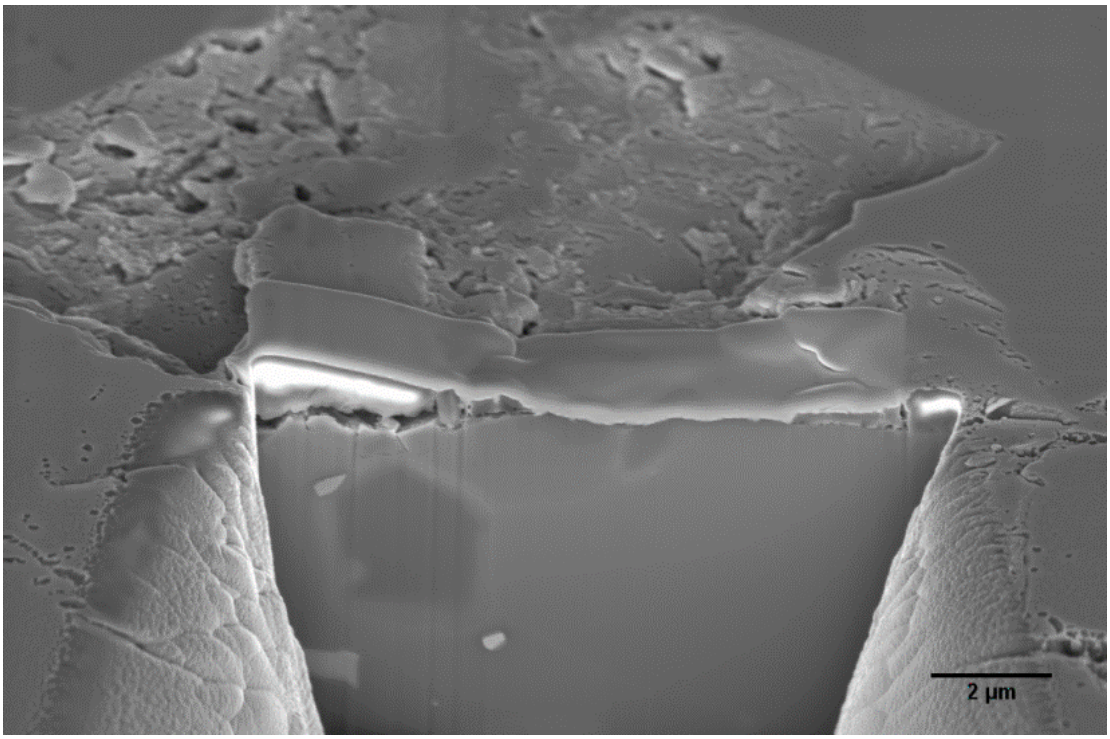

Figure 26. Cross-section of the zone 2 of Figure 23.

Curves of scratch penetration depth as a function of applied load and distance are plotted in Figure 27 a for three of the tests performed. Again, there is a linear increase in the penetration as the indenter progress along the scratch track, during the scratching and post scratching stages.

An abrupt variation in the penetration depth is registered by the nanoindenter at a scratch distance of $l \approx 40$ µN, corresponding to a load level of $P \approx 110$ mN. This discontinuity observed in the penetration is also patent in the curves of friction coefficient (Figure 27 b) and friction force (Figure 27 c) when plotted as a function of scratch length (and applied load). This event observed in the curves coincides with the onset of film chipping evidenced in the surface and the subsurface characterization of the damage (Figure 23 to 25). Consequently, it can be stated that in the scratches conducted at the high load condition, critical load for film chipping is about $P_c \approx 110$ mN.

At loads higher than P_c, the discontinuity in the penetration and friction curves is kept until the maximum load is reached (see Figure 27). This is related with the subsequent chipping processes observed in the characterization of the damage.

It is interesting to comment that lateral cracking evidenced within the film, occurring before the chipping process, is not reflected in the response recorded by the nanoindenter in terms of penetration and friction data.

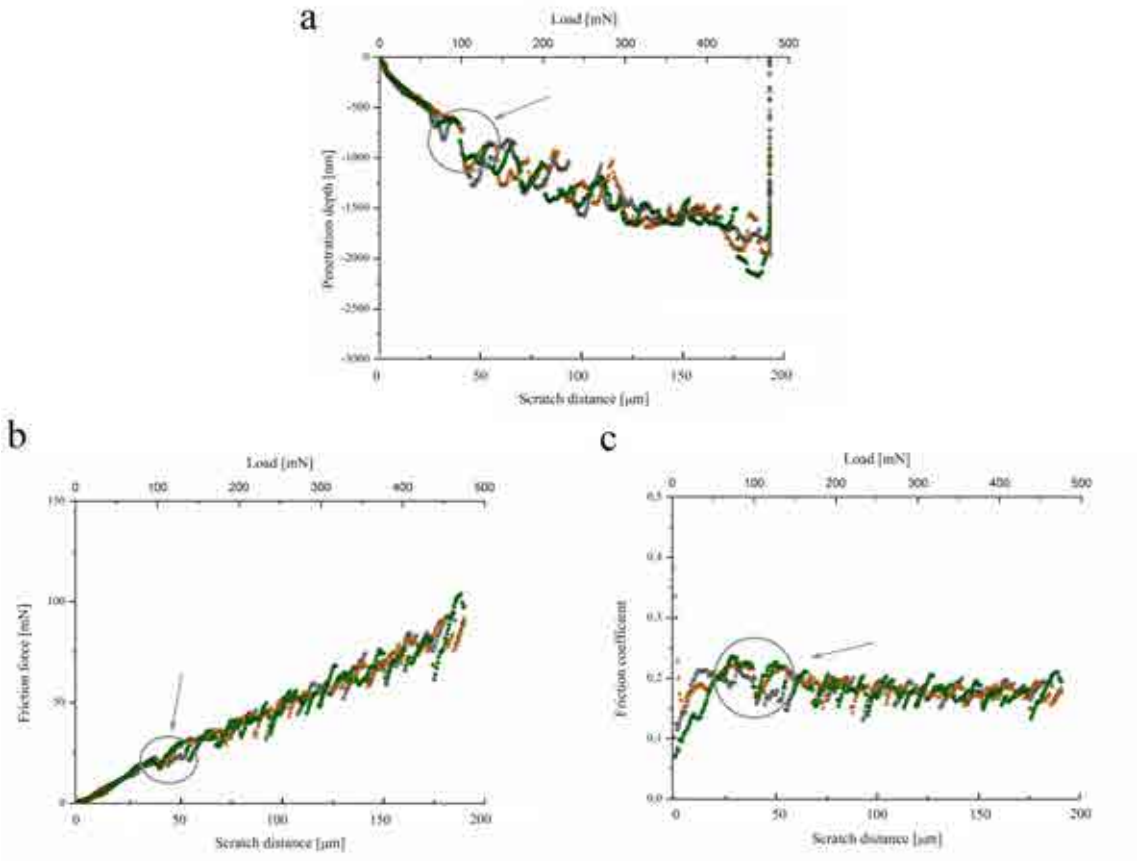

Figure 27. Curves of the scratches at the high load condition on sample *M3thin*. (a) Indenter penetration vs scratch distance in the pre-loading, loading and post-loading stages. (b) Friction coefficient and (c) friction force vs scratch distance.

4.4.2.3 Sliding contact resistance of the $3Al_2O_3{\cdot}2SiO_2$ thin film

The normal and lateral forces imposed by the indenter as it scratches the $3Al_2O_3{\cdot}2SiO_2$ film induce a progressive damage in the coated $3Al_2O_3{\cdot}2SiO_2$ /SiC system.

Within the low load condition, cracking in the SiC was evidenced. It may be stated that the coated system acts as a structural unit since the load applied by the indenter to the film is transferred to the substrate. Only a slight radial cracking contained into the film is observed.

As the maximum load and the load rate are further increased in the high load condition, the scratches induce damage within the film in the form of lateral cracks in addition to the referred radial ones. This lateral cracking in the film is similar to the one generated in the scratch testing of bulk ceramics, and it is common in brittle coatings deposited on brittle substrates[20]. It may be speculated that these lateral cracks are produced in the film by shear stresses induced as a consequence of the lateral movement of the indenter. When these cracks reach the interface at higher loads, the coating is chipped out from the substrate at a critical load of $P_c \approx 110$ mN.

In Figure 28 a, it is shown an AFM micrograph of one of the scratches performed at the high load condition together with surface profiles measured right before (Figure 28 b) and right after (Figure 28 c) the critical load is reached. From Figure 28 c, it can be seen that penetration depth at the center of the scratch track coincides with the coating thickness, indicating that film is chipped out from the SiC substrate at the interface. Chipping is one of the typical damage mechanisms occurring when scratching hard and brittle coatings deposited on hard and brittle substrates[42].

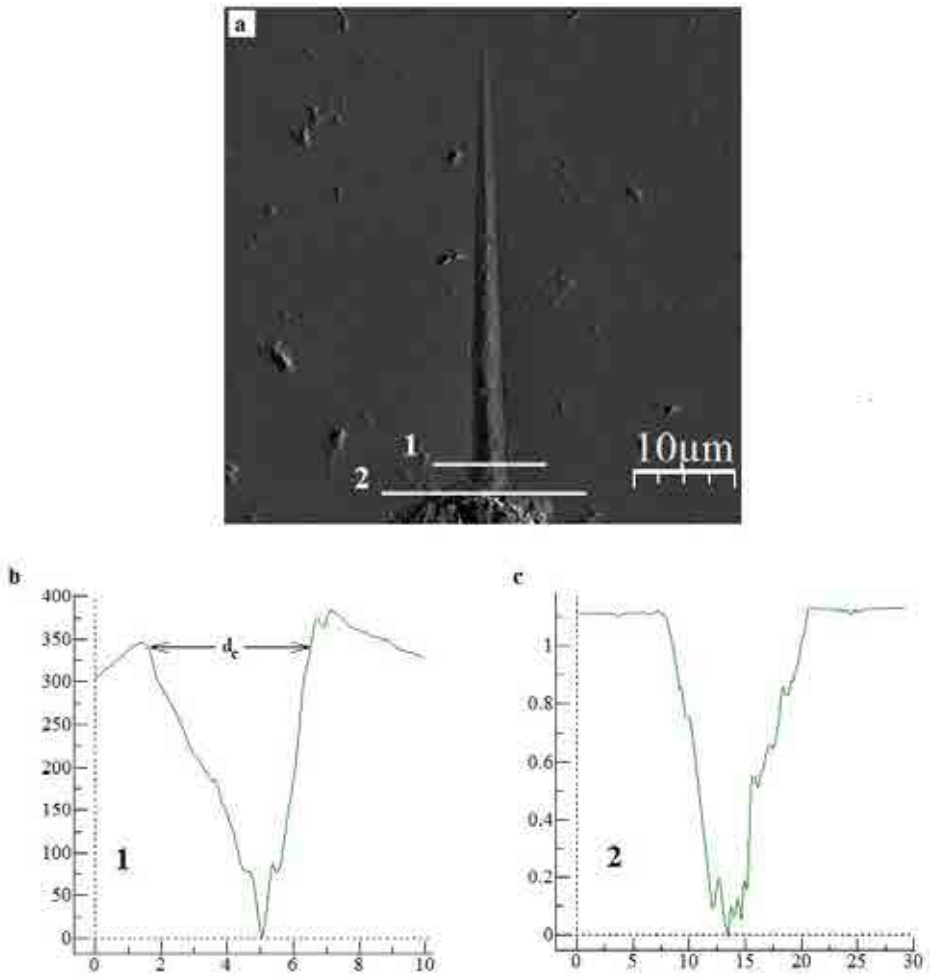

Figure 28. AFM micrograph of the first section of one of the scratches performed at the high load condition together with profiles right (1) before and (2) after film delamination and chipping.

4.4.2.4 Energy of adhesion and interface toughness

During the nanoscratch test, the $3Al_2O_3{\cdot}2SiO_2$ /SiC interface delamination and chipping occurred once the applied shear stresses at the interface are higher than the interface adhesion strength. By using Equation 4.8, and introducing the critical load for the coating detachment (P_c = 110 mN) and the critical scratch track width as the interface gets delaminated (d_c = 4.5 μm, measured from Figure 28 b), together with the measured friction coefficient μ given by the nanoscratch tester (μ = 0.2, see Figure 27 c) and the film poisson ratio v_f = 0.25, the critical stresses for delamination of the $3Al_2O_3{\cdot}2SiO_2$/SiC coated system σ_{int}, also regarded as the adhesion strength, can be obtained.

$$\sigma_{int} = \left(\frac{2P_c}{\pi d_c^2}\right)\left[\frac{(4+\nu_f)3\pi\mu}{8} - (1-2\nu_f)\right] \quad \textbf{Equation 4.8}$$

Using equation 4.9, the fracture energy release rate for the interface in the $3Al_2O_3{\cdot}2SiO_2$/SiC system was calculated, yielding $G_{int} \approx 12$ J·m^{-2}

$$G_{int} = \frac{\sigma_c^2 t}{2E_f} \quad \textbf{Equation 4.9}$$

If the calculated G_c value is included in equation 4.7, the interface fracture toughness can also be calculated from the scratch tests, yielding K_{int} = 1.2 MPa·m$^{1/2}$. These adhesion values are a bit lower than the ones calculated through nanoindentation tests referred in the previous section. The most important difference between these two tests is that in the scratch ones, the indenter tip provides lateral shear besides the normal compressive stress, and even some tensile stresses moving forward with the indenter tip. The shear component of stress at the interface and even the tensile component on the film applied during the scratch tests are higher than those introduced in the nanoindentation test, thus causing early interface delamination and film fracture.

4.4.2.5 Low load condition scratches in thick coatings

In the case of thick $3Al_2O_3{\cdot}2SiO_2$ specimens, the nanoscratch tests performed at low and high load conditions permitted to evaluate the integrity of the coatings with a negligible influence of the substrate.

Imprints of the scratches performed at the low load condition are presented in Figure 29. It is evident from the LSCM micrograph of Figure 29 a the absence of any failure event such as spallation or cracking at the surface level. It denotes a good tolerance of the

$3Al_2O_3{\cdot}2SiO_2$ coatings to the friction forces imposed by the indenter. Moreover, the scratches did not induce any damage at the subsurface at this load condition, as suggested by the optical image of Figure 29 b.

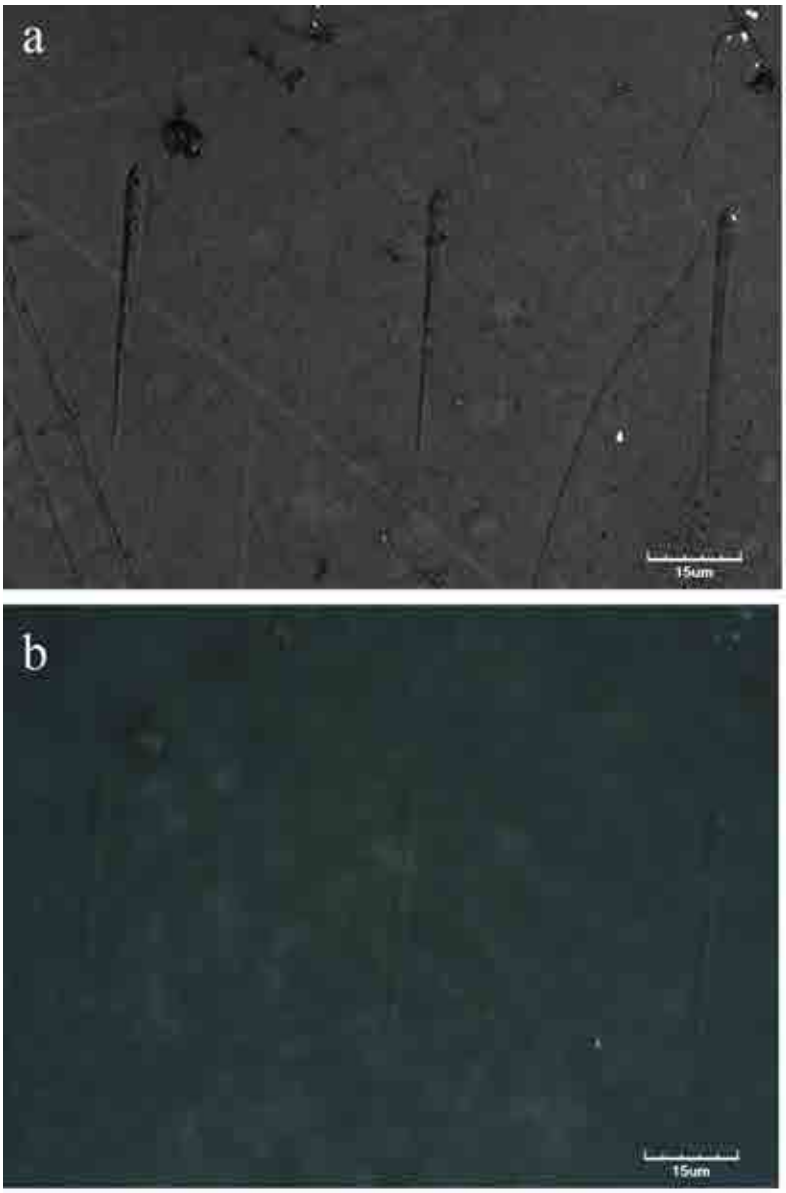

Figure 29. (a) LSCM micrograph of three imprints corresponding to the scratches performed on sample *M3-I* at the low load condition. (b) Optical image of the same scratch imprints.

In Figure 30, a 3D image is presented including a profile of the surface of the coatings at the maximum scratch load. This image shows the scratch tracks and their surrounding

region without any considerable damage. At some points a slight pile up of material is appreciated, as it can be observed in the profile of the scratches, especially in 1 and 3.

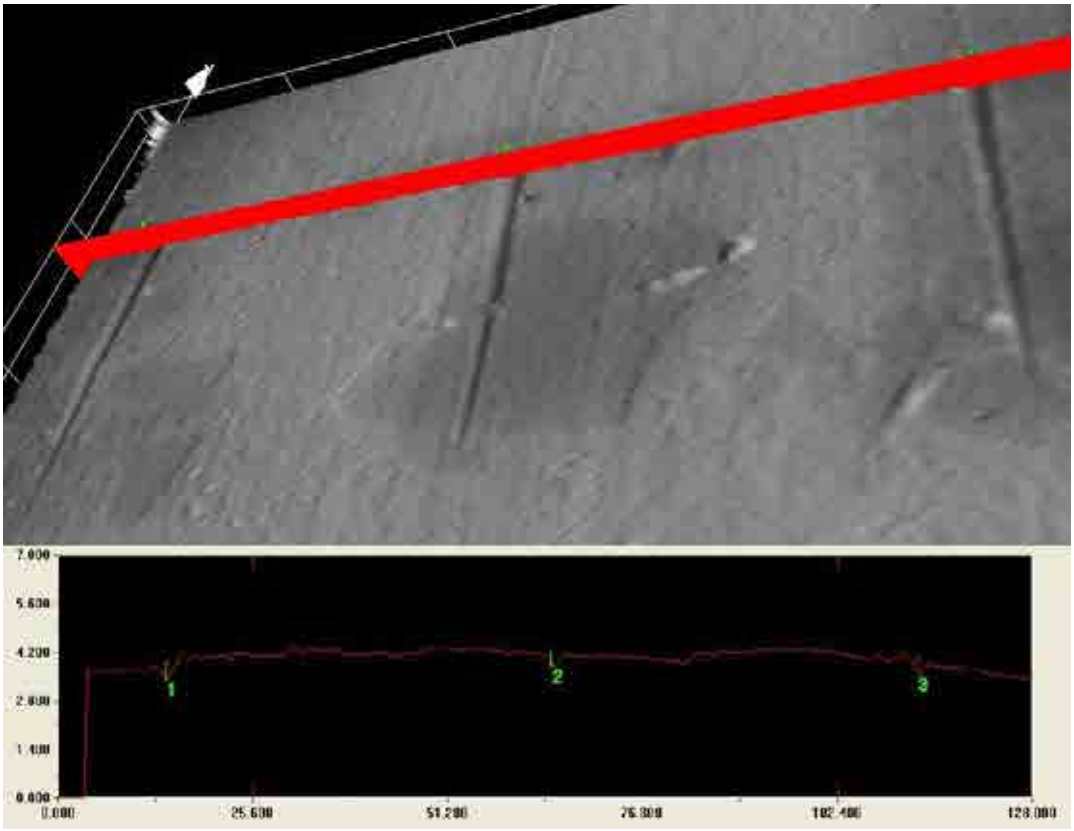

Figure 30. LSCM 3D image of the scratches performed on sample *M3-III* at the low load condition, together with the surface profile at maximum load.

Curves of penetration depth as a function of scratch distance are plotted in Figure 31 for three scratch tests. These plots show a linear increase in the penetration as the indenter progress along the scratch track, during both scratching and post scratching stages. As it may be assessed from the Figure 31 a, curves are continuous, and the lack of abrupt changes during penetration confirms that the coating retains its integrity throughout such stages at this load condition. The homogeneity in the plots of the friction coefficient (b) and friction force (c) along the scratch track confirm again the absence of any considerable damage at the stoichiometric $3Al_2O_3{\cdot}2SiO_2$ coatings during these tests.

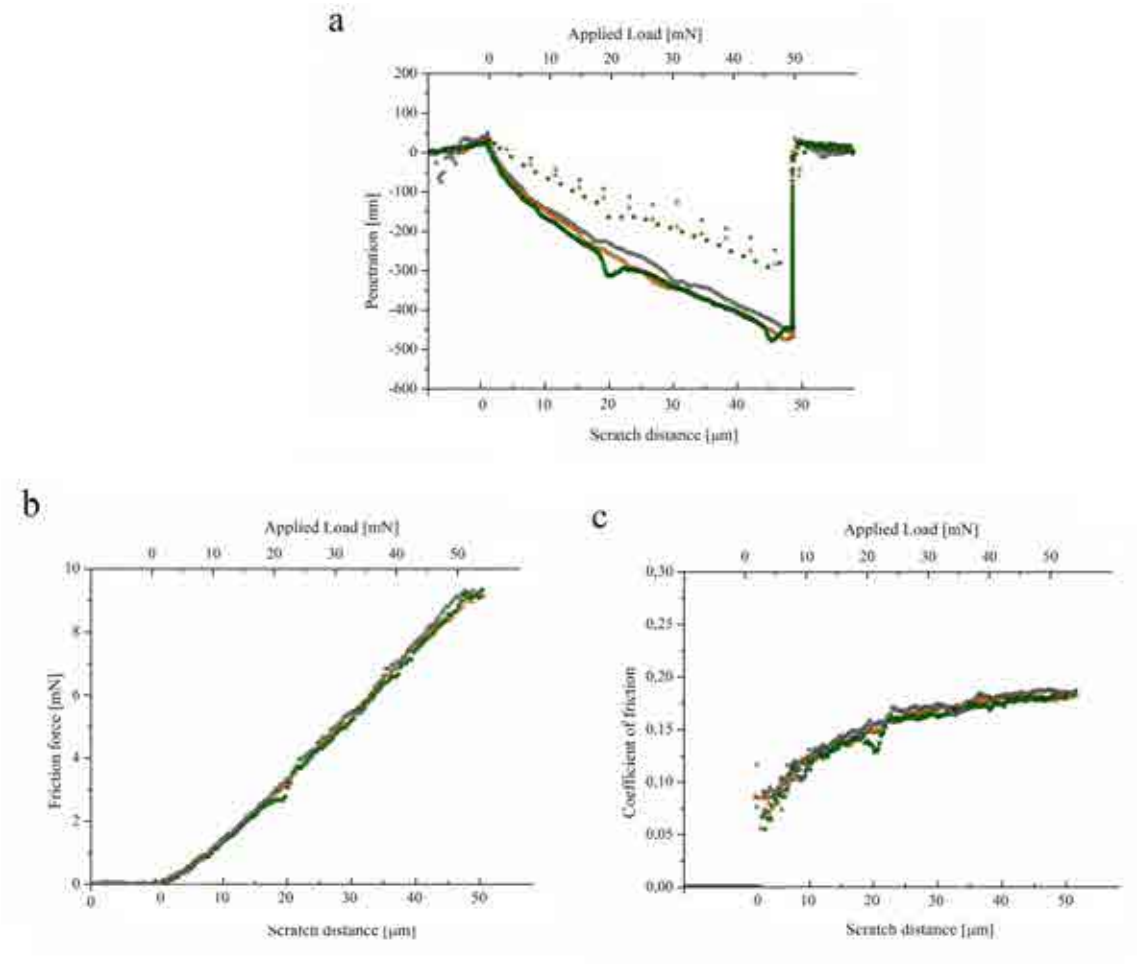

Figure 31. Curves of scratches performed at the low load condition on sample *M3-I*. (a) Indenter penetration as a function of scratch distance in pre-loading, loading and post-loading stages. (b) Friction coefficient and (c) friction force as a function of scratch distance.

4.4.2.6 High load condition scratches in thick coatings

Regarding the scratches conducted at the high load condition, an imprint generated during one of the scratch tests is presented in Figure 32. In contrast with the delamination and chipping produced in thin films under the same loading conditions (see Figure 24 to 27), no damage is appreciated at the surface of thick coatings as shown in the LSCM image of Figure 32 a. However, a subsurface damage event is noticeable from the optical image of Figure 32 b, again in the form of a bright area around the scratch track. This finding is analogous to the radial cracking induced within the $3Al_2O_3{\cdot}2SiO_2$ thin films by nanoscratch tests, as observed in Figure 25. The onset of the subsurface cracking present in these scratches was found to occur at a load level of $P \approx$

250 mN, corresponding to a scratch distance of $l \approx 100$ μm (almost at the midpoint of the total scratch length).

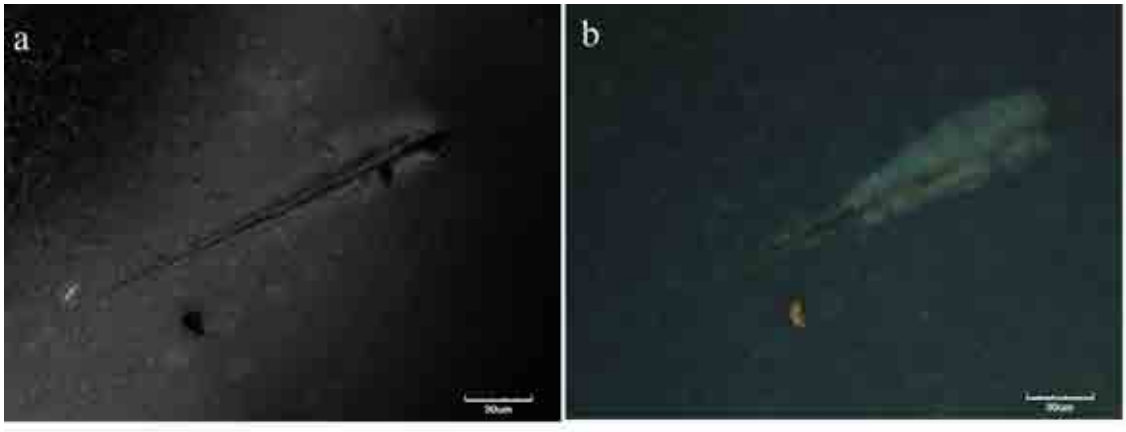

Figure 32. LSCM micrograph of three imprints corresponding to scratches performed at a load of 500 mN and a scratch length of 200 μm. (b) Optical image of the same scratch imprints. (a)

Again, curves of penetration depth as a function of scratch load and distance are plotted in Figure 33 for three scratch tests. As in the case of the nanoscratches performed at the low load condition, there is a linear penetration increase as the indenter progresses along the scratch track during both scratching and post scratching stages. From these curves, no sudden variations are observed in the penetration as the indenter is moved along the scratch length during the loading stage. Moreover, by examining the curves of friction coefficient (b) and friction force (c) as a function of penetration depth (and applied load), it can be remarked the absence of any discontinuity. According to this result, and taken into account that some subsurface damage was induced in these coatings by the nanoscratch test, it may be stated that this type of cracking, occurring below and parallel to the surface, is not reflected in the response recorded by the nanoindenter from the tests, in terms of penetration and friction data.

Finally, it should be underlined that scratch tests conducted on the top surface of stoichiometric $3Al_2O_3{\cdot}2SiO_2$ coatings, induced elastic and inelastic deformation in the coatings with no cracking, spalling or chipping of the coating material at the surface level. The nanoscratch tests conducted at the high load condition induced a subsurface

cracking at a critical load level of of $P \approx 250$ mN, corresponding to a scratch distance of $l \approx 100$ µm and an indenter penetration of $h \approx 1.2$ µm.

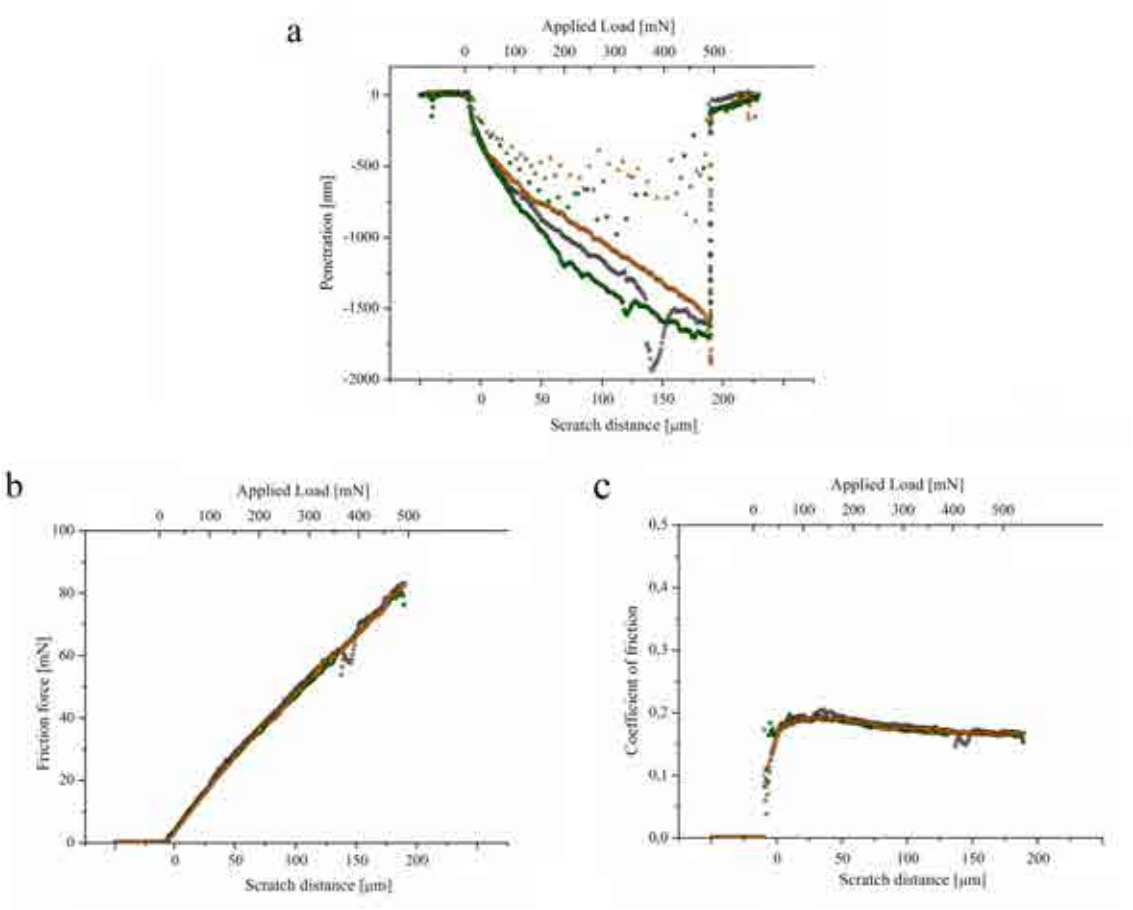

Figure 33. Curves of scratches at the high load condition on sample *M3-I*. (a) Indenter penetration vs scratch distance in pre-loading, loading and post-loading stages. (b) Friction coefficient and (c) friction force vs scratch distance.

4.5 Summary

The intrinsic properties of $3Al_2O_3{\cdot}2SiO_2$ thin films and thick coatings as well as the structural integrity of the $3Al_2O_3{\cdot}2SiO_2$/SiC system were assessed through the implementation of nanoindentation and nanoscratch tests on *M3thin*, *M3-I and M3-II* samples using different indenter tip geometries together with advanced characterization techniques. The influence of both substrate and residual stresses on indentation

response, deformation, and damage micromechanisms was accounted and documented, particularly regarding evaluation of intrinsic mechanical properties of the thin films and interfacial toughness of the thin coated systems. As the thickness increased, the extracted properties did not change drastically with increasing loads or penetration depths implemented in the tests. From the attained results the following conclusions may be drawn:

- Through Berkovich nanoindentations, a hardness value of $H_f \approx 10$ GPa was obtained whereas stiffness values in the range of $E_f \approx 100\text{-}145$ were assessed for stoichiometric $3Al_2O_3{\cdot}2SiO_2$ coatings.

- The use of thin film nanoindentation models allowed for the assessment of the intrinsic elastic modulus of $3Al_2O_3{\cdot}2SiO_2$ thin films taken into account the SiC influences on the measured apparent response.

- Spherical indentation at very low loads permitted calculation of the indentation stress-strain curves. From these data, a second value of the intrinsic elastic modulus as well as the indentation yield strength of the $3Al_2O_3{\cdot}2SiO_2$ thin films, were estimated ($\sigma_y \approx 3.5$ GPa).

- By increasing the applied load in cube corner nanoindentations, a controlled and progressive damage was induced in the studied coatings. Only cracks with increasing length were produced and promoted within thick coatings, whereas in thin films cracking and subsequent delamination were induced. From the indentation cracks confined into the coating, the intrinsic $3Al_2O_3{\cdot}2SiO_2$ film fracture toughness was calculated, $K_f \approx 1.1 - 1.7$ MPa·m$^{-1/2}$. On the other hand, analysis of the delamination scenario allowed to assess the interface energy of adhesion $G_{int} = 21.3 - 30.9$ J·m$^{-1/2}$ and the interface fracture toughness $K_{int} \approx 1.5 - 2.2$ MPa·m$^{-1/2}$.

- The structural integrity of the stoichiometric $3Al_2O_3{\cdot}2SiO_2$ coatings and thin films studied, and of the coated $3Al_2O_3{\cdot}2SiO_2$/SiC system, were also evaluated by means of nanoscratch tests. A progressive damage was induced by increasing nanoscratch load at low and high load conditions.

- In the case of thick coatings, the integrity of the film is retained after the nanoscratch tests as neither fracture within the film nor loss of material was observed at both high and low load conditions. Only a subsurface damage event was observed at the high load condition at $P_c \approx 250$ mN. A considerable elastic recovery was evidenced in the film after the nanoscratch tests.

- In the case of thin coated systems, no chipping or spallation of the coating material is observed in the nanoscratch at the low load conditions. At the high load conditions, a lateral cracking in the coating was induced. This cracking was promoted until the delamination and chipping of the film was induced at a critical load of $P_c \approx 100$ mN.

- A relatively highly plastic behavior of the $3Al_2O_3{\cdot}2SiO_2$ coatings was observed in the nanoscratch tests at the low load condition, as considerable plastic deformation takes place without any surface cracking, spallation or chipping of the coatings.

- Through the delamination induced by the nanoscratch tests in the thin coated system of sample *M3thin*, it was also possible to obtain a second assessment of the mechanical integrity of the interface. The energy of adhesion calculated by means of the scratch tests was $G_{int} \approx 12$ J·m^{-2}. The interfacial fracture toughness was $K_f \approx 1.2$ MPam$^{1/2}$.

4.6 References

1. Basu, S., Kulkarni, T., Wang, H., Sarin, V.K. Functionally graded chemical vapor deposited mullite environmental barrier coatings for Si-based ceramics. *J. Eur. Ceram. Soc.* **28**, 437-445 (2008).

2. Kulkarni, T., Huang, H., Basu, S., Sarin, V. K. Compositionally graded mullite-based chemical vapor deposited coatings. *J. Mater. Res.* **24**, 470-474 (2009).

3. Song, H. Selected mechanical problems in load- and depth-sensing indentation testing. Ph.D. Thesis. Rice University. Houston, USA. p. 85 (1999).

4. Saha, R., Nix, W.D. Effects of the substrate on the determination of thin film mechanical properties by nanoindentation. *Acta Mater.* **50**, 23-38 (2002).

5. Rar, A., Song, H., Pharr, G.M. Assessment of new relation for the elastic compliance of a film-substrate system. *Mater. Res. Soc. Symp. Proc.* 431-436 (2002).

6. Xu, H., Pharr, G.M. An improved relation for the effective elastic compliance of a film/substrate system during indentation by a flat cylindrical punch. *Scr. Mater.* **55**, 315-318 (2006).

7. Bec, S., Tonck, A., Loubet, J. A simple guide to determine elastic properties of films on substrate from nanoindentation experiments. *Philos. Mag.* **86**, 5347-5358 (2006).

8. Gaillard, Y., Rico, V.J., Jiménez-Piqué, E., González-Elipe, A.R. Nanoindentation of TiO_2 thin films with different microstructures. *J. Phys. D: Appl. Phys.* **42**, 1-9 (2009).

9. Hay, J., Crawford, B. Measuring substrate-independent modulus of thin films. *J. Mater. Res.* **26**, 727-738 (2011).

10. Field, J.S., Swain, M.V. A simple predictive model for spherical indentation. *J. Mater. Res.* **8**, 297-306 (1993).

11. Herbert, E. On the measurement of stress–strain curves by spherical indentation. *Thin Solid Films* **398-399**, 331-335 (2001).

12. He, L.H., Swain, M.V. Nanoindentation derived stress-strain properties of dental materials. *Dent. Mater.* **23**, 814-821 (2007).

13. Chintapalli, R.K., Jiménez-Piqué, E., Marro, F.G., Yan, H., Reece, M., Anglada, M. Spherical instrumented indentation of porous nanocrystalline zirconia. *J. Eur. Ceram. Soc.* **32**, 123-132 (2011).

14. Chen, J., Bull, S. Assessment of the toughness of thin coatings using nanoindentation under displacement control. *Thin Solid Films* **494**, 1-7 (2006).

15. King, S., Chu, R., Xu, G., Huening, J. Intrinsic stress effect on fracture toughness of plasma enhanced chemical vapor deposited SiN_x:H films. *Thin Solid Films* **518**, 4898-4907 (2010).

16. Marshall, D.B., Evans, A.G. Measurement of adherence of residually stressed thin films by indentation. I. Mechanics of interface delamination. *J. Appl. Phys.* **56**, 2632-2638 (1984).

17. Volinsky, A.A., Moody, N.R., Gerberich, W.W. Interfacial toughness measurements for thin films on substrates. *Acta Mater.* **50**, 441-466 (2002).

18. Chen, J., Bull, S.J. Approaches to investigate delamination and interfacial toughness in coated systems: an overview. *J. Phys. D: Appl. Phys.* **44**, 1-19 (2011).

19. Benayoun, S., Fouilland-Paille, L., Hantzpergue, J.J. Microscratch test studies of thin silica films on stainless steel substrates. *Thin Solid Films* **352**, 156-166 (1999).

20. Malzbender, J., Toonder, J.M.J.D., Balkenende, A.R., With, G.D. Measuring mechanical properties of coatings: a methodology applied to nano-particle-filled sol–gel coatings on glass. *Mat. Sci. Eng. R* **36**, 47-103 (2002).

21. Chang, S. Mechanical property analyses of porous low-dielectric-constant films for stability evaluation of multilevel-interconnect structures. *Thin Solid Films* **460**, 167-174 (2004).

22. Chang, S., Huang, Y. Analyses of interface adhesion between porous SiO_2 low-k film and SiC/SiN layers by nanoindentation and nanoscratch tests. *Microelectron. Eng.* **84**, 319-327 (2007).

23. Oliver, W.C., Pharr, G.M. An improved technique for determining hardness and elastic modulus using load and displacement sensing indentation experiments. *J. Mater. Res.* **7**, 1564-1583 (1992).

24. Oliver, W.C., Pharr, G.M. Measurement of hardness and elastic modulus by instrumented indentation: advances in understanding and refinements to methodology. *J. Mater. Res.* **19**, 3-20 (2004).

25. Jiménez-Piqué, E., Gaillard, Y., Anglada, M. Instrumented indentation of layered ceramic materials. *Key Eng. Mater.* **333**, 107-116 (2007).

26. Bartolome, J.F., Diaz, M., Moya, J.S. Influence of the metal particle size on the crack growth resistance in mullite-molybdenum composites. *J. Am. Ceram. Soc.* **85**, 2778-2784 (2002).

27. Anggono, J. Mullite Ceramics : Its Properties , Structure , and Synthesis. *J. Tek. Mes.* **7**, 1-10 (2005).

28. Basu, S.N., Sarin, V.K. *Chemical vapor-deposited mullite coatings (CVD Coatings)* In *Mullite.* p. 487. Wiley VCH, Weinheim, Germany (2005).

29. Schneider, H., Schreuer, J., Hildmann, B. Structure and properties of mullite-A review. *J. Eur. Ceram. Soc.* **28**, 329-344 (2008).

30. Roa, J.J., Jiménez-Piqué, E., Capdevila, X.G., Segarra, M. Nanoindentation with spherical tips of single crystals of YBCO textured by the Bridgman technique: Determination of indentation stress–strain curves. *J. Eur. Ceram. Soc.* **30**, 1477-1482 (2010).

31. Anstis, G.R., Chantikul, P., Lawn, B.R., Marshall, D.B. A critical evaluation of indentation techniques for measuring fracture toughness: I, direct crack measurements. *J. Am. Ceram. Soc.* **64**, 533-538 (1981).

32. Pharr, G. Measurement of mechanical properties by ultra-low load indentation. *Mater. Sci. Eng. A* **253**, 151-159 (1998).

33. Marshall, D.B., Lawn, B.R. An indentation technique for measuring stresses in tempered glass surfaces. *J. Am. Ceram. Soc.* **60**, 86-87 (1977).

34. Smith, S.M., Scattergood, R.O. Crack-shape effects for indentation fracture toughness measurements. *J. Am. Ceram. Soc.* **75**, 305-315 (1992).

35. Casellas, D., Baudin, C., Osendi, M., Llanes, L., Anglada, M. Fracture resistance of mullite under static and cyclic loads. *Scr. Mater.* **38**, 39-44 (1997).

36. Gerberich, W.W., Kramer, D.E., Tymiak, N.I., Volinsky, A.A., Bahr, D.F., Kriese, M.D. Nanoindentation-induced defect–interface interactions: phenomena, methods and limitations. *Acta Mater.* **47**, 4115-4123 (1999).

37. Evans, A.G., Hutchinson, J.W. On the mechanics of delamination and spalling in compressed films. *Int. J. Solids Struct.* **20**, 455-466 (1984).

38. Zheng, X. Use of nanomechanical fracture-testing for determining the interfacial adhesion of PZT ferroelectric thin films. *Surf. Coat. Technol.* **176**, 67-74 (2003).

39. An, T., Wen, M., Hu, C., Tian, H., Zheng, W. Interfacial fracture for TiN/SiN_x nano-multilayer coatings on Si(111) characterized by nanoindentation experiments. *Mater. Sci. Eng. A* **494**, 324-328 (2008).

40. Li, X., Diao, D., Bhushan, B. Fracture mechanisms of thin amorphous carbon films in nanoindentation. *Acta Metall. Mater.* **45**, 4453-4461 (1997).

41. Beake, B.D. , Vishnyakov, V.M., Harris, A.J. Relationship between mechanical properties of thin nitride-based films and their behaviour in nano-scratch tests. *Tribol. Int.* **44**, 468-475 (2011).

42. Bull, S.J. Failure mode maps in the thin film scratch adhesion test. *Tribol. Int.* **30**, 491-498 (1997).

5 *Chapter*

Influence of the Al/Si ratio on the mechanical properties of the $3Al_2O_3{\cdot}SiO_2$ coatings: Al-rich compositions

5.1 Introduction

There is a strong motivation to eliminate the silicon content in the surface of mullite coatings, aiming to protect silicon carbide from corrosive environments. In this regard, the most effective approach has been to increase the Al/Si ratio in mullite by using the chemical vapor deposition technique.[1–8] By tailoring the ratio of the input gases during the deposition process, in constant or graded options, high Al/Si ratios can be achieved at the top surface of the coatings. The effectiveness of such approach has been proven as Al-rich coatings obtained present high temperature resistance and improved protection to SiC against oxidation at elevated temperatures[3,6,8].

In this chapter, the effect of the composition (Al/Si ratio) on the mechanical behavior of mullite coatings is investigated by using nanoindentation and nanoscratch tests. Mullite coatings with different increasing Al/Si ratio, obtained by keeping the input gases constant during deposition, are studied. Specific details concerning the composition and thickness of these samples are given in Table 2 of *Chapter 3*.

The assessment of the mechanical properties of the studied Al-rich coatings is approached by conducting nanoindentation tests on their polished surface, using

Berkovich and cube corner tips. A special emphasis is placed on evaluating of the film hardness (H_f), elastic modulus (E_f) and fracture toughness (K_f). The mechanical performance and structural integrity of the coatings is characterized by conducting nanoscratch tests on their polished surface, using a Berkovich indenter. These tests are performed with the aim to induce and evaluate controlled and progressive damage in the studied coatings. The penetration curves and the characterization of the damage induced by these tests are analyzed.

5.2 Experimental procedure

The experimental procedure followed in this chapter is analogous to the one detailed in sections 4.2.1 and 4.2.2 of *Chapter 4*, for the micro- and nanomechanical characterization of sample *M3thick*.

For the assessment of H_f and E_f, matrices of 3 x 3 Berkovich indentations were performed at h_{max} = 2000 nm and 100 nm on the polished top surface of samples *M5*, *M6*, *M7* and *M8*. These depths permitted an easy localization, observation and imaging of the resulting imprints, together with a satisfactory evaluation of the properties and their variation along a significant depth with respect to coating thickness. H_f and E_f were determined by implementing the model proposed by Oliver and Pharr[9].

Aiming to calculate K_f, controlled cracking was induced in the coatings by performing indentations using a cube corner tip. By applying increasing maximum loads (P_{max} = 20 mN, 30 mN, 40 mN and 50 mN), it was possible to identify the most adequate load range to generate suitable cracks for toughness estimation. Samples *M7* and *M8* were exclusively selected for the assessment of K_f, as they present both adequate thickness and good stability of H_f and E_f values measured at the surface.

Indentation imprints and induced cracks were imaged using AFM. Cracks were measured from the obtained images, and intrinsic indentation fracture toughness of the samples, K_f , was estimated using the formulation proposed by Anstis *et al*.[10] and Marshall and Lawn[11] by following the procedure described in sections 4.4.1.3 and 4.4.1.4 of *Chapter 4*.

Nanoscratch tests were conducted on the top surface of of all studied samples following the "low load" condition (P_{max} = 50 mN, l_{max} = 50 µm and loading rate = 1 mN/µm) and the "high load" condition (P_{max} = 500 mN, l_{max} = 200 µm and loading rate = 2.5 mN/µm). These conditions permitted to induce and study different damage features in the coatings using the whole range of load capacity of the equipment. The penetration of the tip during scratching and post-scanning stages during the test, together with the induced damage along the scratch track (and its surroundings), were analyzed.

Residual imprints and tracks on the surface of the studied samples, generated by nanoindentation and nanoscratch tests respectively, were characterized at the surface level by means of OM, LSCM, AFM and SEM. To characterize the damage induced at the subsurface level, FIB cross-sections were exclusively prepared for sample *M8* both for nanoindentation and nanoscratch tracks. The experimental details concerning the preparation of the FIB cross-sections, are given in section 4.2.3 of *Chapter 4*.

5.3 Results

5.3.1 Hardness and elastic modulus

Three micrographs corresponding to Berkovich indentations performed in sample *M7* at h_{max} = 2000 nm (Figure 1 a), and in sample *M8* at h_{max} = 100 nm (Figure 1 b-c), are presented. From the FIB cross-section of the indentation at h_{max} = 100 nm in sample *M8* (Figure 1 c), it may be observed a significant portion of coating underlying the surface

at the indentation point. This observation supports the fact that, at this penetration depth, the indentation response mostly comes from the coating itself, and the substrate influence in such response may be neglected.

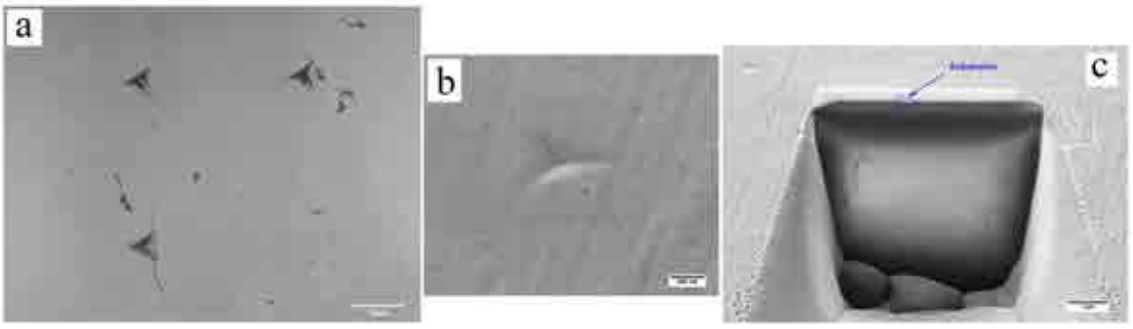

Figure 1. (a) Confocal micrograph of three indentations at h_{max} = 2000 nm in sample *M7*. SEM image of a nanoindentation at (b) h_{max} = 100 nm and (c) its FIB cross-section in sample *M8*.

Average curves of the apparent hardness and elastic modulus (H_a and E_a) as a function of penetration depth, as measured from the indentations at h_{max} = 100 nm for all the studied materials, are presented in Figure 2. The H_a and E_a data for sample *M3*, as measured previously in *Chapter 4*, is also included for comparison purposes. In the curves, the error bars correspond to standard deviations for the different measurements for each material.

In general terms, it may be stated that at this penetration regime, all the coatings present apparent H_a and E_a values practically stable with increasing depth. A significantly higher scatter is observed for measurements in sample *M6*, relative to those attained for all other samples. Furthermore, there is a correspondence of these properties with chemical composition, except for sample *M6* which presents apparent values significantly higher than the ones measured for all other coatings.

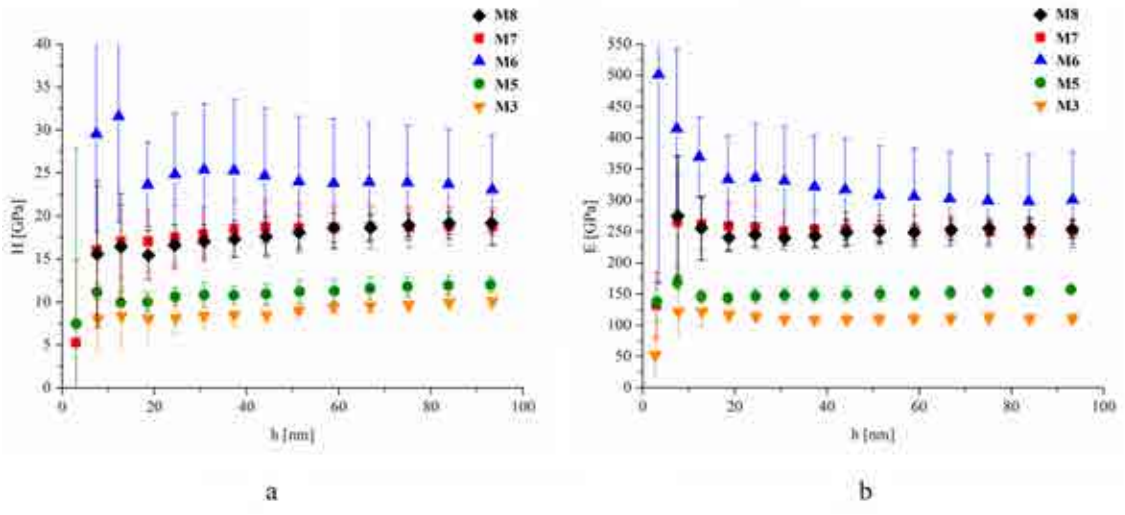

Figure 2. Average curves of (a) H_a and (b) E_a as a function of h, corresponding to indentations at P_{max} = 300 nm on the polished top surface of samples *M5, M6, M7* and *M8*. Curves of H_f and E_f for sample *M3,* as calculated in *Chapter 4*, are also included.

In Figure 3 average curves of H_a and E_a for all tested materials are presented for the case of h_{max} = 2000 nm. From these curves it may be seen that samples *M7* and *M8* exhibit stable values along the penetration depth, in correspondence with the ones measured at h_{max} = 100 nm (Figure 2). Thus, they are taken as the intrinsic film H_f and E_f values, and are listed in Table 1. On the other hand, H_a and E_a vary with h for samples *M5* and *M6*.

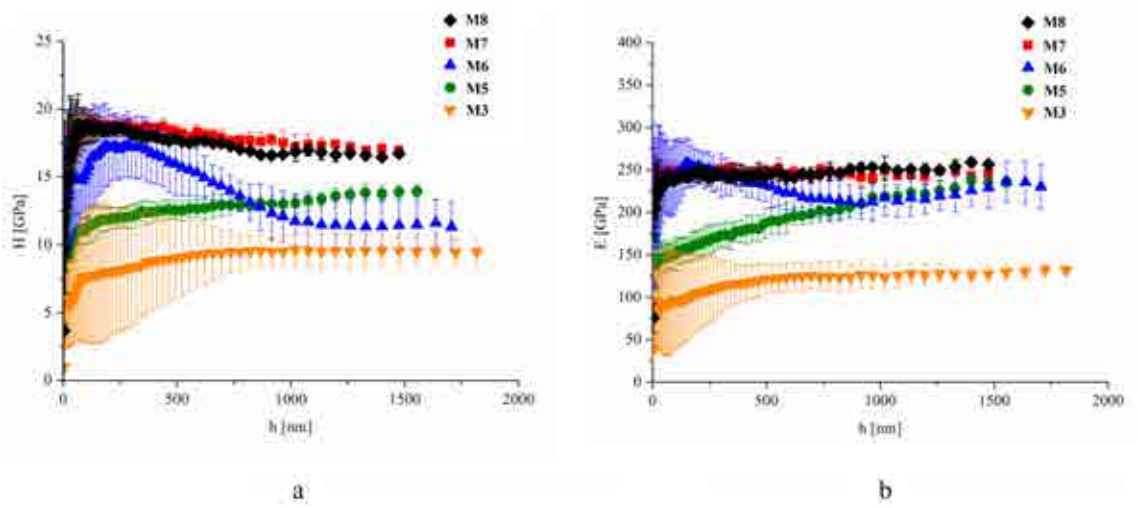

Figure 3. Average curves of (a) H_a and (b) E_a as a function of h, corresponding to nanoindentations at P_{max} = 2000 on the polished top surface of samples *M5, M6, M7* and *M8*. Curves of sample *M3* attained in *Chapter 4* are also included.

In the case of sample *M6*, there is an initial rise of H_a and E_a in the first nanometers depth, followed by a decrease and final stabilization of these properties in the last 800 nm of the penetration regime. Such a behavior, more appreciable in the case of hardness (see Figure 3 a), points out the existence of a superficial layer of harder and stiffer nature as compared with the underlying layer. This observation is in correspondence with the finding of an outer layer deposited on top of the mullite coating in sample *M6*, as indicated in *Chapter 3*. Accounting for the presence of this layer, the intrinsic film hardness and elastic modulus values listed for coating *M6* in Table 1 are those averaged in the stable part of the curves (h = 800-1600 nm).

In the case of sample *M5*, the increase in measured H_a and E_a with the penetration depth suggests a possible SiC substrate influence. This observation is in agreement with the fact that this sample presented a lower thickness in the "as deposited" state, which is reduced even more after polishing. In this regard, the average properties measured during unloading at h_{max} =100 nm are taken as the intrinsic film H_f and E_f values for sample *M5*, and those are the ones included in Table 1.

	M3	***M5***	***M6***	***M7***	***M8***
H_f [GPa]	10 ± 2	12 ± 1	12 ± 2	17 ± 1	17 ± 2
E_f [GPa]	127 ± 37	150 ± 20	220 ±19	243 ± 13	253 ± 14

Table 1. Average values of H_f and E_f of samples *M5, M6, M7* and *M8* evaluated from the nanoindentation tests at different h_{max}. Values for *M3* (calculated in *Chapter 4*) are also included.

5.3.2 Fracture toughness

5.3.2.1 Sample *M7*

A general AFM micrograph of cube corner indentation matrices performed at different loads, with the height image and its z scale included as an inset, is shown in Figure 4 a. A higher magnification image of the same micrograph, which provides complementary

information as well as a more detailed idea of the real surface appearance, is presented in Figure 4 b. Within the micrographs, the imprints of tests are aligned from top left to bottom right as P_{max} decreases from 50 mN to 20 mN. FromFigure 4, it is also possible to see the polished surface appearance with great resolution, revealing an irregular morphology with marked lines that could represent the boundaries of the columns.

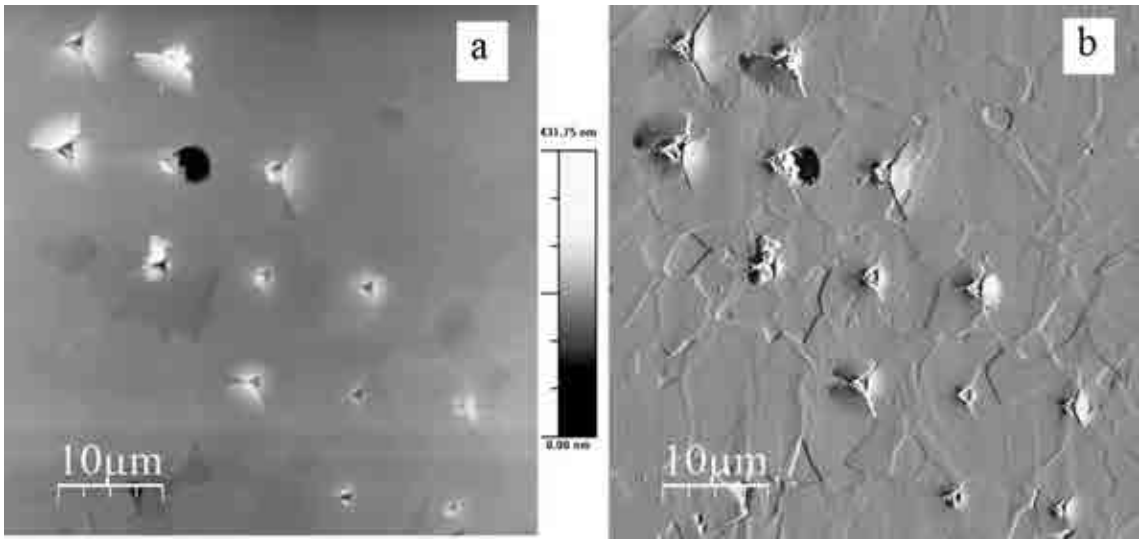

Figure 4. AFM micrographs of a matrix of cube corner indentations performed on the polished top surface of sample *M8* at different loads. (a) Height image and (b) amplitude image.

In Figure 4 b, it may be seen how indentations at P_{max} = 40 and 50 mN induce a significant damage in the coating, observed as relevant pile-up around the imprints and coating spallation. On the other hand, imprints for P_{max} = 20 and 30 mN resulted in radial cracking in the coating, allowing for the measurement of K_f.

An AFM image corresponding to an individual indentation performed at P_{max} = 20 mN is presented in Figure 5. Again, height and amplitude channels are complementary used to distinguish the full crack length, and the corresponding *z* scale is also included. This image shows a well-defined imprint with three associated cracks, being one of them only discernible in the height image.

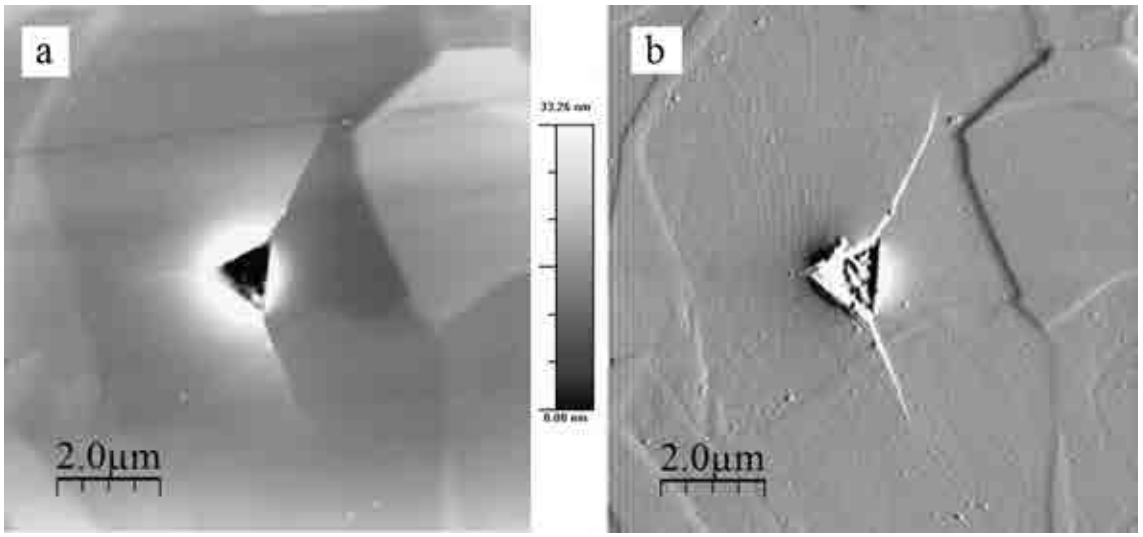

Figure 5. AFM micrographs of the cracks arising from a cube corner indentation at P_{max} = 20 mN in sample *M7*: (a) height image, and (b) amplitude image.

Similarly, one of the indentation imprints and associated crack system left by the indenter tip at 30 mN is presented in Figure 6. A slight pile-up of material can be observed from the height image of Figure 6 a.

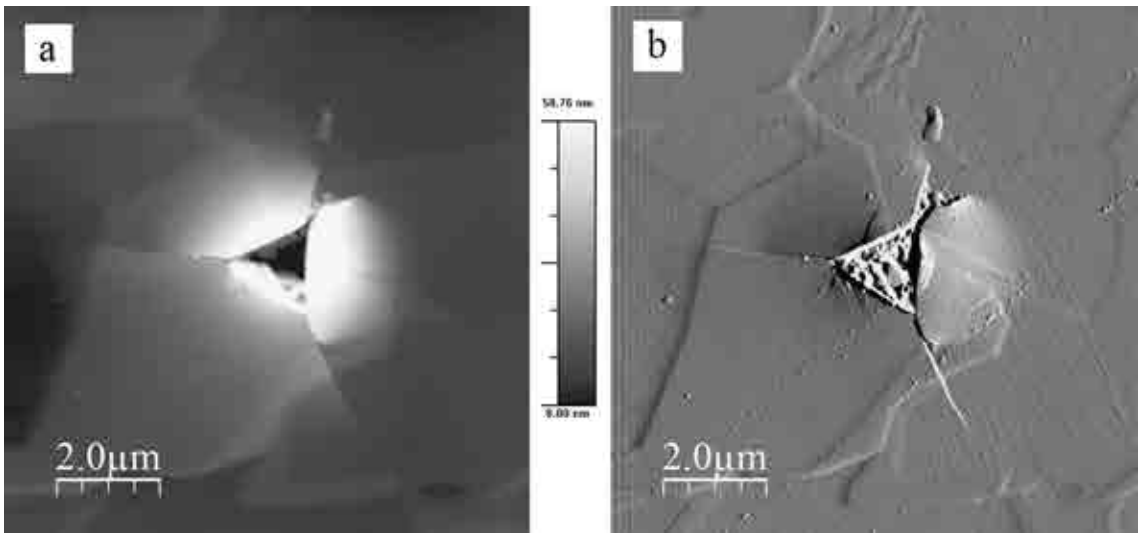

Figure 6. AFM micrographs of the cracks arising from a cube corner indentation at P_{max} = 30 mN in sample *M7*. (a) Height image and (b) amplitude image.

Cracks measurements were used for the assessment of fracture toughness for sample *M7*. Crack lengths measured from indentations performed at P_{max} = 20 and 30 mN are

presented in Table 2. These values satisfy the conditions required for toughness estimation.

c (μm)	
P = 20 mN	**P = 30 mN**
3.27 ± 0.01	3.98 ± 0.01
2.98 ± 0.01	3.63 ± 0.01
2.66 ± 0.01	3.30 ± 0.01
2.40 ± 0.01	2.64 ± 0.01
2.26 ± 0.01	3.40 ± 0.01
2.03 ± 0.01	3.46 ± 0.01

Table 2. Cracks lengths measured from the cube corner indentations at P_{max} = 20 mN and P_{max} = 30 mN performed at the surface for sample *M7*.

Accounting for the *c* values measured for sample *M7* (Table 2), and average H_f and E_f values calculated for this sample through Berkovich indentation, an estimation of the indentation fracture toughness may be done. Inserting these parameters as inputs in the formulation proposed by Anstis *et al.*[10], the apparent indentation fracture toughness measured yields $K_c = 0.7 \pm 0.1$ MPa·m^{½}.

However, the calculation of the intrinsic film fracture toughness K_f requires further consideration of the influence of residual stress level existing within the coatings.

5.3.2.2 Sample *M8*

Cube corner indentations were also performed to calculate K_f in the case of sample *M8*. A general AFM micrograph, corresponding to an indentation matrix performed at P_{max} = 30 mN on the surface of sample *M8*, is displayed as the height image in Figure 7 a. An individual imprint and the associated cracking may be observed in Figure 7 b.

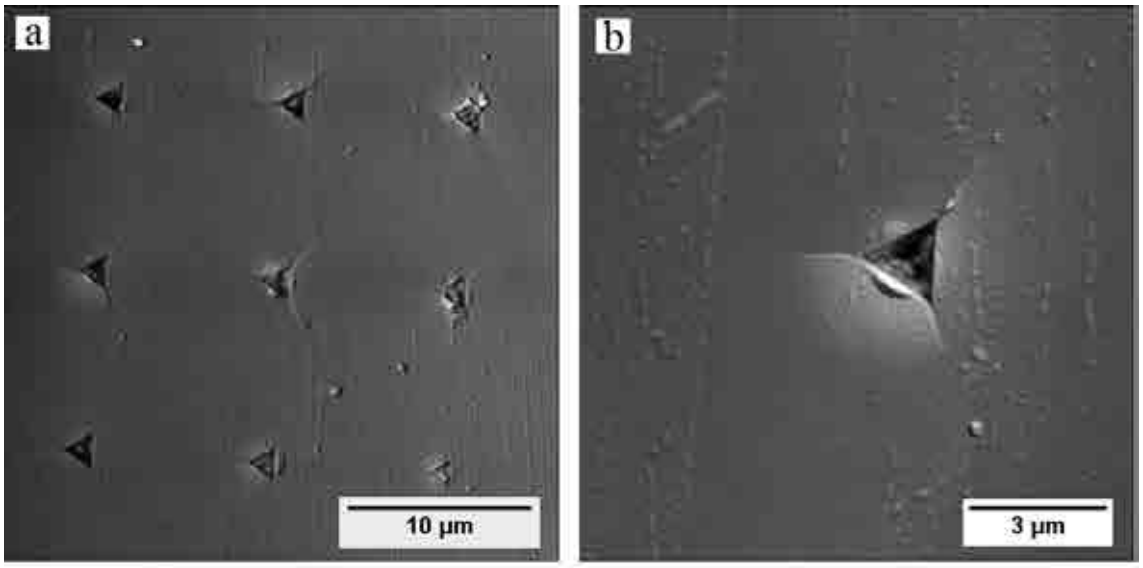

Figure 7. Matrix of cube corner indentations performed on the polished top surface of sample *M8* at (a) P_{max} = 30 mN. (b) Detail of an individual indentation.

Again, the *c* values measured from different cracks in the AFM images are presented in Table 3.

c (µm)	
P = 20 mN	**P = 30 mN**
2.71 ± 0.01	2.86 ± 0.01
3.38 ± 0.01	3.81 ± 0.01
2.76 ± 0.01	4.38 ± 0.01
2.56 ± 0.01	3.77 ± 0.01
	3.06 ± 0.01
	4.30 ± 0.01
	3.26 ± 0.01

Table 3. Cracks lengths measured from cube corner indentations at P_{max} = 20 mN and P_{max} = 30 mN performed on the surface of sample *M8*.

From the *c* values included in Table 3 for sample *M8*, together with H_f and E_f values measured from the Berkovich tests, the apparent fracture toughness may be calculated. Setting in these values directly on Anstis *et al.*[10] formulation, a K_c value of 0.6 ± 0.1 MPa·m^{½} was estimated. Again, it is important to mention that residual stresses effect must be accounted for final estimation of intrinsic film fracture toughness K_f.

5.3.3 Sliding contact resistance

The sliding contact behavior for samples *M5*, *M7* and *M8* is presented in the following sections. Results of nanoscratch corresponding to sample *M6* are not included in the analysis due to the presence of the outer layer on top of the mullite coating, as previously discussed.

5.3.3.1 Sample *M5*

Nanoscratches corresponding to the high and low load conditions, conducted on sample *M5*, may be observed in the optical micrograph of Figure 8. No signs of damage were observed in the residual tracks of the tests performed at the low load condition, either at the surface or subsurface level. At the high load condition a bright zone appears around the scratch track, together with associated cracking at the surface.

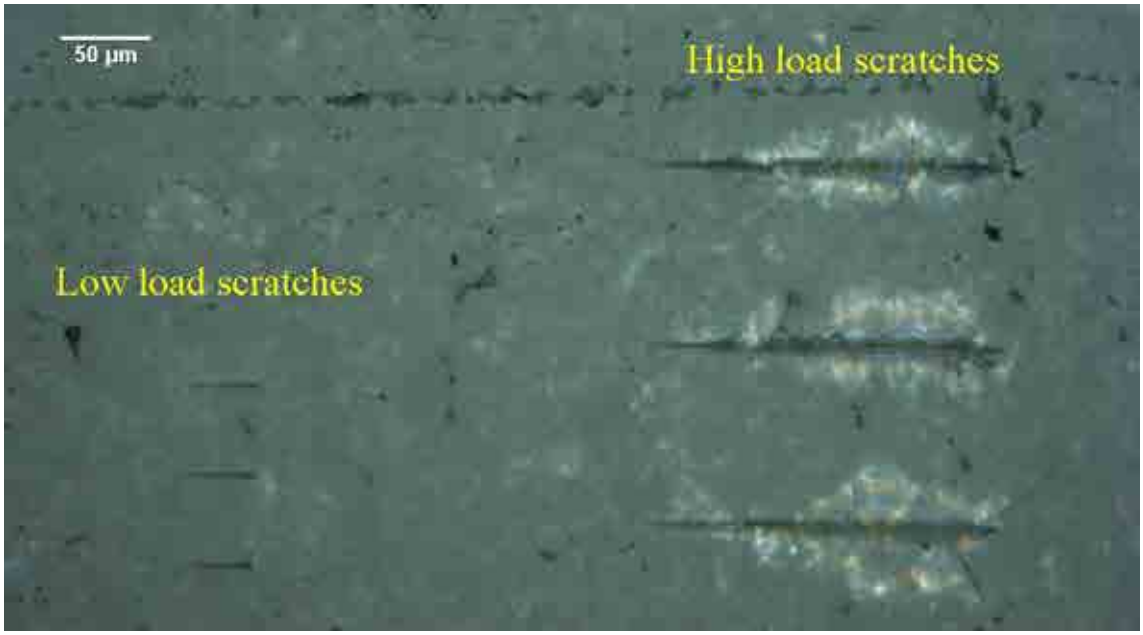

Figure 8. Optical image of high and low load scratches performed on sample *M5*. Scratches are displayed horizontally in the micrograph, with the applied load increasing from left to right.

This bright zone is similar to the one found in the nanoscratches performed in sample *M3* (referred previously in sections 4.2.2.2 and 4.2.2.6 of *Chapter 4*). This zone may be related to subsurface cracking or delamination, appearing at load levels around $P \approx$ 150-200 mN in sample *M5*.

In order to observe the damage at the surface in detail, LSCM micrographs for the low and high load conditions are presented in Figure 9 and 10 respectively.

From Figure 9 it is possible to observe that no spallation, cracking or chipping processes are produced in the coatings by the nanoscratches at low load condition. Only plastic deformation is induced in those tests, and appears in this image in the form of residual track imprints. Some isolated cracks are also evident in the micrograph at random locations on the surface of sample *M5*, possibly introduced due to the sample preparation process.

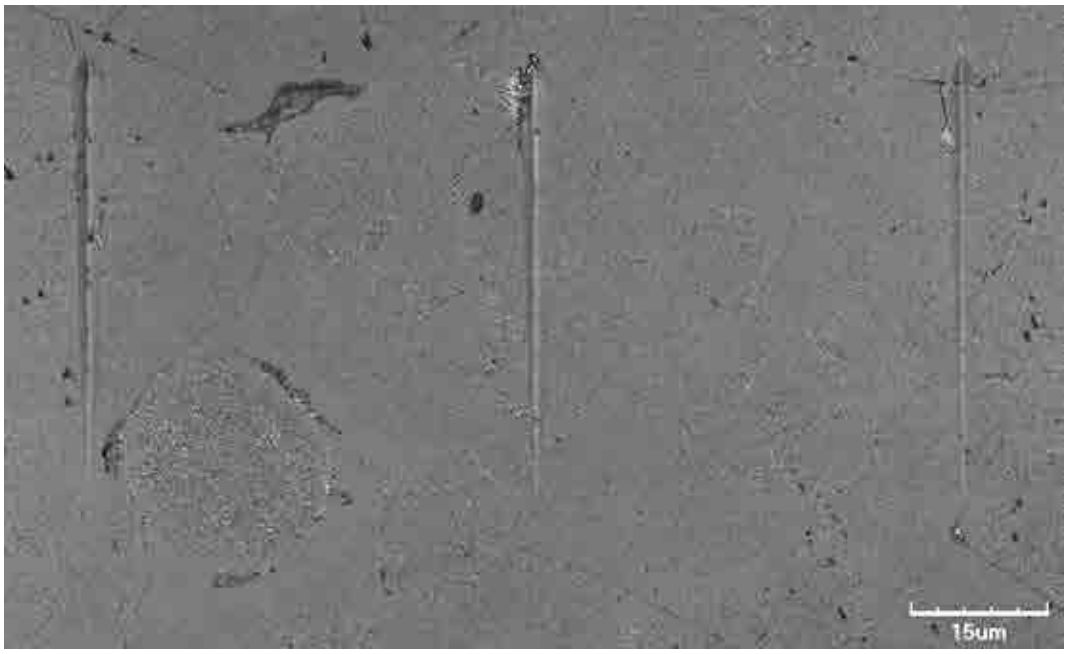

Figure 9. Three low load scratches performed on sample *M5*. Scratches are positioned vertically in the micrograph, with the applied load increasing upwards.

The surface features of the residual tracks corresponding to scratches at high load condition in sample *M5* are displayed in the confocal micrograph of Figure 10. In this figure, some cracks emanating from the edges of the scratch tracks, at an angle of approximately 45º respect to the scratch direction, may be distinguished. It appears clear from the image that such cracks are produced in the coating as a consequence of the nanoscratch tests. This damage event is first identified at a distance of $l \approx 50$ μm, with an associated load of $P \approx 100$ mN. As it can be discerned from Figure 8, the onset of the surface cracking precedes the zone at which subsurface damage takes place in the coating. Again, it is important to underline that no spalling or chipping processes that imply the partial or complete loss of the coating material are observed. In summary, high load scratches induce slight cracking in *M5*, in addition to certain level of plasticity denoted by the residual scratch tracks.

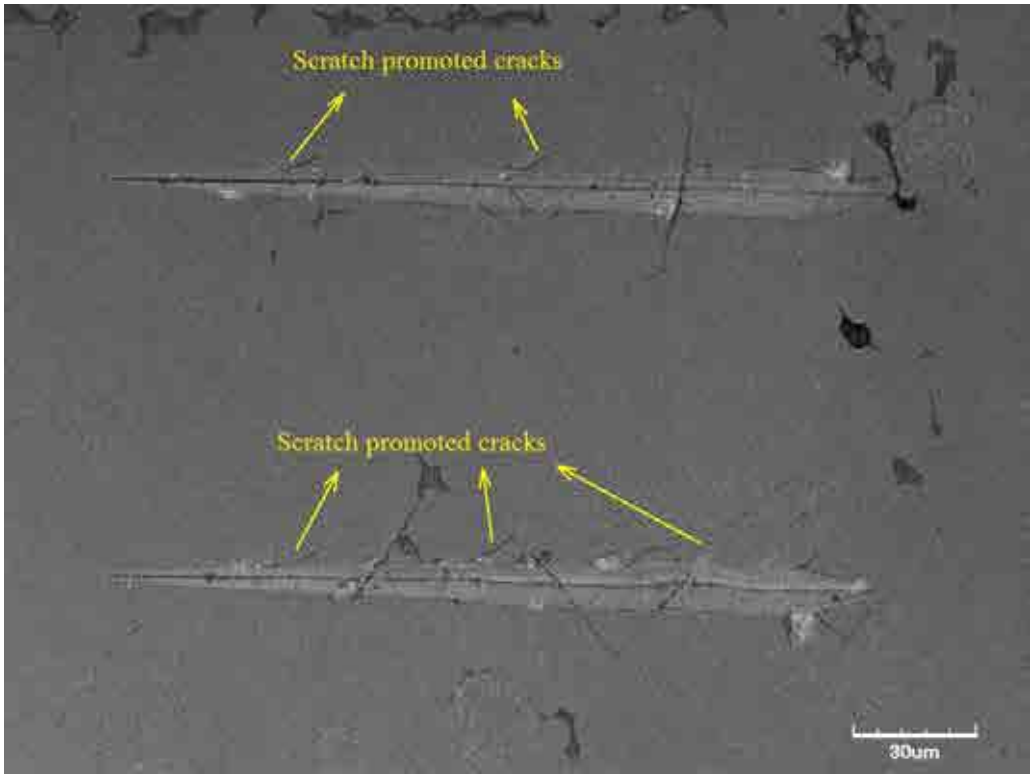

Figure 10. Confocal image of two of the high load scratches performed on sample *M5*. Scratches are displayed horizontally in the micrograph, with the applied load increasing from left to right.

5.3.3.2 Sample *M7*

An optical image showing the high and low load scratches performed on *M7,* is presented in Figure 11. Similarly to the case of sample *M5*, no considerable damage at both surface and subsurface could be evidenced in the low load scratches. It points out the high tolerance of *M7* against friction forces imposed by the indenter, as plastic deformation takes place without cracking. As load is increased in the high load condition, the same bright zone around the scratch tracks appears. Although such zone does not emerge clearly defined in the case of sample *M7*, it is evident that the onset of this subsurface damage takes place at $l > 50$ µm, and $P > 100$ mN.

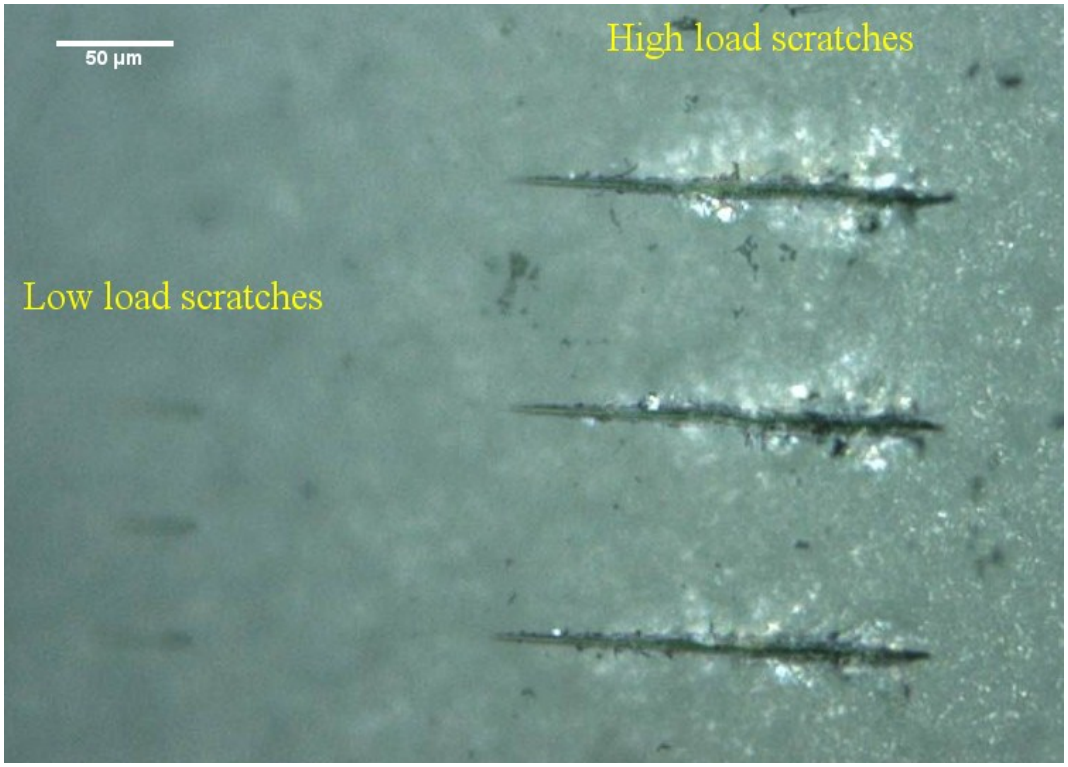

Figure 11. Optical image of high and low load scratches performed on sample *M7*. Scratches are displayed horizontally in the micrograph, with the applied load increasing from left to right.

The LSCM image of Figure 12, corresponding to one of the scratches performed at the low load condition, depicts the lack of significant cracking at the coating in sample *M7*.

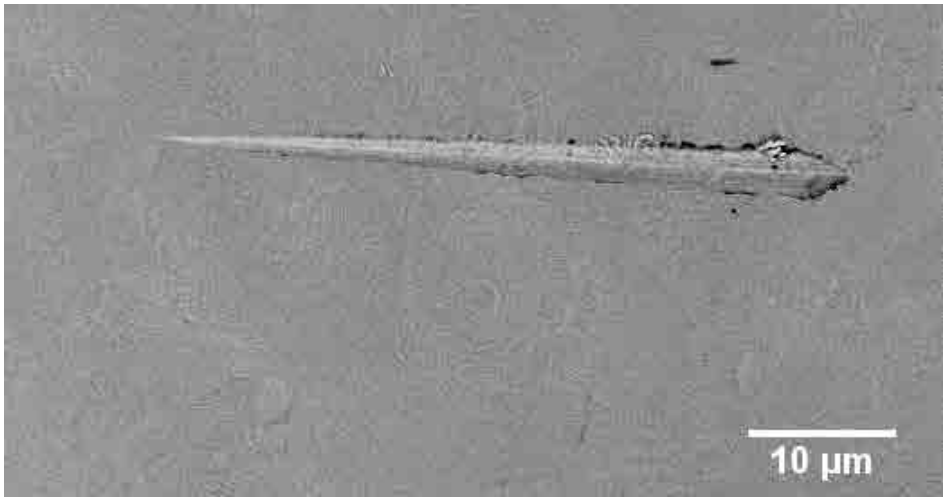

Figure 12. Low load scratch performed on sample *M7*. Scratches are displayed horizontally in the micrograph, with the applied load increasing rightwards.

The LSCM micrograph of Figure 13 shows damage progression at the surface level for two of the scratches performed at the high load condition. A cracking scenario similar to the one observed for sample *M5* (Figure 10), where cracks appear at 45º with respect to the scratch direction, is evidenced for *M7* specimen.

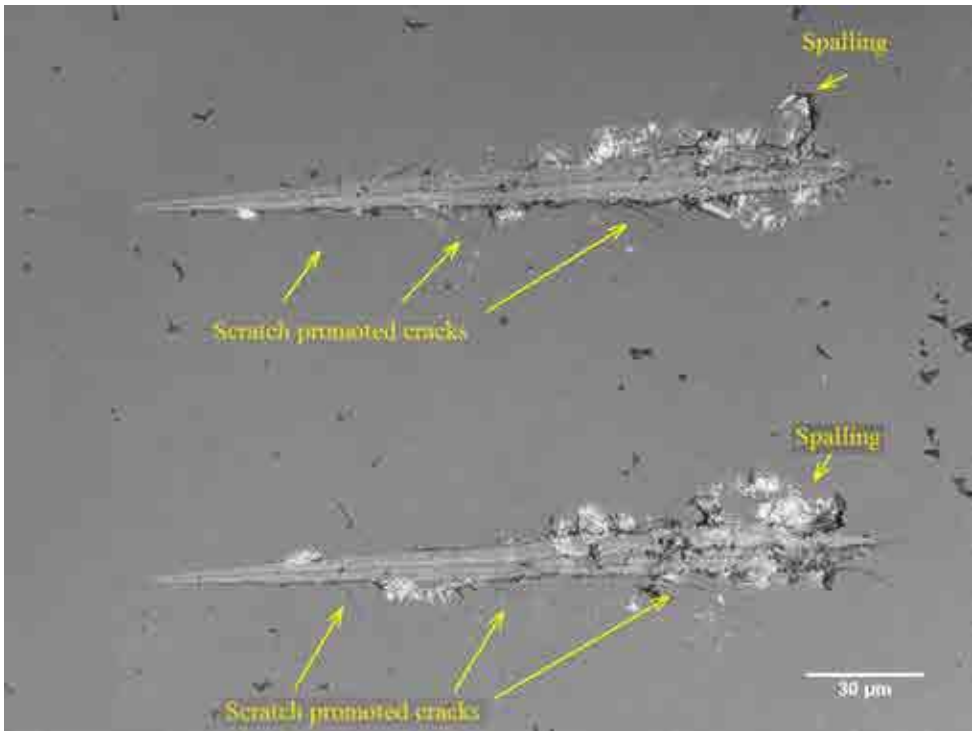

Figure 13. Two of the high load scratches performed on sample *M7*. Scratches are displayed horizontally in the micrograph, with the applied load increasing from left to right.

By detailed examination of micrograph in Figure 13, first cracks may be recognized at $l \approx 40$ µm and $P \approx 80$ mN in sample *M7*. In addition, the onset of a spalling phenomenon is clear around the scratches, especially at the end of the track $l \approx 130$ µm and $P \approx 360$ mN.

5.3.3.3 Sample *M8*

The confocal micrograph of Figure 14 a includes three scratches performed at the low load condition on sample *M8*. A higher magnification of an individual scratch track is included in Figure 14 b. Besides the residual tracks left by the scratch tests, small cracks are first evidenced at $l = 20$ µm and $P = 20$ mN. Such cracks are similar to the ones induced at the high load condition in samples *M5* and *M7*.

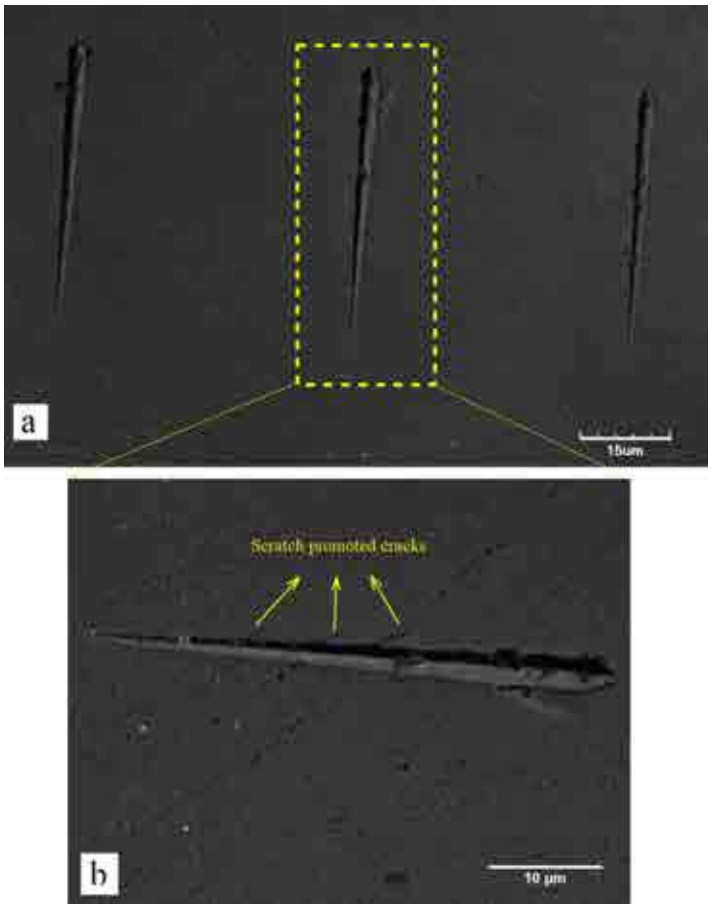

Figure 14. (a) Confocal micrograph of three low load scratches performed on sample *M8*. These scratches are displayed vertically in the micrograph, with the applied load increasing upwards. (b) Detail of an individual scratch depicting slight cracking. This scratch is displayed horizontally in the micrograph, with the applied load increasing from left to right.

In the optical images of Figure 15, one of the scratches performed on sample *M8* at the high load condition is shown. Taking advantage of the transparence of the polished mullite coating, the SiC substrate underneath is focused in the micrograph of Figure 15 a. As it may be observed, a bright zone suggests that the substrate is also affected as a consequence of the scratch test. It may be commented that, in sample *M8*, this zone is less defined and extended than for all other studied coatings.

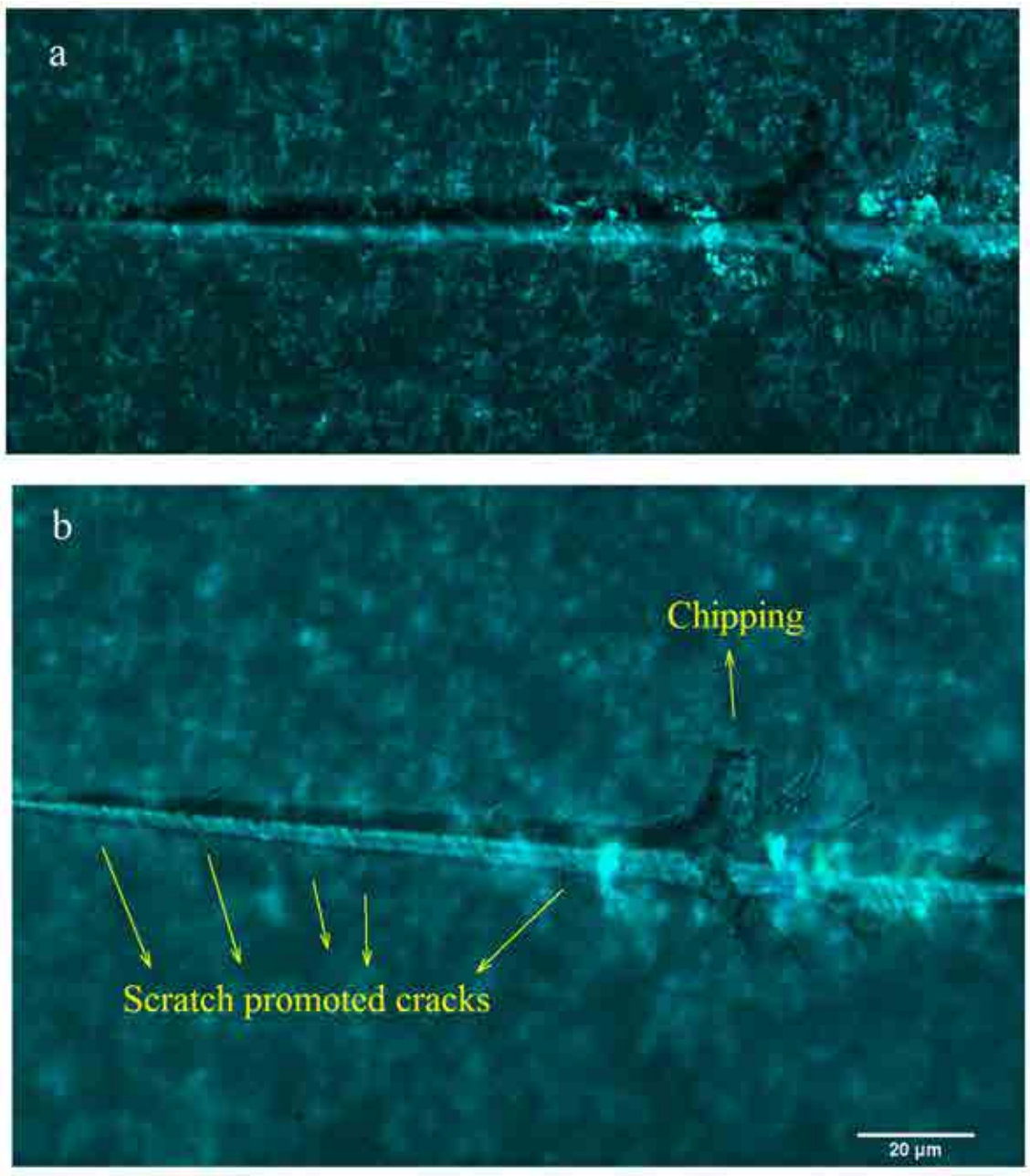

Figure 15. Optical image of a high load scratch performed on sample *M8*. (a) Focus on the substrate and (b) on the coating top surface. This scratch is displayed horizontally in the micrograph, with the applied load increasing from left to right.

As the surface of the coating is focused in the image of Figure 15 b, the features of the damage can be distinguished. Again, cracks arising from the edges of the scratch track at 45º are evidenced from the beginning of the track, and a slight chipping process may be observed at higher loads ($l \approx 145$ μm corresponding to $P \approx 385$ mN).

In order to investigate the damage events discerned at the subsurface, two FIB cross-sections were prepared at the locations shown in the SEM micrograph of Figure 16.

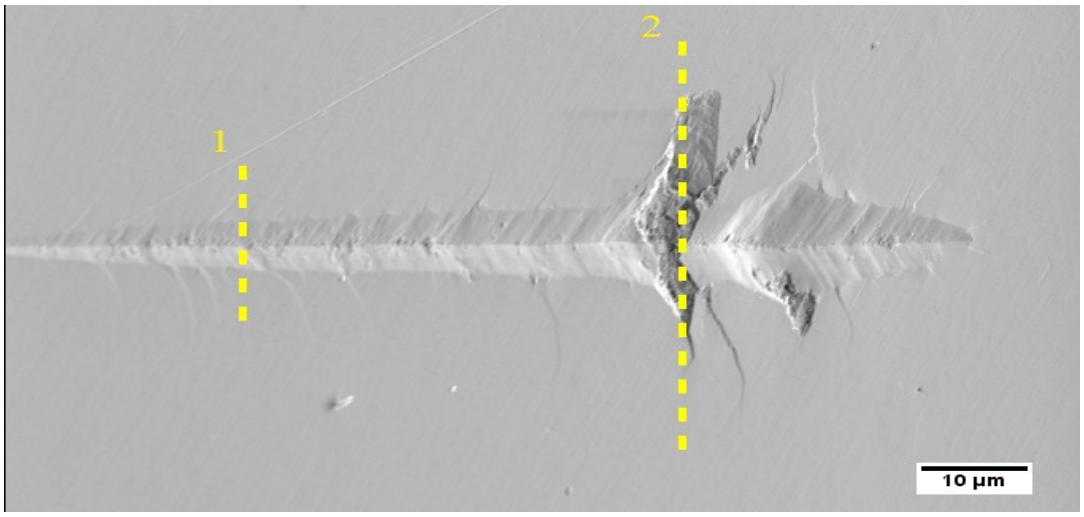

Figure 16. SEM image of a high load scratch in sample *M8* denoting the positions 1 and 2 for the FIB cross-sectioning. This scratch is displayed horizontally in the micrograph, with the applied load increasing from left to right.

The FIB cross-sections at positions 1 and 2 in Figure 16, are displayed in Figure 17 (a and b respectively). Positions 1 and 2 corresponds to a scratch distance of $l \approx 65$ μm ($P \approx 200$ mN) and $l \approx 150$ μm ($P \approx 400$ mN), respectively.

From Figure 17 a, there may be observed three cracks (marked with arrows) located within the coating at an angle of approximately 45º with respect to the interface. These cracks converge in a point located right below the centre of the scratch track width. However, it is interesting to comment that these cracks do not reach the surface; and furthermore, one of them appears to propagate into the substrate following an

intergranular path. It is not clear whether these cracks were produced within the coating or in the substrate.

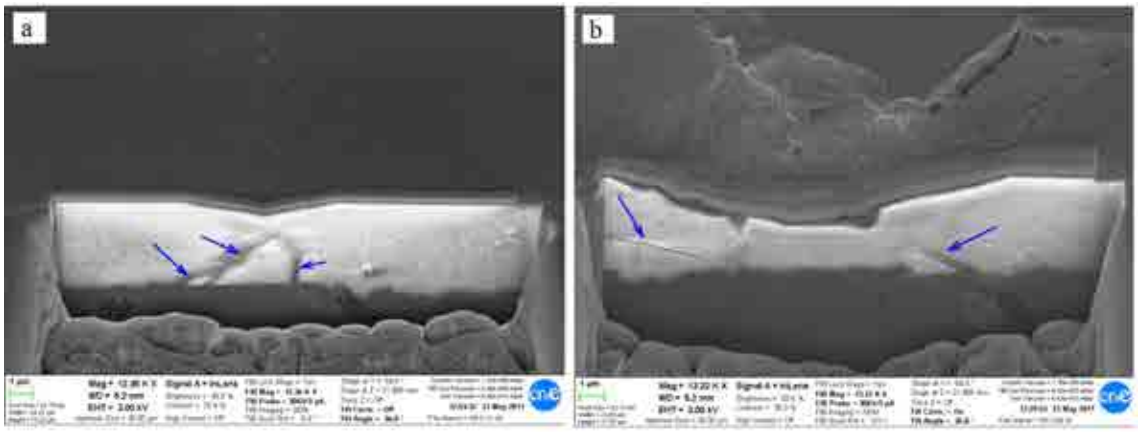

Figure 17. FIB cross-sections of the high load scratch of sample *M8* at positions 1(a), and 2 (b) of Figure 16.

From the cross-section shown in Figure 17 b, there may be discerned the chipping phenomenon occurring at the coating. In addition to this chipping event, two cracks also at 45º of the interface are evident, and a slight delamination of the coating may be discerned right below the centre of the scratch width. It should be mentioned that removal of coating material involved in the chipping process does not reach the SiC substrate.

5.4 Discussion

5.4.1 Influence of composition on H_f and E_f

Average H_f and E_f values measured at the top surface of the different samples (including sample *M3*), and listed in Table 1, are plotted in Figure 18.

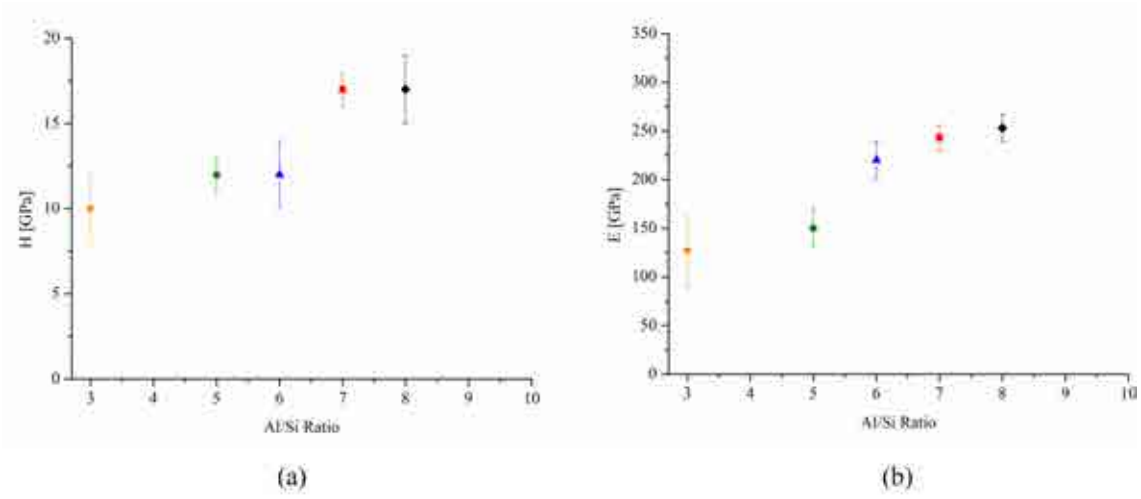

Figure 18. Increase in (a) H_f and (b) E_f values with Al/Si ratio for the coatings studied.

It is evident from this figure that both film hardness and elastic modulus increase with Al/Si ratio. As observed in Figure 18 a, samples *M5* and *M6* exhibit comparable average hardness values. A similar observation applies for samples *M7* and *M8*. A more gradual increase is presented by the elastic modulus, as shown in Figure 18 b.

It is believed that alumina enrichment of mullite occurs accompanied by the introduction of oxygen vacancies in the mullite structure.[2,3] Such an increase in oxygen vacancies has been reported to be the main reason for the higher *H* and *E* exhibited by mullite when compared to sillimanite, from whose structure derives the mullite by substituting certain silicon by aluminium atoms. This replacement requires oxygen vacancies to maintain charge balance, inducing an ordered vacancy structure that obstructs dislocation movement and, thus, plastic deformation.[12] Following this idea, the hardness enhancement evidenced for the different tested coatings as the Al/Si ratio is increased may be rationalized on the basis of this phenomenon. Moreover, rising Al/Si ratio has also been shown to yield an increase in the elastic modulus.[13] The higher average mechanical properties exhibited by the studied coatings as Al/Si ratio is increased may be partly rationalized on the basis of similar ideas.

5.4.2 Influence of composition on K_c

As it may be seen from Figure 19, the apparent fracture toughness of mullite coatings decreases with increasing Al/Si ratio. Samples *M7* and *M8* are approximately 50% more brittle than the stoichiometric mullite (sample *M3*). Therefore, in addition to the hardness and elastic modulus rise, it appears clear that an increase in the Al/Si ratio results in a reduction of the apparent fracture toughness of CVD mullite.

As it was commented above, dislocation movement becomes more difficult as the crystalline structure of CVD mullite gets enriched in Al. Thus, it may be speculated that the more brittle character of the Al-enriched mullite coatings is also in direct relation with such observation. Consequently, the decrease found for fracture toughness of mullite coatings as the Al/Si is raised, may also be directly tied with the increase evidenced in their hardness and stiffness.

In addition, as the aluminium content in the coatings is increased, the mullite structure gets rich in Al_2O_3. Therefore, an increase in the residual stresses developed in the coatings during the fabrication process may be expected due to the thermal mismatch with the SiC during the deposition process. Schneider *et al.*[14] found that, as the Al_2O_3 and the amount of oxygen vacancies increase, the thermal expansion coefficients α_{11} and α_{33} of mullite also increase linearly, while α_{22} decreases. The net effect is an increase in the effective thermal expansion coefficient of mullite with the Al_2O_3 content. From the information provided by these investigators, a thermal expansion coefficient of $\alpha_{mullite} = 6.0 \times 10^{-6}$ °C^{-1} may be extracted for a mullite with an Al_2O_3 content of 78% mol, corresponding to an Al/Si ratio of 7. Using this thermal expansion coefficient for sample *M7*, together with the E_f value measured for this specimen, a residual stresses value of $\sigma_R \approx 300$ MPa may be estimated. If the Marshall and Lawn[11] modification is then implemented, an intrinsic fracture toughness value ($K_c^0 = K_{f)}$ of 1.3 MPa·m$^{1/2}$ can be assessed for sample *M7*.

A slight increase in the average K_f estimated for sample *M7* was found as compared with that of sample *M3*, as it may be observed also from Figure 19. However, such a difference is not statistically significant, as the dispersion of the measurements for both materials overlap. Based on these considerations, it may be stated that although the measured apparent fracture toughness decreases with Al/Si ratio, the estimated intrinsic film toughness is rather retained by the mullite coatings.

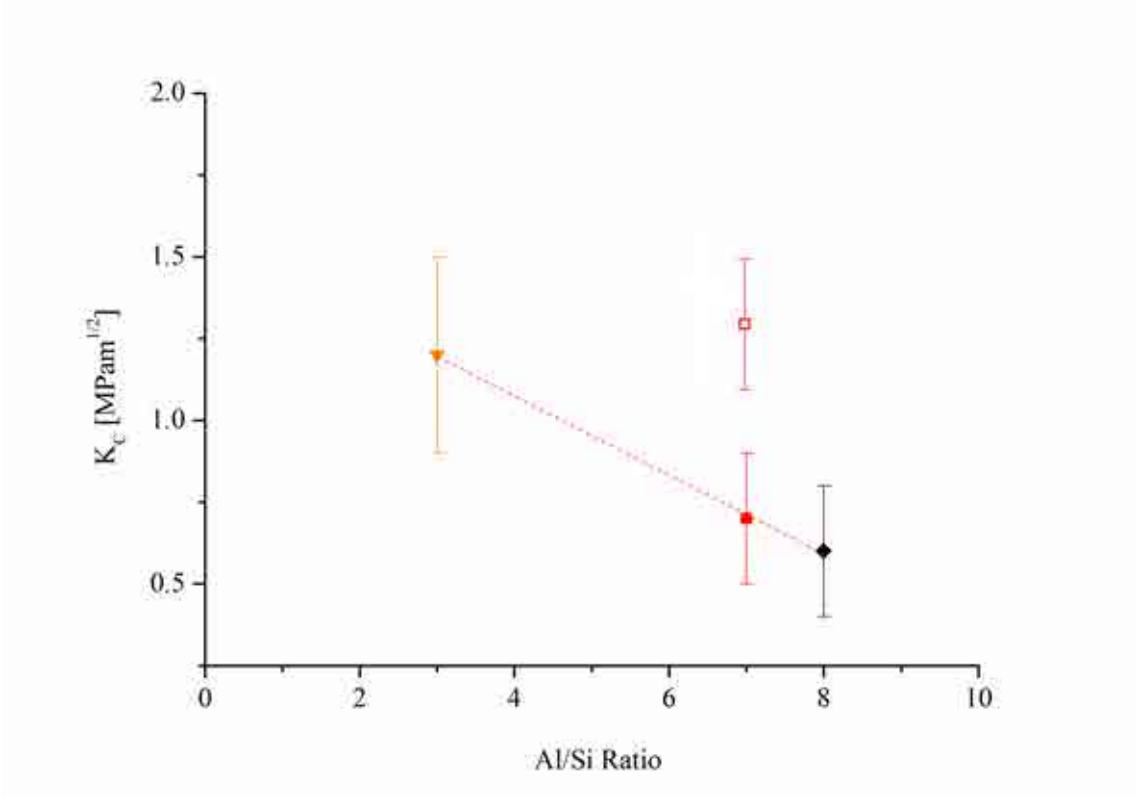

Figure 19. Fracture toughness as a function of Al/Si ratio for samples *M3*, *M7* and *M8*. Estimated K_f is included for sample M7 (□).

5.4.3 Influence of composition on sliding contact resistance

It has been discussed before that Al enhancement attained in mullite coatings yields a rise in their hardness and stiffness, together with a decrease in their apparent indentation fracture toughness. Therefore, as Al/Si ratio is increased it may be expected a more brittle response of the coatings to the scratch tests performed. The influence of the Al/Si

ratio on the sliding contact resistance of the coatings is discussed below, as a function of both scratch penetration and induced damage.

5.4.3.1 Scratch penetration

The curves of indenter penetration recorded during the scratching and post-scanning of samples *M3*, *M5*, *M7* and *M8,* are displayed in Figure 20 a for tests performed at the low load condition. In this figure, the penetration is plotted a function of the scratch distance and applied load. Similarly, the penetration curves corresponding to the high load condition tests, performed on samples *M3* and *M8*, are presented in Figure 20 b.

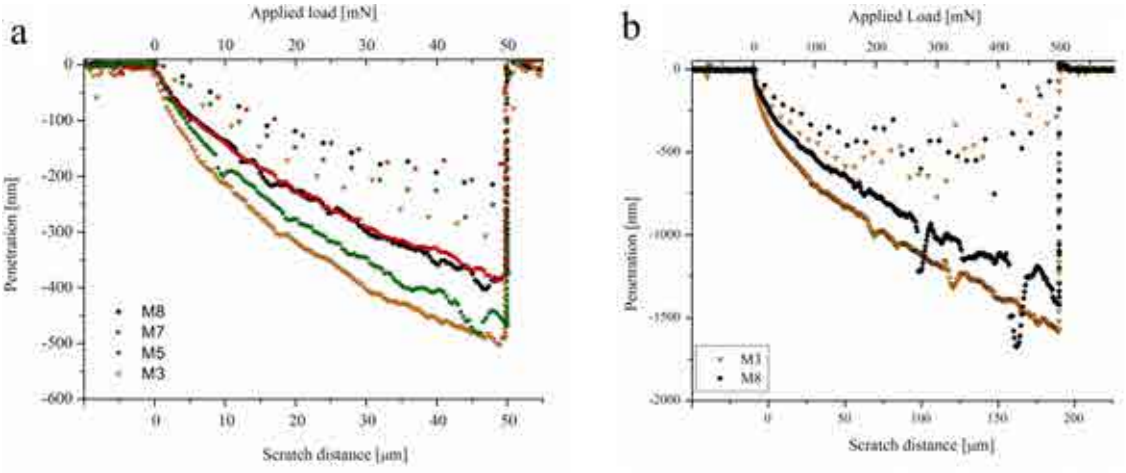

Figure 20. (a) Curves of the indenter penetration as a function of scratch distance in the pre-loading, loading and post-loading stages for scratches performed at the low load condition on samples *M3*, *M5*, *M7* and *M8*. (b) Curves of the indenter penetration as a function of scratch distance in the loading and post-loading stages for scratches performed at the high load condition on samples *M3* and *M8*.

Results plotted in Figure 20 a show how all the studied samples are almost linearly penetrated as the load increases. Furthermore, it may be commented that coatings are penetrated in correspondence to their measured hardness and stiffness values, i.e. as the Al/Si ratio increases, the scratching penetration for a given applied load correspondingly decreases. This correlation is also discerned for the residual penetrations recorded during the post-scanning stage.

On the other hand, a continuous behavior of the penetration curves may be observed for the low load condition scratches, as it is clear in Figure 20 a. Except for the slight cracking documented for sample *M8* (Figure 15 to 17), the referred behavior is in agreement with the absence of significant fracture events produced by the scratches on the studied Al-rich mullite coatings. This may be evidenced by the inspection of the different tracks in Figure 9, 11 and 14.

Regarding the high load scratches, some discontinuities are observed in the penetration curve of sample *M8* in Figure 20 b. This observation contrasts with the continuous character of the curve corresponding to sample *M3*, included in the same figure. The different fracture events observed in the tracks of sample *M8*, may thus be associated with the referred discontinuities in the penetration curves for this sample.

5.4.3.2 Induced damage

The effect of an increased Al/Si ratio on the mechanical performance and structural integrity of mullite coatings was studied by means of nanoscratch tests carried out at the surface of the samples. By conducting these tests at increasing loads, a controlled and progressive damage was induced and analyzed in the studied coatings. Extensive inspection of the residual tracks, together with their surrounding areas, permitted to identify well-differentiated damage events during the nanoscratch tests.

Cracks at 45º with respect to the scratch direction were identified as the first damage event. Such cracks are analogous to the tensile cracks produced behind the indenter during the scratch of hard thick coatings[15,16]. This cracking was followed by damage at the subsurface of the coatings, detected from the optical micrographs. A comparable observation was also found for a thin brittle sol-gel coating deposited on glass[18]. Subsequently, partial spallation of the coatings was evidenced. Partial chipping in the coating, similar to the ones also reported for comparable brittle coated systems, was finally registered[15,16]. These events may be evidenced throughout micrographs acquired for the different Al-rich coatings, (Figure 8 to 17). All the damages events identified,

together with the load associated with their emergence in the different coatings studied, are included in Table 4.

Load [N]	0-50	50-100	100-150	150-250	250-350	350-500
M3	×	×	×	×	*Subsurface damage*	
M5	×	×	*Cracking and Subsurface damage*			
M7	×	*Cracking*	*Cracking and subsurface damage*			*Spalling*
M8	*Cracking*			*Cracking and subsurface damage*		*Chipping*

Table 4. Events of damage observed and the load associated with their emergence in the different samples studied.

Based on the micrographic analysis, as well as on the information collected in Table 4, it may be indicated that the magnitude of the damage events induced in the materials was higher as the applied load was increased along the scratch track for each individual sample. In addition, it must be pointed out that the magnitude of the induced damage also increased as the mullite coatings were enriched in Al. This is in good agreement with the increasingly brittle nature of the Al-rich mullite coatings.

In general terms, it may be stated that the mullite coatings evaluated present a satisfactory response against sliding contact. Considering the coated $3Al_2O_3{\cdot}2SiO_2$ system as a structural unit, the damage produced by the nanoscratches under the load regimes implemented in this thesis can be considered as minor. Cracking, spalling and partial chipping evidenced in the coatings investigated, are typical damage events within the scratch response of ceramic (brittle) materials both in bulk monolithic and thick coated configurations.[15,17] In this regard, it deserves to be highlighted that the most significant damage discerned, among all the studied materials, was a partial decohesion experienced by sample *M8*. Within the range of loads applied in the scratch tests (P = 0-500 mN), complete removal of the coating was not observed in any of the samples. This is an important finding considering the protective role to be played by

these materials as environmental barrier coatings, where an entire loss of the coating material would imply a direct exposure of significant substrate areas to corrosive media.

5.5 Summary

The influence of the composition on the mechanical properties and behavior of CVD mullite coatings was evaluated by nanoindentation and nanoscratch tests conducted on the surface of different Al-rich coatings. The main findings of this investigation may be summarized as follows:

- A rise in hardness was evidenced as the Al/Si ratio increases in mullite coatings. Film hardness values increases from $H_f \approx 12$ to 17 GPa, as evaluated for samples *M5* to sample *M8* respectively.

- The coating stiffness was also found to increase with Al enhancement of mullite. Intrinsic film elastic modulus values of E_f = 150 GPa, 220 GPa, 243 GPa and 253 GPa, were evaluated for samples *M5, M6, M7 and M8* respectively.

- The apparent indentation fracture toughness of mullite coatings decreased with rising Al/Si ratio. Film fracture toughness values of K_c = 0.6 and 0.7 MPa·m^{½} were found for the samples *M7* and *M8* respectively. Those values contrast with the one determined for of stoichiometric mullite (sample *M3*), K_f= 1.2 MPa·m^{½}.

- The intrinsic fracture toughness of sample *M7*, estimated considering the effect of residual stresses, yielded $K_f \approx 1.3$ MPa·m^{½}. Comparing this value with that of the stoichiometric mullite coating ($K_f \approx 1.2$ MPa·m^{½}), it may be underlined that intrinsic toughness is kept for the Al-rich coating of sample *M7*.

- An increasingly brittle response to the sliding contact was evidenced for the mullite coatings as they are enriched in Al. Within this context, different sequential fracture events were observed and documented: cracks at 45º of the scratch direction, subsurface damage, and partial coating spallation and chipping. The magnitude of the damage increases with the indenter load and the Al/Si ratio of the investigated samples.

- All the EBCs investigated presented a satisfactory response under the nanoscratches performed, as no complete loss of the coating material was registered under the load spectrum analysed.

5.6 References

1. Auger, M., Sarin, V.K. The development of CVD mullite coatings for high temperature corrosive applications. *Surf. Coat. Technol.* **94-95**, 46-52 (1997).

2. Basu, S., Hou, P., Sarin, V.K. Formation of mullite coatings on silicon-based ceramics by chemical vapor deposition. *Int. J. Refract. Met. Hard Mater.* **16**, 343-352 (1998).

3. Hou, P., Basu, S.N., Sarin, V.K. Structure and high-temperature stability of compositionally graded CVD mullite coatings. *Int. J. Refract. Met. Hard Mater.* **19**, 467-477 (2001).

4. Basu, S.N., Kulkarni, T., Wang, H.Z., Steen, T., Murray, T.W., Sarin, V.K. Structure and properties of functionally graded environmental barrier coatings for ceramic components in gas turbines. *Proc. Int. Conf. Adv. Mat. Comp.* 1050-1060 (2007).

5. Kulkarni, T., Basu, S.N., Sarin, V.K. Advanced environmental barrier coatings (EBCs). *Key Eng. Mater.* **333**, 59-70 (2007).

6. Basu, S., Kulkarni, T., Wang, H., Sarin, V.K. Functionally graded chemical vapor deposited mullite environmental barrier coatings for Si-based ceramics. *J. Eur. Ceram. Soc.* **28**, 437-445 (2008).

7. Kulkarni, T., Wang, H.Z., Basu, S.N., Sarin, V.K. Compositionally graded mullite-based chemical vapor deposited coatings. *J. Mater. Res.* **24**, 470-474 (2009).

8. Kulkarni, T., Wang, H.Z., Basu, S.N., Sarin, V.K. Protective Al-rich mullite coatings on Si- based ceramics against hot corrosion at 1200°C. *Surf. Coat. Technol.* **205**, 3313-3318 (2011).

9. Oliver, W.C., Pharr, G.M. An improved technique for determining hardness and elastic modulus using load and displacement sensing indentation experiments. *J. Mater. Res.* **7**, 1564-1583 (1992).

10. Anstis, G.R., Chantikul, P., Lawn, B.R., Marshall, D.B. A critical evaluation of indentation techniques for measuring fracture toughness: I, direct crack measurements. *J. Am. Ceram. Soc.* **64**, 533-538 (1981).

11. Marshall, D.B., Lawn, B.R. An indentation technique for measuring stresses in tempered glass surfaces. *J. Am. Ceram. Soc.* **60**, 86-87 (1977).

12. Pitchford, J.E., Stearn, R.J., Kelly, A., Clegg, W.J. Effect of oxygen vacancies on the hot hardness of mullite. *J. Am. Ceram. Soc.***68**, 1167-1168 (2001).

13. Murray, T., Balogun, O., Steen, T., Basu, S., Sarin, V.K. Inspection of compositionally graded mullite coatings using laser based ultrasonics. *Int. J. Refract. Met. Hard Mater.* **23**, 322-329 (2005).

14. Schneider, H., Schreuer, J., Hildmann, B. Structure and properties of mullite—A review. *J. Eur. Ceram. Soc.* **28**, 329-344 (2008).

15. Bull, S., Berasetegui, E. An overview of the potential of quantitative coating adhesion measurement by scratch testing. *Tribol. Int.* **39**, 99-114 (2006).

16. Bull, S.J. Failure mode maps in the thin film scratch adhesion test. *Tribol. Int.* **30**, 491-498 (1997).

17. Malzbender, J., Toonder, J.M.J.D., Balkenende, A.R., With, G.D. Measuring mechanical properties of coatings: a methodology applied to nano-particle-filled sol–gel coatings on glass. *Mat. Sci. Eng. R* **36**, 47-103 (2002).

6 *Chapter*

Influence of the composition on mechanical properties of functionally graded $3Al_2O_3{\cdot}SiO_2$ coatings

Conventionally, nanoindentation and nanoscratch tests are performed on the surface of films to evaluate their mechanical integrity: elastic modulus, hardness, toughness and adhesion strength. However, in complex systems such as compositionally graded thin films, small spatial variations in mechanical properties are difficult to distinguish using this approach.

In this chapter, the evaluation of the parameters mentioned above was conducted on compositionally graded mullite coatings. Nanoindentation tests carried out on the polished cross-sections and wedges of compositionally graded mullite coatings, permitted the assessment of spatial variations in H and E. A gradual rise in such properties with the thickness was evidenced. Additionally, transverse nanoscratch tests allowed for the evaluation of cohesive and adhesive resistance of the coatings.

Compositionally graded mullite coatings exhibited an optimum combination of hardness/stiffness and cohesive/adhesive scratch strength.

6.1 Introduction

To resolve the problem of long-term corrosion, functionally graded CVD mullite coatings on SiC substrates, in which the Si content is varied, have been developed. [1–7]. These coatings combine both the good match achieved in the mullite/SiC interface due to their similar thermal expansion coefficients, and the excellent corrosion and recession resistance of the Al-rich top surface of the coating in contact with corrosive atmospheres. Additionally, abrupt changes in phase and composition are eliminated, resulting in a reduction of internal residual stresses generated during heating and cooling in the fabrication process, as well as during thermal cycling in service conditions[8]. Although the protective nature of graded mullite coatings against SiC corrosion, as well as their microstructure, has been well characterized, similar information about their mechanical properties is quite scarce.

Aiming to evaluate the mechanical properties of thin coatings and the structural integrity of coated systems, nanoindentation and nanoscratch tests are conventionally performed on the surface of the coating[9–16]; and then the mechanical properties of the coating are extrapolated and separated from those of the substrate. However, in more complex scenarios such as functionally graded thin films, changes in mechanical properties within the coating are difficult to discern by following this approach[17]. In these cases, the implementation of nanoindentation on cross-sectional and wedge configurations of layers and coatings with spatial variations in properties, have been shown to be effective approaches.[18–20] Additionally, assessment of interfacial adhesion response in multi-layer thin films through nanoscratch tests executed on the corresponding cross-section is also possible[21].

This chapter focuses on the nanomechanical characterization of functionally graded mullite coatings. Nanoindentation tests were conducted on both mullite coatings with fixed and graded Al/Si deposition ratios following the cross-sectional and wedge approaches. Intrinsic coating hardness (H_f) and elastic modulus (E_f) were evaluated, including their variation across the thickness of the coating. The effect of the residual

stresses (σ_r) on the measured mechanical properties is also discussed. Attempting to identify critical load ranges for the emergence of distinct cohesive and decohesive damage modes, nanoscratch tests on cross-sections were conducted following both `top to bottom´ and `bottom to top´ sliding directions.

6.2 Experimental

Two categories of coatings were investigated, namely compositionally graded films deposited under variable Al/Si ratio (samples *Graded-I* and *Graded-II*), and coatings with constant ratios of Al/Si (3, 5, 7, 8 and 11), and labeled as *M3-I and M3-II, M5, M7, M8* and *M11*, respectively, as it was already indicated in *Chapter 3*.

For the cross-sectional approach, nanoindentation was performed in all studied samples, whereas nanoscratch tests were exclusively conducted in samples *M3-II*, *M11* and *Graded-I* exclusively. For the wedge approach, nanoindentation was uniquely carried out on sample *Graded-II*.

6.2.1 Composition of graded samples

To investigate compositional changes in the compositionally graded coatings, cross-sections were prepared using FIB, following the procedure described in section 3.5.3 of *Chapter 3*. Elemental chemical analyses were conducted in different points along the coating thickness by using energy dispersive X-Ray spectroscopy (EDX).

6.2.2 Cross-sectional and wedge nanoindentation

Nanoindentation tests were performed at a penetration depth of h_{max} = 100 nm in all cases. Separation between indents of 2.5 μm was selected in the case of the cross-sectional approach. As schematically shown in Figure 1 a, indentation matrices of

3 columns and a variable number of rows, depending on the particular sample thickness, were performed. For the wedge approach, similar indentation matrices were conducted. In this case, separation between indents was varied according to the film thickness, aiming to conduct 10 indentation rows across the coating, as it may be observed in Figure 1 c. H_f and E_f values were calculated for all studied coatings as a function of the penetration depth using the Oliver and Pharr method [22].

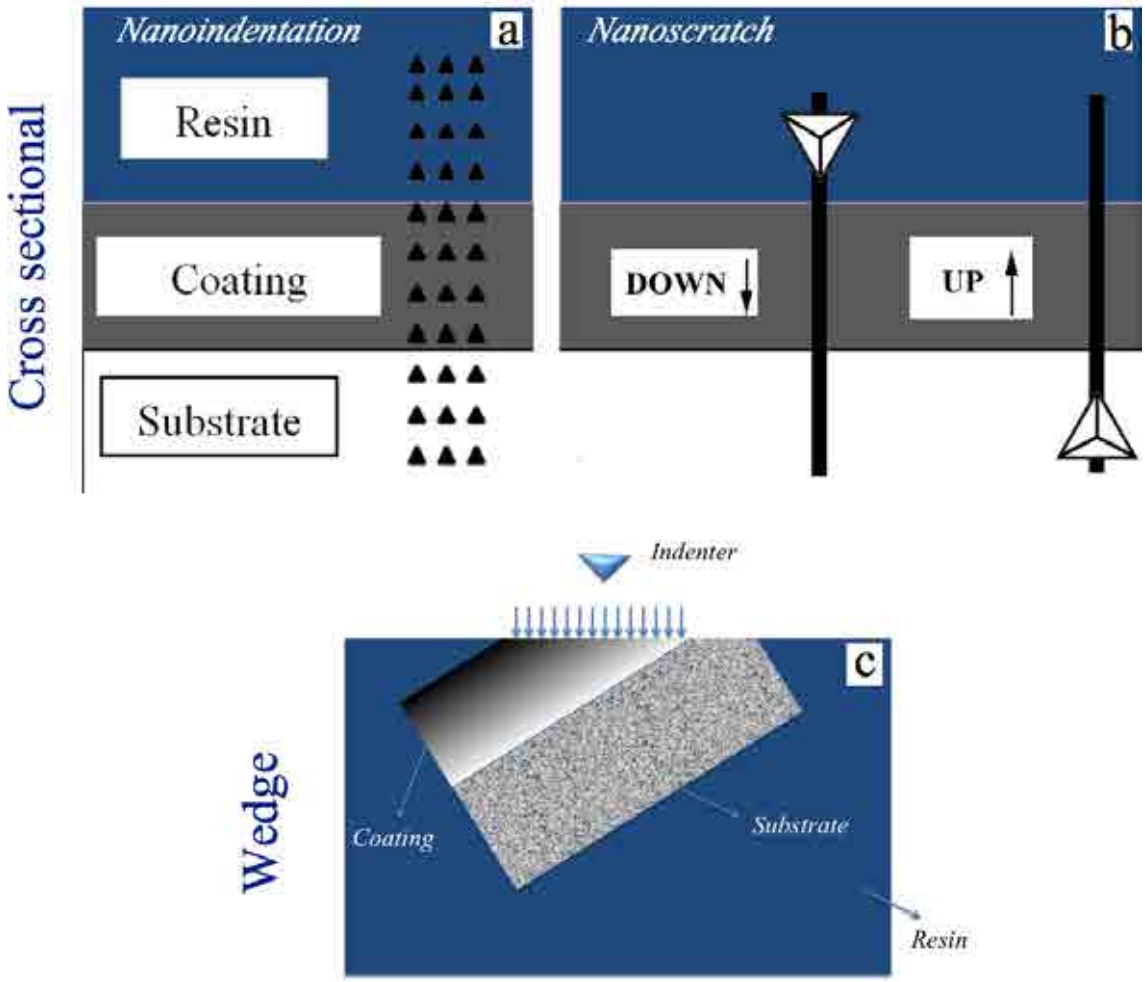

Figure 1. Mechanical tests in the cross-sectional approach : (a) Nanoindentation; and (b) Nanoscratch, *UP* ("Bottom to top") and *DOWN* ("Top to bottom") directions. (c)Nanoindentation in the wedge approach.

Mechanical tests were carried out in mirror-polished cross-sections as the example shown in Figure 2.

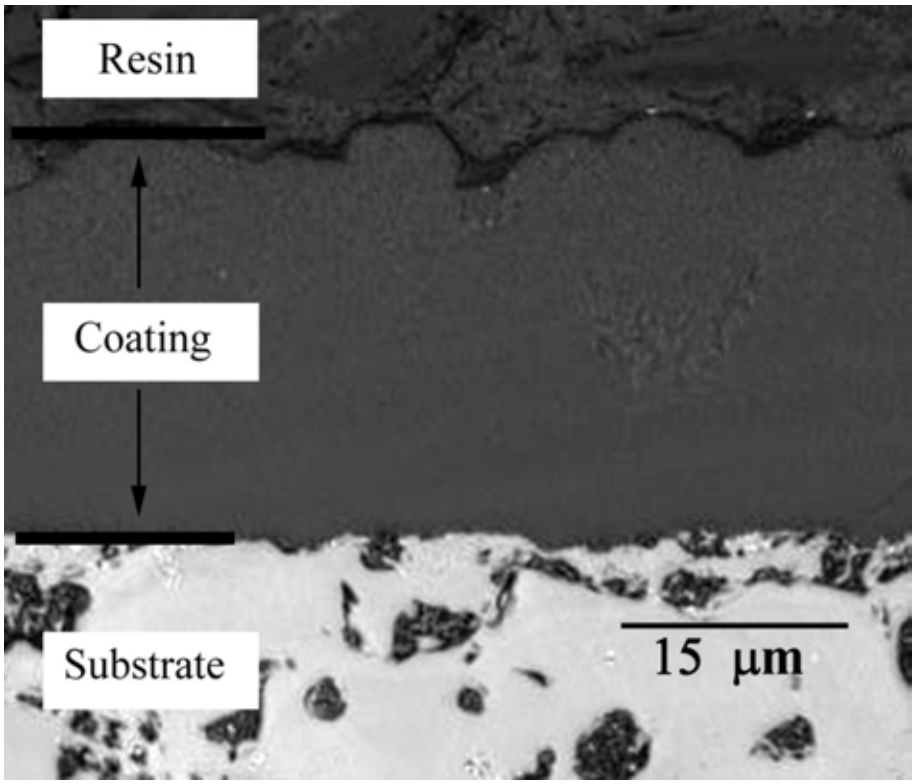

Figure 2**.** LCSM image of prepared cross-section, sample *M11*.

6.2.3 Coating separation

In order to evaluate the potential effect of the residual stresses present in the compositionally graded coatings, a portion of the specimen *Graded II* was mechanically separated from the coating, following a three-step procedure (Figure 3). The detached portion of the coating (see Figure 3 b), with a thickness of ≈ 18 µm, was re-embedded in resin and re-polished (see Figure 3 c). The freestanding cross-section of the coating was indented with a matrix of 10 rows and 6 columns, with rows parallel to the coating/substrate interface.

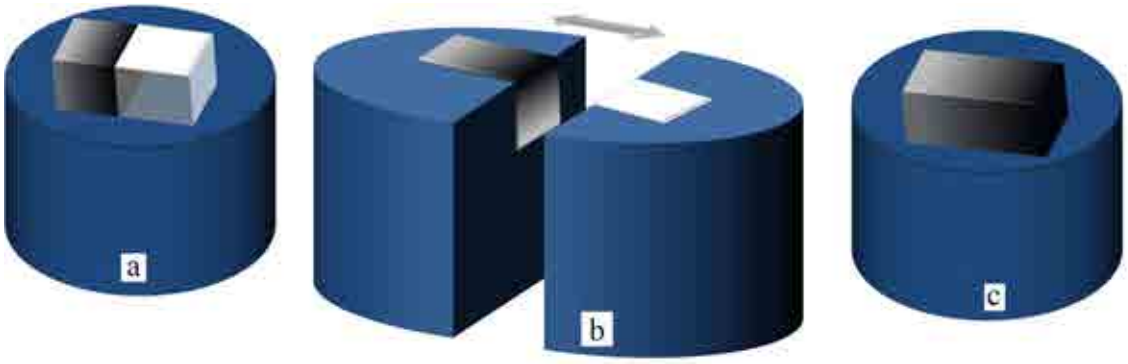

Figure 3. Illustration of the process followed to detach the coating in sample *Graded II*. (a) "Supported" coating, (b) coating separation by mechanical means and (c) "freestanding" coating.

6.2.4 Cross- sectional nanoscratch

Polished cross-sections were subjected to constant load nanoscratches using a Berkovich indenter at a sample displacement rate (scratch velocity) of 1 μm/s.

Tests were conducted following two opposite direction paths (Figure 1 b): *i*) from the substrate, through the coating, into the resin (i.e. `bottom to top´); and *ii*) from the resin, through the film, into the substrate (i.e. `top to bottom´). In this investigation, these two unidirectional sliding paths are referred to as *UP* and *DOWN* respectively. In both cases, tests were performed with one corner of the Berkovich indenter pointing the scratch direction.

The two-way testing approach was implemented for assessing properties of the systems ascribed to emergence of damage of different nature: cohesive within the film in the *DOWN* path and adhesive at the interface in the *UP* one. The applied load spectrum for damage occurrence was found to be below 300 mN. Thus, nanoscratch characterization was conducted as series of constant load tests with 50 mN step-increasing applied loads: 50 mN, 100 mN, 150 mN, 200 mN, 250 mN and 300 mN for the three coated systems studied.

6.3 Results and Discussion

6.3.1 Compositional profile of graded samples

A SEM micrograph of the FIB cross-section for *Graded-II* sample is shown in Figure 4. The dense and compact nature of these coatings is evident. EDX elemental analysis was performed on the coating cross-section along a line, at different distances from the interface. Al/Si ratios were determined at each point of the line, and are shown in Figure 4, superposed on the FIB cross-section. In this functionally graded coating the aluminum to silicon ratio was observed to increase from the coating/substrate interface up to the coating surface with a maximum ratio of around 18 at the top.

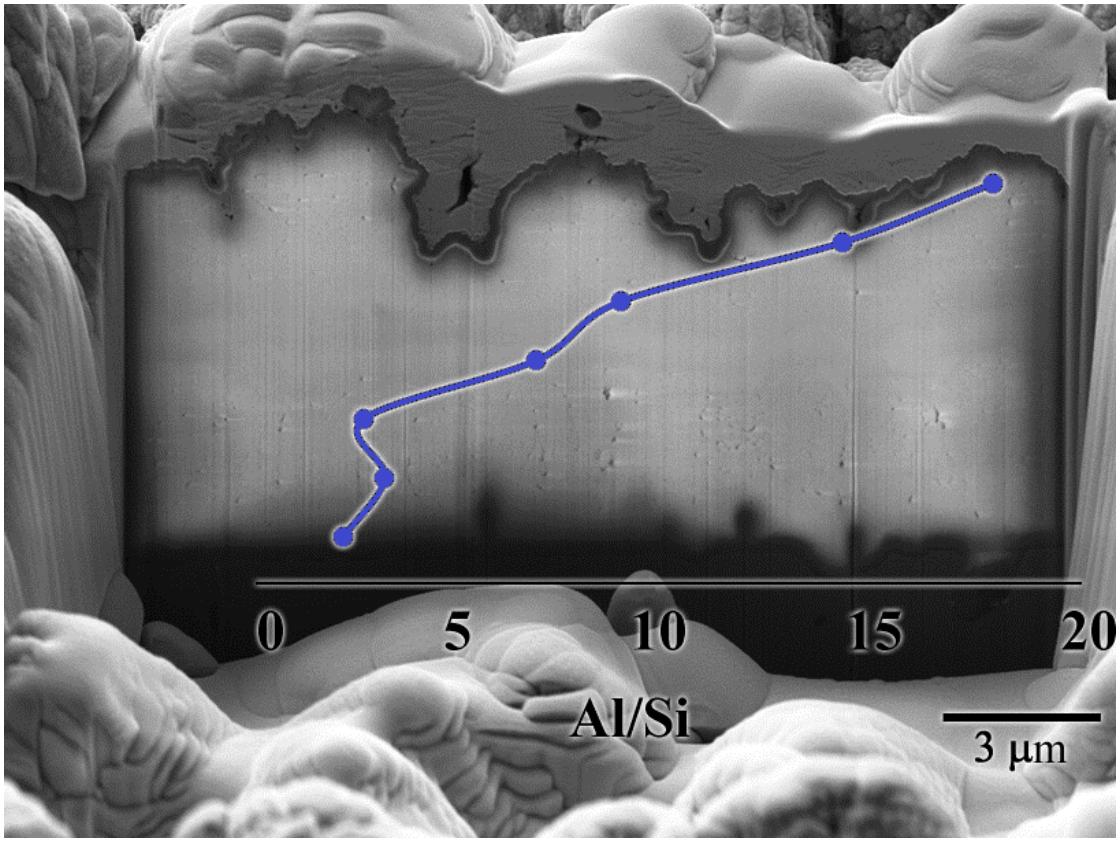

Figure 4. FIB cross-section of *Graded-II* sample. Superposed, Al/Si ratio as a function of distance from the interface.

6.3.2 Hardness and stiffness

6.3.2.1 Cross-sectional approach

Nanoindentation matrices were performed on the cross-sections to evaluate hardness and stiffness as a function of depth within the coating thickness. As an example, a residual matrix of imprints for the sample *M11* is shown in Figure 5.

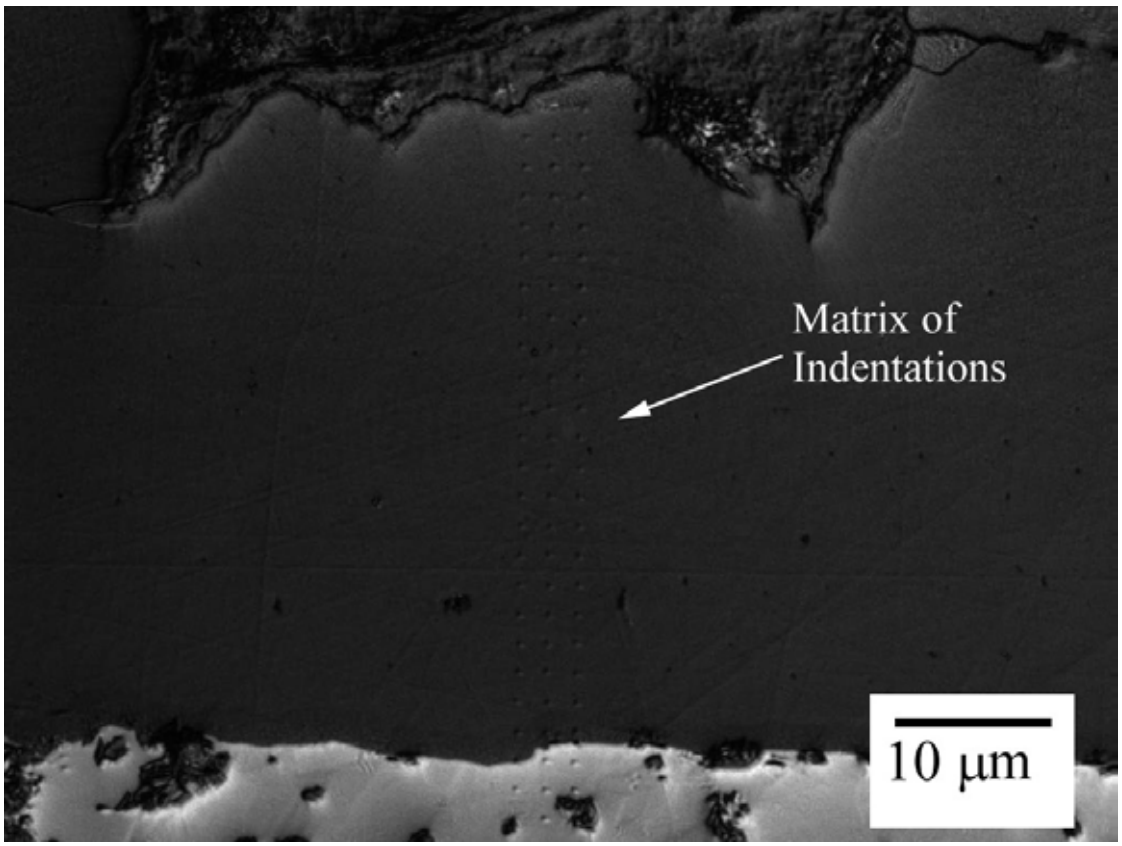

Figure 5. Matrix of nanoindentations, sample *M11*.

The average H_f and E_f values, and their standard deviations for the materials with fixed Al/Si compositions (*M3-I, M5*, *M6*, *M7* and *M11*), are given in

Table 1, and are plotted in Figure 6.

	M3	***M5***	***M6***	***M7***	***M11***
H [GPa]	10 ± 1	12 ± 1	16 ± 3	16 ± 2	22 ± 2
E [GPa]	137 ± 1	138 ± 16	224 ± 16	226 ± 52	274 ± 27

Table 1. Average intrinsic hardness H_f and elastic modulus E_f in samples *M3-I*, *M5*, *M6*, *M7 M8* and *M11*.

Calculated hardness and elastic modulus for sample *M3-I* ($H_f \approx 10.5$ GPa and $E_f \approx 137$ GPa), are within the range of values determined following the top surface approach for stoichiometric mullite coatings, as presented in *Chapter 4*. Average H_f and E_f measured following the cross-section approach for individual specimens with Al-rich compositions were found to increase as a linear function of the Al/Si ratio. Cross-sectional properties in each sample are comparable with those measured following the surface approach (as listed in table 1 of *Chapter 5*).

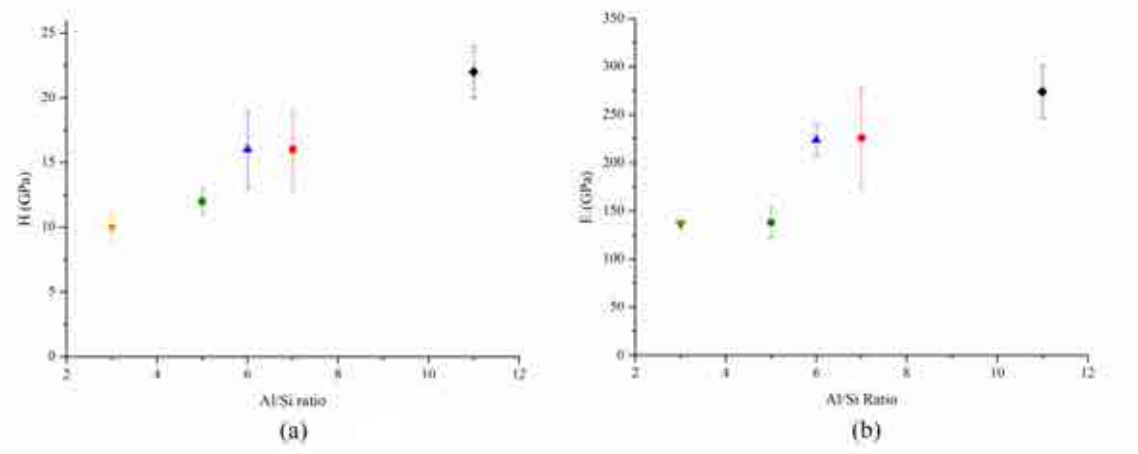

Figure 6. Cross-sectional intrinsic (a) hardness and (b) stiffness of mullite coatings with constant Al/Si ratios as a function of the Al/Si ratio.

Hardness and stiffness values for sample *Graded-I* were found to change as a function of position along the coating thickness; thus, they are not listed as single-value properties in

Table 1. The response of this sample is graphically presented in Figure 7 and 8 in terms of the input gases Al/Si ratio (bottom horizontal axis) as well as of the distance from the interface (top horizontal axis).

In these figures, average data for the extreme conditions (*M3-I* and *M11* samples) are also included. Error bars correspond to the standard deviation of 3 measurements at each relative position, corresponding to nanoindentations performed on the cross-section for each condition.

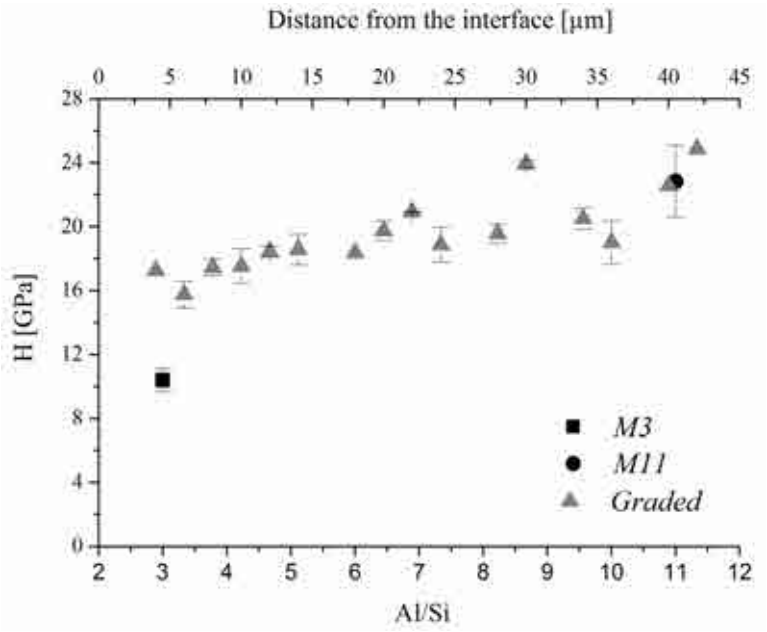

Figure 7. Average hardness of studied samples as a function of the input Al/Si ratio (bottom horizontal axis); and of the distance from the interface for sample Graded (top horizontal axis).

As the Al/Si ratio increases through the thickness, hardness and stiffness of the compositionally *Graded* mullite rises from values close to those exhibited by *M3-I* (stoichiometric ratio) to levels similar to the ones measured for *M11* (Al-richest composition).

It may be speculated that the rises in hardness and stiffness, evidenced as the Al/Si ratio increase with the thickness in the functionally graded coatings, is also related to the introduction and ordering of oxygen vacancies in the mullite structure. Thus, it may be

stated that the individual mechanical behavior observed in samples with fixed Al/Si ratio, is resembled by that of functionally graded coatings across its thickness.

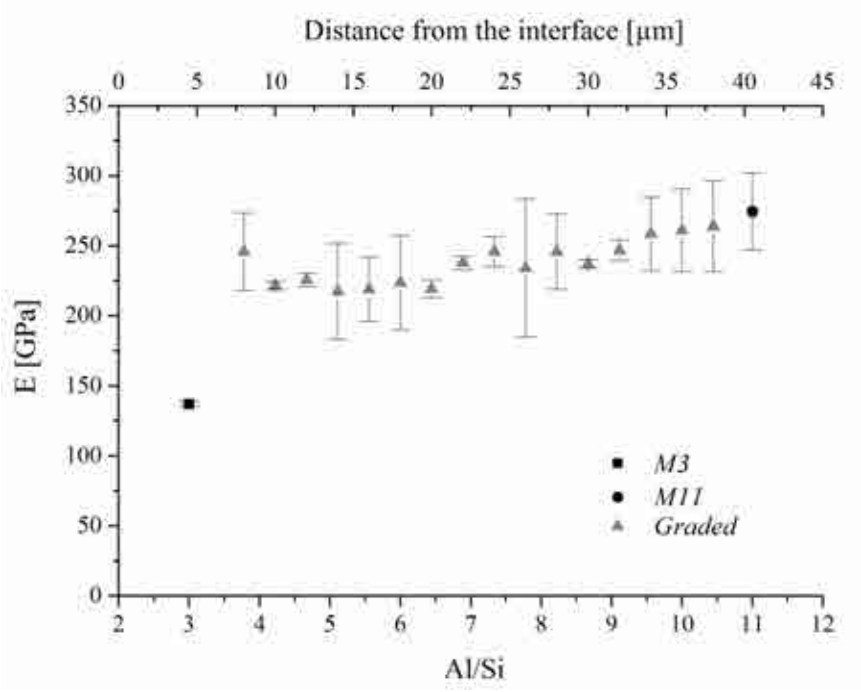

Figure 8. Average elastic modulus of the studied samples as a function of the input Al/Si ratio (bottom horizontal axis); and of the distance from the interface for sample Graded (top horizontal axis).

6.3.2.2 Effect of residual stresses on *H* and *E*

The effect of σ_r in the measurement of H_f and E_f of functionally graded mullite coatings was evaluated by comparing the results obtained in both supported and freestanding coatings.

In Figure 9, the separation process of a coating portion of sample *Graded-II* is shown. Results of H_f and E_f measured through the cross-section of the supported (Figure 9a) and freestanding (Figure 9 c) coating are compared in the graphs of Figure 10.

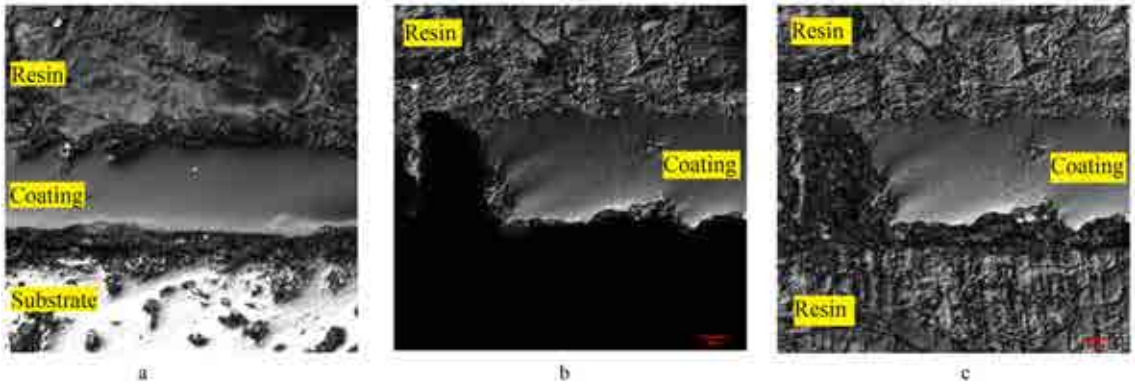

Figure 9. Separation process of the mullite coating from the SiC substrate in sample *Graded-II*. (a) Supported coating, (b) intermediate step in separation process and (c) freestanding coating.

In spite of the considerable scatter of data, it may be observed that both hardness and elastic modulus exhibited the same rising trend as the measurements were conducted across the thickness. The fact that coatings were supported or freestanding did not have a marked effect on the measured mechanical properties.

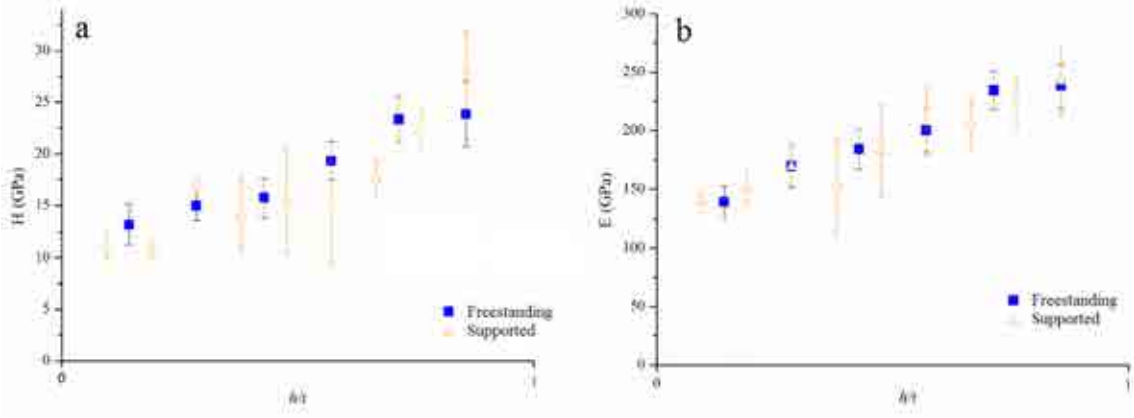

Figure 10. Comparison between the (a) hardness and (b) elastic modulus of supported (▲) and freestanding (■) coatings for sample *Graded-II*.

This finding may be understood on the basis of two considerations. First, it is believed that gradation in composition across the thickness reduces the internal stresses during CVD process of mullite coatings[6,8]; and consequently, low residual stresses may be expected in the samples tested. Second, it has been demonstrated that residual stresses do not affect considerably the hardness and elastic modulus obtained by

nanoindentation as far as their magnitude is not close to the value of hardness[12].This is in agreement with the negligible influence of residual stresses on the nanoindentation hardness found for both functionally graded WC-Co composites[19] and yttria-stabilized zirconia (YSZ) coatings with gradient mechanical properties[20]. In the study involving YSZ films, the effect of residual stresses was evaluated following the same "wedge" methodology implemented in the present thesis.

As it is shown in Figure 11 a, an indentation matrix was conducted on the freestanding coating of sample *Graded-II*, covering an area of 30x15 µm. An *x-y* grid was created from the indentation points, and corresponding *H* and *E* values were assigned to each point of the grid. A color code was assigned to the minimum and maximum values, and a color map of the indented area was constructed by interpolating both hardness (Figure 11 b) and elastic modulus (Figure 11 c) values.

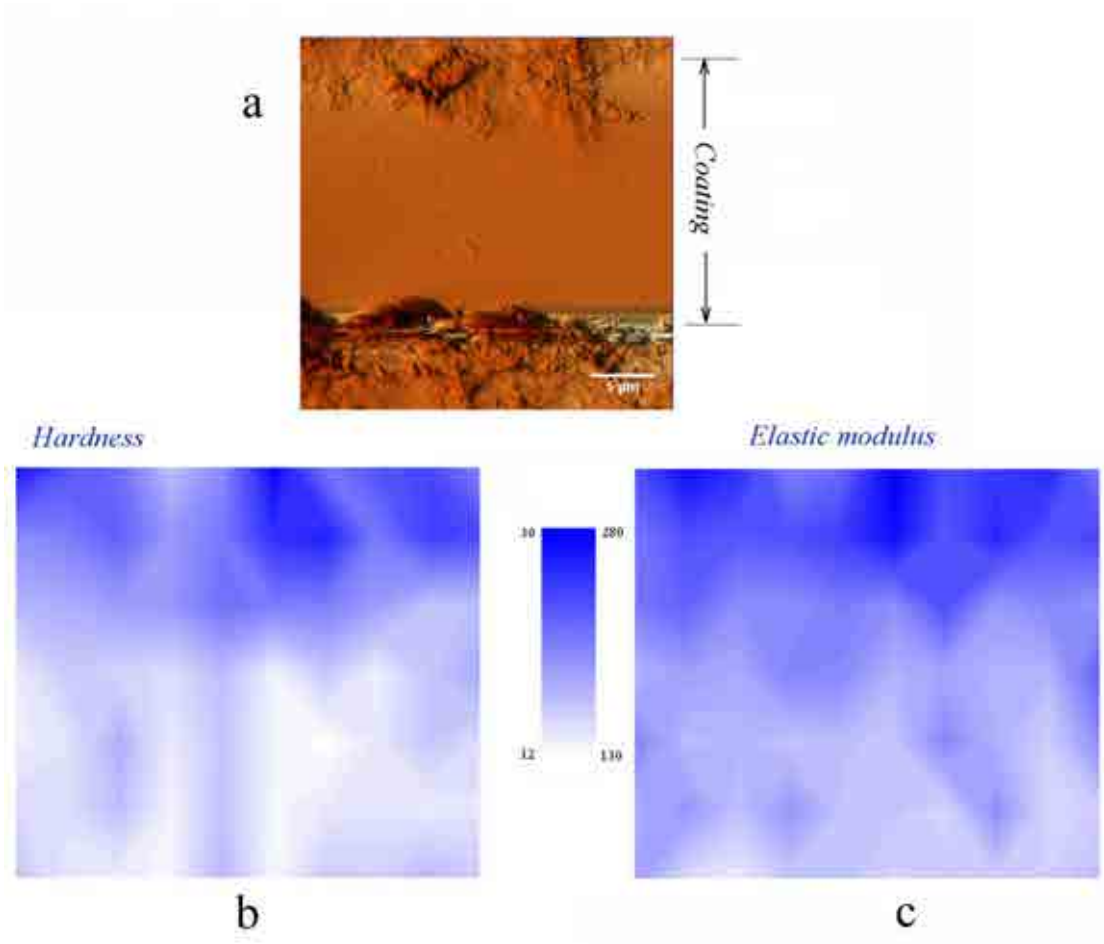

Figure 11. (a) AFM image of a matrix of 10x6 indentations in a freestanding portion of the coating of sample *Graded-II*. (b) Hardness and (c) elastic modulus maps for a coating area of 30x15 µm.

The spatial variation in properties may be observed from the maps. Although it is evident that both *H* and *E* increase with the thickness towards the coating surface, such a rise in properties is not homogeneous. The slight scatter in the measurements may be directly linked with the columnar nature of the coatings.

6.3.2.3 Wedge approach

The sample *Graded-II* was also indented in the wedge configuration. Micrographs corresponding to the location of indentations in this sample are presented in Figure 12.

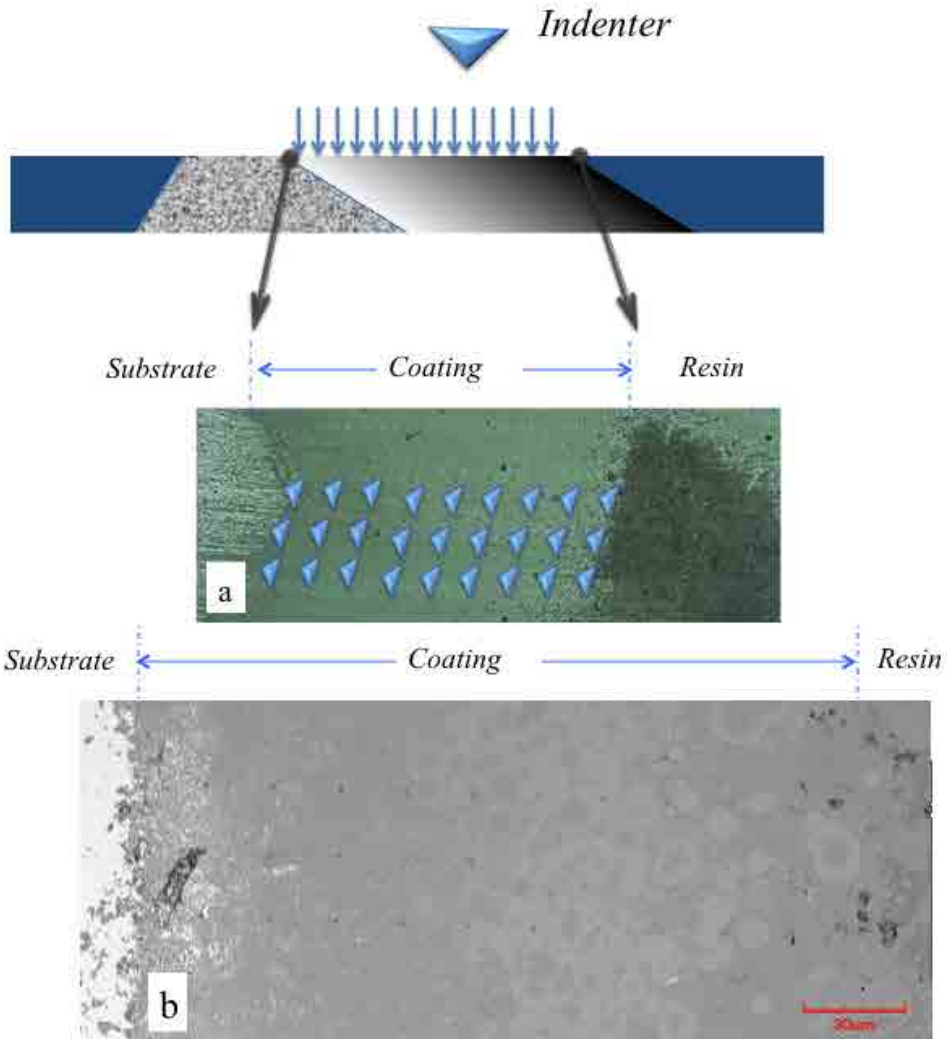

Figure 12. (a) Top optical micrograph indicating indentation sites in the polished wedge of sample *Graded -II*. (b) Top confocal micrograph showing imprints across coating thickness.

Profiles of the average H_f and E_f measured across the thickness are presented in Figure 13. For comparison reasons, data of the indentations obtained at the cross-section in sample *Graded-II* are also included in this figure.

A gradient in mechanical properties with thickness may be assessed evaluated by means of the wedge approach. In addition, from Figure 13 is evident that measured properties yield similar results when evaluated following both wedge and cross-sectional approach. Furthermore, regarding the properties of samples with fixed Al/Si ratios, it should be recalled the relative agreement among results evaluated at the surface and those evaluated at the cross section. Based on such considerations, it may be stated that, within the range of the experimental scatter, the three approaches implemented in this thesis are effective and complementary methods to assess the mechanical properties of CVD mullite coatings.

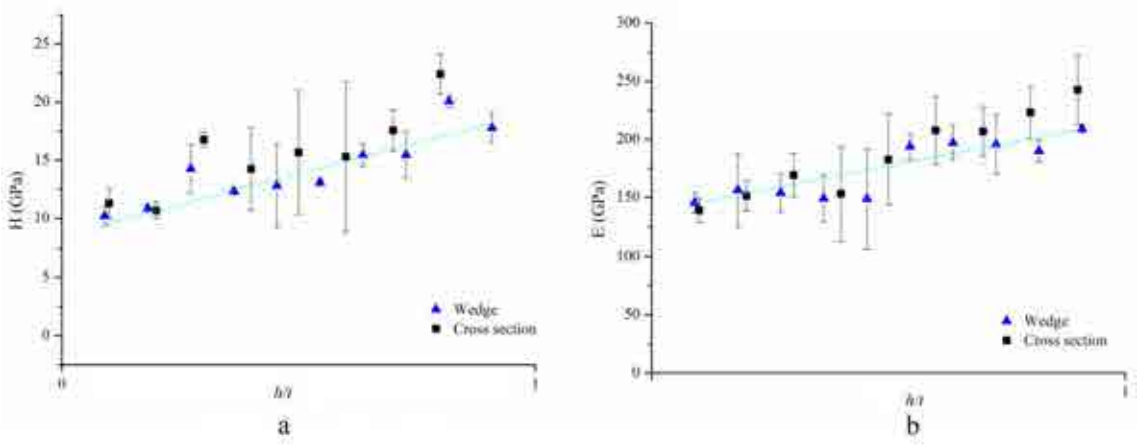

Figure 13. (a) Hardness and (b) elastic modulus profiles using the wedge approach in sample *Graded-II* (▲). Data obtained in the cross-section of sample *Graded-II* (■) is also included for comparison reasons.

6.3.3 Cohesive and adhesive strength

Damage resistance was evaluated by means of nanoscratch testing using a Berkovich indenter. For the three systems studied, nanoscratch tests were performed following two opposite paths (*DOWN* and *UP*), although always with one corner of the Berkovich

indenter in the scratch direction, at different constant applied loads. Figure 14 shows a series of tests, run in the *DOWN* direction for specimen *M11*.

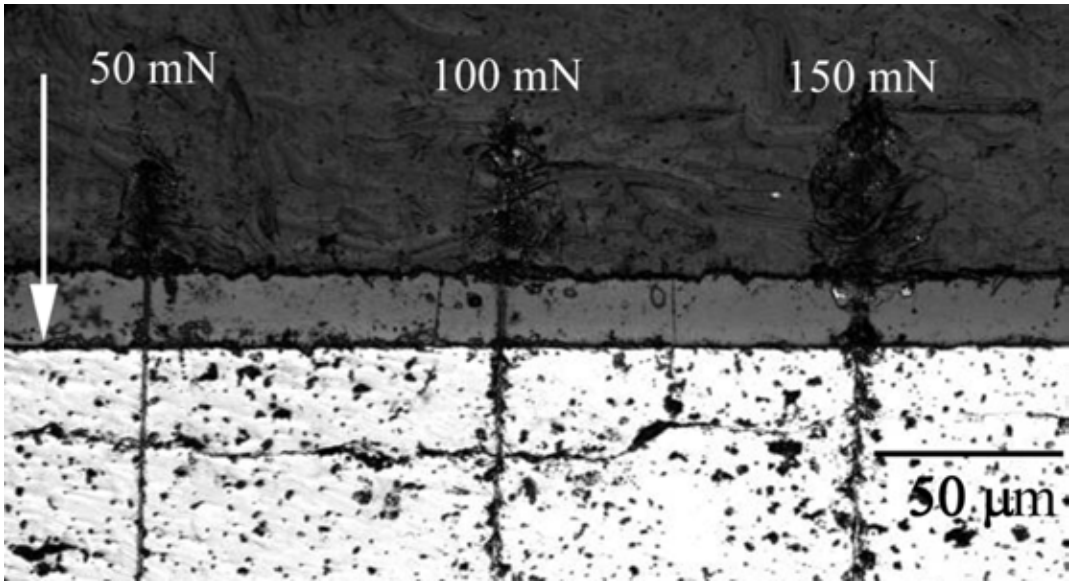

Figure 14. Tracks of nanoscratches performed at different loads in DOWN direction on sample M11.

As a result of the nanoscratch tests performed on the cross-sections, four different damage morphologies were distinguished, as illustrated in Figure 15. These damage phenomena originated in the two scratching direction paths employed. Before discussing them in detail, it should be highlighted that even though some local damage on the interface was observed at given applied loads, there was not any evidence of delamination as a consequence of the nanoscratches performed, at least within the load range here investigated. This suggests good interfacial adhesion between coating and substrate. Indeed, such good bonding should be rather expected after considering the similarities in thermal expansion coefficients between layer and substrate as well as the alike chemical nature of mullite and SiC.

During nanoscratch testing in the *UP* direction, as the indenter progresses the first element of the system subjected to load is the interface. Therefore, the load level for appearance of damage at the interface (Figure 15), defines in *UP*-direction tests the

"adhesive" failure limit state. On the other hand, the load for which damage emerges within the coating (Figure 15), when scratches are conducted in the *DOWN* direction, denotes the "cohesive" resistance of the system.

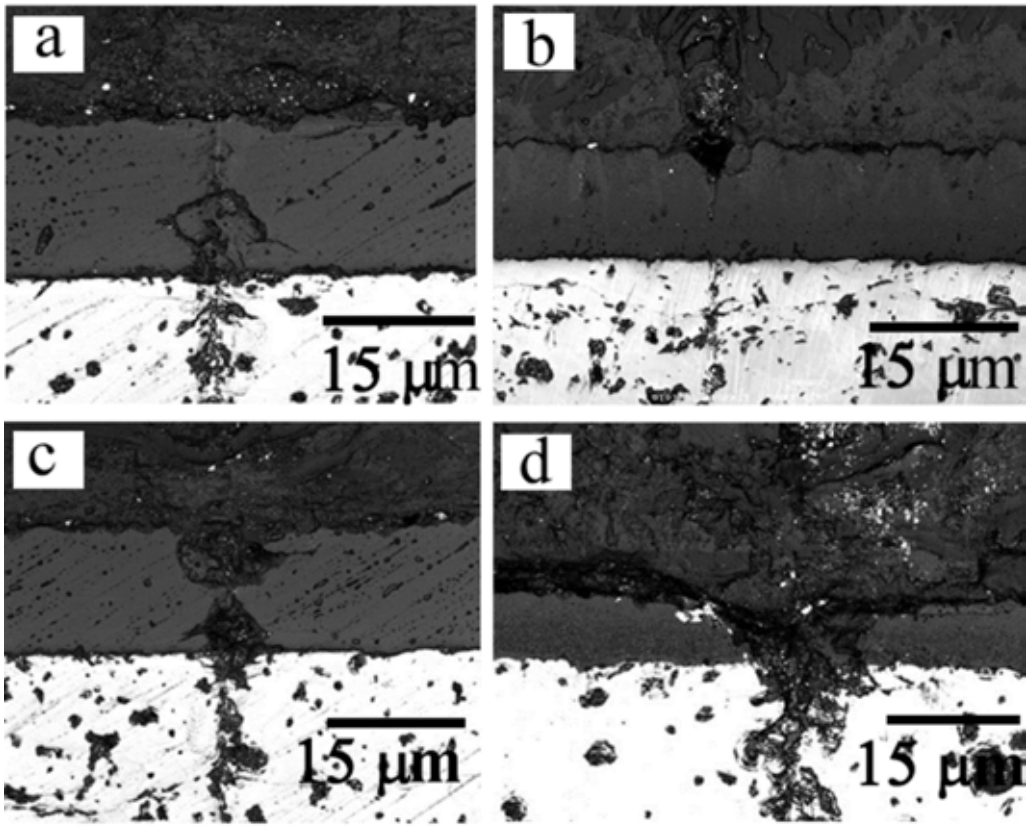

Figure 15. Different damage morphologies evidenced: (a) adhesive at the interface; (b) cohesive in the coating; (c) combined adhesive and cohesive; and (d) catastrophic failure.

The critical loads for the emergence of damage, within the coating or at the interface depending upon the test direction, are shown in Table 2.

Sample	***DOWN* Direction**	***UP* Direction**
	Critical load range (mN)	**Critical Load range (mN)**
M3-I	50-100	0-50
M11	50-100	100-150
Graded	150-200	150-200

Table 2. Critical load ranges for the observation of the first damage during nanoscratch tests of the coatings studied.

It is interesting to note that the ranges of critical loads for damage observation are higher for the *Graded* specimen than for *M3-I* and *M11* specimens. In Figure 16, the tracks of nanoscratches performed at 150 mN in the *DOWN* direction are presented. It is evident that the *Graded* sample remains free of cracks after the scratch test at this load, whereas samples *M3-I* and *M11* show considerable cracking and/or spalling. Hence, it may be stated that, under the nanomechanical characterization approach implemented in this work, thin films of compositionally *Graded* mullite exhibit an optimum combination of properties from the mechanical standpoint in terms of cohesive and adhesive resistance. Such optimization comes from the compromising effect of thermal residual stresses (lower as Al/Si ratio decreases) and effective hardness/stiffness (higher as Al/Si ratio increases) which are better balanced in the compositionally graded coatings, as compared to the ones presenting just stoichiometric or extreme Al-enriched compositions.

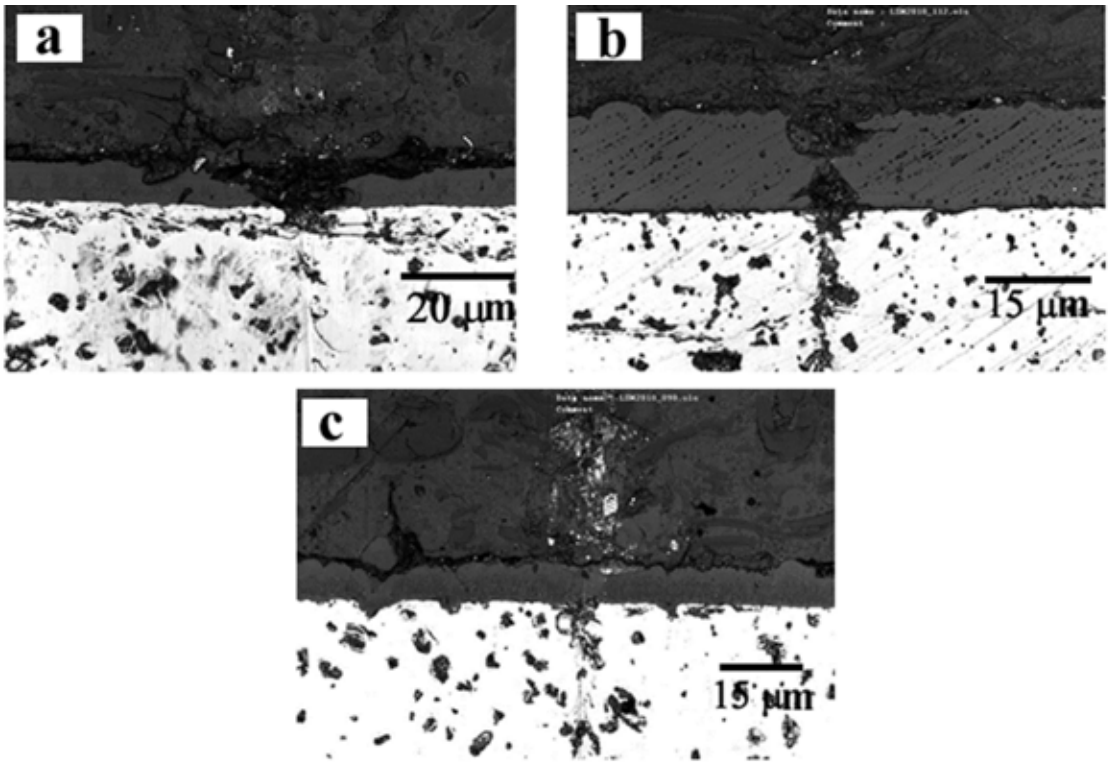

Figure 16. Damage at 150 mN in DOWN-direction nanoscratch track for samples: (a) M3-I; (b) M11; and (c) Graded.

6.4 Summary

From the results presented in this chapter, the following conclusions may be drawn:

- Nanoindentation tests performed on the cross-sections and wedges are effective and complementary approaches for the assessment of mechanical properties of complex coated systems, with spatial variation in properties occurring in small volumes.

- Nanoscratch conducted at the cross-section is an excellent methodology to characterize and evaluate the mechanical integrity of coatings with constant and graded properties across the thickness.

- An enhancement in H_f and E_f with the increase in the Al-content was evidenced both in the cross-sections of different coatings with fixed Al/Si ratio, and through the thickness of individual samples with graded compositions.

- H_f and E_f maps showed that the increase in properties observed across the thickness in the compositionally graded coatings is not homogeneous, due to the columnar nature of the studied coatings.

- Accounting for the experimental scatter observed, insignificant differences were found in the properties measured, following the distinct testing approaches implemented.

- Residual stresses have an insignificant effect on H_f and E_f calculated through nanoindentation.

- Compositionally graded mullite coatings studied in this work presented an optimum combination of stiffness/hardness and cohesive/adhesive scratch strength, as compared to coatings with stoichiometric or extreme Al-enriched compositions.

6.5 References

1. Sarin, V.K., Mulpuri, R.P. Chemical vapor deposition of mullite coatings. US Patent No. 5763008. 6 (1998).

2. Basu, S., Hou, P., Sarin, V.K. Formation of mullite coatings on silicon-based ceramics by chemical vapor deposition. *Int. J. Refract. Met. Hard Mater.* **16**, 343-352 (1998).

3. Hou, P., Basu, S.N., Sarin, V.K. Structure and high-temperature stability of compositionally graded CVD mullite coatings. *Int. J. Refract. Met. Hard Mater.* **19**, 467-477 (2001).

4. Auger, M., Sarin, V.K. A kinetic investigation of CVD mullite coatings on Si-based ceramics. *Int. J. Refract. Met. Hard Mater.* **19**, 479-494 (2001).

5. Basu, S.N., Sarin, V.K. *Chemical vapor-deposited mullite coatings (CVD Coatings)* In *Mullite.* p. 487. Wiley VCH, Weinheim, Germany (2005).

6. Basu, S., Kulkarni, T., Wang, H., Sarin, V.K. Functionally graded chemical vapor deposited mullite environmental barrier coatings for Si-based ceramics. *J. Eur. Ceram. Soc.* **28**, 437-445 (2008).

7. Kulkarni, T., Wang, H.Z., Basu, S.N., Sarin, V.K. Protective Al-rich mullite coatings on Si- based ceramics against hot corrosion at 1200°C. *Surf. Coat. Technol.* **205**, 3313-3318 (2011).

8. Basu, S.N., Kulkarni, T., Wang, H.Z., Steen, T., Murray, T.W., Sarin, V.K. Structure and properties of functionally graded environmental barrier coatings for ceramic components in gas turbines. *Proc. Int. Conf. Adv. Mat. Comp.* 1050-1060 (2007).

9. Volinsky, A.A. Nanoindentaion techniques for assessing mechanical reliability at the nanoscale. *Microelectron. Eng.* **69**, 519-527 (2003).

10. Li, X., Bhushan, B., Takashima, K., Baek, C.-W., Kim, Y.-K. Mechanical characterization of micro/nanoscale structures for MEMS/NEMS applications using nanoindentation techniques. *Ultramicroscopy* **97**, 481-94 (2003).

11. Xia, J., Li, C.X., Dong, H., Bell, T. Nanoindentation and nanoscratch properties of a thermal oxidation treated γ-TiAl based alloy. *Surf. Coat. Technol.* **200**, 4755 - 4762 (2006).

12. Jiménez-Piqué, E., Ceseracciu, L., Gaillard, Y., Barch, M., De Portu, G., Anglada, M. Instrumented indentation on alumina–alumina/zirconia multilayered composites with residual stresses. *Philos. Mag.* **86**, 5371-5382 (2006).

13. Gaillard, Y., Rico, V.J., Jiménez-Piqué, E., González-Elipe, A.R. Nanoindentation of TiO_2 thin films with different microstructures. *J. Phys. D: Appl. Phys.* **42**, 1-9 (2009).

14. Ballarre, J., Jiménez-Piqué, E., Anglada, M., Pellice, S., Cavalieri, A.L. Mechanical characterization of nano-reinforced silica based sol–gel hybrid coatings on AISI 316L stainless steel using nanoindentation techniques. *Surf. Coat. Technol.* **203**, 3325-3331 (2009).

15. Roa, J.J., Jiménez-Piqué, E., Capdevila, X.G., Segarra, M. Nanoindentation with spherical tips of single crystals of YBCO textured by the Bridgman technique: Determination of indentation stress–strain curves. *J. Eur. Ceram. Soc.* **30**, 1477-1482 (2010).

16. Beake, B.D. , Vishnyakov, V.M., Harris, A.J. Relationship between mechanical properties of thin nitride-based f lms and their behaviour in nano-scratch tests. *Tribol. Int.* **44**, 468-475 (2011).

17. Bertarelli, E., Carnelli, D., Gastaldi, D., Tonini, D., Di Fonzo, F., Beghi, M., Contro, R., Vena, P. Nanomechanical testing of alumina–titanium functionally graded thin coatings for orthopaedic applications. *Surf. Coat. Technol.* **205**, 2838-2845 (2011).

18. Lugscheider, E. Mechanical properties of EB-PVD-thermal barrier coatings by nanoindentation. *Surf. Coat. Technol.* **138**, 9-13 (2001).

19. Larsson, C., Odén, M. Hardness profile measurements in functionally graded WC-Co composites. *Mater. Sci. Eng. A* **382**, 141-149 (2004).

20. Lu, X., Wang, X., Xiao, P. Nanoindentation and residual stress measurements of yttria-stablized zirconia composite coatings produced by electrophoretic deposition. *Thin Solid Films* **494**, 223 - 227 (2006).

21. Sumitomo, T., Huang, H., Zhou, L. Deformation and material removal in a nanoscale multi-layer thin film solar panel using nanoscratch. *Int. J. Mach. Tool Manu.* **51**, 182-189 (2011).

22. Oliver, W.C., Pharr, G.M. An improved technique for determining hardness and elastic modulus using load and displacement sensing indentation experiments. *J. Mater. Res.* **7**, 1564-1583 (1992).

7 *Chapter*

Influence of temperature and corrosion on mechanical properties and structural integrity of mullite EBCs

Materials for components installed in the hot section of gas turbines must endure highly aggressive conditions, such as elevated temperatures and corrosive environments. Under these scenarios, functionally graded mullite coatings obtained by CVD have demonstrated excellent thermal stability and protection to SiC against corrosion and recession. It is essential that, in addition to the excellent protective behavior exhibited by CVD mullite coatings, their structural integrity and mechanical properties can be retained after their exposure under such aggressive conditions. In this chapter, the effect of the temperature and hot-corrosion on the main mechanical properties and performance of mullite-based EBCs is investigated.

7.1 Introduction

7.1.1 Thermal stability of CVD mullite coatings

One of the key issues in the durability of materials for EBCs is their resistance to prolonged exposures at high temperatures. Several investigations have been conducted to evaluate the behavior of mullite-containing EBCs on Si-based substrates when exposed to high temperatures conditions[1–5]. In such studies materials are subjected to high temperatures (around 1300 ºC) by their introduction into furnaces for long periods, under constant and cyclic exposures. In the particular case of compositionally graded

CVD mullite coatings, their thermal stability at elevated temperatures has been addressed in a previous investigation.[6] In such study, mullite coated SiC samples were subjected to different high-temperature heat treatments in the range of 1100-1400 ºC. Main transformations taking place during the annealing and thermal stability tests, may be described as follows:

- Almost insignificant changes in composition occur after exposing the samples to 1250 ºC during 100 h.

- Because the high rate (≈ 5 μm/h) and low temperatures (≈ 950 ºC) used for the depositon, as-deposited CVD mullite coatings have a metastable tetragonal structure. Tetragonality has also been found to be function of the Al content in mullite[7]. Due to the higher mobility of atoms when increasing the annealing temperature, the metastable tetragonal structure of mullite coatings is transformed to an orthorhombic one. Such transformation was evidenced by the splitting of mullite peaks in the X-Ray diffraction spectra.

- The amorphous layer of the as-deposited coatings, known as the nanocrystalline layer (composed of γ-Al_2O_3 nanocrystals embedded in vitreous silica), undergoes a mullitization process. Thus, when annealed for 100 h at temperatures higher than 1150 ºC, the nanocrystalline layer is transformed into crystalline mullite grains by a dissolution, nucleation and growth process of the mullite nanocrystals. As a consequence, the entire microstructure of mullite coatings is converted into equiaxed crystalline mullite grains.

- After performing a two-step annealing process of 1250 ºC for 100 h, followed by one at 1400 ºC during other 100 h, nanosized α-alumina precipitates were observed in the Al-rich regime of the coatings. This was accompanied by twinning of mullite in this composition regime.

7.1.2 Thermal shock of CVD mullite coatings

Adhesion of mullite coatings was qualitatively evaluated by cycling between 1250 ºC and room temperature[6]. In this cyclic thermal shock test, samples were subjected to sudden and drastic changes in temperature. This was attained by rapid insertion and removal of the samples from the hot zone of a furnace, holding the specimens for 1 h at each temperature during 500 cycles. After the tests, coatings showed no signs of cracking and/or spallation.

7.1.3 Corrosion of CVD mullite coatings

Other important issue in the performance of mullite EBCs is the hot corrosion in molten salts environments. Studies have been carried out to evaluate the behavior of mullite-containing EBCs to elements such as Na and V under oxidizing conditions.[1,2,8–11] The hot corrosion of different CVD mullite coatings has also been adressed in a recent investigation[12]. Mullite coatings with different Al-rich compositions at the surface were tested. Coatings were deposited by both keeping input gas ratios constant (Al/Si at surface: 3, 4, 4.5, and 8) and grading such ratio during depositon (ending with an Al/Si at surface of 16). Coated mullite/SiC specimens were coated with Na_2SO_4 and subjected to flowing oxygen environments at 1200 ºC for 100 h. Results were compared to those of hot corrosion of uncoated SiC, mullite and alumina specimens subjected to the same conditions.

Main findings of this work show that corrosion protection increase with the Al/Si ratio at the surface of the tested coatings. This was evidenced by the decreasing values of weight gain and silica activity with the increase of Al in coatings. After the tests, none of the coatings was visibly affected by corrosion even under the severe circumstances simulated in the study. Although there was evidence of some minor reactions at isolated parts of the Al-rich coatings, Na penetration into the bulk was negligible.

7.1.4 Temperature and corrosion effects on mechanical behavior of CVD mullite coatings

The influence of temperature and corrosion on the mechanical properties and structural integrity of CVD mullite coatings has not been documented. Such effects are investigated in this chapter. Nanomechanical tests are conducted on selected coated specimens subjected to thermal stability, thermal shock and corrosion tests similar to the ones described in sections 7.1.1 to 7.1.3. Nanoindentation tests were conducted to estimate hardness, elastic modulus and fracture toughness of coatings, whereas nanoscratch tests were performed to evaluate their structural integrity. Results obtained in this chapter are compared with those found for the same systems without subjecting them to any thermal or corrosion treatments, as presented previously throughout chapters 4 to 6. Hereafter, results obtained on these control specimens are referred to as in the "As-deposited" condition.

7.2 Experimental procedure

Experimental details of the heat treatments performed under normal and corrosive conditions are presented in sections 3.6.1 to 3.6.3 of *Chapter 3*. Thermal stability tests were implemented specifically on samples *M3-III*, *M7* and *Graded-II*. Thermal shock tests were exclusively performed on samples *M3Thick* and *M8-I*, whereas sample *M8-II* was selected for the hot-corrosion tests.

After the heat and corrosion treatments, matrices of Berkovich nanoindentations were performed at h_{max} = 100 nm in all specimens following the "cross-sectional" and "wedge" approaches. Similarly Berkovich nanoindentations were conducted following the top approach at h_{max} = 2000 nm in samples *M3-III* and *M7*, and at h_{max} = 1000 nm in samples *M3-I* and *M8-I.* Moreover, cube corner nanoindentation matrices in the range of P_{max} = 2-5 mN were performed on samples *M3-III* and *M7* specifically, to evaluate their fracture toughness. K_c of samples *M3-III* and *M7* was estimated following the procedure described in Chapters *4* and *5*.

Furthermore, nanoscratch tests under the "high load" condition (P_{max} = 500 mN, l_{max} = 200 µm and loading rate = 2.5 mN/µm) were carried out on the surface of all specimens. Tests were conducted on three surface conditions: "polished, semi-polished and non-polished". In the case of samples with constant composition across the coating thickness (*M3-I*, *M3-III*, *M7, M8-I* and *M8-II*), nanoscratches were carried out on the polished surface of specimens. In the case of the graded coating (*Graded-II*) as well as of *M8-II* condition, nanoscratches were performed both in the "non-polished" and "semi-polished" surface conditions. The "semi-polished" condition of the surface was attained by fine polishing using a 3 µm diamond paste for 20 minutes, finishing with colloidal silica suspension (5 minutes). Main surface irregularities were removed, while keeping the surface of coatings as close as possible to the "non-polished" condition. These approaches permitted to evaluate (i) structural integrity of coatings without losing information of compositional gradient, (ii) real surface topography effects on the structural integrity of coatings, and (iii) potential effect of thermal and corrosion treatments on the structural integrity of coatings as a function of surface conditions.

7.3 Influence of temperature on mechanical properties

7.3.1 Thermal stability test

7.3.1.1 Samples *M3-III* and *M7*

- ***Hardness and elastic modulus***

Values for H_f and E_f are presented in Figure 1 as a function of penetration depth for samples *M3-III* and *M7*. In the plots, properties of coatings resulting from thermal stability tests are compared to the ones measured in the "As-deposited" condition (before the exposure).

From Figure 1, it is noticeable that sample *M3-III* undergoes an increase in hardness and stiffness with thermal stability (annealing) treatment applied. On the other hand, properties of sample *M7* are unchanged after same thermal exposure. It may also be

observed that thermal stability tests yield higher scatter of measured properties, especially relevant in the curves of sample *M3-III*.

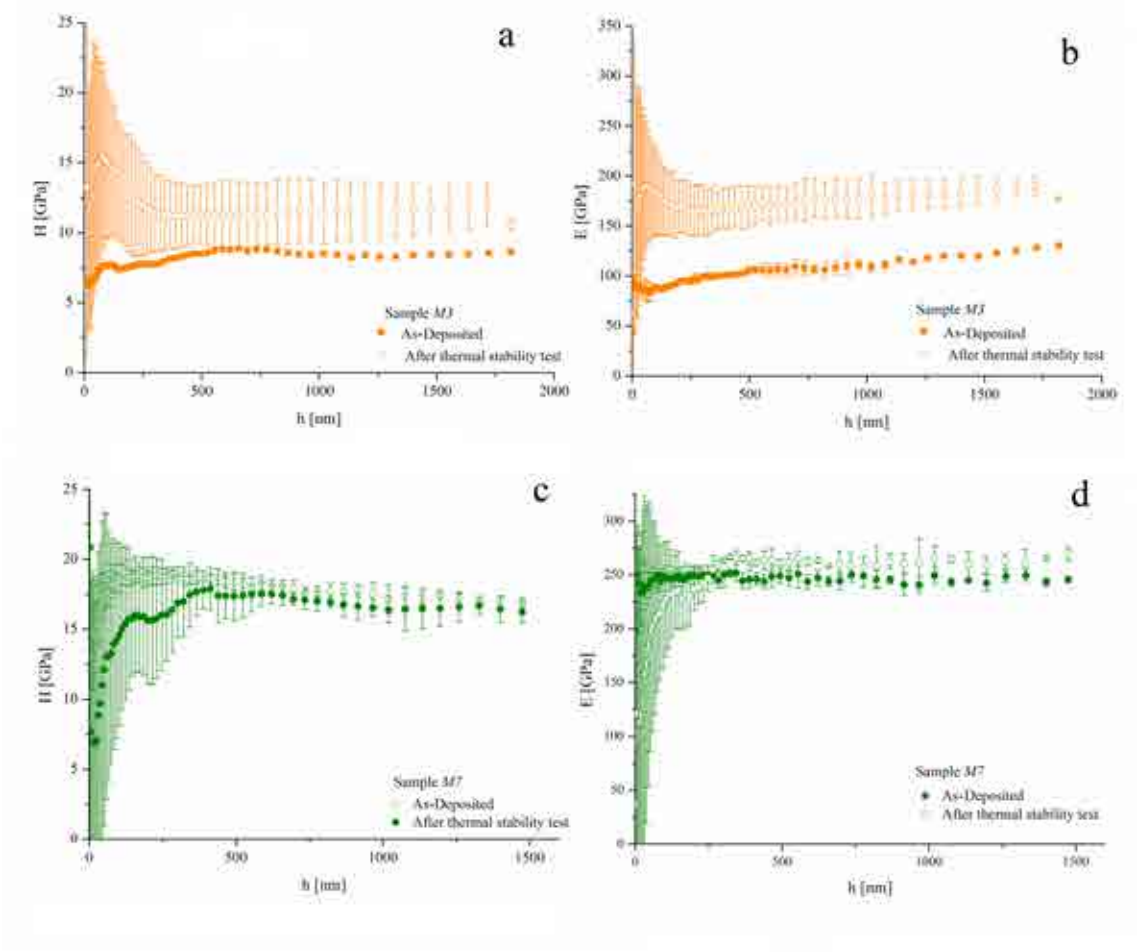

Figure 1. (a,c) Hardness and (b,d) elastic modulus as a function of penetration depth obtained for samples (a,b) *M3-III* and (c,d) *M7*. Filled symbols correspond to indentations in the "As-deposited" condition and void symbols correspond to indentations after thermal stability test.

These results must be rationalized on the basis of transformation occurring in the coating material by the effect of temperature. As it was pointed out in section 7.1.1., the influence of temperature, under the conditions of tests performed on compositionally graded coatings, was insignificant in terms of compositional changes. However, two main variations were observed in structure: a phase change from tetragonal to orthorhombic, and a coating microstructure change from the mullite columns growing from the nanolayer to equiaxed crystalline mullite grains. Considering these transformations, it may be expected an increase in mechanical properties, especially by

the effect of the complete crystallization of the coatings. Thus, it may be speculated that this effect is more prominent in sample *M3-III*, probably due to the higher silica content when compared to sample *M7*.

- ***Fracture toughness***

In Figure 2, AFM images of the cube corner imprints left in sample *M3-III* (a-b) and *M7* (c-d) may be observed.

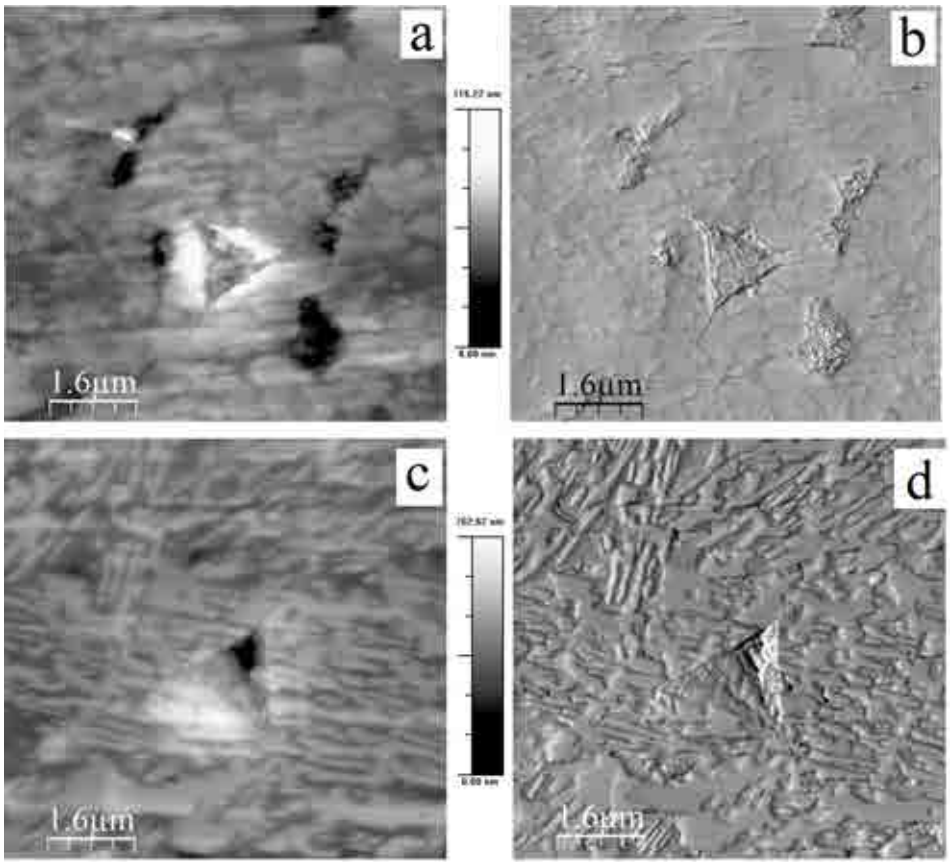

Figure 2. AFM micrographs of cube corner indents at P = 20 mN in (a,b) sample *M3-III*, and (c,d) sample *M7*. (a,c) Height images, and (b,d) phase images.

Fracture toughness of sample *M3-III* after thermal stability tests was $K_c = 0.8 \pm 0.3$ MPa·m$^{1/2}$. This value is lower than the one obtained for the same sample in the as-deposited condition, $K_c = 1.2 \pm 0.3$ MPa·m$^{1/2}$. On the other hand, in the case of

sample *M7*, fracture toughness assessed after the thermal stability tests yields K_c = 0.8 ± 0.3 MPa·m$^{1/2}$. This value is comparable with the one obtained for the same sample in the as-deposited condition, K_c = 0.7 ± 0.1 MPa·m$^{1/2}$. Hence, whereas the fracture toughness remains constant for sample *M7*, this property decreases in sample *M3-III* as a consequence of the thermal stability test. Again, this may be attributed to the structural changes taking place in the studied coating.

- ***Structural integrity***

The penetration profiles, and the micrographs corresponding to the nanoscratches conducted on the polished surface of samples *M3-III* and *M7*, are presented in Figure 3 (a and b respectively).

In the graphs, filled and void symbols correspond to nanoscratches in coatings at the "As-deposited" condition and after the thermal stability test, respectively. As it may be observed from the curves of Figure 3 b, the penetration of the indenter during the scratching process is almost similar before and after thermal heat treatment for sample *M7*. This observation is in agreement with the fact that H_f and E_f remained almost constant for this sample after the exposure. On the other hand, penetration of the indenter in sample *M3-III* was lower after the thermal stability test, as shown in Figure 3 a. This observation is also in agreement with the *H* and *E* increase registered for this sample.

Regarding characterization of the surface areas encompassing the residual scratch tracks, it may be commented that no significant damage may be identified as related to the scratch tests. Partial chipping is only evidenced at high loads in one of the scratches of sample *M7*. Hence, the decrease registered in K_c for sample *M3-III* does not translate in an integrity lessening for this coating, as it may by observed in the micrograph of Figure 3 a. In general terms, it must be underlined that coatings of samples *M3-III* and *M7* coatings retain their structural integrity after thermal exposure to 1250ºC during 100 hours, as assessed by surface nanoscratch tests.

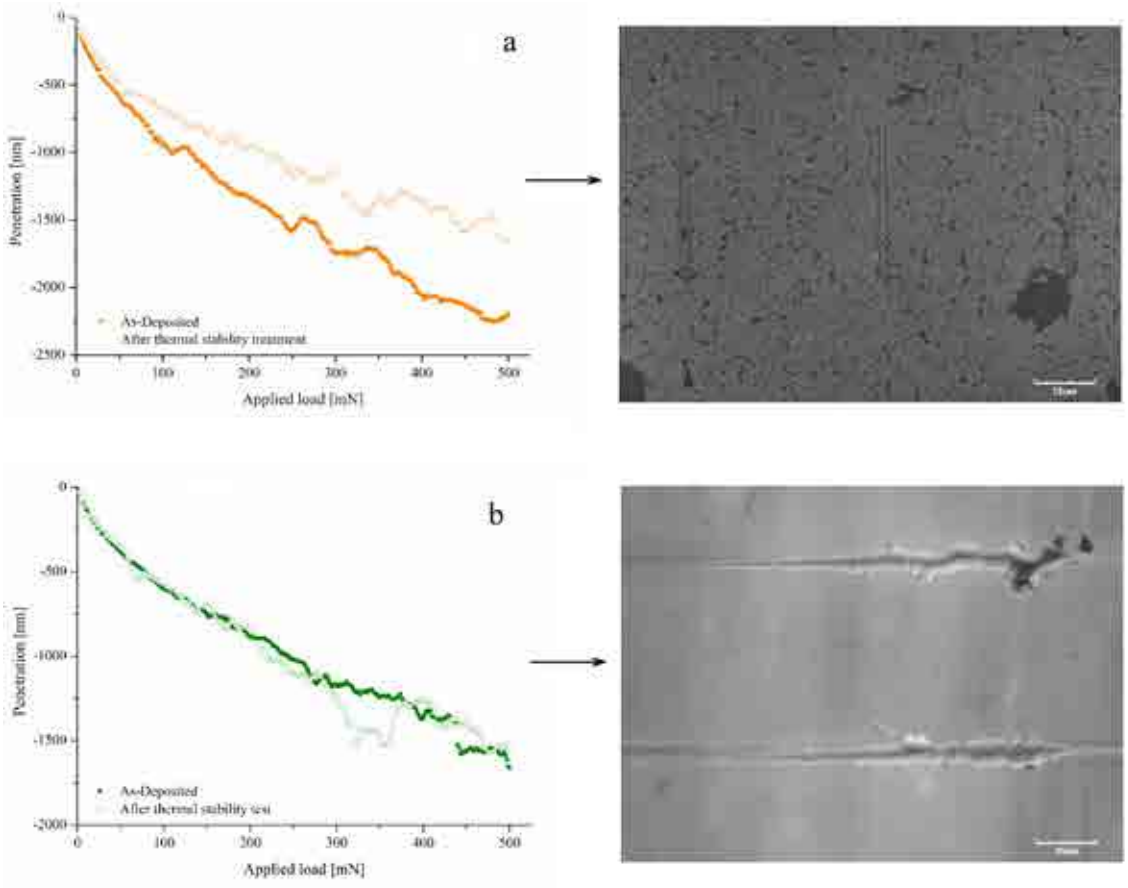

Figure 3. Penetration depth as a function of applied load, and corresponding micrographs of the scratch paths, for samples (a) *M3-III* and (b) *M7*. Load increase downwards in the image of sample *M3-III* and from left to right in the case of sample *M7*. Filled and void symbols correspond to scratches in the "As-deposited" condition and after thermal stability test respectively.

7.3.1.2 Sample *Graded-II*

- ***Surface appeareance***

In Figure 4 the surface appearance of sample *Graded-II* before (a), and after (b) its exposure to the referred thermal stability test, are compared. As it is clear from the images, surface integrity is preserved after the test, as no major cracking or spallation of the coating occurs as a consequence of the heat treatment. This absence of generalized damage is in agreement with similar observations reported in the literature[6].

Nevertheless, bright spots of approximately 60 µm in diameter may be discerned along the surface of the coating after the thermal exposure. As it is observed from the detailed

micrograph of Figure 4 c, this bright spots are located in the outermost zones of the coating, corresponding to the regions with the Al-richest compositions in mullite. This finding is in accordance to the one of nanosized α-alumina precipitates in the Al-rich regime of similar coatings after their exposure to high temperatures[6], as it was described before in section 7.1.3. Such nanosized alumina was accompanied by twinning of mullite in this composition regime.

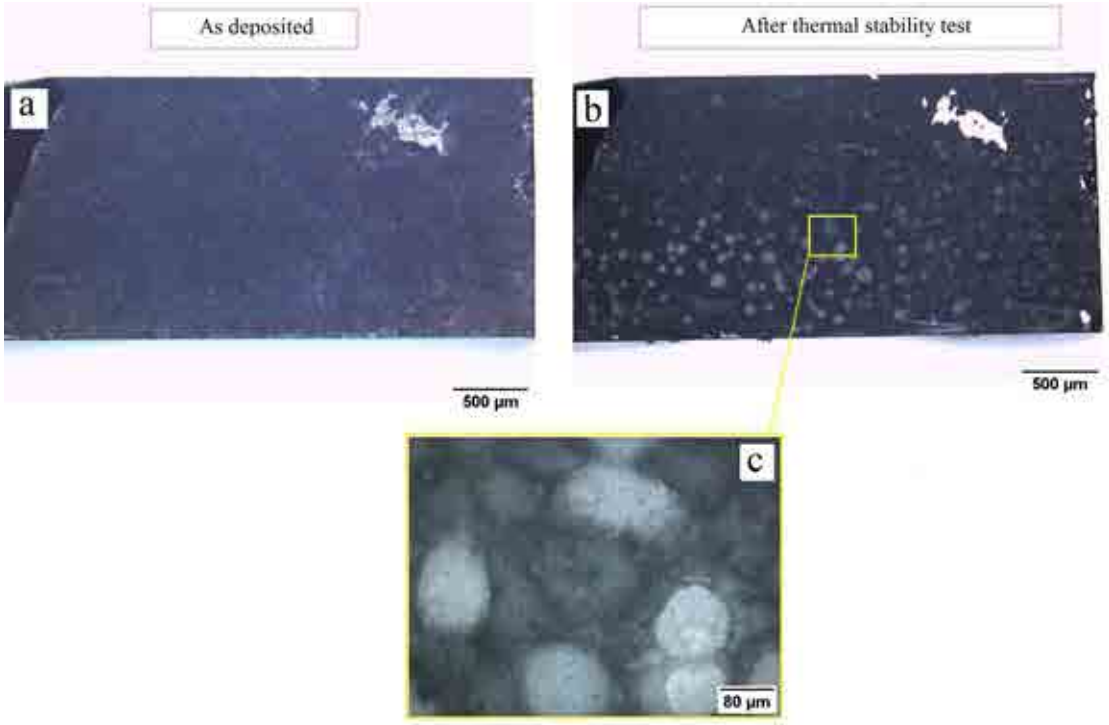

Figure 4. Surface aspect of sample *Graded-III* in the (a) As-deposited condition and (b) after the thermal stability test perfomed. Detail of the bright spots observed after thermal exposure (c).

- ***Hardness and elastic modulus***

The polished wedge of sample *Graded-II* is presented in Figure 5. As it may be confirmed by observing the polished areas in this image, there is no major cracking in the coating as a consequence of the heat treatment. Moreover, some circular areas of the coating appear to be removed by the polishing process. These zones coincide with the location and size of the bright spots observed in Figure 4. It is believed that the differences in properties of these areas may cause the differential removal of material, resulting in partial chipping of the coating at such areas. Nevertheless, it was possible to

carry out nanoindentation matrices across the polished wedge of the coating, as outlined in Figure 5.

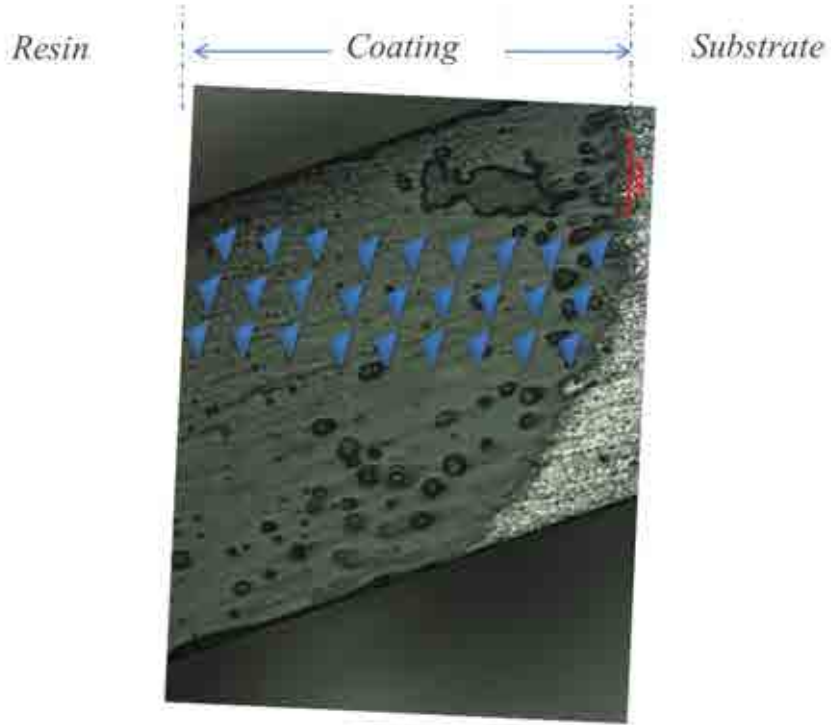

Figure 5. Polished wedge and nanoindentation sketch superposed for sample *Graded-II*.

Results of hardness and elastic modulus for sample *Graded-II* are presented as a function of coating thickness in Figure 6. For comparison reasons, the referred properties evaluated in the same coating in the "As-deposited" condition are also included in the plots.

Although the scatter in the data corresponding to the thermally treated samples is relatively higher than for the control condition, differences in both stiffness and hardness are not significant, and the trend of such properties with the thickness, as related to compositional grading, is similar to that estimated in the As-deposited condition. Considering the scatter of measurements, it may be stated that H and E are not significantly affected by the thermal treatment conducted in this coating.

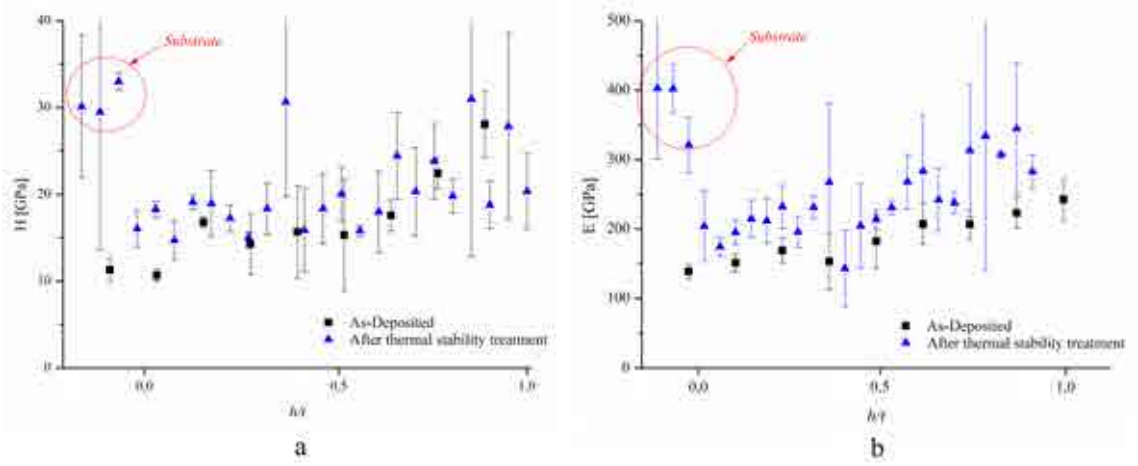

Figure 6. (a) Hardness and (b) elastic modulus for sample *Graded-II* in the As-deposited condition (■) and after thermal stability treatment (▲).

- ***Structural integrity***

After the thermal stability test, the influence of temperature on the structural integrity of graded mullite coatings was studied through nanoscratch tests performed in sample *Graded-II* in the "non-polished" and "semi-polished" surface conditions. In Figure 7 the optical and LSCM micrographs of two of the referred scratches are shown.

The residual tracks left by the scratches evidence a very slight damage produced by the tests in the surface of sample *Graded-II*, as it is discerned in Figure 7 a-c. The perspective view of a particular zone of the track presented in Figure 7 d suggests that the indenter produces a flattening effect on the surface irregularities as load is increased during the scratch test. However, coating spallation or chipping are completely absent.

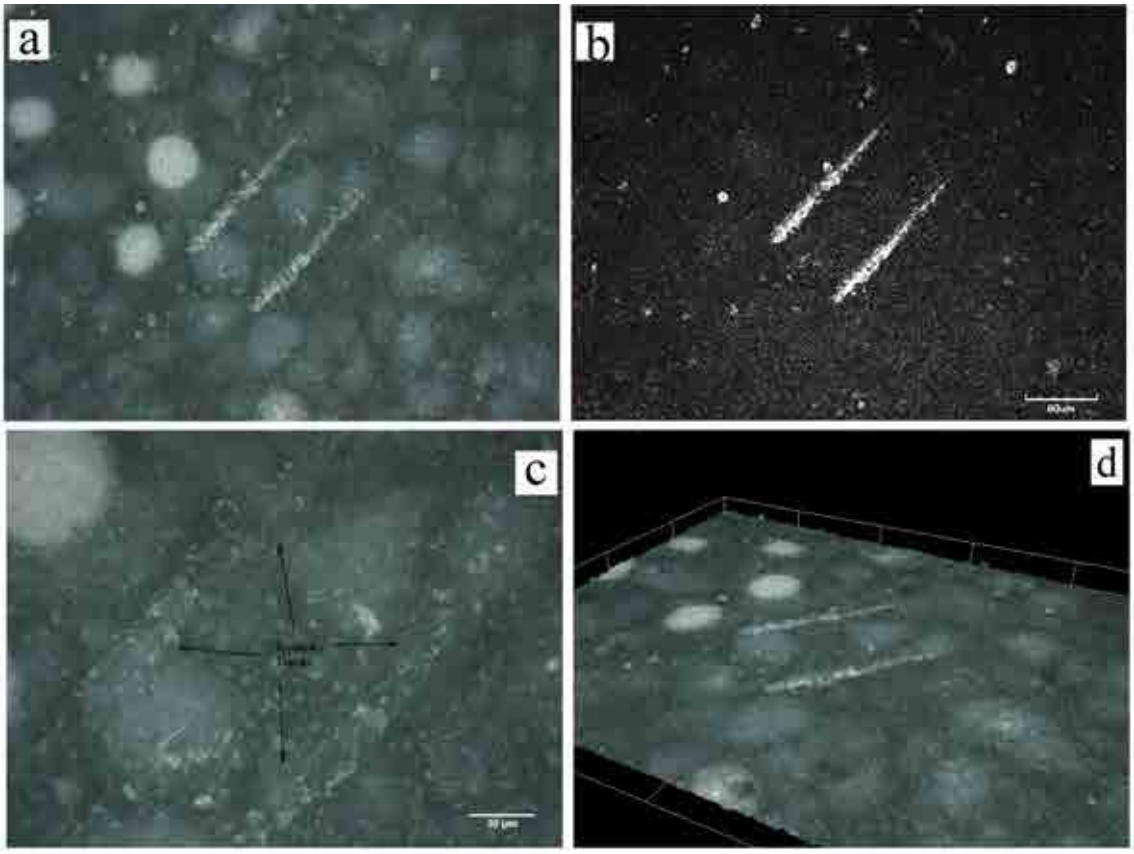

Figure 7. (a) Optical and (b) LSCM micrographs of nanoscratches performed on the "non-polished" surface of sample Graded-II, after the thermal stability test. (c) Detail of the scratch tracks. (d) 3D-perspective of surface. In the images nanoscratches are placed in an oblique situation, from up right towards bottom left.

Nonetheless, since surface is not polished, details of the nanoscratch effects on the surface and subsurface are hindered by the topography of the coating. Figure 8 shows the tracks of the nanoscratches performed on the "semi-polished" surface of sample *Graded-II*. As it may be observed from these images, tests produced insignificant cracking, spallation or chipping of the coating material. Furthermore, from the optical image of Figure 8 b, subsurface damage zones, similar to those referred in Chapter 5 for different coatings, are observed. These damage zones appear at approximately the midpoint of the scratch length.

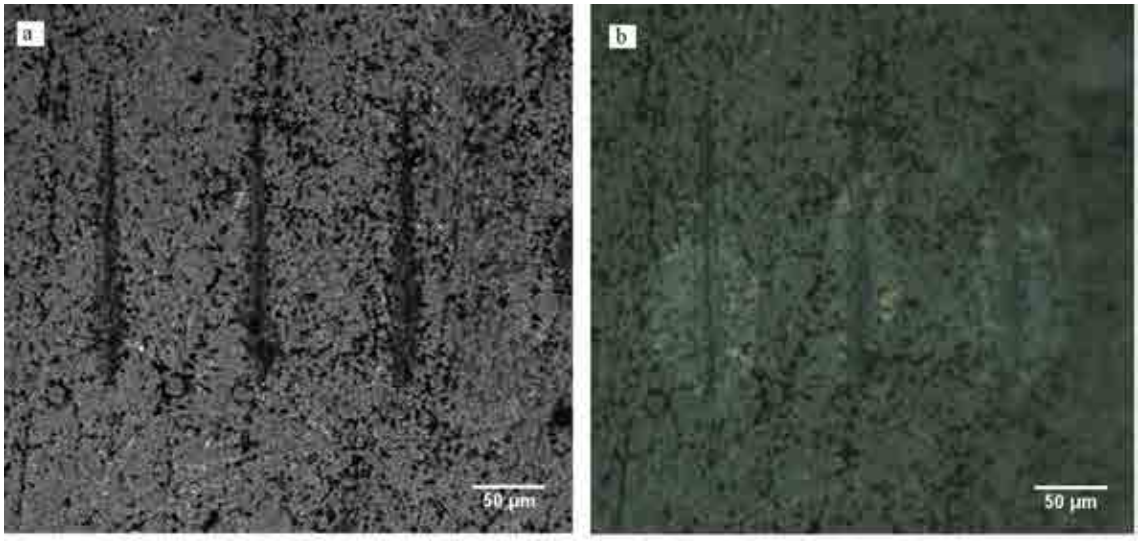

Figure 8. (a) LSCM and (b) optical images of nanoscratches performed on the surface of sample *Graded-II* in the "semi-polished" condition, after the thermal stability test.

7.3.2 Thermal shock

7.3.2.1 Surface appeareance

The surface appearances of samples *M3-I* and *M8-I* after the thermal shock treatment performed are displayed in Figure 9 a and b, respectively. It is clear that sample *M3-I* did not present any sign of cracking or spallation of the coating material after the treatment. On the other hand, some cracking and minor coating spallation may be observed in sample *M8-I*, especially in the zones close to the edges. However, in the interior of the sample, in locations far from the edges, these cracks disappear and the coating remains undamaged after the thermal shock.

Differences observed between samples may be explained by the higher internal stresses present within the coating in sample *M8-I*, due to its higher thermal expansion mismatch with the SiC substrate, as compared with those of sample *M3-I*. Moreover, it may be speculated that the cracking observed in zones near the edges of sample *M8-I*, and their surroundings, arise from the higher internal stress concentration in these locations produced during the fabrication process and/or induced during the polishing process.

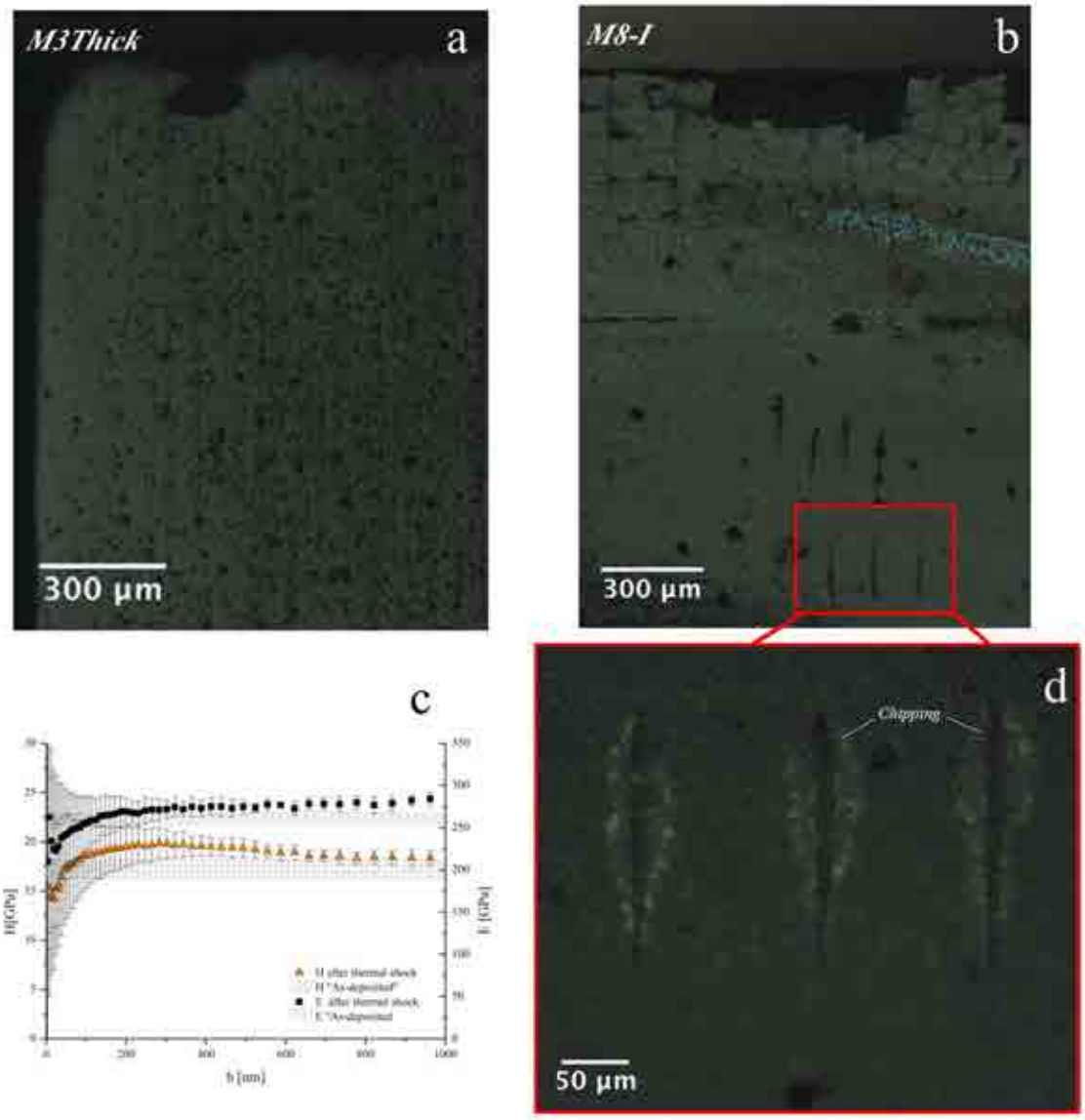

Figure 9. Surface appearances of samples (a) *M3-I* and (b) *M8-I* after the thermal shock test. (c) *H* and *E* as a function of penetration depth for samples *M3-I* and *M8-I* evaluated after the thermal shock. (d) Nanoscratches performed after the thermal shock of sample *M8-I*.

7.3.2.2 Hardness and elastic modulus

The hardness and the elastic modulus of sample *M8-I* evaluated after the thermal shock treatment are presented in Figure 9 c. In the same figure, H and E ranges of values evaluated for the same samples in the "As-deposited" condition, are also included. In practical terms, accounting for the experimental variability, it may be stated that hardness and elastic modulus remain unchanged after the thermal shock.

7.3.2.3 Structural integrity

The nanoscratch tracks corresponding to the tests performed in sample *M8-I* after the thermal shock treatment are presented in Figure 9 d. The bright zone around the tracks, previously referred to as the subsurface damage zone is evident in the images. In addition, some minor surface cracks appear along the track, accompanied by a slight chipping of the coating material at the high-load end of the scratch length. Despite of the "brittle" character observed in Figure 9 d, it may be stated that the overall integrity of sample *M8-I* is kept after the thermal shock treatments performed.

7.4 Influence of corrosion on mechanical properties

7.4.1 Hardness and elastic modulus

The LSCM micrograph of Figure 10 shows the cross-section of sample *M8-II* indented after exposure of this sample to the hot-corrosion test.

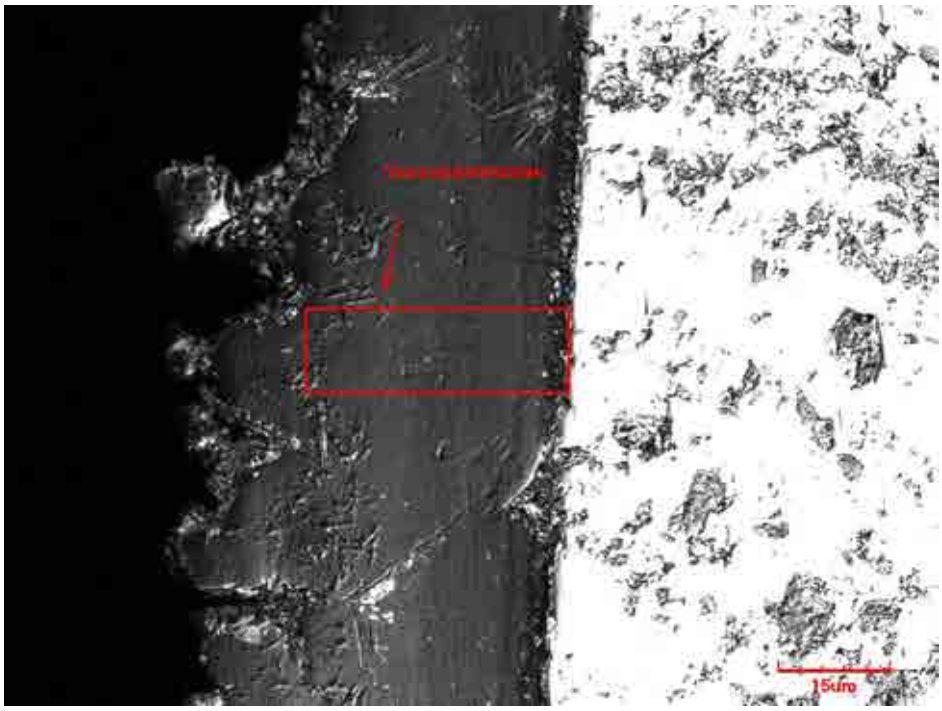

Figure 10. Nanoindentations matrix on the coating cross-section of sample *M8*, previously subjected to the corrosion test.

Average results of the elastic modulus and hardness evaluated from the referred cross-sectional Berkovich nanoindentations are presented in Figure 11 (a and b respectively). For comparison purposes, the average values obtained from sample *M8-I* in the "As-deposited" condition are included in the graphs as a meshed region.

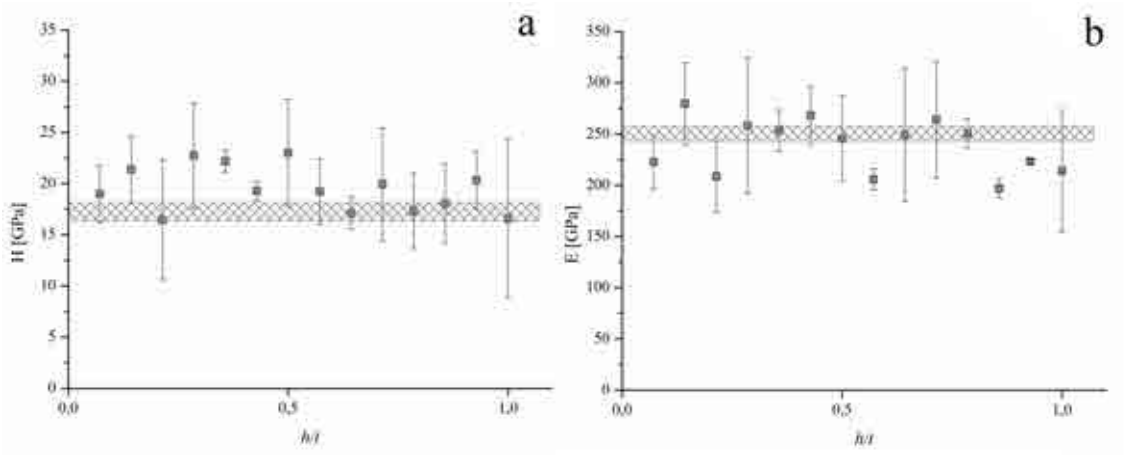

Figure 11. Cross-sectional (a) hardness and (b) elastic modulus of sample *M8-II* after the corrosion test. The meshed zone superposed to the plots indicates the average values found for sample *M8-I* in the "As-deposited" condition.

Despite of the scatter in the measurements registered across the cross-section, it may be mentioned that stiffness and hardness of sample *M8-II* subjected to hot-corrosion conditions are comparable to those observed for sample *M8-I* in the "As-deposited" condition. Hence, effect of hot-corrosion is insignificant in terms of these mechanical properties.

7.4.2 Structural integrity

Nanoscratch tests were conducted both in non-polished and polished surface conditions of sample *M8-II*. In Figure 12, three nanoscratches performed on the non-polished surface of this coating are presented.

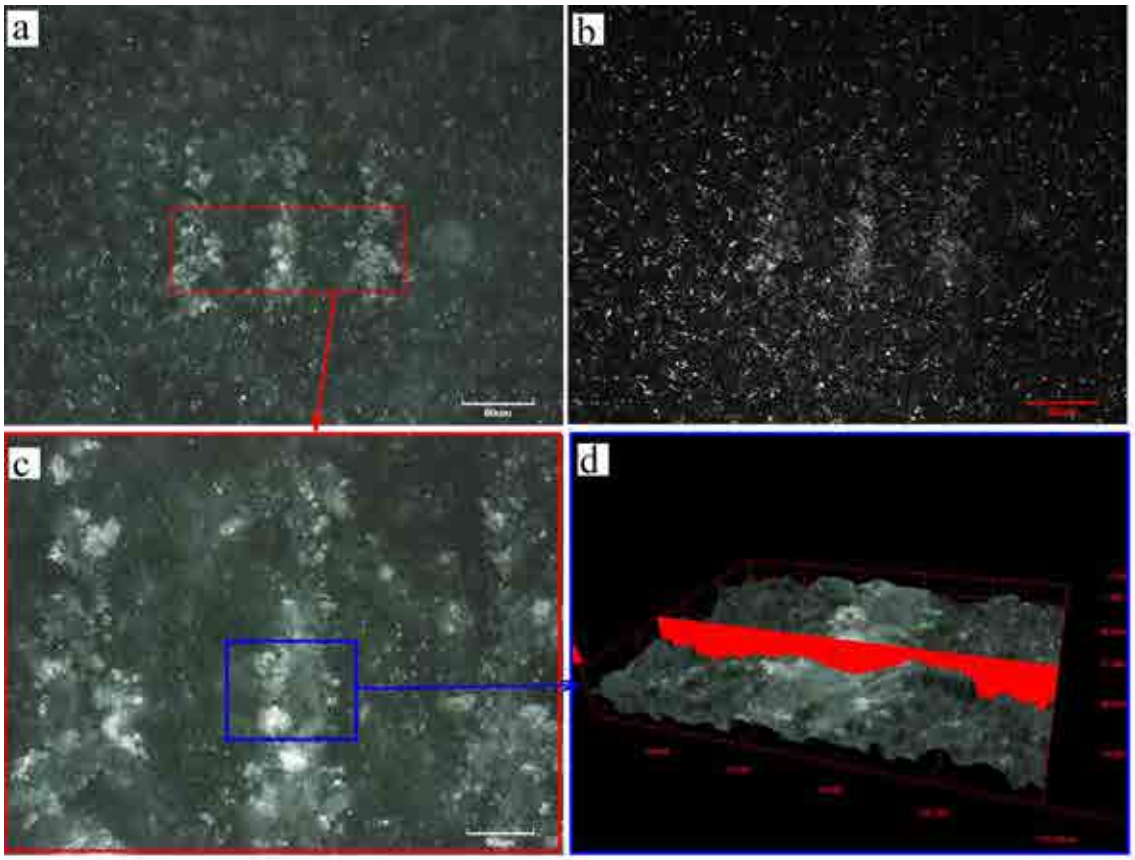

Figure 12. (a) General optical and (b) LSCM micrographs of three nanoscratches performed on the surface of coating *M8* in the "non-polished" condition. (c) Detailed 2D and (d) 3D views of the scratch track.

Again, minor damage is observed as a consequence of the scratch tracks for this sample. The same flattening effect presented previously in Figure 7 for sample *Graded-II*, is evidenced in the 3D image of Figure 12 d. One of the nanoscratches conducted on the polished surface of sample *M8-II* is presented in the LSCM and optical micrographs of Figure 13.

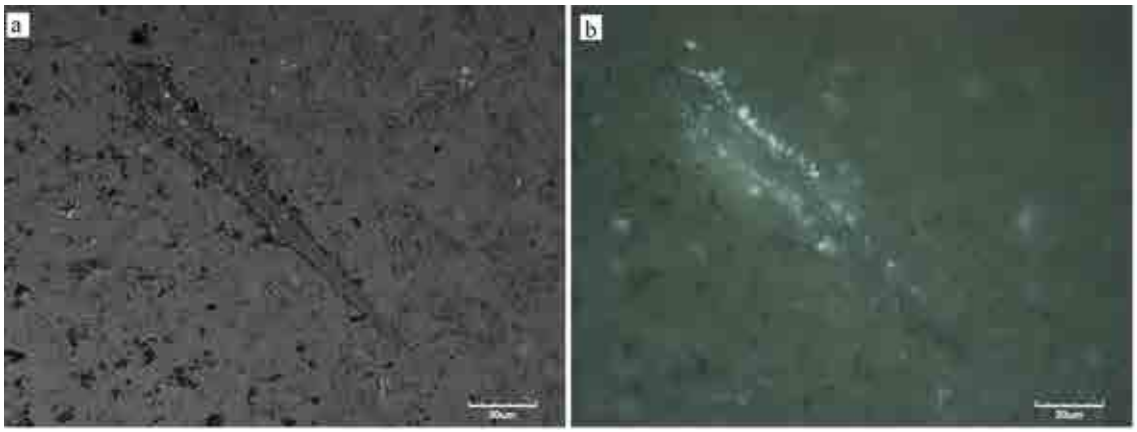

Figure 13. (a) LSCM and (b) optical micrographs of a nanoscratch performed on the polished surface of sample *M8-II* after being subjected to corrosion test.

Minor chipping of the coating material may be discerned at the edges of the scratch track, especially at the end of its length, as shown in Figure 13 a. Moreover, in the optical image of Figure 13 b a slight bright zone, denoting a potential subsurface damage, is observed close to the midpoint of the scratch length. In general terms, the surface appears to be undamaged at the surface level, denoting a negligible effect of the hot-corrosion treatment on the structural integrity of this coating.

7.5 Conclusions

The influence of temperature and hot-corrosion on the mechanical properties and structural integrity of CVD mullite coatings was studied in selected specimens with constant and graded Al/Si ratios. The following conclusions may be drawn:

- An increase in H_f and E_f, accompanied by a decrease in K_c, was found to occur in sample *M3-III*. On the other hand, none of these properties was altered for sample *M7*. This may be rationalized by the microstructural transformations experienced by these coatings as a consequence of thermal exposure.

- Hardness and stiffness of the compositionally graded coating (*Graded-II*) were practically unchanged after the thermal stability tests, denoting an insignificant effect of temperature in these properties.

- Samples *M8-I* and *M8-II* did not exhibit any relevant change in mechanical properties as a consequence of the hot-corrosion treatments to which they were exposed.

- Nanoscratches performed on samples exposed to thermal stability (samples *M3-III*, *M7* and *Graded-II*), thermal shock (samples *M3-I* and *M8-I*) and hot-corrosion (sample *M8-II*) tests induced only minor changes. Thus, the effect of temperature and hot-corrosion in the structural integrity of tested coatings may also be considered as negligible.

- The fact that coatings subjected to the combined effect of temperature and hot corrosion keep their structural integrity practically unaltered under the nanoscratch tests performed is an interesting finding as CVD mullite coatings are expected to be used in applications such as gas turbines, under same conditions.

7.6 References

1. Lee, K.N. Protective coatings for gas turbines. *The gas turbine handbook* 419-437 (2006).

2. Lee, K.N. Key durability issues with mullite-based environmental barrier coatings for Si-based ceramics. *Trans. ASME* **122**, 632 (2000).

3. Lee, K.N., Fox, D.S., Eldridge, J.I., Zhu, D., Robinson, R.C., Bansal, N.P., Miller, R.A. Upper Temperature Limit of Environmental Barrier Coatings Based on Mullite and BSAS. *Technology* **306**, 1299-1306 (2003).

4. Lee, K., Miller, R.A., Veitch, L. *Plasma-sprayed refractory oxide coatings on silicon-base ceramics.* NASA (1997), In http://wayback.archive-it.org/1792/20100201190134/http://hdl.handle.net/2060/19980007581

5. Shibin, L. A study on the cycling oxidation behavior of mullite-coated silicon carbide. *Mater. Chem. Phys.* **78**, 655-659 (2003).

6. Hou, P., Basu, S.N., Sarin, V.K. Structure and high-temperature stability of compositionally graded CVD mullite coatings. *Int. J. Refract. Met. Hard Mater.* **19**, 467-477 (2001).

7. Schneider, H., Rymon-Linpinski, T. Occurrence of pseudotetragonal mullite. *J. Am. Ceram. Soc.* **71**, 65-68 (1988).

8. Jacobson, N.S., Lee, K.N., Yoshio, T. Corrosion of mullite by molten salts. *J. Am. Ceram. Soc.* **79**, 2161-2167 (1996).

9. Ueno, S., Jayaseelan, D., Kondo, N., Ohji, T., Kanzaki, S. Water vapor corrosion of mullite containing small amount of sodium. *Ceram. Int.* **31**, 177-180 (2005).

10. Ramasamy, S., Tewari, S.N., Lee, K.N., Bhatt, R.T., Fox, D.S. Environmental durability of slurry based mullite–gadolinium silicate EBCs on silicon carbide. *J. Eur. Ceram. Soc.* **31**, 1123-1130 (2011).

11. Ramasamy, S., Tewari, S.N., Lee, K.N., Bhatt, R.T., Fox, D.S. Mullite-gadolinium silicate environmental barrier coatings for melt infiltrated SiC/SiC composites. *Surface & coatings technology* **205**, 3578-3581

12. Kulkarni, T., Wang, H.Z., Basu, S.N., Sarin, V.K. Protective Al-rich mullite coatings on Si- based ceramics against hot corrosion at 1200°C. *Surf. Coat. Technol.* **205**, 3313-3318 (2011).

8 *Chapter*

Conclusions

Nanoindentation and nanoscratch are essential and complementary tools for the characterization of the mechanical behavior of protective environmental barrier mullite coatings deposited on silicon carbide substrates. Key mechanical properties intrinsic to the $3Al_2O_3{\cdot}2SiO_2$ coatings were assessed, and the structural integrity of the coated $3Al_2O_3{\cdot}2SiO_2$/SiC system was evaluated. Main conclusions accomplished in this investigation may be summarized as follows:

1. The use of nanoindentation with different tip geometries together with advanced characterization techniques permitted the assessment of the main intrinsic mechanical properties of $3Al_2O_3{\cdot}2SiO_2$ coatings with stoichiometric composition (Al/Si = 3), in thin and thick coated configurations. In the former case, influences of both substrate and residual stresses on indentation response, deformation, and damage micromechanisms were accounted and documented. Main properties attained yield $H_f \approx 10$ GPa, $E_f \approx 130$ GPa, $K_f \approx 1.1$ - 1.7 MPa·m$^{-1/2}$ and $\sigma_y \approx 3.5$ GPa. Hardness, stiffness and toughness evaluated in this investigation are lower as compared with the values reported in the literature for stoichiometric bulk polycrystalline mullite. This may be explained by the microstructural features of the studied coatings, i.e. columnar nature and the amorphous silica layer from which mullite columns grow.

2. Controlled delamination was induced in a thin coated $3Al_2O_3{\cdot}2SiO_2$/SiC system by means of increasing load nanoindentation using a cube corner indenter. With the aid of 3D FIB tomography the area delaminated was characterized, and by using formulations proposed in the literature the strength of the interface was evaluated. The energy of adhesion yields G_{int} = 21.3 – 30.9 $J{\cdot}m^{-1/2}$ and the fracture toughness of the interface yields $K_{int} \approx 1.5 – 2.2$ $MPa{\cdot}m^{-1/2}$.

3. Nanoscratch tests performed on stoichiometric $Al_2O_3{\cdot}2SiO_2$ thick coatings and thin films allowed for the evaluation of the intrinsic structural integrity of stoichiometric coatings as well as that of the coated $3Al_2O_3{\cdot}2SiO_2$/SiC system, respectively. A progressive damage was evidenced by increasing load nanoscratches. The integrity of the coatings may be catalogued as satisfactory, as considerable plastic deformation takes place without any surface cracking, spallation or chipping. In the case of thin films a lateral cracking in the coating was induced at relatively high loads. This cracking was promoted until the delamination and chipping of the film was induced at $P_c \approx 100$ mN.

4. Influence of composition expressed in terms of Al/Si ratio on the main mechanical properties of mullite coatings, was studied in different specimens with fixed compositions (Al/Si = 5, 6 7 and 8). A rise in hardness and stiffness was evidenced as the Al/Si ratio increases in mullite coatings; from $H_f \approx 12$ GPa and $E_f \approx 130$ for sample *M3* to $H_f \approx 17$ GPa and $E_f \approx 253$ GPa for sample *M8*. On the other hand, due to the effect of residual stresses with Al enhancement of mullite, the apparent indentation fracture toughness of coatings decreases to $K_c \approx 0.6$ $MPa{\cdot}m^{½}$ for samples *M7* and *M8*.

5. An increasingly brittle response to the sliding contact was evidenced for the mullite coatings as they are enriched in Al. Different sequential fracture events were observed and documented, and their magnitude was found to increase with indentation load and the Al/Si ratio of the investigated samples. Nevertheless, it must be underlined that all the EBCs investigated presented a satisfactory response under the nanoscratches performed, as no complete loss of the coating material was registered under the load spectrum analysed.

6. Nanoindentation and nanoscratch following the top, cross-sectional and wedge testing approaches are successful methodologies to evaluate the mechanical behavior of compositionally graded mullite coatings. Enhancement in H_f and E_f with Al content, similar to those evidenced in Al-rich coatings with fixed Al/Si ratios, were also found to occur across the thickness of individual samples with graded compositions. Compositionally graded mullite coatings studied in this work presented an optimum combination of stiffness/hardness and cohesive/adhesive scratch strength, as compared to coatings with stoichiometric or extreme Al-enriched compositions.

7. The effect of temperature and hot-corrosion on the mechanical properties and structural integrity of CVD Al-rich mullite coatings with constant, and graded Al/Si ratios, may be considered as minor. Hardness and stiffness remain practically constant after the thermal stability and hot corrosion tests, denoting an insignificant effect of temperature and corrosion conditions in these properties. Similarly, the effect of temperature and hot-corrosion in the structural integrity of tested coatings may also be considered as negligible under the conditions studied in this thesis, as nanoscratches performed produced only minor damage in samples exposed to thermal stability and hot-corrosion tests.

8. In general, the CVD mullite coatings investigated in this thesis exhibit high structural integrity, as evidenced through the results of nanoscratch tests. Only minor damage was observed in the coatings under the load conditions evaluated. This may be underlined as an interesting finding as mullite coatings are expected to be used under the aggressive conditions of gas turbines, where an important loss of material may result in the loss of the protection of the coatings to the SiC substrate.

9 *Chapter*

Future Work

During the development of the work that conducted to this Thesis it was attempted to study, and comprehend, the mechanical behavior and structural integrity of mullite coatings deposited by CVD on silicon carbide, proposed as environmental barriers to be installed in components of gas turbines and microturbines for power generation. Attending to the microstructural length and features of the studied systems, micro/nanometric scale techniques such as nanoindentation and nanoscratch were used. As the time for this study is limited, main future lines of research in this field may be proposed:

- Although the outcomes of this investigation are essential pieces towards the implementation of mullite EBCs in real applications, the accomplishment of such objective calls for the study of the mechanical behavior of these materials in real service operating scenarios (high temperature and aggressive conditions, i.e. molten salts and water vapor environments). Nanoindentation at high temperatures may be a suitable technique in this regard.

- The micro/nanometric study conducted in this thesis allowed the assessment of local intrinsic mechanical properties and behavior of mullite EBCs. Macroscopic mechanical tests such as Hertzian (spherical) contact and impact testing (sandblasting), performed in larger specimens, may be of interest for understanding of the overall mechanical behavior of these systems.

- Fabrication of real components made of Si-based materials, and coated with mullite EBCs, and their testing at a “pilot” scale are the next steps towards the implementation of these systems in real applications.